

Performance Enhancement Techniques for Visible Light Communication Systems

Borja Genovés Guzmán

in partial fulfillment of the requirements for the degree of Doctor in

Multimedia and Communication Interuniversity PhD Program

Universidad Carlos III de Madrid

Advisor/Tutor:
Dr. Víctor P. Gil Jiménez

July 2019

Esta tesis se distribuye bajo licencia “Creative Commons **Reconocimiento – No Comercial – Sin Obra Derivada**”.



A mi familia, Rebeca y amigos.

Abstract

The increasing demand for ubiquitous wireless Internet access is gradually exhausting the existing radio-frequency (RF) resources. To prevent the looming spectrum crunch, the research community is considering diverse new technologies operating in higher frequency bands, such as the millimeter-wave and the visible light communication (VLC) band. The VLC solutions rely on light-emitting diodes (LEDs) that are capable of supporting high data rates on the order of Gbps.

In this Thesis, VLC point-to-point issues are investigated both in indoor and outdoor scenarios. Besides, following the trend of the cell-densification to increase the system spectral efficiency, multi-cell fully networked scenarios are also considered, where cooperative transmission techniques are proposed to address the line-of-sight (LoS) link blockage and the inter-cell interference problems.

When using optical orthogonal frequency division multiplexing (O-OFDM) schemes, the time-domain signal at the input of the LED has a high peak-to-average-power ratio (PAPR) or cubic metric (CM). It strongly degrades the performance due to the great back-off necessary to avoid the clipping effect in the LED. Thus, PAPR and CM reduction techniques become crucial to improve the system performance. In this Thesis, an adaptive network-based fuzzy inference system (ANFIS) is proposed to obtain efficient direct current optical orthogonal frequency division multiplexing (DCO-OFDM) signals with a low power envelope profile. First, signals especially designed for DCO-OFDM with very low CM, as the ones obtained from the raw cubic metric (RCM)-active constellation extension method, are used to train the fuzzy systems in time and frequency domains. Second, after the off-line training, the ANFIS can generate a real-valued signal in a one-shot way with a considerable RCM reduction from the original real-valued signal, which involves gains in the input power back-off, illumination-to-communication conversion efficiency and considerable improvements in bit error rate.

The application of VLC has been primarily oriented to indoor scenarios, but the proliferation of LEDs in the streets warrants its investigation in outdoor scenarios as well. This Thesis presents a pioneering study about the feasibility of VLC in a conventional outdoor scenario, when O-OFDM techniques are employed. The presence of sunlight reduces the system per-

formance, hence sophisticated adaptive techniques must be applied. Closed-form expressions of the signal-to-noise ratio (SNR) and of the mean cell data rate are derived and simulations demonstrate their accuracy. Besides, the outage probability when adaptive modulation and coding schemes are employed is analytically expressed. It is shown that, when modulation bandwidth adaptation is carried out depending on the time of day and the illuminance from ambient light, the mean cell data rate is increased, and the outage probability is reduced.

VLC strongly depends on the existence of a LoS link between the transmitter and the receiver to guarantee a good data rate performance, which is often a condition that is difficult to satisfy in practice. When a multi-cell VLC system is deployed, cooperative transmission schemes can be implemented in order to decrease the detrimental effect of LoS-link blockages and the high inter-cell interference levels commonly produced in such scenarios. An initial study based on a single-carrier scheme is proposed for corridor scenarios. The main idea behind the proposal is a simple cooperative transmission scheme where the receiver terminal will obtain the signal from different APs at the same time using a pulse position division multiplexing technique. This proposal outperforms traditional VLC schemes, especially when there is a LoS-link blockage, where around 3 dB of gain with respect to traditional schemes can be obtained for unoptimized parameters, and larger than 3 dB could be easily achieved.

Due to the advantages that multi-carrier schemes such as O-OFDM offer, cooperative transmission techniques based on O-OFDM schemes are studied. A preliminary study is presented, which is based on phosphor-coated white LEDs and time division multiple access (TDMA). The potential of cooperative transmission schemes in O-OFDM schemes is notable, but the use of TDMA decreases the cell data rate considerably and new alternatives must be investigated. Thus, red-green-blue(-yellow) (RGB(Y)) illumination technology and wavelength division multiplexing (WDM) are proposed to increase the communication dimensions and flexibility of the VLC system, avoiding the use of TDMA. This Thesis studies different resource allocation patterns for multi-cell cooperative transmission schemes when tri- and tetra-chromatic LEDs and O-OFDM are utilized. Firstly, guidelines are derived for maintaining the same spatial distribution of the signal-to-interference-plus-noise ratio (SINR) in every sector of the multi-cell environment in case of single-point (non-cooperative) and multi-point (cooperative) transmission. Thanks to this spatial homogeneity property, the performance characterization in the whole coverage area is simplified to the study of the SINR in a reference sector and cell. Secondly, all the possible transmission schemes are classified in terms of the LED type and avail-

Abstract

able orthogonal resources (number of frequency sub-bands per color and number of sectors per cell). The achievable data rate of each of the possible transmission schemes is evaluated under different realistic working conditions. Finally, the performance gain of different cooperation strategies among APs is also studied. The obtained results confirmed that the proper design of cooperative transmission schemes will be of paramount importance to improve the performance of ultra-dense VLC systems.

Finally, interconnection among APs is essential in a current multi-cell VLC network that can perform as a wireless local area network (WLAN), but this fully networked scenario is not easy to implement, especially in large rooms where the number of APs is large. Thus, an alternative reflection-based wireless cooperative system is proposed, where no wires are required to inter-connect APs. SNR and data rate analyses are developed, showing a proper performance and validating analytical results with simulations. Finally, an analysis of the time delay is carried out that confirms this proposal is a valid and easy alternative to deploy robust and cooperative transmission schemes in VLC-based 5G systems.

Acknowledgements

Firstly, I would like to thank my mother, Geni, my father, Goyo, and my sister, Ruth, for their support in all my decisions since I was born. They always encouraged me to accomplish this Thesis. Thanks for being by my side whenever I need you. Also, I am fortunate for having my four grandparents with me and enjoying them, Luchi and Tomás, and Luz and Goyo, who show me their life experiences and are four points of reference in my life. I cannot forget my uncle Oscar, Eva and my darling Yoel, thanks for your affection since I was a child. Finally, Rebeca, who was always in my life but strongly appeared at the beginning of my Thesis. Without your daily support I could not have achieved it.

I would like to thank my supervisor, Dr. Víctor P. Gil Jiménez. Since 2012 I have been collaborating with him, in my Bachelor's degree dissertation, Master Thesis and finally PhD. Thanks for trusting in me and for your endless encouragements during all these years. Thanks for your motivation and for attracting me to the world of research. Besides, I would like to appreciate the support of Prof. Ana García Armada, who with I had the opportunity of working in research projects and I could learn from her passion for the research and education. I appreciate the help of the rest of teachers in the Communication's research group: Máximo, Julia, Mati, Raquel and Joaquín. In addition, I would like to express my gratitude to four of the pillars in my Thesis, from whom I learnt very much and they always were willing to transfer their knowledge to enrich my training: Prof. Lajos Hanzo, Prof. Harald Haas, Prof. Mari Carmen Aguayo and Dr. Alexis Dowhuszko.

Of course, I would like to thank my colleagues in the university who with I could share my concerns in the best and worst moments, coffee breaks, trips... They know who they are, but I need to name some of them: Alancho, Afuente, Juanjo, Ana, Alberto, Juan Carlos, Estefanía, Kun, Ahmad, Hema, Ignasi, Manuel... and colleagues in The University of Edinburgh such as Mo, Anil, Enrique, Venecia, Cheng, Hamada, Mohamed...

Last but not least, I would like to thank my friends, in my hometown, Leganés, and in Oropesa, who have helped me and encouraged me not only during my academic experience, but also as far back as we are friends.

Published and submitted content

The following journal papers are included as part of this Thesis:

1. B. Genovés Guzmán and V. P. Gil Jiménez, “DCO-OFDM signals with derated power for visible light communications using an optimized adaptive network-based fuzzy inference system,” in *IEEE Transactions on Communications*, vol. 65, no. 10, pp. 4371-4381, Oct. 2017. doi: 10.1109/TCOMM.2017.2722477.

This work is wholly included in Chapters 2, 3 and 6.

The material from this source included in this thesis is not singled out with typographic means and references.

2. B. Genovés Guzmán, V. P. Gil Jiménez, M. C. Aguayo-Torres, H. Haas and L. Hanzo, “Downlink performance of optical OFDM in outdoor visible light communication,” in *IEEE Access*, vol. 6, pp. 76854-76866, 2018. doi: 10.1109/ACCESS.2018.2882919.

This work is wholly included in Chapters 2, 3 and 6.

The material from this source included in this thesis is not singled out with typographic means and references.

3. B. G. Guzmán, A. L. Serrano and V. P. G. Jiménez, “Cooperative optical wireless transmission for improving performance in indoor scenarios for visible light communications,” in *IEEE Transactions on Consumer Electronics*, vol. 61, no. 4, pp. 393-401, November 2015. doi: 10.1109/TCE.2015.7389772.

This work is partly included in Chapter 4.

The material from this source included in this thesis is not singled out with typographic means and references.

4. B. Genovés Guzmán, A. A. Dowhuszko, V. P. Gil Jiménez and A. I. Pérez-Neira, “Robust cooperative multicarrier transmission scheme for optical wireless cellular networks,” in *IEEE Photonics Technology Letters*, vol. 30, no. 2, pp. 197-200, 15 Jan.15, 2018. doi: 10.1109/LPT.2017.2781184.

This work is partly included in Chapter 4.

The material from this source included in this thesis is not singled out with typographic means and references.

5. B. Genovés Guzmán, A. A. Dowhuszko, V. P. Gil Jiménez and A. I. Pérez-Neira, “On the allocation of resources for cooperative transmission schemes in optical wireless cellular networks,” submitted to *IEEE Transactions on Wireless Communications*, 2019.

This work is wholly included in Chapters 2, 4 and 6.

The material from this source included in this thesis is not singled out with typographic means and references.

6. B. Genovés Guzmán, C. Chen, V. P. Gil Jiménez, L. Hanzo and H. Haas, “Reflection-based relaying techniques in visible light communication,” in preparation.

This work is wholly included in Chapters 2, 5 and 6.

The material from this source included in this thesis is not singled out with typographic means and references.

Other research merits

The following works have also been published:

1. J. C. Estrada Jiménez, B. Genovés Guzmán, M. J. Fernández-Getino García and V. P. Gil Jiménez, “Superimposed training-based channel estimation for MISO optical-OFDM VLC,” in *IEEE Transactions on Vehicular Technology*. doi: 10.1109/TVT.2019.2909428
2. V. P. G. Jiménez, A. L. Serrano, B. G. Guzmán and A. G. Armada, “Learning mobile communications standards through flexible software defined radio base stations,” in *IEEE Communications Magazine*, vol. 55, no. 5, pp. 116-123, May 2017. doi: 10.1109/MCOM.2017.1601219
3. B. Genovés Guzmán, A.A. Dowhuszko, V.P. Gil Jiménez, A. Pérez-Neira, “Cooperative transmission scheme to address random orientation and blockage events in VLC systems,” submitted to *15th International Symposium on Wireless Communication Systems (ISWCS)*, 2019.
4. K. Chen-Hu, B.G. Guzmán, V.P.G. Jiménez, A.G. Armada, “Layered ACO-CP-OFDM with insufficient cyclic prefix for visible light communications,” in *Proc. XXXIII Simposium Nacional de la Unión Científica Internacional de Radio (URSI)*, 2018, Granada, Spain.
5. J.C. Estrada-Jiménez, B.G. Guzmán, M.J. Fernández-Getino García, V.P.G. Jiménez, “Comparativa de técnicas de estimación de canal para VLC en interiores,” in *Proc. XXXIII Simposium Nacional de la Unión Científica Internacional de Radio (URSI)*, 2018, Granada, Spain.
6. R.P. Leal, J.J.E. Garzás, B.G. Guzmán, V.P.G. Jiménez, A.G. Armada, “Tecnología de comunicaciones móviles al alcance de todos: la experiencia del MOOC,” in *Proc. XXXIII Simposium Nacional de la Unión Científica Internacional de Radio (URSI)*, 2018, Granada, Spain.

7. B. Genovés Guzmán, T. Martínez Cortés, A. Rodríguez López and A. G. Armada, “Design of a communication, vision and sensory system for a rescuer robot in coal mine areas,” in *Proc. The International Conference on Wireless Networks and Mobile Communications (WINCOM)*, 1-4 November 2017, Rabat, Morocco.
8. A.A. Dowhuszko, V.P. Gil Jiménez, B. Genovés Guzmán, A. Pérez-Neira, “Distance-aware coordinated multi-point transmission for Terahertz band communication,” in *Proc. 2017 IEEE 18th International Workshop on Signal Processing Advances in Wireless Communications (SPAWC)*, 3-6 July 2017, Sapporo, Japan.
9. J.C. Estrada-Jiménez, B. Genovés Guzmán, M.J. Fernández-Getino García, V.P. Gil Jiménez, “Superimposed training-based channel estimation for visible light communications,” in *Proc. 2017 International Wireless Communications and Mobile Computing Conference (IWCMC)*, 26-30 June 2017, Valencia, Spain.
10. Petr Novak, Jan Babjak, Tomas Kot, Zdenko Bobovský, Petr Olivka, Wojciech Moczulski, Anna Timofiejczuk, Marek Adamczyk, Borja Genovés Guzmán, Ana García Armada, and Angel Rodríguez, “Telerescuer - reconnaissance mobile robot for underground coal mines,” in *Proc. of the Coal Operators’ Conference*, 6-9 February 2017, Wollongong, Australia.
11. Genovés Guzmán B., Adamczyk M., Timofiejczuk A., García Armada A. (2018) “Design of a sensory and vision system for a rescuer robot in coal mine areas”. In: Timofiejczuk A., Łazarz B., Chaari F., Burdzik R. (eds) *Advances in Technical Diagnostics. ICDT 2016. Applied Condition Monitoring*, vol 10. Springer, Cham.
12. B.G. Guzmán, V.P.G. Jiménez, “Señales DCO-OFDM eficientes para VLC utilizando redes neuronales adaptativas difusas (ANFIS),” in *Proc. XXIX Simposium Nacional de la Unión Científica Internacional de Radio (URSI)*, 2014, Valencia, Spain.

Contents

Abstract	iv
Published and submitted content	viii
Other research merits	x
Acronyms and abbreviations	xviii
Nomenclature	xxii
1 Introduction	1
1.1 Motivation	1
1.2 Objectives and contributions	4
1.3 Thesis layout	7
1.4 Summary	8
2 Background	9
2.1 Introduction	9
2.2 Front-end elements	11
2.2.1 Transmitter front-end	11
2.2.2 Receiver front-end	15
2.3 Noise sources	17
2.3.1 Shot noise	17
2.3.2 Thermal noise	18
2.3.3 Clipping noise	18
2.4 Transmission schemes	20
2.4.1 Single-carrier modulation	20
2.4.2 Multi-carrier modulation (O-OFDM)	20
2.4.3 Multiple access	24
2.4.4 Adaptive modulation and coding (AMC)	24
2.5 Optical wireless communication channel	25
2.5.1 Front-end elements channel	26
2.5.2 Free-space channel	26
2.6 Multi-cell networks	27
2.6.1 Downlink transmission	28
2.6.2 Interference mitigation	28
2.6.3 Handover	29
2.6.4 Backhaul	30
2.6.5 Multi-cell deployments	30
3 Single-cell VLC	33
3.1 Introduction	33
3.2 State of the art	35
3.3 Indoor	37
3.3.1 PAPR reduction technique	37
3.4 Outdoor	54

3.4.1	System model of a downlink optical-OFDM	56
3.4.2	System parameter evaluation	59
3.4.3	Results and discussion	60
3.5	Summary	69
4	Multi-cell VLC	71
4.1	Introduction	71
4.2	State of the art	72
4.3	Cooperative transmission technique in single-carrier modulation	73
4.3.1	System model	73
4.3.2	System parameter evaluation	77
4.3.3	Results and discussion	78
4.4	Cooperative transmission technique in multi-carrier modulation	79
4.4.1	Preliminary study	79
4.4.2	System model	86
4.4.3	Analysis of the SINR homogeneity requirement for the resource allocation schemes	89
4.4.4	Achievable data rate of the VLC system	98
4.4.5	Verification of the illumination requirements	103
4.4.6	Results and discussion	106
4.5	Summary	113
5	CoMP transmission based on relay-assisted techniques	115
5.1	Introduction	115
5.2	State of the art	115
5.3	Reflection-based relaying technique	116
5.3.1	System model	116
5.3.2	Downlink study	119
5.3.3	System analysis	124
5.3.4	LiFi squared-attocell network	128
5.3.5	Results and discussion	132
5.4	Summary	136
6	Conclusions and future research	137
6.1	Summary and conclusions	137
6.2	Future research	140
Bibliography		142

List of figures

1.1 The electromagnetic spectrum.	2
2.1 Ideal LED model (green and solid line) and non-linear LED model (red and dashed line) with its input-output characteristics.	14
2.2 Block diagram of an O-OFDM system.	21
2.3 Geometry of a single VLC link.	27
2.4 Cell deployments: (a) Hexagonal cell deployment. (b) Square cell deployment.	31
3.1 Block diagram of the O-OFDM system with the proposed RCM-ANFIS.	38
3.2 ANFIS diagram.	41
3.3 Symbols distribution in RCM-ACE and RCM-ANFIS techniques for a QPSK constellation.	43
3.4 Training scheme for Time-Domain model (Mod^{TD}) and Time-Frequency-Domain models (Mod_1^{TFD} , Mod_2^{TFD} , Mod_3^{TFD} , Mod_4^{TFD}) for real and imaginary parts.	44
3.5 Simplified diagram of the RCM-ANFIS training scheme.	44
3.6 Real-time scheme for Time-Domain model (Mod^{TD}) and Time-Frequency-Domain models (Mod_{Re}^{TFD} , Mod_{Im}^{TFD}) for each quadrant.	46
3.7 Simplified diagram of the RCM-ANFIS real-time scheme.	46
3.8 CCDF of RCM of a DCO-OFDM signal for a QPSK constellation.	49
3.9 CCDF of RCM of a DCO-OFDM signal for a 16-QAM constellation.	49
3.10 EVM versus biasing ratio for QPSK and 16-QAM constellations with an IBO of 8.9 dB and 10.4 dB, respectively.	51
3.11 ICE versus brightness factor for EVM = 10 % with QPSK and 16-QAM constellations.	52
3.12 ICE improvement versus brightness factor for EVM = {10 %, 15 %, 20 %} and QPSK constellation.	52
3.13 ICE improvement versus brightness factor for EVM = {10 %, 15 %, 20 %} and 16-QAM constellation.	53
3.14 BER versus SNR for EVM = 10 % with QPSK and 16-QAM constellations.	54
3.15 Block diagram of the VLC transmitter in an outdoor VLC scenario.	56
3.16 Block diagram of the VLC receiver in an outdoor VLC scenario.	56
3.17 AP radiating in an outdoor VLC scenario.	57
3.18 Single-cell scenario performance for $W = 360$ MHz, DCO-OFDM and different ambient conditions (2D: top, 3D: bottom).	62
3.19 CDF of the SNR at FD subcarrier index $k = 0$ (DC) and at a $W = 360$ MHz for different conditions. $F_{\Gamma k=0,W=360\text{MHz}}(\gamma_{\text{th}})$	64
3.20 Average data rate \bar{R} vs. bandwidth W at capacity, with AMC_1 and AMC_2 , during daytime ($E_{v,\text{ab-vr}} = 52622$ lux).	66
3.21 Average data rate \bar{R} vs. bandwidth W at capacity, with AMC_1 and AMC_2 , at night ($E_{v,\text{ab-vr}} = 0$ lux).	66
3.22 Outage probability vs. modulation bandwidth W with AMC_1 and AMC_2 , during daytime ($E_{v,\text{ab-vr}} = 52622$ lux).	67

3.23	Outage probability vs. mean cell data rate with AMC ₁ and AMC ₂ , during daytime ($E_{v,ab-vr} = 52622$ lux).	67
3.24	Optimal modulation bandwidth for maximizing the average data rate throughout the day.	68
3.25	Achievable maximal average data rate throughout the day.	68
4.1	Overhead view of a corridor scenario with 5 APs.	74
4.2	Perspective of a corridor scenario with 5 APs.	74
4.3	OOK PPDM with cooperation.	75
4.4	OOK PPDM without cooperation.	76
4.5	Person with a LoS-link blockage.	77
4.6	SNR with CoMP in a scenario where some users are obstructed.	78
4.7	SNR without CoMP in a scenario where some users are obstructed.	79
4.8	Frequency bands assignment to four types of AP (A _I , B _I , C _Q , and D _Q). Equal electrical power allocation is performed on all frequency bands.	80
4.9	Illustration of the proposed cooperative optical wireless cellular scenario in which the central cell A _I is used as reference.	80
4.10	CDF of the SINR at DC for different transmission schemes, cell radii, and LoS blockage conditions.	84
4.11	Mean cell data rate of different schemes. (a) Effect of the cell radius R . (b) Effect of the blockage probability ρ_{block} in the direct link ($R = 2.5$ m)	85
4.12	Two-tier multi-cell VLC network with $ \mathcal{C} =3$, $ \mathcal{S} =3$, and $ \mathcal{F} =3$	87
4.13	Illustration of the probability (red shaded area) that $\cos(6\theta)$ takes a value larger than Λ for different ranges of θ	92
4.14	A cooperative set with four APs cannot provide a homogeneous distribution of the SINR with cooperation, as no point is equidistant to all the APs. Red line: equidistant points between two APs (AP ₁ and AP ₂). Red triangle: equidistant point between three APs (AP ₁ , AP ₂ and AP ₃).	94
4.15	Demonstration of the fact that M must be equal to S_{coop}	94
4.16	Illustration of the cooperation sets that can be established for all possible number of sectors per cell.	96
4.17	Block diagram of a VLC transmission using O-OFDM modulation with a RGB LED. Note that, when a RGBY LED is used, an additional stream for the yellow color LED must be included.	99
4.18	Average illuminance E_{avg} (blue lines) and illuminance uniformity U_{light} (red lines) as function of the circular cell radius R for different half-power semi-angle $\phi_{1/2}$	105
4.19	CDF of the SINR when $R = 1.5$ m, $\phi_{1/2} = 60^\circ$ and no cooperation ($M = 1$) are assumed for the different resource allocation schemes.	107
4.20	Mean cell data rate $\bar{R}_{RGB(Y)}$ as function of the circular radius R of the cell when $\phi_{1/2} = 60^\circ$ and no cooperation ($M = 1$) are utilized for different resource allocation schemes.	108
4.21	Mean cell data rate $\bar{R}_{RGB(Y)}$ as function of the half-power semi-angle of the LED $\phi_{1/2}$ when $R = 1.5$ m and no cooperation ($M = 1$) are utilized for different resource allocation schemes.	109

4.22	Mean cell data rate $\bar{R}_{\text{RGB(Y)}}$ as function of the half-power semi-angle of the LED $\phi_{1/2}$ when RGB LEDs ($ \mathcal{C} =3$), $R=1.5$ m and a blockage probability $\rho_{\text{block}}=40\%$ are utilized for different resource allocation schemes.	110
4.23	Average data rate $\bar{R}_{\text{RGB(Y)}}$ as function of the blockage probability ρ_{block} when RGB LEDs ($ \mathcal{C} =3$), $R=1.5$ m, $\phi_{1/2}=60^\circ$ and some cooperation modes with tri-sector multi-cells are utilized to serve users in different areas of the cell.	112
5.1	Reflection-based relaying scenario.	117
5.2	Illustration of channel impulse responses in a simple scenario where coordinates of source S, relay R and destination D are in meters [0.5; 2.5; 3], [3; 2.5; 3] and [1.5; 2.5; 0.75], respectively. Parameters: $\rho_{\text{floor}}=0.6$, $\rho_{\text{ceil}}=0.8$, $K = 512$ subcarriers, $W=280$ MHz, $n_{\text{ref}}=1.5$, $\psi_{\text{FoV}} = 90^\circ$, $\phi_{1/2} = 60^\circ$, $G_f = 1$, $A_{\text{pd}} = 8.72$ mm ²	118
5.3	Half-duplex and full-duplex cooperative relaying techniques since the source S transmits a symbol until it arrives to the destination D.	119
5.4	Representation of the optimum power allocation factor (β_{opt}) for $k = 0$ against the horizontal distance ratio that determines the user location when a wired backhaul (a)-(b), DF/FDX cooperative-relaying in presence of RLI (c)-(d) or DF/FDX cooperative-relaying with perfect RLI cancellation is utilized (e)-(f). Also, SNR [dB] values for every β and $r_{\text{SD}}/r_{\text{RD}}$ are represented.	127
5.5	Square tessellation cellular model.	129
5.6	CDF of the SNR at subcarrier index $k = 0$ (DC) for different schemes with $\lambda_b=0.1$ user/m ²	133
5.7	CDF of the spectral efficiency for different schemes.	133
5.8	Mean user data rate vs. blocker density.	134
5.9	Jain's index of fairness vs. cell radius for different schemes.	135
5.10	Representation of the penalization when using reflection-based relay techniques (end to end time delay).	135

List of tables

3.1	Complexity summary of RCM reduction techniques.	48
3.2	RCM reductions at CCDF = 10^{-4}	50
3.3	IBO values and IBO gains.	51
3.4	ICE gain measured at BF = 0.5.	53
3.5	System parameters of the outdoor scenario.	61
3.6	Average illuminance from ambient light in the visible range and incident irradiance after blue filter throughout the day.	63
3.7	Adaptive modulation and coding SINR regions (outdoor study).	65
4.1	System parameters for the single-carrier and multi-cell scenario.	77
4.2	Adaptive modulation and coding SINR regions in the uncoded QAM and the uncoded MAM for a BER = 10^{-3}	83
4.3	Terminology used to define the different resource allocation schemes for (cooperative) multi-cell transmission.	89
4.4	Minimum number of resources needed for each cooperation setup.	95
4.5	Cluster sizes (numbers with no brackets) and possible cooperation setups (numbers between brackets) for a RGB LED ($ \mathcal{C} = 3$). Gray-shaded cells indicate the configurations that verify the previously listed requirements for homogeneity.	97
4.6	Cluster sizes (numbers with no brackets) and possible cooperation setups (numbers between brackets) for a RGBY LED ($ \mathcal{C} = 4$). Gray-shaded cells indicate the configurations that verify the previously listed requirements for homogeneity.	97
4.7	System parameters for the multi-carrier and multi-cell scenario.	104
4.8	AP optical power configuration, average illuminance E_{avg} [lux] (upper number in every cell) and illuminance uniformity values U_{light} (lower number between brackets in every cell). Brown-shaded numbers do not comply with the illumination requirements.	105
5.1	System parameters in the reflection-based relaying study.	131
5.2	Adaptive modulation and coding SINR regions (reflection-based relaying study).	132

Acronyms and abbreviations

AC	alternating current
ACE	active constellation extension
ACO-OFDM	asymmetrically clipped optical orthogonal frequency division multiplexing
AF	amplify and forward
AMC	adaptive modulation and coding
AMC _{MAM}	AMC corresponding to the uncoded MAM
AMC _{QAM}	AMC corresponding to the uncoded QAM
AMPS	Advanced Mobile Phone System
ANFIS	adaptive network-based fuzzy inference system
AP	access point
APD	avalanche photodiode
ARQ	automatic repeat request
AWGN	additive white Gaussian noise
BER	bit error rate
BF	brightness factor
BR	biasing ratio
BS	base station
CCDF	complementary cumulative distribution function
CCMC	continuous-input continuous-output memoryless channel
CDF	cumulative distribution function
CDMA	code division multiple access
CIR	channel impulse response
CLT	central limit theorem
CM	cubic metric
CoMP	coordinated multipoint
CP	cyclic prefix
CRC	cyclic redundancy check
CSK	color-shift keying
DAC	digital-to-analog converter

DC	direct current
DCMC	discrete-input continuous-output memoryless channel
DCO-OFDM	direct current optical orthogonal frequency division multiplexing
DD	direct detection
DF	decode and forward
DPPM	differential pulse position modulation
DR	dynamic range
E/O	electrical-to-optical
EPA	equal-power allocation
EVM	error vector magnitude
FD	frequency domain
FDCHTF	frequency domain channel transfer function
FDX	full duplex
FEC-aided	forward error correction-aided
FER	frame error rate
FFR	fractional frequency reuse
FFT	fast Fourier transform
FoV	field-of-view
FR	frequency reuse
FSO	free-space optical
GSM	Global System for Mobile Communications
HDX	half duplex
HetNets	heterogeneous networks
HPA	high power amplifier
IBO	input power back-off
ICE	illumination-to-communication conversion efficiency
IEEE	Institute of Electrical and Electronics Engineers
IFFT	inverse fast Fourier transform
IM	intensity modulation
IR	infrared
IrDA	Infrared data association
ISI	intersymbol interference
JT	joint transmission

LACO-OFDM	layered asymmetrically clipped optical orthogonal frequency division multiplexing
LED	light-emitting diode
LD	laser diode
LiFi	light fidelity
LoS	line-of-sight
LTE	Long Term Evolution
LTE-A	Long Term Evolution Advanced
MAM	M-ary amplitude modulation
MCFR4	multi-cell transmission scheme with frequency reuse factor 4
MIMO	multiple-input multiple-output
MISO	multiple-input single-output
mmWave	millimeter wave
NLoS	non-line-of-sight
NMT	Nordic Mobile Telephone
OFDM	orthogonal frequency division multiplexing
OFDMA	orthogonal frequency division multiple access
O-OFDM	optical orthogonal frequency division multiplexing
OOK	on-off keying
OWC	optical wireless communication
PAM	pulse amplitude modulation
PAPR	peak-to-average power ratio
PD	photodiode
PIN	positive-intrinsic-negative
PLC	power line communication
PPDM	pulse position division multiplexing
PPM	pulse position modulation
PSAM	pilot symbol assisted modulation
PWM	pulse width modulation
QAM	quadrature amplitude modulation
QPSK	quadrature phase shift keying
RCM	raw cubic metric
RCM-ACE	raw cubic metric reduction technique based on ACE

RCM-ANFIS	raw cubic metric reduction technique based on ANFIS
RF	radiofrequency
RGB	red-green-blue
RGBY	red-green-blue-yellow
RLI	residual loop interference
SCFR1	single-cell transmission scheme with frequency reuse factor 1
SCFR3	single-cell transmission scheme with frequency reuse factor 3
SDMA	spatial division multiple access
SIC	successive interference cancellation
SINR	signal-to-interference-plus-noise ratio
SNR	signal-to-noise ratio
SSL	solid state lighting
ST	superimposed training
TACS	Total Access Communications System
TD	time domain
TDM	time division multiplexing
TDMA	time division multiple access
TIA	transimpedance amplifier
TIG	topic interest group
UE	user equipment
UL	uplink
UMTS	Universal Mobile Telecommunications System
UV	ultraviolet
V2I	vehicle-to-infrastructure
V2V	vehicle-to-vehicle
VL	visible light
VLC	visible light communication
VPPM	variable pulse position modulation
WDM	wavelength division multiplexing
WDMA	wavelength division multiple access

Nomenclature

Note: The following notation will be used throughout this Thesis: boldface symbols will denote vectors whereas normalface, scalars; time-domain signals will be written in small-case letters, and frequency-domain signals will be used in capitalized letters. The dot product operator is indicated by $[\cdot] \cdot [\cdot]$, the convolution operator is denoted by $[\cdot] \otimes [\cdot]$ and finally the complex conjugate operator is written as $[\cdot]^*$.

$1(\psi)$	FoV indicator
1_{block}	indicator that is 1 or 0 if there is LoS or NLoS, respectively, between the LED and the PD
a_i	premise parameter associated with the i -th node in an ANFIS
A_{pd}	physical area of the PD
b	starting angular point of the sectorization of a cell
B_{DC}	DC-bias voltage
c_i	premise parameter associated with the i -th node in an ANFIS
c_{speed}	speed of light in vacuum
$ \mathcal{C} $	number of colors (LED chips)
d	Euclidean distance between an LED and a PD
d_v	vertical distance between an LED and a PD
\tilde{D}	variant of desired received power in the simplified SINR equation in the preliminary study of CoMP with multi-carrier modulation
\mathcal{D}	set with indices of cooperating APs
D_{input}	standard deviation of the input electrical signal in the LED
D_{output}	standard deviation of the output intensity in the LED
$D(r_0, \theta)$	received signal power at the output of the PD in polar coordinates (r_0, θ) from the serving APs
$E\{\cdot\}$	statistical expectation
E_{avg}	average illuminance
$E_{\text{r,ab}}$	incident irradiance by ambient light
$E_{\text{v}}(r_0, \theta)$	illuminance at polar coordinates (r_0, θ)
$E_{\text{v,ab}}$	illuminance from ambient light after the optical blue filter

$E_{\text{v,ab-vr}}$	illuminance from ambient light in the visible range
f_i	function computed with the consequent parameters associated with the i -th node in an ANFIS
$f_N(\cdot)$	probability density function of a standard normal distribution
F_{fe}	bandwidth factor
$F_{\Gamma}(\gamma_{\text{th}})$	CDF of the SNR evaluated in γ_{th}
$F_{\Gamma k=1}(\gamma_{\min})$	outage probability in a VLC scenario
$F_{\eta_s}(x)$	CDF of capacity η_s
$ \mathcal{F} $	number of orthogonal frequency sub-bands of the electrical signal
g_c	gain of the optical concentrator considering the FoV indicator
G	extension gain in the ACE technique
G_{AF}	amplification factor in AF
G_c	gain of the optical concentrator without considering the FoV indicator
G_f	loss of the optical filter at the receiver
$h(t)$	channel impulse response at time instant t
$h_{\text{fe}}(t)$	channel impulse response due to the front-end devices at time instant t
$h_{\text{fs}}(t)$	channel impulse response due to the free-space propagation at time instant t
$h_i(t)$	channel impulse response between the i -th AP and the user under study
$h_{\text{LoS}}(t)$	LoS component of the channel impulse response at time instant t
$h_{\text{NLoS}}(t)$	NLoS component of the channel impulse response at time instant t
$h^{\text{RD}}(t)$	CIR between the relay and the destination
$h^{\text{RR}}(t)$	CIR between the relay and its own arriving reflection
$h^{\text{SD}}(t)$	CIR between the source and the destination
$h^{\text{SR}}(t)$	CIR between the source and the relay
$H(f)$	frequency-domain channel transfer function at frequency f
$H(r, \theta)$	frequency-domain channel transfer function at polar coordinates (r, θ)
$H_{\text{fe}}(f)$	frequency-domain channel transfer function of the front-end devices
$H_{\text{fs}}(f)$	frequency-domain channel transfer function of the free-space propagation
$H_{\text{fs},i}(r_0, \theta)$	free-space path loss in frequency domain between the i -th AP and a PD located at polar coordinates (r_0, θ)
H_{LoS}	frequency-domain channel transfer function by LoS path
H_{NLoS}	frequency-domain channel transfer function by NLoS path
$H(k, r, W)$	frequency-domain channel transfer function as a function of subcarrier k , horizontal distance r and bandwidth W

$H^{\text{RD}}[k]$	FD channel response between the relay and the destination
$H^{\text{RR}}[k]$	FD channel response between the relay and its own arriving reflection
$H^{\text{SD}}[k]$	FD channel response between the source and the destination
$H^{\text{SR}}[k]$	FD channel response between the source and the relay
\mathcal{I}	set with indices of interfering APs
I_{DC}	DC-bias (current)
$I_{\text{DC},c}$	DC-bias (current) at color chip c
$I_{\text{photocurrent}}$	photocurrent generated by the PD
$I(r_0, \theta)$	received signal power at the output of the PD in polar coordinates (r_0, θ) from the interfering APs
$I(t)$	forward current of an LED in time-domain
\tilde{I}	variant of interfering received power in the simplified SINR equation in the preliminary study of CoMP with multi-carrier modulation
\mathcal{I}	set of indices of interfering APs
k	subcarrier index
K	number of subcarriers
$K_{\text{e/v}}$	luminous efficacy
\mathcal{K}_*	set of subcarriers indices that carry useful information
L	maximum allowable value of a I/Q symbol in the ACE technique
$\text{LCM}(\cdot, \cdot)$	least common multiple of two numbers
m	Lambertian emission order
M	number of APs that cooperate at every location
$n_{\text{rx}}(t)$	time-domain noise produced at the receiver
$n_{\text{rx},c}(t)$	time-domain noise produced at the receiver of color c
N	number of channel quality regions when AMC is employed
N_0	power spectral density of the total receiver noise
$N_{0,c}$	power spectral density of the total receiver noise at color c
$N_{0,\text{ab}}$	power spectral density of the shot noise produced by the natural ambient light
N_{res}	number of resources
$N_{\text{res,min}}$	minimum number of resources required for satisfying the coverage homogeneity at resource distribution level
$N_{\text{rx},c}[k]$	equivalent FD noise in reception at color c and subcarrier k
$N_{0,s}$	power spectral density of the shot noise produced by artificial light

$N_{0,s,c}$	power spectral density of the shot noise produced by artificial light at color c
$N_{0,\text{tn}}$	power spectral density of the thermal noise
O_{AVG}	average optical power
O_{SAT}	saturation output optical power
p	period of $\cos(6\theta)$
p_i	consequent parameter associated with the i -th node in an ANFIS
P	total electrical transmit power in the relaying-proposed technique
P_{opt}	optical transmit power
P_{optArea}	optical transmit power per unit area
$P_{\text{opt},c}$	optical transmit power by color chip c
$P_{\text{opt,max}}$	maximum possible optical transmit power
$P_{\text{opt,min}}$	minimum possible optical transmit power
$P_{\text{opt,rx}}$	received optical power
$P_{\text{R,tx}}$	electrical power transmitted by the relay in the relaying-proposed technique
$P_{\text{S}}(\Lambda)$	solar spectral irradiance at wavelength Λ
$P_{\text{S,tx}}$	electrical power transmitted by the source in the relaying-proposed technique
q	charge of an electron
q_i	consequent parameter associated with the i -th node in an ANFIS
$Q(\cdot)$	Gaussian Q-function
Q_0	cluster size without cooperation
Q	final cluster size including cooperation (if cooperation exists)
Q_{coop}	number of cooperation areas in which an AP cooperates
r	horizontal distance between an LED and a PD
$r_i(r_0, \theta)$	horizontal distance between the user located at (r_0, θ) and AP with index i
R	attocell circular radius
R_{L}	load resistance in the receiver circuit
R_{d}	reuse distance for hexagonal scenarios
R_{sq}	square cell radius
$\bar{R}(W)$	average cell data rate according to the bandwidth W
$\bar{R}_{\text{AMC}}(W)$	average cell data rate according to the bandwidth W
$\bar{R}_{\text{capacity}}(W)$	attainable throughput according to the bandwidth W
$\bar{R}_{\text{RGB(Y)}}(W)$	attainable throughput with a multi-carrier scheme using RGB(Y) LEDs

\tilde{R}	HEX radius
\mathfrak{R}_n	n -th channel quality region when AMC is employed
s	index of the sector
S_{coop}	number of sectors within a cooperation area
\mathcal{S}	set of sector indices
SE	spectral efficiency using AMC schemes
$\text{SE}_{\text{Shannon}}$	Shannon spectral efficiency
t_{RD}	time delay produced in the link relay to destination
t_{SD}	time delay produced in the link source to destination
t_{SR}	time delay produced in the link source to relay
t_{wired}	total time delay in a traditional wired backhaul scheme
T_{abs}	absolute temperature
$T_f(\Lambda)$	transmittance of the optical bandpass filter at wavelength Λ
$ \mathcal{T} $	number of orthogonal time slots
$U[\cdot]$	unit-step function
U_{light}	illuminance uniformity
$V[\cdot]$	signal clipping function
V_{AVG}	average input voltage
$V_{\text{ACO}}[\cdot]$	signal clipping function when ACO-OFDM is used
V_{clip}	clipping threshold in the ACE technique
$V_{\text{DCO}}[\cdot]$	signal clipping function when DCO-OFDM is used
V_{SAT}	saturation input voltage in an LED's transfer function
V_{TOV}	turn-on voltage in an LED's transfer function
W	modulation bandwidth
$x(t)$	time-domain transmitted signal (current in the LED) in the time instant t before scaling and clipping
$x[n]$	real signal after the IFFT transmitted by color chip c
$x_{\text{ANFIS}}[n]$	bipolar real-valued signal in the discrete time domain after the proposed RCM-ANFIS module
$x_{c,s}(t)$	time-domain transmitted signal (current in the LED) in the time instant t after scaling and clipping
$x_{\text{input,volt}}(t)$	time-domain input voltage of an LED after scaling and biasing
$x_{\text{R}}(t)$	signal transmitted by the relay

$x_S(t)$	signal transmitted by the source
$\hat{x}_S(t)$	signal forwarded by the relay coming from the source in decode and forward scheme
\mathbf{x}_{tr}^{TD}	TD signal obtained after the ANFIS Mod^{TD} in the training stage
$\mathbf{x}_{tr,RA_1.4}^{ACE}$	training signal resulting from the RCM-ACE technique with $L=1.4$
$\mathbf{x}_{tr,RA_3}^{ACE}$	training signal resulting from the RCM-ACE technique with $L=3$
\mathbf{X}_{tr}^{TD}	FD signal obtained after the ANFIS Mod^{TD} in the training stage
\mathbf{x}_{ts}^{TD}	TD signal obtained after the ANFIS Mod^{TD} in the test stage
$\tilde{x}_c(t)$	time-domain transmitted signal (current in the LED) in the time instant t after scaling and clipping in color chip c
$x_{tx}(t)$	optical time-domain transmitted signal
$x_{tx,c}(t)$	optical time-domain transmitted signal in color chip c
$x_{tx,i}(t)$	optical time-domain signal transmitted by the i -th AP
$x_{volt}(t)$	time-domain input voltage of an LED before scaling and biasing
$\mathbf{X}_{ts,Im}^{TD}$	imaginary part of the symbols after the ANFIS Mod^{TD} in the test stage
$\mathbf{X}_{ts,Im}^{TFD}$	FD signal obtained after the ANFIS Mod^{TD} and the corresponding ANFIS Mod_{Im}^{TFD} in the test (real-time) stage
$\mathbf{X}_{ts,Re}^{TD}$	real part of the symbols after the ANFIS Mod^{TD} in the test stage
$\mathbf{X}_{ts,Re}^{TFD}$	FD signal obtained after the ANFIS Mod^{TD} and the corresponding ANFIS Mod_{Re}^{TFD} in the test (real-time) stage
$X[k]$	FD symbol transmitted in the k -th subcarrier
$X_c[k]$	FD symbol transmitted in the k -th subcarrier transmitted by color chip c
$\tilde{X}_{i,c}[k]$	QAM symbol transported on the k -th subcarrier of color c from AP with index i
\mathbf{X}_H	O-OFDM symbol before the IFFT that satisfies an Hermitian symmetry
$\mathbf{X}_{H,c}$	O-OFDM symbol before the IFFT that satisfies an Hermitian symmetry transmitted by color chip c
$y(t)$	received time-domain signal
$y_R(t)$	signal received by the relay
$Y[k]$	frequency-domain symbol received in the k -th subcarrier
Z	noise simplification for cooperative schemes with RGB(Y) LEDs
$Z[k]$	variant of noise power in the simplified SINR equation in the preliminary study of CoMP with multi-carrier modulation

α	real value for scaling the time-domain input voltage of an LED
β	power allocation factor between a source and a relay
β_{th}	threshold of power allocation factor used for computing the optimal value
β_{opt}	optimal power allocation factor
$\Gamma(k, d, W)$	SNR as a function of subcarrier k , Euclidean distance d and bandwidth W
$\Gamma(k, r, W)$	SNR as a function of subcarrier k , horizontal distance r and bandwidth W
Γ_c	SINR at color chip c
$\Gamma_{\text{coop}}(r_0, \theta)$	SINR in cooperation mode at location (r_0, θ) in polar coordinates
$\Gamma_{\text{sa}}(r_0, \theta)$	SINR in stand-alone mode (without cooperation) at location (r_0, θ) in polar coordinates
$\Gamma_{\text{single}}[k]$	SNR obtained with single transmission from source to destination at subcarrier k
Γ_{SD}	SNR received by the destination from the source
Γ_{SRD}	SNR received by the destination from the source passing through the relay
Γ_{total}	total SNR received from the source and relay
Δ	reuse factor
$\epsilon[n]$	efficiency of the n -th region when AMC is used
ζ	ratio of DC-bias level to the electrical signal's standard deviation
ζ_c	ratio of DC-bias level to the electrical signal's standard deviation at color c
ζ_{ACO}	ratio of DC-bias level to the electrical signal's standard deviation when ACO-OFDM is used
ζ_{DCO}	ratio of DC-bias level to the electrical signal's standard deviation when DCO-OFDM is used
η_{AMC}	AMC throughput
$\eta_{\text{clip}}(t)$	clipping noise sample in the time domain
η_{led}	electrical-to-optical conversion efficiency
$\eta_{\text{led},c}$	electrical-to-optical conversion efficiency in LED color c
η_{pd}	PD's responsivity
η_{ref}	refractive index of the material that composes the concentrator at the PD
η_s	Shannon capacity
η_{sun}	sun's luminous efficacy
$\theta_{\text{lightNLoS}}$	percentage of light arriving to PD in NLoS case
θ_{sector}	angles of user locations that are within a specific sector

κ	ratio of peak amplitude to the standard deviation of the signal
κ_B	Boltzmann constant
λ_b	normalized time-domain bottom clipping level
$\lambda_{b,ACO}$	normalized time-domain bottom clipping level when ACO-OFDM is used
$\lambda_{b,DCO}$	normalized time-domain bottom clipping level when DCO-OFDM is used
λ_{lr}	learning rate in the least squares estimation for the consequent and premise parameters in an ANFIS
λ_t	normalized time-domain top clipping level
$\lambda_{t,ACO}$	normalized time-domain top clipping level when ACO-OFDM is used
$\lambda_{t,DCO}$	normalized time-domain top clipping level when DCO-OFDM is used
λ_{ue}	user equipment density in a scenario
λ_b	blocker density in a scenario
Λ	threshold of $\cos(6\theta)$ function for demonstrating the coverage homogeneity at cell level
μ	number of sectors per AP of the cooperation set
ν	number of frequency sub-bands at each color that are active in an AP
ξ	energy allocation factor in an O-OFDM symbol
ξ_{ACO}	energy allocation factor in an ACO-OFDM symbol
ξ_{DCO}	energy allocation factor in a DCO-OFDM symbol
ρ	attenuation factor related to the clipping effect
ρ_{ceil}	reflectance of the ceil surface
ρ_{floor}	reflectance of the floor surface
$\rho_{sidelobe}$	amplitude level of the sidelobes compared to the main lobe
ρ_{wall}	reflectance of the wall surface
σ_{clip}^2	variance of the clipping noise
$\sigma_{clip,ACO}^2$	variance of the clipping noise when ACO-OFDM is used
$\sigma_{clip,DCO}^2$	variance of the clipping noise when DCO-OFDM is used
σ_P	power reduction factor that measures the relation between the received optical power at the cell center and cell edge
σ_{rx}^2	noise variance at the receiver
$\sigma_{rx,c}^2$	noise variance at the receiver of color c
$\sigma_{rx,ACO}^2$	noise variance in ACO-OFDM
$\sigma_{rx,DCO}^2$	noise variance in DCO-OFDM

σ_{shot}^2	variance of the shot noise
$\sigma_{\text{thermal}}^2$	variance of the thermal noise
σ_x	electrical signal standard deviation (scaling factor in the input current of the LED)
$\sigma_{x,c}$	electrical signal standard deviation (scaling factor in the input current of the LED) in color chip c
$\sigma_{x,\text{volt}}^2$	variance of $x_{\text{volt}}(t)$
τ_{LoS}	time delay between the LED and the PD
$\epsilon_{\text{process}}$	processing time required at the relay and user equipment
ϕ	transmission direction angle from an LED
$\phi_{1/2}$	half-power semi-angle
ϕ_{input}	first input in the ANFIS example
Φ	output luminous flux of an AP
Φ_i	linguistic label associated with the i -th node in an ANFIS
Φ_{label}	first label of a fuzzy set in the ANFIS example
ψ_{input}	second input in the ANFIS example
Ψ_{FoV}	field-of-view angle at the receiver
Ψ_{label}	second label of a fuzzy set in the ANFIS example
ω_i	firing strength of the i -th node in an ANFIS
$\bar{\omega}_i$	normalized firing strength of the i -th node in an ANFIS
Ω_i^1	i -th membership function at layer 1 in an ANFIS
Ω_i^2	i -th membership function at layer 2 in an ANFIS
Ω_i^3	i -th membership function at layer 3 in an ANFIS
Ω^4	overall output of an ANFIS

Chapter 1

Introduction

1.1 Motivation

The demand of wireless communication services has rocketed in the last years. The mobile data traffic will be multiplied by seven in 2022 in comparison to the 2017 mobile data traffic and it will mean a 71% of the total Internet traffic in the world [Cisco Visual Networking Index, 2018]. At the same time, the existing radiofrequency (RF) spectrum between 300 kHz and 30 GHz is being exhausted. Researchers are making much effort to propose RF techniques that are capable of satisfying the increasing wireless data rate demand. For example, massive multiple-input multiple-output (MIMO) was proposed as a novel technique [Larsson *et al.*, 2014] where many transmitting and receiving antennas are utilized to increase the capacity. However, it is expected that the RF frequency band no longer fulfill the future wireless data services. Thus, new technologies that work at higher frequencies are being investigated.

Mainly two new high-frequency technologies are being investigated: millimeter wave (mmWave) [Rappaport *et al.*, 2013] and optical wireless communication (OWC) [Komine and Nakagawa, 2004]. The former utilizes frequencies between 30 and 300 GHz. Due to the intrinsic characteristics of such frequencies, mmWave needs line-of-sight (LoS) between transmitter and receiver to work properly. Thus, a small multi-cell network will be used, where the hardware cost is much higher than in optical wireless networks. This makes mmWave deployment hard.

Differently, OWC utilizes frequencies in the range of 3 THz and 790 THz, including infrared (IR) and visible light (VL) frequencies. Figure 1.1 shows the well-known electromagnetic spectrum. Note that the frequency range available for OWC is around 25000 times larger than the one dedicated to traditional RF services, and around 3000 times larger than the one estimated to be used by mmWave. This encouraging fact shows the potential of OWC that can be exploited by employing transmission and detection techniques to achieve a huge capacity in the near future. On top of that, OWC attracts the attention of many researchers because of the following advantages:

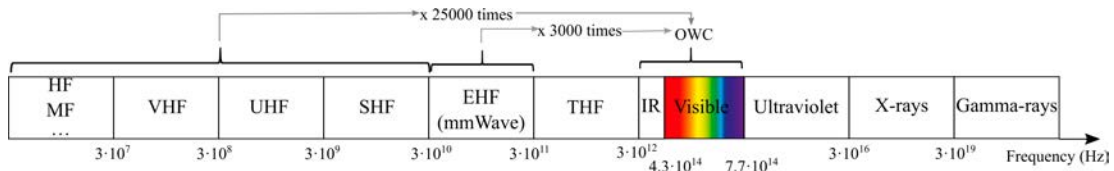


Figure 1.1: *The electromagnetic spectrum.*

- Complementarity: Since the signals in OWC do not interfere with RF systems, both technologies can perform jointly. In addition, OWC technology can be installed in scenarios where RF services are not allowed such as hospitals and airplanes.
- Security: One of the main concerns of RF waves is the control of its propagation. In indoor scenarios, any RF system could jam other systems located in nearby rooms. However, optical waves do not go through walls and so systems in separate rooms will be independent of each other.
- Cost: The optical spectrum is unlicensed and the components in OWC are low-cost and off-the-shelf.

When the VL range is utilized for communication purposes, the technology is named visible light communication (VLC). The widespread deployment of light-emitting diode (LED)-based lighting facilitates the VLC installation creating a dense cell deployment. VLC is capable of providing illumination and high-speed wireless communication simultaneously. Thus, VLC is a potential technology to prevent the looming RF spectrum crunch and guarantee the demanded wireless communication services in the future.

In the last decades there is a trend of reducing the cell size in favor of augmenting the spectral efficiency [Bhushan *et al.*, 2014]. Currently, operators are offering the installation of femtocells to offload users from the macro-cells and, in that way, to increase the network efficiency [Andrews *et al.*, 2012]. The networks are becoming heterogeneous, where macro, micro, pico, femto cells and relays cooperate together to improve the signal-to-noise ratio (SNR) and, at the same time, optimize the network efficiency and throughput. Thus heterogeneous networks (HetNets) are being created. VLC performs along the same lines as this cell densification concept where few users share the same resources. In VLC, a fully-networked multi-cell scenario, named attocell network, can be created to guarantee a seamless connectivity and mobility [Haas *et al.*, 2016].

VLC is still an immature technology of which great benefits are expected. VLC must be further developed and the research community must solve important issues to turn VLC into a communication technology of everyone's daily life: regarding the intrinsic characteristics of VLC and its components, transmission and reception techniques must be further discovered to solve the limited bandwidth of the front-end devices, the channel estimation and the non-linearity of the LED's transfer function; since VLC has a potential also in outdoor scenarios as the smart cities of the near future, a thorough study of its viability in such scenarios is required; finally, when working in indoor multicell scenarios, both the inter-cell interference level and LoS-link blockage probability are higher in comparison to what occurs in RF systems, then mitigation inter-cell interference techniques capable of tackling the LoS-link blockage must be investigated.

In indoor single-cell scenarios, a simple transmission and reception model can be utilized. The issues that appear in such scenarios are typical of the physical layer: the narrow bandwidth of the front-end devices (few tens of MHz) limits the achievable data rate and some techniques must be applied such as blue filtering when using phosphor-coated LEDs, or transmitter, receiver and adaptive equalization; the non-linear LED's transfer function, when working with multi-carrier modulation techniques that produce a high peak-to-average power ratio (PAPR), degrades the VLC system performance. This PhD Thesis proposes a novel PAPR reduction technique to facilitate the use of multi-carrier modulation techniques in VLC.

When working in outdoor single-cell scenarios, the shot noise produced by the sunlight and the skylight degrades the system performance. Thus, a study in a realistic scenario must be developed in order to determine the feasibility of VLC in outdoor scenarios. There is a large variety of system metrics for evaluating the downlink system performance. Among them, the SNR and the consequent estimated data rate are straightforward metrics to determine the link quality. Although several works studied the OWC in outdoor scenarios, few of them relied on LED access points (APs) located in outdoor scenarios such as street lights or LED boards at railway stations, which will be key elements in future smart cities. A section of this Thesis investigates the viability of VLC in these scenarios to open new research works in the field.

An attocell network is required to provide a seamless coverage and guarantee mobility in a certain way. When a multi-cell system is deployed, the inter-cell interference level increases, but, if interference management techniques are properly implemented, the system performance augments and also the LoS-link blockage may be tackled. The inter-cell interference charac-

teristics in VLC scenarios are different from the ones in RF, where cell-edge users are mainly affected. In an attocell network, lighting must come from more than one AP in order to comply with the illumination requirement [EN 12464-1:2002 E, 2002]. It makes inter-cell interference increase but, at the same time, it favors the proposals of coordinated multipoint (CoMP) techniques. For these reasons, these techniques are also considered and investigated in this PhD Thesis.

1.2 Objectives and contributions

This Thesis focuses on proposing solutions to some of the physical layer issues of VLC and investigating the inter-cell interference and LoS-link blockage problems in attocell networks. This Thesis addresses the following research objectives:

- Identify and provide solutions to single-cell VLC issues, both in indoor such as the non-linear LED's transfer function and outdoor such as the extreme shot noise induced at the receiver.
- Improve the performance of single-carrier multi-cell scenarios with high inter-cell interference level and LoS-link blockage probability.
- Improve the performance of multi-carrier multi-cell scenarios with high inter-cell interference level and LoS-link blockage probability.

Several contributions are established by following these objectives.

Regarding the first objective, it was found that the LED model has a non-linear transfer function similar to the well-known high power amplifiers (HPAs) in RF systems. However, the intensity modulation/direct detection (IM/DD) technique required in VLC systems compels to individually study this problem in VLC. Several proposals to reduce the PAPR have been presented in the existing research publications. Differently, we opt to optimize the cubic metric (CM) instead of the PAPR because of being considered as a more effective metric to evaluate the power derating factor [TDoc R1-060023, 2006]. Different from previous research works in VLC, well-balanced constellations are obtained by using an adaptive network-based fuzzy inference system (ANFIS) trained by the active constellation extension (ACE) method. Thus, signals with low power envelope profile are achieved. This contribution is presented in:

-
- B. Genovés Guzmán and V. P. Gil Jiménez, “DCO-OFDM signals with derated power for visible light communications using an optimized adaptive network-based fuzzy inference system,” in *IEEE Transactions on Communications*, vol. 65, no. 10, pp. 4371-4381, Oct. 2017. doi: 10.1109/TCOMM.2017.2722477

In outdoor scenarios, the most predominant noise source of VLC systems is the shot noise produced by the large sunlight and skylight. The illuminance coming from ambient light is multiplied by 100 in comparison to indoor scenarios, which may blind the receiver. We derive SNR analytical expressions that are valid for a further real deployment of VLC outdoor scenarios. We demonstrate the need of an adaptive scheme that modifies the modulation bandwidth depending on the sunlight- and skylight-induced performance degradation, when a multi-carrier transmission scheme is used. This work is published in:

- B. Genovés Guzmán, V. P. Gil Jiménez, M. C. Aguayo-Torres, H. Haas and L. Hanzo, “Downlink performance of optical OFDM in outdoor visible light communication,” in *IEEE Access*, vol. 6, pp. 76854-76866, 2018. doi: 10.1109/ACCESS.2018.2882919

With regard to the second objective, the main issues in indoor VLC multi-cell scenarios are the inter-cell interference and the possibility of LoS-link blockage. The need of a homogeneous lighting causes great inter-cell interference when light fixtures are also employed for communication purposes. Besides, LoS-link blockages in VLC are often and decrease the SNR in several tens of dB [Chen and Haas, 2017]. Thus, CoMP techniques are considered to be adopted in attocell networks in order to decrease the inter-cell interference level. Additionally, CoMP techniques can provide a more robust downlink where every user receives constructive signals from more than one AP. To further evaluate this technique, a simple scenario is considered when employing single-carrier modulation schemes. This contribution can be found in:

- B. G. Guzmán, A. L. Serrano and V. P. G. Jiménez, “Cooperative optical wireless transmission for improving performance in indoor scenarios for visible light communications,” in *IEEE Transactions on Consumer Electronics*, vol. 61, no. 4, pp. 393-401, November 2015. doi: 10.1109/TCE.2015.7389772

The third research objective leads to the fourth contribution. Muti-carrier modulation schemes are known to provide much better performance than single-carrier ones because, among other

reasons, by using orthogonal frequency subcarriers such as in orthogonal frequency division multiplexing (OFDM), the achieved data rate is much higher than in single-carrier transmissions. Thus, CoMP techniques are adapted to multi-carrier modulation schemes. Previous works in the literature proposed adaptive CoMP techniques where constant channel sensing are required to detect a LoS-link blockage and then re-allocate resources. A static CoMP technique is conceived in this PhD Thesis to provide a stable and robust communication. The importance of providing a homogeneous coverage encourages to study all the possible resource-reuse patterns that guarantee such a homogeneity. To this respect, two journal contributions were written:

- B. Genovés Guzmán, A. A. Dowhuszko, V. P. Gil Jiménez and A. I. Pérez-Neira, “Robust cooperative multicarrier transmission scheme for optical wireless cellular networks,” in *IEEE Photonics Technology Letters*, vol. 30, no. 2, pp. 197-200, 15 Jan.15, 2018. doi: 10.1109/LPT.2017.2781184
- B. Genovés Guzmán, A. A. Dowhuszko, V. P. Gil Jiménez and A. I. Pérez-Neira, “On the allocation of resources for cooperative transmission schemes in optical wireless cellular networks,” submitted to *IEEE Transactions on Wireless Communications*, 2019.

Finally, the fifth contribution is also included within the third objective. The great advances in the development of analytical VLC non-line-of-sight (NLoS) channel impulse response (CIR) calculation can be leveraged to provide precise downlink models based on NLoS links. Since LoS-link blockages are likely in VLC indoor scenarios, a reflection-based relaying technique is studied to strengthen the downlink communication. Neighboring APs are provided of an additional photodiode (PD) which enables them to relay data coming from floor reflections by using conventional relaying techniques such as amplify and forward and relay and forward, in full duplex or half duplex modes. It is presented as a suitable alternative to the traditional wired backhaul link and it is in preparation to be submitted to an international journal:

- B. Genovés Guzmán, C. Chen, V. P. Gil Jiménez, L. Hanzo and H. Haas, “Reflection-based relaying techniques in visible light communication,” in preparation.

1.3 Thesis layout

The rest of this Thesis is structured as follows. In Chapter 2, the background of VLC is presented. Firstly, the history of OWC and, namely, VLC, is introduced highlighting the milestones and the current state of its standardization to formalize such advances. Later, the relevant concepts of a VLC system and its impairments are detailed, which includes: the front-end elements describing its classification, characteristics, components and fundamental analysis; noise sources and its characterization; transmission schemes, detailing the single-carrier and multi-carrier modulation schemes, multiple access and adaptive modulation and coding schemes; optical wireless communication channel, defining the front-end elements channel and the free-space channel; and finally the concepts related to the multi-cell VLC networks, including the downlink transmission, interference mitigation, handover, backhaul and types of multi-cell deployments.

Chapter 3 analyzes the common issues that are presented in a VLC point-to-point or single-cell system. Namely, the issue related to the high PAPR or CM in optical-OFDM (O-OFDM) systems is introduced, and an alternative of CM reduction technique is proposed and compared with previous methods presented in the literature. Besides, a first study of VLC in an outdoor environment when using O-OFDM is presented and analyzed, providing closed-form expressions that evaluate and allow optimizing the system performance in such scenarios.

Chapter 4 introduces the multi-cell VLC scenario as a solution to prevent the damage of LoS-link blockages in VLC by using cooperative transmission techniques. Differently from the state-of-the-art solutions where dynamic resource allocation and AP assignment techniques are used, the use of static resource allocation techniques is motivated by the reliability, stability and low complexity required in VLC systems. Thus, static resource allocation techniques are presented where cooperation among adjacent cells is carried out. Firstly, a proposal using a single-carrier cooperative transmission technique is presented, but the potential of multi-carrier modulation techniques inspires to develop cooperative techniques based on O-OFDM schemes. A preliminary study of a cooperative transmission technique in multi-carrier modulation using phosphor-coated white LEDs is presented. However, a time division multiple access (TDMA) technique is required to cooperate among neighboring cells, which decreases the average cell data rate considerably. Thus, RGB and wavelength division multiplexing (WDM) are proposed to increase the communication dimensions and flexibility of the VLC system, avoiding the use of TDMA. All the possible resource allocation schemes that guarantee a homogeneous cover-

age are presented in terms of number of colors, number of sub-bands per color and number of sectors per cell. Finally, the possible number of cooperating APs guaranteeing the coverage homogeneity is studied, and a comparison of these schemes is shown complying with the regulation of illumination.

Chapter 5 presents a novel alternative based on relaying techniques to minimize the harmful effect of LoS-link blockage in VLC. Since the wired backhaul network limits the deployment of the system when the topology needs to be changed or the room becomes large, a wireless relaying-based technique is proposed to perform as a wireless backhaul link, which uses the reflections in the floor as a relaying path for transmitting the information to neighboring APs provided of an additional PD. Thus, decode-and-forward and amplify-and-forward techniques are studied to perform and increase the reliability and spectral efficiency of the VLC system.

Chapter 6 summarizes the main contributions of this Thesis and presents the future research directions.

1.4 Summary

The deployment of VLC attocells has been considered in recent research studies. Whilst the inter-cell interference problem in such scenarios are considered in a same way as traditional RF systems, the inter-cell interference in VLC must be addressed with specific techniques. Besides, LoS-link blockage is often in indoor scenarios, which motivates the development of cooperative transmission techniques. Very limited research has been conducted on proposing static transmission techniques that boost the stability and robustness in the network. The research presented in this Thesis focuses on the development of static cooperative transmission schemes that guarantee a homogeneous coverage in the whole network. They tackle the high inter-cell interference levels and the likely LoS-link blockage problem that is typical in VLC indoor scenarios. In addition, this Thesis proposes a wireless backhaul network based on the reflected paths in order to simplify the deployment of a VLC fully-networked system. Finally, this Thesis helps to solve some of the point-to-point issues both in indoor and outdoor scenarios, such as the non-linearity in the LED's transfer function and the large shot noise induced at the receiver by the sunlight and skylight.

Chapter 2

Background

2.1 Introduction

An OWC is defined as a transmission without wires between two points separated at a certain distance using the optical frequencies in the electromagnetic spectrum. The earliest forms of optical wireless communications are dated thousands of years ago, where the ancient Greeks and Romans sent signals using fire beacons. It is also known that American Indians used smoke signals to advertise their presence in a hostile territory. Besides, some of the ancient optical wireless communication system are still being used at this time, such as the lighthouses employed to indicate the proximity of coastlines to ships. The first advanced system of OWC is the photophone invented by Alexander Graham Bell [Bell, 1880]. A speech signal was transmitted at a distance of around 213 meters by using, at the transmitter, a reflective membrane that vibrates with the voice signal and, at the receiver, a selenium cell photodetector.

OWC progressed with the advances produced in optoelectronic devices such as the invention of LEDs, PDs and laser diodes (LDs), which allowed to get high-speed communications using IR, VL and ultraviolet (UV) wavelengths. For outdoor long-distance applications, free-space optical (FSO) communications were demonstrated during 1960s and 1970s [Khalighi and Uysal, 2014]. The pioneer work in short-range OWC was published in [Gfeller and Bapst, 1979] where a 100 kbps system with a diffused IR radiation was demonstrated. Besides, the authors analytically discovered that transmission rates at hundreds of Mbps can be achieved. With the progress in the IR technology, in 1993 the infrared data association (IrDA) published a set of protocols for IR communication [Barker and Boucouvalas, 1998]. Solid state lighting (SSL) has considerably evolved during last years and LED lamps have replaced gradually other kinds of lighting technologies (e.g., incandescent, fluorescent and/or halogen lamps). Thus, this trend in lighting infrastructures inspires the deployment of wireless communications using the lighting network, known as VLC [Pathak *et al.*, 2015]. VLC technology can provide Internet access and lighting simultaneously. Several works demonstrated VLC links achieving Gbps using off-the-shelf LEDs [Chun *et al.*, 2016] [Tsonev *et al.*, 2014]. In 2011, the Institute of Electrical

and Electronics Engineers (IEEE) published the standard [IEEE Std. 802.15.7-2011, 2011] for short-range VLC, where primarily on-off keying (OOK), variable pulse-position modulation (VPPM) and color-shift keying (CSK) modulation schemes were used. Currently, a topic interest group (TIG) in IEEE was created with the aim of determining the opportunities presented by the SSL infrastructure for optical wireless communications and standardizing its performing in [IEEE 802.11bb, 2017].

A VLC network is typically arranged in a cellular structure. A cellular system is a wireless network whose coverage area is divided in non-overlapping cells [Goldsmith, 2005]. User equipments (UEs) within a cell are served by the corresponding AP usually located in the middle of the cell. Besides, APs are interconnected through a backhaul that allows the network to connect with external ones. This backhaul also connects the APs with a central entity that manages the whole network. Thus, functionalities such as power control, resource allocation and handover procedures can be easily conducted to increase the global network performance. Different from single-cell scenarios, a cellular system where there are multiple cells can accommodate multiple users connected simultaneously in a more efficient way. Since APs in a cellular system can reuse resources, the area spectral efficiency is increased. Because of these advantages, cellular systems are used since the beginning of mobile wireless networks:

- Mobile 1G: The first generation of mobile networks laid the foundation for current cellular systems by using frequency reuse (FR) and providing a seamless coverage allowing mobility. They offered analog voice services. Standards such as Nordic Mobile Telephone (NMT), Advanced Mobile Phone System (AMPS) or Total Access Communications System (TACS) belonged to the 1st generation of mobile networks.
- Mobile 2G: In this generation the TDMA was employed to serve multiple users allocating the traffic in time slots. Analog voice services were replaced by digital data using small packets, which allows reducing the size of user equipments considerably. The most extended 2G standard was the Global System for Mobile communications (GSM) standard [Rahnema, 1993] and it keeps working nowadays.
- Mobile 3G: This generation introduced the code division multiple access (CDMA) to serve multiple users at the same time and frequency [Dahlman *et al.*, 1998]. The first 3G standards were Universal Mobile Telecommunications System (UMTS) or CDMA2000 [Dahlman *et al.*, 1998]. The increasing demand for wireless services saturated such standard and new alternatives were needed.

- Mobile 4G: The huge demand on wireless data services pushed to look for new and more efficient transmission techniques. In the 4rd mobile generation [ETSI TS 136 300 V13.2.0, 2016], OFDM and MIMO techniques were standardized in Long Term Evolution (LTE) and LTE-Advanced (LTE-A).

The 5th generation of mobile communications is characterized by an extreme heterogeneity and flexibility in the network [Andrews *et al.*, 2014]. However, since cellular systems have demonstrated its efficiency in a more than enough way, it is also included in this current standard. Thus, cellular systems are developed over the world and it is known that a network densification is an efficient way to satisfy the increasing demand of wireless data services [Bhushan *et al.*, 2014].

Additionally, the SSL technology is also gradually replacing the halogen lighting in outdoor scenarios. Hence, we witness a proliferation of scenarios capable of transmitting information by means of light: LED boards, street lights, traffic lights, head lights, etc. The number of these scenarios is increasing, which may lead to the vision of a smart city where all these sources provide Internet access. This fact opens the door for research studies of VLC techniques in outdoor scenarios.

2.2 Front-end elements

Both ends of a VLC link are key elements for a correct transmission. On one side, the light source, performing as a transmitter, converts electrical signals into optical ones. On the opposite side, a light sensing device converts the arriving optical signal into electrical one, usually with the help of a concentrator and an optical filter. This subsection describes the key aspects of these front-end devices.

2.2.1 Transmitter front-end

An LED is usually employed as transmitter in OWC. An LED has a diffused radiation pattern that can be controlled by using a collimator. Lately, high efficiency LEDs have been developed and they are being installed in the current lighting systems. Due to its lighting and modulation speeds characteristics, LED is considered as the best suitable device for VLC [Hanzo *et al.*, 2012]. IM is carried out at the LED because it is an incoherent source and, as a consequence,

it is not possible to control the phase of the output signal. Thus, the optical output signal is proportional to the amplitude of the input signal.

2.2.1.1 Types of LEDs

VLC is thought to perform with white light taking advantage of the light fixtures installed in a room. There are typically two kinds of LEDs to provide white light:

- Phosphor-coated LED: made mostly of a blue LED with a yellow phosphor whose combination forms a white light. The use of a phosphor material produces a slower temporal response and the available bandwidth is limited to a few of MHz. However, the slow response of the yellow component is usually blocked at the receiver by using a blue optical filter.
- Red-green-blue (RGB) LEDs: single LEDs that emit the primary colors and then its combination forms a white light. This method can also be used with red-green-blue-yellow (RGBY) LEDs, where a yellow LED contributes to the formation of white light. RGB(Y) LEDs can provide high capacity values due to the use of independent tri(tetra)-chromatic chips that do not suffer from a slow response of the phosphor material. Besides, RGB(Y) LEDs give the possibility of using WDM transmission techniques [Cui *et al.*, 2016].

2.2.1.2 Optical transmit power and illumination requirements

The power transmission of an LED varies with the direction, i.e., the luminous intensity over a surface is not the same. The optical transmit intensity at an angle ϕ can be calculated with a generalized Lambertian law as [Kahn and Barry, 1997]

$$P_{\text{opt}}R(\phi) = P_{\text{opt}} \frac{m+1}{2\pi} \cos^m(\phi) \quad [\text{W}/\text{sr}], \quad (2.1)$$

where P_{opt} is the total optical transmit power, $R(\phi)$ is the radiation profile of the LED dependent on the transmission direction angle ϕ and m is the Lambertian emission order computed according to the half-power semi-angle $\phi_{1/2}$ as

$$m = -\frac{1}{\log_2 (\cos(\phi_{1/2}))}. \quad (2.2)$$

By using proper optical elements, the Lambertian emission order can be modified by adjusting $\phi_{1/2}$ according to the necessities.

Special attention is needed to meet the illumination regulation which, in practice, implies the verification of two optical metrics [EN 12464-1:2002 E, 2002]. Firstly, the average illuminance E_{avg} in the whole room must be higher than a minimum value. Secondly, the illuminance uniformity U_{light} , which evaluates the ratio between the minimum illuminance level to the average illuminance in the room, must be high enough such that people would not notice different lighting levels in the same room. Both requirements depend on the task that will be carried out in the room.

The illuminance at polar coordinates (r_0, θ) is formulated as

$$E_v(r_0, \theta) = \Phi \cdot \frac{\sum_{\forall i} |H_{\text{fs},i}(r_0, \theta)|}{A_{\text{pd}}}, \quad (2.3)$$

where $|H_{\text{fs},i}(r_0, \theta)|$ denotes the path loss between the i -th AP and the user located at (r_0, θ) , and Φ is the output luminous flux of every AP computed as

$$\Phi = K_{e/v} \cdot P_{\text{opt}}, \quad (2.4)$$

where $K_{e/v}$ is the luminous efficacy measured in lm/W [Meyer-Arendt, 1968]. The PD's physical area is denoted by A_{pd} .

2.2.1.3 Non-linear LED's transfer function

As in RF systems when using HPAs, a VLC system is limited by the dynamic range (DR) of the LED defined as

$$\text{DR} = V_{\text{SAT}} - V_{\text{TOV}}, \quad (2.5)$$

where V_{SAT} is the saturation input voltage and V_{TOV} the turn-on voltage that is the minimum threshold required to emit light. The transfer function of the LED is linear in a restricted range and the input signal will be distorted if it includes samples out of this range. Not only the direct current (DC) and alternating current (AC) signal values must be within a DR in order not to distort the signal, but also to avoid overheating the LED. The input real signal must be scaled

and biased to make it work within the DR as

$$x_{\text{input,volt}}(t) = \alpha \cdot x_{\text{volt}}(t) + B_{\text{DC}}. \quad (2.6)$$

The real value B_{DC} is used for guaranteeing a unipolar signal, whereas the real value α is used for scaling $x_{\text{volt}}(t)$ within the DR of the LED.

By using an ideal linear LED input-output characteristic [Garcia Doblado *et al.*, 2015] as Figure 2.1 represents, these parameters give rise to others, such as the average optical power (O_{AVG}), associated with the input average voltage (V_{AVG}), and the saturation output optical power (O_{SAT}), associated with V_{SAT} . Indeed, O_{AVG} is also defined as the required illumination level and establishes the B_{DC} that is the mean value of $x_{\text{input,volt}}(t)$. As introduced in [Garcia Doblado *et al.*, 2015], the B_{DC} and α parameters determine the biasing ratio (BR) and the input power back-off (IBO) [Yu, 2014], defined as

$$\text{BR} = (B_{\text{DC}} - V_{\text{TOV}})/\text{DR}, \quad (2.7)$$

and

$$\text{IBO} = \text{DR}^2/(\alpha^2 \cdot \sigma_{x,\text{volt}}^2), \quad (2.8)$$

where $\sigma_{x,\text{volt}}^2$ is the variance of $x_{\text{volt}}(t)$.

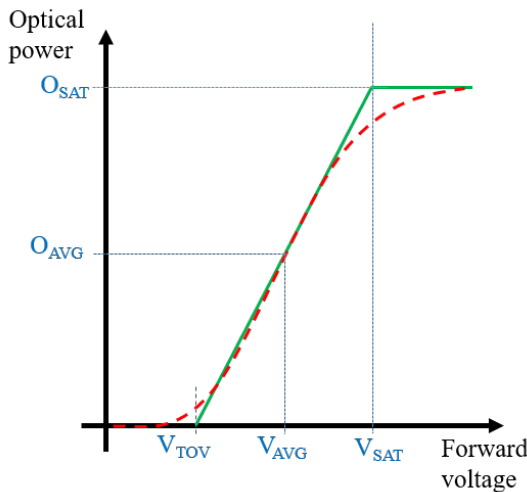


Figure 2.1: Ideal LED model (green and solid line) and non-linear LED model (red and dashed line) with its input-output characteristics.

Figure 2.1 represents an ideal (realistic) LED transfer function in green and solid (red and

dashed). The output optical power is linear with the forward current $I(t)$ by means of an electrical-to-optical (E/O) conversion efficiency η_{led} . Thus, the mean optical power is

$$P_{\text{opt}} = \eta_{\text{led}} \cdot \mathbb{E}\{I(t)\}. \quad (2.9)$$

Thus, the transfer function can be straightforwardly represented with the forward voltage as the input signal and optical power as the output signal.

A low value of α implies a low variance of $x_{\text{input,volt}}(t)$ in (2.6) which means a poor use of the DR of the LED, whereas a high value of α can result in a clipping of the optical signal. Thus, the scale factor α controls the necessary IBO defined in (2.8). The IBO represents a decrease in the maximum output optical power level in order to guarantee that the entire signal is within the linear region of the LED.

The lower the IBO, the higher the power of the signal at the input of the LED, but at the same time the signal distortion increases due to the clipping effect.

2.2.2 Receiver front-end

Devices with a high sensitivity and wide bandwidth are desired on the receiver side in order to build a high-speed VLC communication system. The receiver front-end is in charge of converting, proportionally, the detected received optical power into a photocurrent. Thus, the DD technique is utilized at the receiver. There is a great variety of optical devices that can be employed as receptor: imaging sensors [Takai *et al.*, 2013], solar panels [Wang *et al.*, 2015] and even LEDs [Giustiniano *et al.*, 2012]. However, these devices are not suitable for high-speed communication because they suffer from a slow frequency response. The most appropriate device for high-speed VLC applications is the PD [Elgala *et al.*, 2009].

2.2.2.1 Types of PDs

There are mainly two types of PDs:

- Positive-intrinsic-negative (PIN) PD: It is built by a p -type semiconductor and a n -type semiconductor separated by an undoped intrinsic semiconductor. The charge carriers from p and n semiconductors are stored in the intrinsic semiconductor until an equilibrium point is reached. From this point on, the flow of free electrons and holes generates a

photocurrent. The high-level injection process transports charge carriers from the semiconductor *p* to *n* at a high speed, which makes PIN PD suitable for applications that require a high frequency response. The responsivity of a PIN PD is in the range of 0.2 and 0.4 A/W, and the achievable 3-dB bandwidth is around hundreds of MHz and even GHz. Thus, the PIN PD will not be a bandwidth-limiting device in VLC.

- Avalanche photodiode (APD): This type of PD shows a high current gain due to an impact ionization when applying a high reverse bias voltage. The responsivity of an APD is typically larger than unity. However, the impact ionization effect can cause extra noise and it is sensitive to temperature changes.

2.2.2.2 Characteristics

As mentioned in Section 2.2.1.2, the light emitted power is diffused following an emission pattern. Thus, only a small portion of power arrives to the PD. High-sensitivity PDs must be used to allow a desired performance. The photocurrent generated by the PD is proportional to the received optical power $P_{\text{opt,rx}}$ as follows

$$I_{\text{photocurrent}} = \eta_{\text{pd}} P_{\text{opt,rx}}, \quad (2.10)$$

where η_{pd} is the PD's responsivity. The received optical power, also called, the detected optical power, is directly proportional to the PD's area. Then, the larger the PD, the larger the collected power is. However, PD is a capacitive device whose capacitance increases with its area. Thus, large capacitance values decrease the PD's response speed and degrade the performance of communications requiring high-modulation bandwidth. As a conclusion, a trade-off between the sensitivity and the speed response must be considered to determine the PD's area. A solution is the use of multiple PDs in order to increase the equivalent area without degrading the speed response.

2.2.2.3 Optical concentrator and filter

An optical concentrator is usually employed at the receiver for improving the receiving signal and, at the same time, avoiding the reception of interfering optical power. Its gain is formulated

as [Kahn and Barry, 1997]

$$g_c = G_c 1(\psi) = \frac{n_{\text{ref}}^2}{\sin^2(\psi_{\text{FoV}})} 1(\psi) \quad (2.11)$$

where G_c is the concentrator gain, n_{ref} is the refractive index of the material that composes the concentrator and ψ_{FoV} is the field-of-view (FoV) angle at the receiver. A variable denoted by $1(\psi)$ indicates whether the LoS transmission is within the FoV of the receiver or not, and it is defined as

$$1(\psi) = \begin{cases} 1, & \text{if } \psi \leq \psi_{\text{FoV}} \\ 0, & \text{if } \psi > \psi_{\text{FoV}} \end{cases}, \quad (2.12)$$

where ψ is the incident angle.

Besides, on the receiver side, an optical filter is typically added in order to eliminate extra signals that are out the desired optical band. This filter is commonly made by glass or plastic that causes an extra loss denoted by G_f due to the absorption and reflection phenomena [Kahn and Barry, 1997]. Thus, both the optical concentrator gain and the filter loss must be considered to compute the receiver optical power.

2.3 Noise sources

A VLC system experiences impairments due to three main noise sources: the shot and the thermal noise, which are produced at the receiver side and have been well studied in the literature [Komine and Nakagawa, 2004]; and the clipping noise, which has been lately considered [Dimitrov *et al.*, 2012] when multi-carrier systems were adopted to be used in VLC, and it is produced at the transmitter and subsequently propagated.

2.3.1 Shot noise

The fluctuation in number of photons that arrive to the destination produces the so-called shot noise. The photons are randomly emitted in time from a source following a Poisson distribution. However, when the number of photons is large, this fluctuation can be modeled as a Gaussian distribution. Then, the shot noise is considered as an additive white Gaussian noise (AWGN)

with variance

$$\sigma_{\text{shot}}^2 = (N_{0,\text{s}} + N_{0,\text{ab}}) \cdot W = (2qP_{\text{opt,rx}}\eta_{\text{pd}} + 2qE_{\text{r,ab}}A_{\text{pd}}\eta_{\text{pd}}) \cdot W, \quad (2.13)$$

where $N_{0,\text{s}}$ and $N_{0,\text{ab}}$ are the power spectral density of the shot noise produced by the light power coming from LEDs ($P_{\text{opt,rx}}$) and from the ambient light ($E_{\text{r,ab}}A_{\text{pd}}$), respectively. The modulation bandwidth is denoted by W . The incident irradiance by ambient light is represented by

$$E_{\text{r,ab}} = \int_{\Lambda_1}^{\Lambda_2} P_{\text{S}}(\Lambda) \cdot T_{\text{f}}(\Lambda) \, d\Lambda, \quad (2.14)$$

where $P_{\text{S}}(\Lambda)$ is the solar spectral irradiance and $T_{\text{f}}(\Lambda)$ is the transmittance of the optical band-pass filter from wavelength Λ_1 to Λ_2 in the event that one is utilized. Finally, the charge of an electron is denoted by $q = 1.6 \cdot 10^{-19}$ C.

2.3.2 Thermal noise

Another noise produced in a VLC system is the thermal noise. This noise is typical in every electrical circuit and happens because of the thermal agitation of electrons in the resistive units at the receiver. It is commonly modeled as an AWGN with a variance

$$\sigma_{\text{thermal}}^2 = N_{0,\text{tn}} \cdot W = \frac{4\kappa_{\text{B}}T_{\text{abs}}}{R_{\text{L}}} \cdot W, \quad (2.15)$$

where $N_{0,\text{tn}}$ is the power spectral density of the thermal noise, $\kappa_{\text{B}} = 1.38 \cdot 10^{-23}$ J/K denotes the Boltzmann constant, the absolute temperature is T_{abs} and R_{L} is the load resistance in the receiver circuit.

Thus, the power spectral density of the total receiver noise can be written as

$$N_0 = N_{0,\text{s}} + N_{0,\text{ab}} + N_{0,\text{tn}} = 2q(P_{\text{opt,Rx}} + E_{\text{r,ab}}A_{\text{pd}})\eta_{\text{pd}} + \frac{4\kappa_{\text{B}}T_{\text{abs}}}{R_{\text{L}}}. \quad (2.16)$$

2.3.3 Clipping noise

As indicated in Section 2.2.1.3 the LED model has a dynamic range to which the input signal must be adapted. Otherwise, the clipping effect would distort the input signal. Multi-carrier

transmission schemes were adapted to perform in VLC as Section 2.4.2 will explain. When these transmission schemes are used, time-domain (TD) signals with large envelope fluctuations are generated. Thus, these signals suffer from non-linear distortions when passing through an LED because of its non-linear transfer function. To avoid an overheating at the LED, a clipping of the input signal must be carried out that introduces the so-called clipping noise.

When multi-carrier modulation schemes are employed, a fast Fourier transform (FFT) is used for demodulation at the receiver, where the clipping noise component is assumed to be Gaussian distributed according to the central limit theorem (CLT), with zero mean and a variance of σ_{clip}^2 [Dimitrov *et al.*, 2012] [Dardari *et al.*, 2000]. Using the statistics of a truncated Gaussian distribution, σ_{clip}^2 can be determined according to the multi-carrier transmission scheme that is employed. Two main multi-carrier transmission schemes are used in this Thesis: direct current optical orthogonal frequency division multiplexing (DCO-OFDM) [Carruthers and Kahn, 1996] and asymmetrically clipped optical-OFDM (ACO-OFDM) [Armstrong and Lowery, 2006] as they will be detailed in Section 2.4.2. Thus, the variance of the clipping noise for each of them is written as [Dimitrov *et al.*, 2012]

$$\begin{aligned}\sigma_{\text{clip}, \text{DCO}}^2 = & Q(\lambda_b) - Q(\lambda_t) + f_N(\lambda_b)\lambda_b - f_N(\lambda_t)\lambda_t + [1-Q(\lambda_b)]\lambda_b^2 + Q(\lambda_t)\lambda_t^2 - \rho^2 \\ & - [f_N(\lambda_b) - f_N(\lambda_t) + [1-Q(\lambda_b)]\lambda_b + Q(\lambda_t)\lambda_t]^2,\end{aligned}\quad (2.17)$$

for DCO-OFDM, whereas in ACO-OFDM it becomes

$$\begin{aligned}\sigma_{\text{clip}, \text{ACO}}^2 = & -2\rho^2 + 2f_N(\lambda_t)\lambda_b - f_N(\lambda_t)\lambda_t - f_N(\lambda_b)\lambda_b \\ & + (\lambda_b^2 + 1)[Q(\lambda_b) - Q(\lambda_t)] + Q(\lambda_t)(\lambda_t - \lambda_b)^2,\end{aligned}\quad (2.18)$$

where ρ is an attenuation factor related to the clipping effect that can be approximated as

$$\rho = Q(\lambda_b) - Q(\lambda_t),\quad (2.19)$$

where $Q(x)$ is the well-known Gaussian Q-function. The normalized TD bottom and top clipping levels are denoted by λ_b and λ_t , respectively. Finally, $f_N(x)$ represents the probability density function of a standard normal distribution.

2.4 Transmission schemes

As mentioned in Section 2.2, only modulation schemes based on IM/DD must be employed in a VLC system. This means that the modulating signal must be real and unipolar, and then conventional RF modulation schemes must be adapted to be suitable for VLC.

2.4.1 Single-carrier modulation

Single carrier modulation schemes mainly include [Wang *et al.*, 2018]:

- OOK: It is the simplest modulation technique, where the LED switches between high and low levels as fast that the human eye cannot detect this variation. To get a DC balance, Manchester coding may be used [Rajagopal *et al.*, 2012].
- Pulse position modulation (PPM): L-PPM sends a pulse in one of L time slots within a symbol period. The average power required is lower than in OOK but it is less bandwidth efficient. Transceiver and receiver must be strictly synchronized [Elgala *et al.*, 2011]. There are other techniques resulting from PPM such as differential PPM (DPPM) [Da-Shan Shiu and Kahn, 1999] or VPPM [Modepalli and Parsa, 2013], among others.
- Pulse width modulation (PWM): In this scheme the information is sent in the pulse width that influences directly in the illumination level [Ntogari *et al.*, 2011].
- Pulse amplitude modulation (PAM): It is bandwidth efficient but can suffer from nonlinearities when passing through LEDs. Data is modulated with the amplitude of the signal pulse [Barros *et al.*, 2012].

2.4.2 Multi-carrier modulation (O-OFDM)

VLC communication systems suffer from a limited coherence bandwidth. The front-end elements limit the available bandwidth as mentioned in Section 2.2. Thus, it is likely to transmit beyond the 3-dB bandwidth if a high-speed communication system is desired and a proper equalization is carried out at the receiver. The traditional OFDM facilitates transmission in a fading channel because of the granularity of the communication bandwidth that allows transmitting according to the channel quality of the corresponding frequency region. Besides, a simple one-tap equalizer in frequency is possible and the intersymbol interference (ISI) produced by

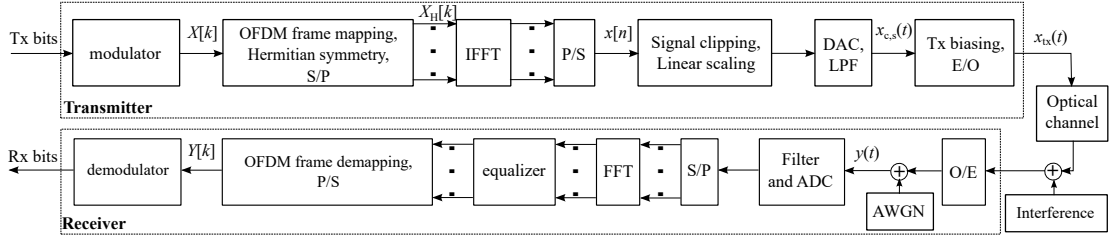


Figure 2.2: Block diagram of an O-OFDM system.

the multipath is easily eliminated using a cyclic prefix (CP). By using O-OFDM techniques, over 3 Gb/s and 10 Gb/s can be achieved when white LEDs [Tsonev *et al.*, 2014] and RGB LEDs with WDM [Chun *et al.*, 2016] are employed, respectively.

Conventional OFDM schemes are adapted to perform in OWC and create O-OFDM schemes. Figure 2.2 illustrates the O-OFDM system model. The input bits are mapped to quadrature amplitude modulated (QAM) symbols of an M-ary constellation. A set of K symbols are mapped to K frequency-domain (FD) subcarriers. Two O-OFDM schemes are considered in this PhD Thesis: DCO-OFDM [Carruthers and Kahn, 1996] and ACO-OFDM schemes [Armstrong and Lowery, 2006]. In the DCO-OFDM, $K/2 - 1$ symbols are mapped onto the first half of FD subcarriers, leaving the 0-th FD subcarrier set to zero and the information is sent in the rest of the subcarriers having indices of $k = 1, 2, \dots, K/2 - 1$. In the ACO-OFDM, $K/4$ symbols are mapped onto the first half of the odd FD subcarriers with indices of $k = 1, 3, \dots, K/2 - 1$, leaving the even subcarriers set to zero. In both schemes, the information in the FD subcarrier $K/2$ is set to zero and the information transported on the second half of the FD subcarriers (with indices from $K/2 + 1$ to $K - 1$) are Hermitian symmetric with respect to the information conveyed in the first half (with indices from 1 to $K/2 - 1$)

$$\mathbf{X}_{\text{H}} = \left[0 \ \{X[k]\}_{k=1}^{K/2-1} \ 0 \ \{X[K/2 - k]^*\}_{k=1}^{K/2-1} \right], \quad (2.20)$$

where $X[k]$ is the symbol transmitted on the k -th subcarrier and $(\cdot)^*$ denotes the complex conjugate. This arrangement allows us to obtain a real-valued output signal $x(t)$ in the TD after the inverse fast Fourier transform (IFFT). To make the energy of the TD OFDM symbol unitary, each QAM symbol must be weighted with a factor of ξ to allocate the energy belonging to the zero-valued QAM symbols into the ones that transport energy. Thus, this factor is

$$\xi_{\text{DCO}} = \sqrt{K/(K - 2)} \quad (2.21)$$

and

$$\xi_{\text{ACO}} = \sqrt{2K/K} \quad (2.22)$$

for DCO-OFDM and ACO-OFDM, respectively.

The TD signal $x(t)$ must be clipped and scaled in order to constrain it to the dynamic range of the LED, resulting in $x_{c,s}(t) = \sigma_x V[x(t)]$, where σ_x is the electrical signal variance and $V[x(t)]$ represents the clipped signal defined as

$$V[x(t)] = \begin{cases} \lambda_t & : x(t) > \lambda_t \\ x(t) & : \lambda_t \geq x(t) \geq \lambda_b \\ \lambda_b & : x(t) < \lambda_b \end{cases} . \quad (2.23)$$

A certain illumination level and a minimum signal clipping are guaranteed thanks to the DC-bias I_{DC} . The optical TD transmitted signal can be written as

$$x_{\text{tx}}(t) = \eta_{\text{led}} [x_{c,s}(t) + I_{\text{DC}}] , \quad (2.24)$$

where η_{led} is the electrical-to-optical conversion efficiency of the LED. Because of the TD differences of the signals transmitted by DCO-OFDM and ACO-OFDM, the scaling factor σ_x and the DC-bias I_{DC} for each case are different. A larger I_{DC} value is needed for DCO-OFDM in order to shift the TD signal to the middle of the LED's dynamic range, whereas a minimum of I_{DC} is needed for ACO-OFDM with the only goal of guaranteeing the required illumination level.

The Bussgang theorem is used for modelling the non-linearly clipped TD signal $V[x(t)]$ of (2.23) as [Dimitrov *et al.*, 2012]

$$V_{\text{DCO}}[x(t)] = \rho x(t) + n_{\text{clip}}(t), \quad (2.25)$$

$$V_{\text{ACO}}[x(t)] = 2U[x(t)] \rho x(t) + n_{\text{clip}}(t), \quad (2.26)$$

where $U[x(t)]$ is the unit-step function, $n_{\text{clip}}(t)$ is the clipping noise sample in the TD and ρ is an attenuation factor related to the clipping effect defined as $\rho = Q(\lambda_b) - Q(\lambda_t)$ in Section 2.3.3. Again, the clipping effects are different for DCO-OFDM and ACO-OFDM. As a

consequence, the parameters ρ and $n_{\text{clip}}(t)$ also differ. Due to the zero-clipping carried out in ACO-OFDM, the DC-bias level necessary for shifting the TD signal to the center of the LED's dynamic range is lower than that in DCO-OFDM. The authors of [Dimitrov *et al.*, 2012] conducted a study of the clipping noise effects in OFDM-based optical wireless communication. The normalized bottom and top clipping levels are selected to minimize the clipping noise: in DCO-OFDM, we use $\lambda_t = 3.2$ and $\lambda_b = -3.2$; whereas in ACO-OFDM, $\lambda_t = 3.2$ and $\lambda_b = 0$. Thus, the DC-bias level required is:

- In DCO-OFDM: $I_{\text{DC}} = \sigma_x \zeta_{\text{DCO}} = \sigma_x \lambda_{t,\text{DCO}}$, where $\zeta_{\text{DCO}} = \lambda_{t,\text{DCO}} = -\lambda_{b,\text{DCO}} = 3.2 = 5.05 \text{ dB}$ is the ratio of DC-bias level to the electrical signal's standard deviation when DCO-OFDM is used.
- In ACO-OFDM: $I_{\text{DC}} = \sigma_x \zeta_{\text{ACO}} = \sigma_x \lambda_{t,\text{ACO}}/2$, where $\zeta_{\text{ACO}} = \lambda_{t,\text{ACO}}/2 = 1.6 = 2.05 \text{ dB}$ is the ratio of DC-bias level to the electrical signal's standard deviation when ACO-OFDM is used.

The optical transmitted power is computed as

$$P_{\text{opt}} = E[x_{\text{tx}}(t)] = \eta_{\text{led}} (\sigma_x E[V(x(t))] + I_{\text{DC}}). \quad (2.27)$$

It was shown in [Dimitrov *et al.*, 2012] that $V[x(t)]$ follows a truncated Gaussian distribution and its mean can be calculated using its statistics [Johnson *et al.*, 1994] as $E[V(x(t))] = f_N(\lambda_b) - f_N(\lambda_t) + \lambda_t Q(\lambda_t) + \lambda_b [1 - Q(\lambda_b)]$. From (2.27), the electrical signal variance σ_x^2 is derived as

$$\sigma_x^2 = \frac{P_{\text{opt}}^2}{\eta_{\text{led}}^2 (\zeta + E[V(x(t))])^2}, \quad (2.28)$$

where $\zeta = \frac{I_{\text{DC}}}{\sigma_x}$ is defined as the ratio of DC-bias level to the electrical signal's standard deviation.

If a multi-cell scenario is considered, the received TD signal is formulated as

$$y(t) = \eta_{\text{pd}} \left[x_{\text{tx},0}(t) \otimes h_0(t) + \sum_{i \in \mathcal{I}} x_{\text{tx},i}(t) \otimes h_i(t) \right] + n_{\text{rx}}(t), \quad (2.29)$$

where $n_{\text{rx}}(t)$ represents the noise produced at the receiver that can be modeled as an AWGN

as detailed in Section 2.3. The signal transmitted by the desired AP (0-th AP) is denoted by $x_{tx,0}(t)$ and the CIR between such an AP and the user under study is $h_0(t)$. The interfering APs are indicated with the sub-index i that takes values in the set \mathcal{I} , whose corresponding transmitted signal and the CIR are denoted by $x_{tx,i}(t)$ and $h_i(t)$, respectively.

2.4.3 Multiple access

In a multi-cell system, multiple users can be located in the same cell and served by the same AP. Thus, a multiple access technique must be invoked. Several access techniques have been traditionally employed in a cellular system and then adapted to a multi-cell VLC network, such as: TDMA [Abdelhady *et al.*, 2019], where each user is served in a different time slot; CDMA [Qiu *et al.*, 2018], where the signal transmitted to a user is uniquely coded at the transmitter and then recovered at the receiver by knowing such a code. In VLC, optical orthogonal coded or Walsh-Hadamard codes are proposed to employ CDMA; and orthogonal frequency division multiple access (OFDMA) [Ling *et al.*, 2018], which uses orthogonal subcarriers to transmit information to multiple users simultaneously. Besides, wavelength division multiple access (WDMA) can be utilized with RGB(Y) LEDs [Genovés Guzmán *et al.*, 2019b], which consists on multiple color chips transmitting parallel information in different wavelengths.

The selection of the multiple access technique depends on system characteristics such as the available bandwidth limited by the front-end devices, the free-space channel and the user density, among others.

2.4.4 Adaptive modulation and coding (AMC)

The Shannon limit of the continuous-input continuous-output memoryless channel (CCMC) is represented by the well-known capacity expression of

$$\eta_s = \log_2(1 + \Gamma), \quad (2.30)$$

with Γ denoting the signal-to-interference-plus-noise ratio (SINR) at the receiver, or the SNR in a single-cell scenario. The cumulative distribution function (CDF) of the CCMC capacity can be written as

$$F_{\eta_s}(x) = \Pr\{\eta_s < x\} = F_\Gamma(2^x - 1), \quad (2.31)$$

where $F_\Gamma(\gamma)$ is the CDF of the SINR.

In practice, only certain discrete throughput modems can be used, hence the associated discrete-input continuous-output memoryless channel (DCMC) capacity can be achieved [Goldsmith, 2005]. Explicitly, in AMC the range of SINRs is divided into $(N+1)$ channel quality regions $\mathfrak{R}_n = \{\gamma_{\text{th}}[n], \gamma_{\text{th}}[n+1]\}$, $n = 0, 1, \dots, N$ with $\gamma_{\text{th}}[0] = 0$ and $\gamma_{\text{th}}[N+1] = \infty$. Within the channel quality region \mathfrak{R}_n , a certain constellation/coding scheme associated with $\epsilon[n]$ bits/symbol is employed. Below $\gamma_{\text{th}}[1]$ no transmission is activated and the system is said to be in outage. Over $\gamma_{\text{th}}[N]$ no further increase in SINR improves the throughput attained.

The set of switching thresholds between the constellations $\{\gamma_{\text{th}}[n]\}_{n=1,\dots,N}$ has to be designed to satisfy the bit error rate (BER) target of the system [Goldsmith, 2005]. The AMC throughput can be written as a function of the SINR as

$$\eta_{\text{AMC}} = \epsilon[n], \quad \text{SINR} \in [\gamma_{\text{th}}[n], \gamma_{\text{th}}[n+1]]. \quad (2.32)$$

For a certain average SNR Γ , the average throughput under AMC can be expressed as

$$\begin{aligned} E[\eta_{\text{AMC}}] &= \sum_{n=1}^N \epsilon[n] \cdot \Pr\{\gamma_{\text{th}}[n] \leq \Gamma < \gamma_{\text{th}}[n+1]\} \\ &= \sum_{n=1}^N \epsilon[n] \cdot [F_\Gamma(\gamma_{\text{th}}[n+1]) - F_\Gamma(\gamma_{\text{th}}[n])]. \end{aligned} \quad (2.33)$$

2.5 Optical wireless communication channel

The TD CIR of a VLC link is the contribution of the free-space and front-end components. The free-space component considers the DC-gain (LoS component) and signals from multiple paths due to the reflective indoor environment. Furthermore, the front-end devices introduce a low-pass filtering that must be considered. Thus, the CIR is formulated as

$$h(t) = h_{\text{fe}}(t) \otimes h_{\text{fs}}(t), \quad (2.34)$$

where $h_{\text{fe}}(t)$ denotes the CIR of the front-end devices and $h_{\text{fs}}(t)$ is the CIR of the free-space contribution. The corresponding frequency domain channel transfer function (FDCHTF) is

computed by using the Fourier transform as

$$H(f) = \int_0^\infty h(t)e^{-2\pi jft}dt = H_{\text{fe}}(f)H_{\text{fs}}(f). \quad (2.35)$$

2.5.1 Front-end elements channel

A low-pass filtering is produced by the front-end devices at both transmitter and receiver sides. Several experimental works were carried out to determine the characteristics of such low-pass filtering [Le Minh *et al.*, 2009] [Vucic *et al.*, 2010] [Khalid *et al.*, 2012]. These works showed that a 3-dB bandwidth is in the range 10-60 MHz. Thus, the selection of a higher modulation bandwidth will affect to the system performance considerably. The FDCHTF of the front-end devices is modeled as [Le Minh *et al.*, 2009]

$$|H_{\text{fe}}(f)| = \sqrt{\exp\left(-\frac{f}{F_{\text{fe}}}\right)}, \quad (2.36)$$

where F_{fe} is the so-called bandwidth factor that controls the FD characteristics of the front-end devices.

2.5.2 Free-space channel

Most of the energy that arrives to the PD comes through the LoS-link between the LED and the PD. The LoS-link can be blocked due to the presence of any obstacle, and it dramatically decreases the system performance [Chen and Haas, 2017]. Thus, the LoS-link blockage must be considered in the calculation of the CIR due to the free-space transmission, which is formulated by

$$h_{\text{fs}}(t) = 1_{\text{block}}h_{\text{LoS}}(t) + h_{\text{NLoS}}(t), \quad (2.37)$$

where 1_{block} is 1 or 0 if LoS or NLoS between the LED and PD occur, respectively. The LoS component is computed as [Kahn and Barry, 1997]

$$\begin{aligned} h_{\text{LoS}}(t) &= \frac{(m+1)G_f G_c A_{\text{pd}}}{2\pi d^2} \cos^m(\phi) \cos(\psi) 1(\psi) \delta(t - \tau_{\text{LoS}})) \\ &= \frac{(m+1)G_f G_c A_{\text{pd}} d_v^{m+1}}{2\pi (r^2 + d_v^2)^{\frac{m+3}{2}}} 1(\psi) \delta(t - \tau_{\text{LoS}})), \end{aligned} \quad (2.38)$$

where m is the Lambertian emission order already defined in (2.2). The geometric parameters of a single VLC link are shown in Figure 2.3. The optical filter loss at the receiver is denoted by G_f and G_c is the concentrator gain. The horizontal and vertical distances between the transmitter and the receiver are denoted by r and d_v , respectively, which determine the Euclidean distance between the transmitter and the receiver $d = \sqrt{r^2 + d_v^2}$. The radiant angle between the transmitter and the receiver is denoted by ϕ , whereas the incident angle is ψ . The time delay between the LED and the PD is represented by $\tau_{\text{LoS}} = d/c_{\text{speed}}$, where $c_{\text{speed}} \approx 3 \cdot 10^8 \text{ m/s}$ is the speed of light in vacuum.

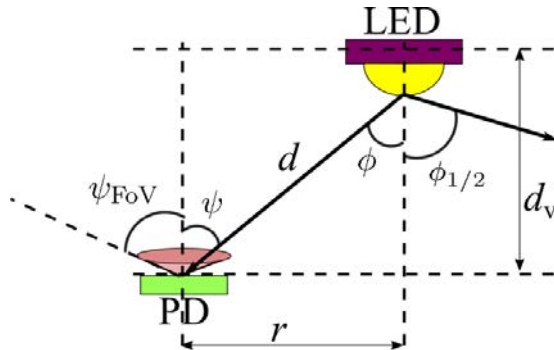


Figure 2.3: Geometry of a single VLC link.

The NLoS component can be computed by accurate methods that involve high computational complexity such as deterministic methods [Barry *et al.*, 1993] or Monte Carlo simulations [Lopez-Hernandez *et al.*, 2000]. However, simplified methods have been proposed to compute the CIR in TD [Chen *et al.*, 2018] and FD [Schulze, 2016]. In this PhD Thesis the NLoS component will be computed by the analytical method presented in [Chen *et al.*, 2018], which uses the transmitter and user locations with respect to the room, their orientations, A_{pd} , m , ψ_{FoV} and the reflectances of the surfaces ρ_{floor} and ρ_{ceil} in order to compute up to the second order reflection.

2.6 Multi-cell networks

A VLC point-to-point link offers great advantages over RF technology. However, if mobility and an extended coverage by using VLC is desired, a fully networked wireless connectivity is required, commonly known as a light fidelity (LiFi) attocell network [Haas, 2013]. These scenarios create a dense small cell network which agrees with the network densification trend and potentially increases the area spectral efficiency [Chen *et al.*, 2013]. In addition, the illumina-

tion regulation is more easily satisfied and cooperative transmission techniques can be carried out in order to overcome VLC issues such as LoS blockage. Differently from RF technologies, the transmission beam can be easily confined in VLC by using optical devices. In that way, the beam can be adjusted to the requirements. A VLC network is expected to have the same functionalities as a cellular system [Haas *et al.*, 2016]. To this end, further studies must be developed in the downlink transmission, interference mitigation, handover, backhaul techniques and the possible types of multi-cell deployment. Some of these key issues are addressed in this PhD Thesis.

2.6.1 Downlink transmission

A considerable number of research contributions are made in a point-to-point VLC system. However, VLC is expected to fulfill the high-data rate demand in indoors where multiple light fixtures are installed. Every light fixture is considered as an AP in this PhD Thesis. Thus, further research is needed in a VLC fully networked scenario. In particular, physical layer issues are tackled to be considered as the key and most different aspects compared to other RF multi-cell technologies. Upper layers techniques can be easily adopted from RF.

The IM/DD technique required in VLC partially determines the features of the downlink transmission. Several modulation schemes are considered and detailed in Section 2.4. Besides, since the shape of the multi-cell deployment influences the system performance, several deployments are analyzed and detailed in Section 2.6.5.

2.6.2 Interference mitigation

A multi-cell scenario allows reusing resources at different APs at the expense of increasing the inter-cell interference. Besides, if neighboring APs use different resources, cooperative techniques can be employed to serve users simultaneously. Different techniques have been traditionally proposed in RF multi-cell systems to mitigate the strong inter-cell interference level that takes place especially in cell-edge areas. For example, fractional frequency reuse (FFR) utilizes different frequency-reuse factors in cell-center and cell-edge areas to keep the inter-cell interference under control [Novlan *et al.*, 2012] [Wang and Yeh, 2011]. The authors of [Chen *et al.*, 2015] and [Kazemi and Haas, 2016] adopted FFR for VLC scenarios, showing a considerable inter-cell interference decrease in those users located at the cell-edge areas.

The light beam can be confined accordingly in order to decrease the inter-cell interference. However, it limits the cooperation capabilities among APs. In this PhD Thesis, the study of inter-cell interference mitigation by using joint transmission (JT) CoMP techniques according to the scenario conditions is carried out, and different multi-cell schemes that provide a homogeneous coverage are proposed. Not only the inter-cell interference is mitigated, but also the LoS-link blockage is overcome due to the multi-point transmission.

2.6.3 Handover

In a cellular telecommunication network, a handover is defined as the procedure to transfer an open session served by an AP to another AP without a large session interruption. The reasons to undergo a handover can be: a channel fading, for example when there is a LoS-link blockage in VLC; an increase in the interference; or an overload of users in the same serving AP(s).

In a hard handover procedure, the UE is disconnected from the current AP before it connects to another AP. Then the communication is momentarily interrupted. It can be solved by using a soft handover, where before disconnecting from the current AP, the user is successfully connected to other AP. Soft handover offers a better quality of experience but, in exchange, it means an extra overhead in the network.

A horizontal handover is named to the handover between two APs that belong to the same network. Otherwise, it is named as a vertical handover [Ahmed *et al.*, 2014]. Algorithms considering hysteresis are recommended to avoid the so-called ‘ping-pong’ effect, where unnecessary handovers are produced in users that experience similar performances from two different APs and it degrades the system performance.

A VLC network has a large number of small cells that potentially increases the handover frequency when user is moving. It can considerably decrease the system throughput and quality of service. Thus, handover techniques must be studied at such scenarios. However, the back-haul connection required for carrying out a handover is shorter than in RF technologies, which simplifies the control and management of the handover procedure. Soft handover is preferable in VLC because of the handover frequency due to the small cell deployment. However, with the aim of decreasing the overhead and optimizing the handover procedures, further research must be developed in VLC [Ahmed *et al.*, 2014]. In addition, as VLC is expected to perform in HetNets, vertical handovers between VLC and RF networks may be useful to offload either

the RF or the VLC network, and deploy a backup system in case of a user connected to the VLC network experiences either a LoS-link blockage or great movements that decrease its performance. To this end, dynamic load balancing schemes in HetNets with VLC are presented in [Wang and Haas, 2015] and [Wang *et al.*, 2015].

2.6.4 Backhaul

A backhaul is the connection between an AP and a controller. Its functionality is fundamental in multi-cell systems to provide a reliable high-speed and low-latency communication accommodating the traffic to different APs.

A backhaul link is essential in cellular networks [Tipmongkolsilp *et al.*, 2011] to connect either base stations (BSs) among them as in LTE [ETSI TS 136 300 V13.2.0, 2016], or BSs with a central entity that manages the traffic and performs as a gateway, as in the GSM standard [Rahnema, 1993]. Thus, the study of a backhaul link and its consideration in a realistic way is crucial to evaluate the communication system performance. Different backhaul wired techniques for VLC have been demonstrated in the literature: the authors of [Song *et al.*, 2015] and [Bouchet *et al.*, 2010] implemented indoor broadband broadcasting systems based on VLC and power line communication (PLC), where they use the power line network as a backbone; Ethernet-VLC can also be combined to provide connectivity to the light fixtures as demonstrated in [Delgado *et al.*, 2010]; finally, optical fiber is a proper alternative shown in [Wang *et al.*, 2015b] to perform as a backbone in LiFi because of its high bandwidth characteristics. Besides, wireless backhaul systems [Kazemi *et al.*, 2019] are starting to be considered because the installation of a fully wired network in VLC is complex when VLC capabilities are incorporated to an already installed lighting infrastructure. For the sake of the scalability and simplicity, this PhD Thesis also proposes a simple wireless backhaul system in VLC that only requires an extra PD per AP [Genovés Guzmán *et al.*, 2019a].

2.6.5 Multi-cell deployments

According to Section 2.5.2, the free-space channel depends on the distance between the AP and the user. Additionally, when a multi-cell scenario is considered, the inter-cell interference is significant and must be evaluated. Thus, the tessellation formed by the AP locations is a key aspect when a multi-cell scenario is deployed. This Chapter presents the tessellations that are

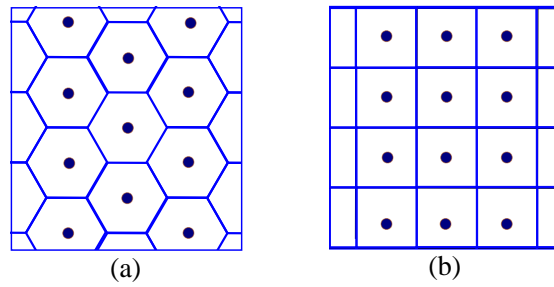


Figure 2.4: Cell deployments: (a) Hexagonal cell deployment. (b) Square cell deployment.

considered in this PhD Thesis, represented in Figure 2.4:

- Hexagonal cell deployment: Although this tessellation can be deployed with difficulty in a lighting infrastructure, it is desired since a hexagon is the shape that approximates better to a circle, which is the realistic coverage shape since LEDs emit omnidirectionally. Additional work is required to deploy such a scenario and respect the proper AP locations according to a hexagonal deployment.
- Square cell deployment: It involves a simple deployment, a proper illumination distribution and it easily adapts to rectangular-shaped rooms. In corridors, equidistant APs are usually located in a line, which is a particular case of square cell deployment with only a row of APs.

These two cell deployments are realistic and expected to provide a proper VLC network.

Chapter 3

Single-cell VLC

3.1 Introduction

A single-cell VLC system is a simplified scenario where one only AP is deployed. This Chapter presents and studies the main issues arisen in a single-cell VLC scenario, both in indoor and outdoor scenarios, and proposes solutions to some of them.

As seen in Section 2.2.1, a realistic LED transfer model is linear only in a restricted region. Thus, the transmission of a signal with a large number of samples out of the linear region will distort the output signal and cause errors at the reception. Multi-carrier modulation schemes such as OFDM have the disadvantage of suffering from a high PAPR and, for this reason, large power back-offs are needed at the LED front-ends. The back-off is necessary to make the signal work in the linear zone and, thus, to avoid a signal degradation. This is the same as the back-off required at the HPAs in radio frequency systems. The larger the PAPR, the larger the back-off is needed and, as a result, the signal is more compressed and inefficient. In that case, the signal does not take advantage of the LED's linear range and its performance is reduced. If the PAPR is reduced, the needed back-off will be lower and the signal will work properly in the linear range with higher efficiency. This is, in systems where multi-carrier modulations are used, PAPR reduction techniques are essential.

In addition to the aforementioned issue that is related to the non-linear LED's transfer function, it is important to consider that most of the power received by a PD comes from the LoS-link with its serving AP. However, a LoS-link blockage can happen and the received signal power may decrease several tens of dB [Chen and Haas, 2017]. In this situation, the communication with users suffering a NLoS will likely be in outage. In a single-cell VLC scenario, only signal coming through reflections will help to maintain the communication. Otherwise, if a multi-cell VLC scenario is deployed, neighboring APs can cooperate and jointly transmit in order to decrease the damage produced by a sudden LoS-link blockage.

Additional issues that may be common in other technologies have been studied. For example, channel estimation techniques need to be considered when very high data rates are used and the

response speed of the front-end devices is not as high as desired, besides the harmful multipath effect caused in a realistic scenario. Besides, multiple-input single-output (MISO) techniques have been mentioned in the literature as interesting approaches to exploit the spatial multiplexing and diversity [Mesleh *et al.*, 2010]. In these MISO schemes, the channel state information can be used at the receiver for equalization, or at the transmitter for precoding purposes. To that end, in several works the authors assumed perfect knowledge of the channel [Yu *et al.*, 2013a], which could be valid if the user is fairly static but it is not always the case. Several channel estimation techniques have been proposed for VLC using dedicated pilot schemes in MISO scenarios [Wu *et al.*, 2017] in quasi-stationary environments where the channel changes after a determined number of OFDM symbols. In [Chen and Jiang, 2017], a Bayesian channel estimator is proposed for VLC using pilot symbol assisted modulation (PSAM) techniques. By contrast, superimposed training (ST) is a channel estimation technique, already proposed in RF systems [Tugnait and He, 2010], where the pilot signal is arithmetically added to the data signal using the same resources without wasting dedicated subcarriers. A ST approach for channel estimation in MISO DCO-OFDM VLC scenarios was presented in [Estrada Jimenez *et al.*, 2019], in order to improve the spectral efficiency of VLC systems and provide an optimal power allocation between pilots and data symbols. Additionally, traditional interference reduction techniques in RF systems, where no knowledge of the channel state information at the transmitter is required, are being adopted in VLC, such as blind interference alignment techniques [Morales-Céspedes *et al.*, 2018] [Adnan-Qidan *et al.*, 2019].

On top of the previous issues, a VLC system in outdoor environments suffer from a large shot noise produced by the skylight and sunlight. The larger the modulation bandwidth, the larger the produced shot noise is.

In this Chapter, two of the aforementioned main issues in a single-cell VLC are addressed:

1. The non-linear distortions produced in the transmitted signals when multi-carrier modulation schemes are used.
2. The large shot noise produced at the receiver when VLC is employed in outdoor scenarios and the optimization of the system parameters when working at such conditions.

The LoS-link blockage is tackled by using JT CoMP techniques in multi-cell VLC scenarios. This subject will be extensively addressed in Chapter 4.

3.2 State of the art

In traditional radiofrequency systems, PAPR reduction techniques were proposed as a solution to the deformities created due to the large fluctuations in the TD signal [Han and Lee, 2005]. The PAPR metric is formulated as

$$\text{PAPR}(x(t)) = 10 \log_{10} \frac{\max |x(t)|^2}{\text{E}\{x(t)\}} \quad [\text{dB}], \quad (3.1)$$

where $\text{E}\{\cdot\}$ represents the statistical expectation. However, the literature demonstrated that the CM is a more effective indicator of the power derating factor because it uses higher order statistics [TDoc R1-060023, 2006], whereas PAPR only considers the maximum signal peak. Thus, in order to evaluate the performance of any proposed scheme in terms of envelope variations, the CM is used in contrast to the classic PAPR metric. It is defined as

$$\text{CM}(x(t)) = \frac{\text{RCM}(x(t)) - \text{RCM}_{\text{ref}}}{K_{\text{CM}}} \quad [\text{dB}], \quad (3.2)$$

where

$$\text{RCM}(x(t)) = 20 \cdot \log \left(\text{rms} \left[\left(\frac{|x(t)|}{\text{rms}[x(t)]} \right)^3 \right] \right) \quad [\text{dB}], \quad (3.3)$$

is the raw cubic metric of $x(t)$ and RCM_{ref} and K_{CM} are constant values depending on the communication system. The operator ‘rms’ stands for the root mean square within a TD OFDM signal. Following the idea in [Garcia Doblado *et al.*, 2015], the aim is to reduce the RCM as much as possible without increasing the signal energy.

A first proposal to reduce the CM in DCO-OFDM VLC systems was published in [Garcia Doblado *et al.*, 2015]. It adapted the well-known ACE algorithm to optical signals, and proposed a new ACE technique (denoted as RCM-ACE from this point forward) by adding two modifications to the traditional one: the optimization by means of CM instead of PAPR, and the change of the clipping stage for a two-valued signal ($[+V_{\text{clip}} -V_{\text{clip}}]$). Although it yielded good results, it had limited flexibility in the saturation process, causing unbalanced constellations because of saturated symbols.

PAPR reduction techniques traditionally applied to RF systems can also be adapted to VLC, such as the one presented in [Zhang *et al.*, 2018], where the companding transform technique is used. These traditional PAPR reduction techniques are typically classified in [Rahmatallah and Mohan, 2013]: distortion techniques, which includes clipping and non-linear processing sub-

categories; and distortionless techniques, where we differentiate between multiple signalling and probabilistic techniques, and coding-based techniques.

Due to the flexibility of an ANFIS, its capacity of being trained and reducing the system complexity [Jang, 1993], the first contribution presented in this Chapter is a CM reduction technique using an architecture based on ANFIS. These fuzzy networks were already applied to RF systems in [Gil Jimenez *et al.*, 2011] to reduce the CM in OFDM signals, but the inherent different nature of RF signals in comparison to optical ones makes that scheme invalid to be used in DCO-OFDM.

On the other hand, VLC solutions have been predominantly focused on indoor scenarios due to their susceptibility to sunlight-induced shot noise. As a benefit, their security was improved, because the propagation of light was confined to a room. In indoor scenarios the number of LED light fixtures is high and the VLC attocells can be readily spotted based on their bright light-cone. However, the SSL technology is gradually also replacing the halogen lighting in outdoor scenarios, and we must evaluate the feasibility of using those light sources as sources of wireless services.

OWC has also been used in long-range systems for outdoor applications such as inter-building communications, last mile access networks [Shaw *et al.*, 2007], high altitude platform based laser communications and satellite communications [Fidler *et al.*, 2010]. These FSO scenarios are often modeled as Gamma-gamma [Yang *et al.*, 2015] or a lognormally distributed fading scenarios [Sun *et al.*, 2017]. Uysal *et al.* presented a performance study of a vehicle-to-vehicle (V2V) and vehicle-to-infrastructure (V2I) communications system in [Uysal *et al.*, 2015]. They highlighted the challenges imposed by outdoor environments, such as severe weather conditions, sunlight and ambient light. The authors of [Lee *et al.*, 2012] characterized the noticeable difference between the indoor and outdoor VLC channels. Explicitly, outdoor VLC has multiple dominant LoS links, but less reflected multipath components. In [Căilean and Dimian, 2017], the challenges related to VLC when it is used in vehicular communications applications are addressed.

Outdoor VLC applications are bound to experience unmodulated parasitic light impinging on the PD. The resultant DC component may be mitigated by capacitive filters, but it still results in strong shot noise, which would often inflict outages. In order to mitigate the background noise, [Chung and Oh, 2013] invoked efficient optical filtering, whereas the authors

of [Lee *et al.*, 2009] designed a selective combining receiver. As a further solution, [Kinoshita *et al.*, 2014] employed an image sensor as their reception device instead of a conventional PD. Experimental frame error rate (FER) results measured in a street lighting aided scenario were disseminated in [Knobloch, 2015], where PWM was used. The authors of [Islim *et al.*, 2018] presented the first experimental study of the impact of solar irradiance on VLC and demonstrated its viability in such an environment.

Against this background, the second main contribution presented in this Chapter is that we quantify the average data rate and optimize the modulation bandwidth, depending on the sunlight- and skylight-induced performance degradation, when a multi-carrier transmission scheme is used. Therefore, the optimum modulation bandwidth will vary depending on the time of the day. This system can rely on any LED AP located in outdoor scenarios, such as street lights, LED boards at railway stations, etc. Analytical SNR expressions are derived and the performance of the system is evaluated in terms of the average cell data rate and the outage probability, when adaptive modulation and coding (AMC) schemes are employed. Since the AP density is typically lower than in indoor scenarios and the predominant noise source in outdoor scenarios is the background noise, a single-cell scenario is studied. The backhaul network is assumed to be capable of managing all the traffic at high data rates. The future popularity of the VLC technology in outdoor scenarios critically depends on its ability to cope with the multiple sources of parasitic light, which motivates part of the research presented in this Chapter.

3.3 Indoor

As mentioned, there are several problems in indoor single-cell VLC systems that must be addressed in order to improve the system performance. On the one hand, the LoS-link blockage between an LED and a PD, which will be addressed by means of multi-point joint transmission techniques detailed in Chapter 4. On the other hand, the high PAPR/CM level suffered when multicarrier modulation schemes are used. It makes that either a great IBO is utilized or the clipping eliminates many important samples of the TD signal. This issue is tackled as follows.

3.3.1 PAPR reduction technique

The objective of a PAPR reduction technique is to decrease the fluctuations of a TD signal without losing information in order to avoid the clipping effect. The diagram of the O-OFDM

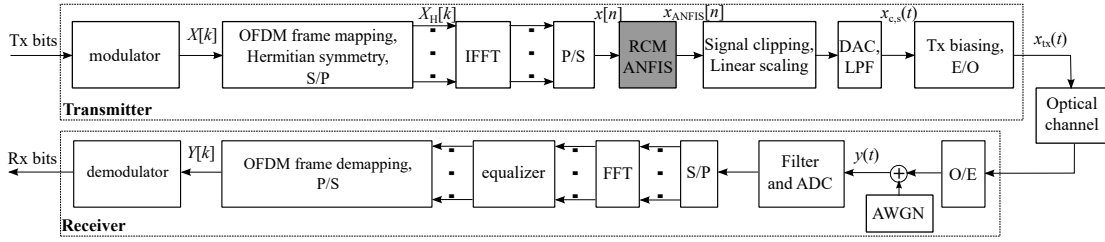


Figure 3.1: Block diagram of the O-OFDM system with the proposed RCM-ANFIS.

system used in this Section is shown in Figure 3.1, which is similar to the conventional O-OFDM diagram represented in Figure 2.2 with the difference of the addition of a RCM ANFIS module at the transmitter. This module, proposed in this Chapter, is in charge of reducing the fluctuations of the TD transmitted signal. Once the symbols of an M-QAM constellation have been generated, an IFFT of K points is applied after having carried out a Hermitian symmetry. The signal is transformed from parallel to serial, and feeds the grey box which is the proposed RCM-ANFIS method. ANFIS is based on fuzzy rules (heuristics) [Jang, 1993] [Aik *et al.*, 2008] that are here optimized to reduce the CM of the input signal. After that, the bipolar real-valued signal in the discrete time domain $x_{\text{ANFIS}}[n]$ is obtained. After a digital-to-analog converter (DAC), the unipolar and well suited to the LED transfer function forward signal $x_{\text{input,volt}}(t)$ results from adding the DC bias and a linear scaling as written in (2.6). On the receiver side, a photodiode detects the optical intensity and turns it into the amplitude of an electrical signal. Binary data are obtained with the reversed transmitter procedure. Note that ANFIS is only necessary on the transmitter side and no side information is needed either. The reason is that ANFIS changes the signal properties before the transmission, which involves that I/Q symbols are distanced from the decision borders always within the allowable region. Thus, it does not affect the demapper procedure at the receiver because the allowable region does not compromise the BER or the symbol demapping [Han and Lee, 2005].

Although channel equalization is out of the scope of this work, note that pilot symbols used for channel estimation purposes must not be modified by any PAPR or CM reduction technique on the transmitter side [Jabrone *et al.*, 2010]. Besides, since FD symbols are distanced from the decision borders, they keep offering benefit even when a channel equalization is carried out.

3.3.1.1 Figures of merit

Two metrics are used to evaluate the performance of this proposal.

1. Error vector magnitude (EVM). It detects the signal distortions, and it is defined for an OFDM symbol as

$$\text{EVM} = \sqrt{\sum_{k=0}^{K-1} |Y[k] - X[k]|^2 / \sum_{k=0}^{K-1} |X[k]|^2}, \quad (3.4)$$

where $Y[k]$ and $X[k]$ are the k -th received and transmitted constellation points, respectively.

2. Illumination-to-communication conversion efficiency (ICE) to study the VLC system efficiency, defined as [Yu, 2014]

$$\text{ICE} = D_{\text{output}}/O_{\text{AVG}} = D_{\text{input}}/(V_{\text{AVG}} - V_{\text{TOV}}), \quad (3.5)$$

being D_{output} the standard deviation of the output intensity, and D_{input} the standard deviation of the input electrical signal after scaling and biasing given by $x_{\text{input,volt}}(t)$ in (2.6). The importance of ICE if that it quantifies the VLC performance in terms of both illumination and communication capabilities, as shown in [Yu *et al.*, 2013b]. The ICE is closely related to a parameter called brightness factor (BF) [Yu, 2014], formulated as

$$\text{BF} = O_{\text{AVG}}/O_{\text{SAT}} = (V_{\text{AVG}} - V_{\text{TOV}})/\text{DR}. \quad (3.6)$$

Since VLC systems illuminate and transmit information simultaneously, we need to consider the illumination level as well. It is given by the aforementioned parameter O_{AVG} , but it is also related to the BF as it can be verified in (3.6).

The parameter BF is theoretically between 0 and 1, but in a practical scenario it must be lower than a BF_{\max} value, which is restricted by the maximum permissible DC voltage of the LED. The communication capacity is related to the illumination using the ICE parameter. Comparing (3.5) and (3.6), the higher the ICE, the lower the BF or illumination level is and thus, the transmission capacity. Therefore, a tradeoff between ICE and BF must be found.

3.3.1.2 Adaptive network-based fuzzy inference system

In this Section, neuro-fuzzy systems are applied to reduce the RCM in DCO-OFDM for VLC systems and, therefore, also the CM. The proposal offers the chance of training in time and frequency domains. Thus, the characteristics of the desired signal for each domain will be improved.

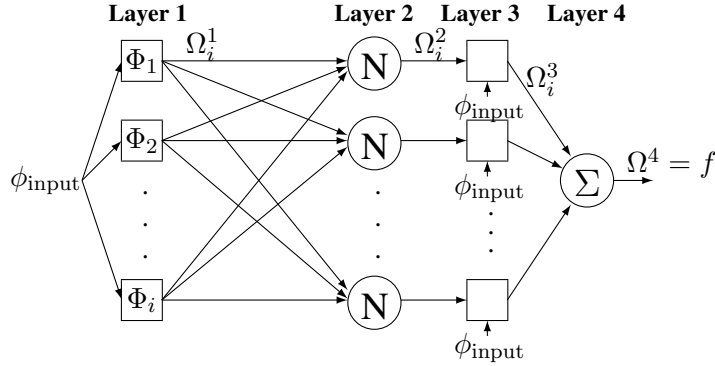
A *fuzzy if then rule* is an expression as *IF* Φ_{label} *THEN* Ψ_{label} , where Φ_{label} and Ψ_{label} are labels of fuzzy sets. This fuzzy form was proposed in [Takagi and Sugeno, 1985], and it has a great capacity to learn how to approximate non-linear functions. Here, the typical fuzzy rule will be utilized in a Sugeno's fuzzy model [Aik *et al.*, 2008], whose format, considering two inputs and one output (for simplicity), is

$$\text{If } \phi_{\text{input}} \text{ is } \Phi_{\text{label}} \text{ and } \psi_{\text{input}} \text{ is } \Psi_{\text{label}} \text{ then } z = f(\phi_{\text{input}}, \psi_{\text{input}}), \quad (3.7)$$

where $z = f(\phi_{\text{input}}, \psi_{\text{input}})$ is a defined function.

An adaptive network has multiple applications because there are barely restrictions on the node functions. Structurally the only limitation of the network configuration is that it should be of the feedforward type [Jang, 1993]. The ANFIS is an adaptive-network-based fuzzy inference system, i.e., it is an adaptive network whose functionality is equivalent to a fuzzy inference system. In our application, the signal is received and the goal is to obtain an output with the desired characteristics. It is obtained with fuzzy rules of the type *if then*. The main drawback of the fuzzy rules is the need of expert knowledge or instructions to define them, and thus, knowing the parameters of the f functions turns into a hard task. However, fuzzy rules and an adaptive network can be combined in such a way that those parameters can be trained in that adaptive network. The system becomes very useful because the disadvantages of using fuzzy rules are overcome with the advantages of using neural networks. This structure results in a hybrid network which combines both a fuzzy system and a neural network. It is denoted ANFIS, and it was proposed in [Jang, 1993].

The implementation of the proposed ANFIS is based on different layers where their corresponding nodes compute an operation. This procedure can be followed in Figure 3.2. Note that only one input exists for our problem.

**Figure 3.2:** ANFIS diagram.

At layer 1: Membership functions with Gaussian shape are considered, and they are defined as

$$\Omega_i^1 = \mu_{\Phi_i}(\phi_{\text{input}}) = \exp\left(-\frac{(\phi_{\text{input}} - c_i)^2}{a_i}\right), \quad (3.8)$$

where Φ_i is the linguistic label (small, large, etc.) associated with the i -th node, and c_i and a_i are the premise parameters. The maximum of Ω_i^1 is equal to 1 and the minimum equals 0. Since only one input exists in our design, Ω_i^1 matches the firing strength: $\Omega_i^1 = \omega_i$.

At layer 2: The i -th node calculates the ratio of the i -th rule's firing strength, called normalized firing strengths

$$\Omega_i^2 = \frac{\omega_i}{\sum_i \omega_i} = \bar{\omega}_i. \quad (3.9)$$

At layer 3: Each node computes its contribution to the overall output as

$$\Omega_i^3 = \bar{\omega}_i f_i = \bar{\omega}_i (p_i \phi_{\text{input}} + q_i), \quad (3.10)$$

where p_i and q_i are the consequent parameters.

At layer 4: The overall output is calculated as the summation of all incoming signals:

$$\Omega^4 = \sum_i \bar{\omega}_i f_i = \frac{\sum_i \omega_i f_i}{\sum_i \omega_i}. \quad (3.11)$$

The first-order Sugeno fuzzy inference system designed for this work contains i if then rules

If ϕ_{input} is Φ_i then $f_i = p_i \phi_{\text{input}} + q_i$

and given the premise parameters (c_i and a_i), the overall output can be expressed as a linear combination of the consequent parameters (p_i and q_i)

$$\Omega^4 = f = \frac{\sum_i \omega_i (p_i \phi_{\text{input}} + q_i)}{\sum_i \omega_i}. \quad (3.12)$$

The premise and consequent parameters are adjusted by using backpropagation and least squares estimation (LSE) [Gil Jimenez *et al.*, 2011] [Aik *et al.*, 2008]

$$\begin{aligned} p_i(t+1) &= p_i(t) - \lambda_{\text{lr}} \frac{\partial E}{\partial p_i} \\ q_i(t+1) &= q_i(t) - \lambda_{\text{lr}} \frac{\partial E}{\partial q_i} \\ c_i(t+1) &= c_i(t) - \lambda_{\text{lr}} \frac{\partial E}{\partial c_i} \\ a_i(t+1) &= a_i(t) - \lambda_{\text{lr}} \frac{\partial E}{\partial a_i} \end{aligned} \quad (3.13)$$

being λ_{lr} the learning rate and E is the error produced.

Due to the need of reducing the CM in DCO-OFDM scenarios, as explained previously, the goal is to obtain a power derating reduction algorithm for DCO-OFDM signals in VLC. The key design premise is to get the best training set of data. For this purpose, the RCM-ACE technique proposed in [Garcia Doblado *et al.*, 2015] is used because, so far, it proposes the algorithm that gets the largest CM reduction. The idea is to design an ANFIS that learns how to obtain DCO-OFDM signals with low crest factor from a flexible design.

In [Garcia Doblado *et al.*, 2015], a recent power derating algorithm for DCO-OFDM signals is proposed. It envisages our benchmark and allows us to select and optimize the combination of the parameters V_{clip} , G and L that gets the largest RCM reduction. These parameters are eligible in an ACE algorithm. V_{clip} represents the threshold to which the time-domain signal is clipped. G is called the extension gain, and is part of the clipping procedure of the ACE algorithm. Finally, L is necessary to guarantee a reasonable level of signal power, i.e., it is the maximum value of the resulting real and imaginary components of the I/Q symbols.

An analysis of the RCM-ACE algorithm proposed in [Garcia Doblado *et al.*, 2015] has been carried out to obtain the best parameters. In the selection process of the V_{clip} , G and L parame-

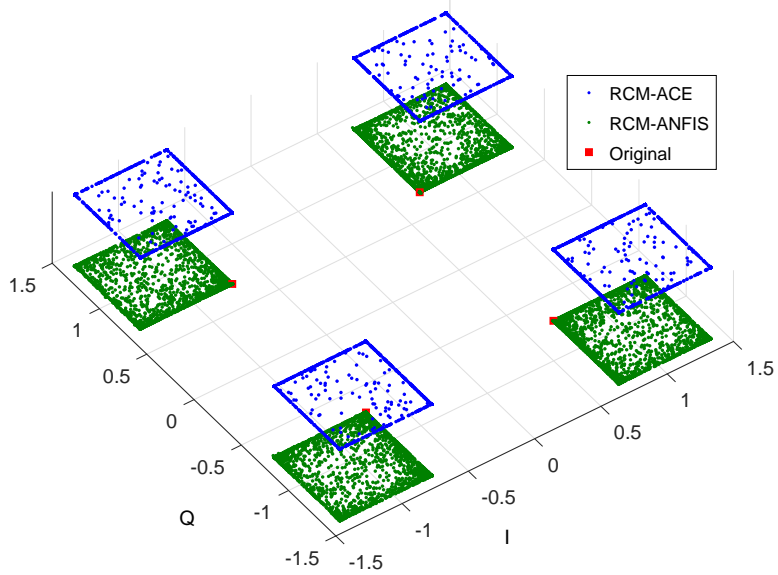


Figure 3.3: Symbols distribution in RCM-ACE and RCM-ANFIS techniques for a QPSK constellation.

ters that better reduce the CM, it turned out that in 100 % of the cases, the saturation procedure was the least severe, that is, the optimal L parameter was always equal to the largest value in the allowed range ($L = [0.7, 1.4]$), i.e., $L = 1.4$. However, the optimal V_{clip} and G parameters were variable. An increased L range up to the coherent value of 3 was also analyzed and the result was that the optimal L parameter is 3 for a 100 % of DCO-OFDM symbols in a quadrature phase shift keying (QPSK) constellation. In the case of 16-QAM constellation, more than 95 % of symbols got this same maximum value as the optimal one. Thus, we can figure out that the larger the L parameter, the better CM reduction is obtained, but also the higher the signal energy is. It makes sense because larger values of L offer more flexibility and room to allocate the constellation points. Then, a trade-off must be found.

The analysis about the L value in the RCM-ACE technique, detailed in the previous paragraph, provided an insight to design a flexible model based on ANFIS: the time-domain system is trained with RCM-ACE signals obtained with $L = 3$, and the following frequency-domain system with $L = 1.4$. The G and V_{clip} parameters are maintained in the range stated by [ETSI EN 302 755, 2012]. In the time-domain system we get signals with very low CM but large mean energy. This mean energy will be reduced in the frequency-domain stage by limiting

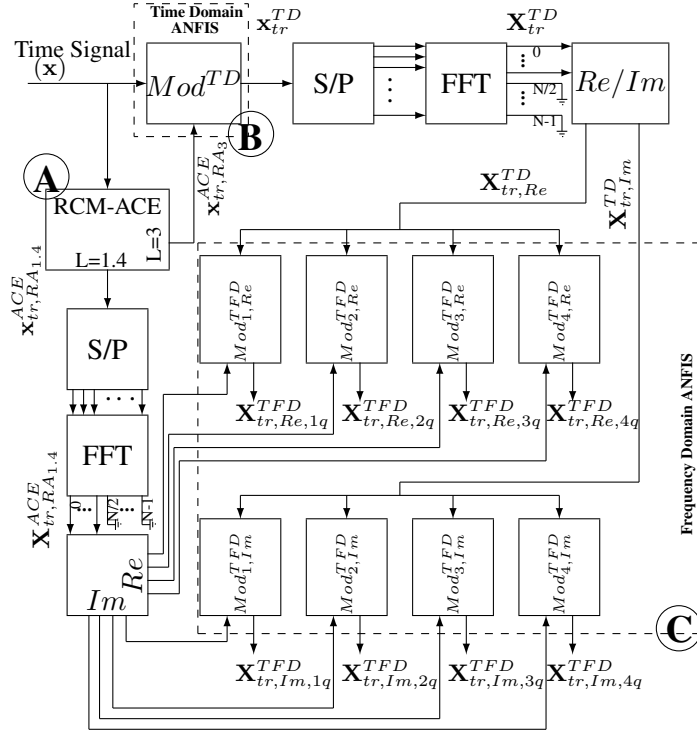


Figure 3.4: Training scheme for Time-Domain model (Mod^{TD}) and Time-Frequency-Domain models ($Mod_1^{TFD}, Mod_2^{TFD}, Mod_3^{TFD}, Mod_4^{TFD}$) for real and imaginary parts.

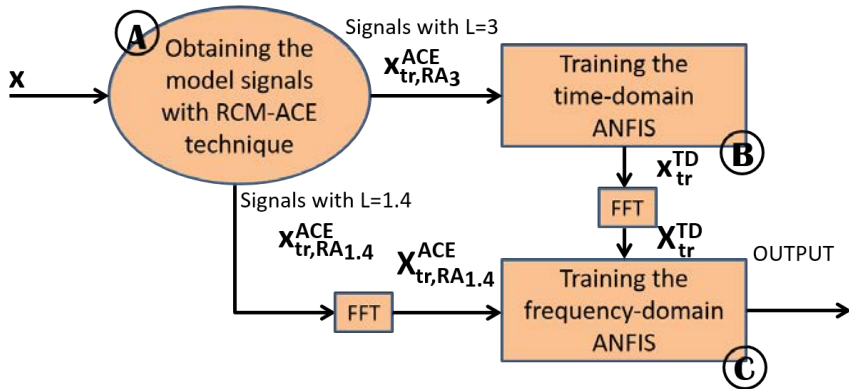


Figure 3.5: Simplified diagram of the RCM-ANFIS training scheme.

the L parameter to 1.4. It brings about a better distribution of symbols within the allowed regions, which are the squares formed from ± 0.7 to ± 1.4 . This distribution can be observed in Figure 3.3, where 100 OFDM symbols for a QPSK constellation and $K = 64$ subcarriers have been represented after using the RCM-ACE and the proposed RCM-ANFIS techniques. For the sake of clarity, the constellations have been drawn at various levels, that is, the third dimension

is only for presentation purposes, and it has been included to distinguish the constellations obtained with the two different procedures. Also, the original constellation has been represented. The percentage of symbols that are moved into the proposed RCM-ANFIS is 56.9 %, whereas only a 27.3 % of symbols are moved in the RCM-ACE for a QPSK constellation.

As mentioned, there are two different ANFIS: the first one in the time domain, whose objective is to get time-domain signals with low RCM but with a relaxed restriction on signal energy (large value of L); the second one is a set of ANFIS in the frequency domain with the aim of learning the desired constellation regions and thus, limiting the magnitude of the individual components (real and imaginary) so as to guarantee a reasonable level of signal energy (low value of L). Both use RCM-ACE signals to train the ANFIS. However, thanks to a combination of ANFIS schemes and a composition of RCM-ACE signals obtained with different parameters, the achieved performance is significantly better than the one resulting from the RCM-ACE proposal [Garcia Doblado *et al.*, 2015]. The training section can be observed in Figure 3.4. Note that once the ANFIS are trained, they can work autonomously.

In the time-domain, signals are real so only one model is needed. In the frequency-domain, divisions into quadrants are carried out to simplify the training process. Each quadrant needs two models because signals are complex and ANFIS models only work with real values. Thus, 8 models are needed in the frequency domain and 9 as a whole.

Each ANFIS is trained with the fuzzy rules specified in (3.8)-(3.13), but with different training signals. The training scheme is represented in detail in Figure 3.4, and in a simplified way in Figure 3.5. It is deployed to obtain the desired ANFIS set and make it ready to work in an autonomous way in the real-time scheme. This real-time scheme is depicted in Figure 3.6 and, in a simplified way, in Figure 3.7. For clarity purposes, Figures 3.4-3.7 are labelled with letters from **A** to **E**.

On the one hand, in **B**, the first model (Mod^{TD}) learns in the time domain how the signals must be in order to have low power fluctuations but with non-strict energy restriction (large L). To this purpose, it is trained with the signal from RCM-ACE algorithm with $L = 3$ ($\mathbf{x}_{tr,RA_3}^{ACE}$). On the other hand, in **C**, the models in the frequency domain ($Mod_{1,Re}^{TFD}, Mod_{1,Im}^{TFD}, Mod_{2,Re}^{TFD}$, etc.) force the symbols to be within the correct regions and thus, we also use them for limiting energy consumption (low L). These models in the frequency domain are trained by using the signal obtained from the RCM-ACE algorithm with $L = 1.4$ ($\mathbf{x}_{tr,RA_{1.4}}^{ACE}$).

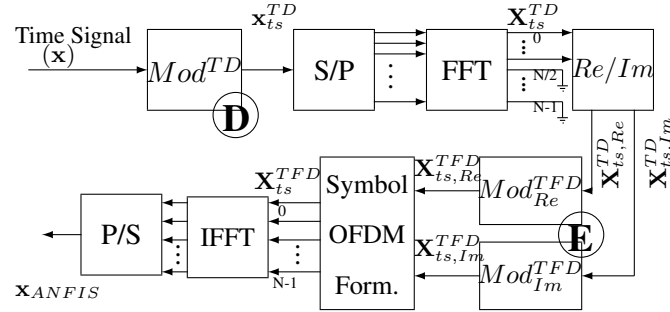


Figure 3.6: Real-time scheme for Time-Domain model (Mod^{TD}) and Time-Frequency-Domain models (Mod_{Re}^{TFD} , Mod_{Im}^{TFD}) for each quadrant.

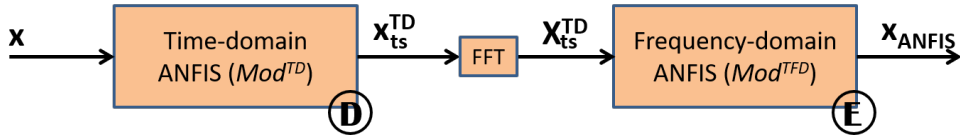


Figure 3.7: Simplified diagram of the RCM-ANFIS real-time scheme.

The procedure is as follows:

1. **Obtaining the training signals for the model** (label A in Figure 3.4 and Figure 3.5): The time-domain original DCO-OFDM signal (\mathbf{x}) is used as the input for the RCM-ACE module to reduce signal fluctuations according to the RCM-ACE scheme [Garcia Doblado *et al.*, 2015]. The resulting signals are $\mathbf{x}_{tr,RA_3}^{ACE}$ and $\mathbf{x}_{tr,RA_{1.4}}^{ACE}$, obtained with $L = 3$ and $L = 1.4$, respectively. These are the model signals that we want to obtain with ANFIS once they are trained. The clipping threshold V_{clip} and the extension gain G are variable but maintained in the range mentioned in [ETSI EN 302 755, 2012].
2. **Training the time-domain ANFIS (Mod^{TD})** (label B in Figure 3.4 and Figure 3.5): Signal \mathbf{x}_{tr}^{TD} is obtained after the ANFIS Mod^{TD} trained with $\mathbf{x}_{tr,RA_3}^{ACE}$ and \mathbf{x} . The original \mathbf{x} specifies the kinds of signals that the ANFIS will receive, whereas $\mathbf{x}_{tr,RA_3}^{ACE}$ means the objective signal. Both are used to compute the premise and consequent parameters and to make the ANFIS trained. Signal \mathbf{x}_{tr}^{TD} will be used as an input to train the frequency-domain models. Note that \mathbf{X}_{tr}^{TD} is formed by only the first half of the subcarriers because the second one is just its Hermitian symmetry.
3. **Training the 8 frequency-domain ANFIS (Mod^{TFD})** (label C in Figure 3.4 and Fig-

ure 3.5): Once the symbol DCO-OFDM ($\mathbf{X}_{tr,RA_{1.4}}^{ACE}$) is obtained by a FFT operation, it is separated in the four quadrants as well as in real and imaginary parts. In that way, there are 8 simple frequency-domain models that can be easily trained: $Mod_{1,Re}^{TFD}$, $Mod_{1,Im}^{TFD}$, $Mod_{2,Re}^{TFD}$, $Mod_{2,Im}^{TFD}$, $Mod_{3,Re}^{TFD}$, $Mod_{3,Im}^{TFD}$, $Mod_{4,Re}^{TFD}$, $Mod_{4,Im}^{TFD}$. These frequency-domain models are trained with $\mathbf{X}_{tr,RA_{1.4}}^{ACE}$ and \mathbf{X}_{tr}^{TD} , after classifying the symbols in 4 quadrants and dividing them in real and imaginary parts. Note that the half of symbols of \mathbf{X}_{tr}^{TD} are formed with the Hermitian symmetry and then discarded because they are repeated. $\mathbf{X}_{tr,RA_{1.4}}^{ACE}$ is the desired signal that is energetically restricted due to the value $L = 1.4$, whereas \mathbf{X}_{tr}^{TD} is the input signal, i.e., the kind of signal that will enter these modules in the real-time scheme.

Once the 9 ANFIS models are trained in an off-line way, we do not need to compute the RCM-ACE scheme ever again. The real-time phase is depicted in Figure 3.6:

1. Time signal (\mathbf{x}) passes through Mod^{TD} , and a signal with large energy but low RCM is obtained (\mathbf{x}_{ts}^{TD}) (label **D** in Figure 3.6 and Figure 3.7).
2. $\mathbf{X}_{ts,Re}^{TD}$ and $\mathbf{X}_{ts,Im}^{TD}$ signals result after a serial-to-parallel transformation, FFT operation, the rejection of the second half of subcarriers because they contain repeated symbols, and finally the separation of real and imaginary parts.
3. $\mathbf{X}_{ts,Re}^{TD}$ and $\mathbf{X}_{ts,Im}^{TD}$ are separated into 4 sets considering the 4 quadrants.
4. The signals are evaluated in the 8 frequency-domain models (only represented in Figure 3.6 by Mod_{Re}^{TFD} and Mod_{Im}^{TFD}), obtaining $\mathbf{X}_{ts,Re}^{TFD}$ and $\mathbf{X}_{ts,Im}^{TFD}$ (label **E** in Figure 3.6 and Figure 3.7).
5. The symbol DCO-OFDM is formed by joining real and imaginary part, and the second half of subcarriers by means of a Hermitian symmetry.
6. \mathbf{x}_{ANFIS} is obtained after an IFFT operation and a parallel-to-serial conversion. It is a signal with derated power and low RCM, energetically restricted ($L = 1.4$) and whose frequency-domain symbols are not in prohibited regions (See Figure 3.3).

For the training phase, 10000 DCO-OFDM symbols and 10 (2) Gaussian input membership functions have been carried out in the time-domain (frequency-domain) ANFIS.

Once the training was carried out off-line, the operational performance of the system is as simple as introducing the input signal, and obtaining the output after computing some additions and multiplications of real values. Concretely, the number of additions and multiplications in our proposal is $28 \times K - 12$ and $60 \times K - 20$, respectively, being K the number of subcarriers. This number of operations can be even reduced in a real implementation with hardware, because the eight quadrants in the frequency domain can be made with the same ANFIS because of having the same behavior [Louiej *et al.*, 2018]. The number of operations results from equations (3.8)-(3.12), and the real-time scheme in Figure 3.6. Since these numbers can change depending on the programming language, a more reliable metric is the asymptotic behavior. This is a linear algorithm $\mathcal{O}(K)$ because it is just based on additions and multiplications without any loop and more complex operations. Table 3.1 presents a comparison in number of the operations between RCM-ACE and RCM-ANFIS algorithms. Note that, although our proposal RCM-ANFIS needs a lower number of operations, both have the same asymptotic behavior $\mathcal{O}(K)$ and, as a result, the computational time is similar.

	RCM-ACE	Proposed RCM-ANFIS
Additions of real values	$40 \times K$	$28 \times K - 12$
Multiplications of real values	$42 \times K$	$60 \times K - 20$
Additions of complex values	$2 \times K$	0
Multiplications of complex values	K	0
Check operations	$6 \times K$	0
(I)FFT	2	2

Table 3.1: Complexity summary of RCM reduction techniques.

3.3.1.3 Simulation results and discussion

The performance of the proposal is evaluated by means of Monte Carlo simulations in a scenario where the used white LED is a Golden Dragon LA W57B [OSRAM, 2003]. Its transfer function is analytically described in [Elgala *et al.*, 2010]. As it has been mentioned, the RCM-ANFIS scheme is only necessary on the transmitter side, being completely transparent on the receiver side (see Figure 3.1). The reason is that we always distort the symbols within the allowable regions, which means that the minimum distance between symbols is not decreased and, thus, the performance of the maximum likelihood decoding algorithm is not modified. The system is assessed for K equal to 64, 256 and 1024 subcarriers, QPSK and 16-QAM constellations.

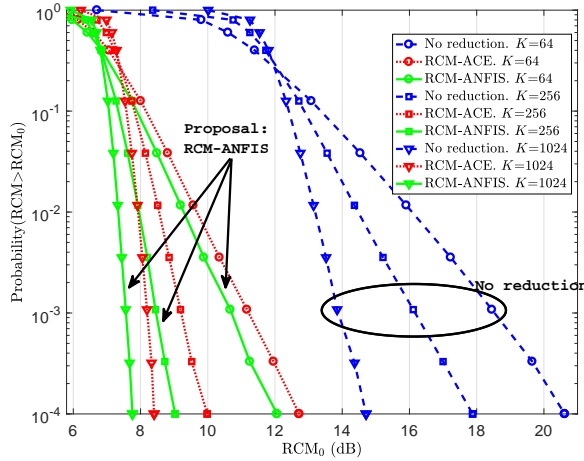


Figure 3.8: CCDF of RCM of a DCO-OFDM signal for a QPSK constellation.

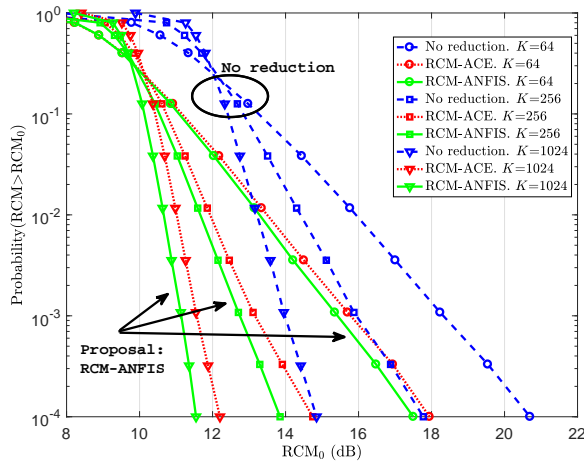


Figure 3.9: CCDF of RCM of a DCO-OFDM signal for a 16-QAM constellation.

The complementary cumulative distribution function (CCDF) is used to show the results. Figure 3.8 and Figure 3.9 show the probability that the RCM metric is higher than a certain value denoted as RCM_0 for QPSK and 16-QAM constellations, respectively. The CCDF curves are obtained with the simulation of 10^5 random DCO-OFDM symbols. In order to simulate a real analogue signal, an oversampling factor of 4 is used [Tellado, 2000]. For each number of subcarriers, three different curves are plotted: CCDF without PAPR/CM reduction, RCM-ACE method and the proposed RCM-ANFIS method. For the sake of clarity, results obtained by the traditional ACE algorithm are not plotted [Garcia Doblado *et al.*, 2015]. For each K and constellation order, a notable reduction is observed in RCM at CCDF = 10^{-4} . Table 3.2

Constellation	Method	$K = 64$	$K = 256$	$K = 1024$
QPSK	RCM-ACE	7.9 dB	7.8 dB	6.3 dB
	RCM-ANFIS (proposal)	8.6 dB	8.9 dB	7.0 dB
16-QAM	RCM-ACE	2.7 dB	3.0 dB	2.5 dB
	RCM-ANFIS (proposal)	3.2 dB	3.9 dB	3.3 dB

Table 3.2: RCM reductions at CCDF = 10^{-4}

summarizes the RCM reductions at CCDF = 10^{-4} for the RCM-ACE and RCM-ANFIS, with respect to the CCDF curve of the signal with no reduction. These reductions correspond to an improvement of EVM, ICE and BER analyzed in the following. The RCM reduction gets lowered at $K = 1024$ because a fixed configuration of membership functions was employed in order to limit the complexity.

A biasing level is necessary in order to illuminate the room in DCO-OFDM systems for VLC. However, energy consumption is as important as in any communication system. Figure 3.3 represents the symbol distribution in a QPSK constellation for RCM-ACE and RCM-ANFIS methods. Note that there is an energy increase with respect to the original constellation, in exchange for a better performance in the general system thanks to a RCM reduction. However, it corresponds only to an increase of approximately 1 % of the total energy consumption, which is almost insignificant.

Signal distortions are evaluated by means of the EVM formulated in (3.4). In Figure 3.10, the curves of EVM versus BR for an IBO of 8.9 dB (10.4 dB) in a QPSK (16-QAM) constellation are shown. This IBO value offers an EVM of 10 % for our proposal when BR is 50 %. Six different curves are represented: without PAPR/CM reduction, with the RCM-ACE technique introduced in [Garcia Doblado *et al.*, 2015] and the proposed RCM-ANFIS method, for QPSK and 16-QAM constellations. As it can be seen, our proposal reduces the EVM with respect to the result when no PAPR/CM reduction technique is applied. For a QPSK constellation and a BR equals to 50 %, an EVM of 22 % is obtained with no PAPR/CM reduction technique, whereas an EVM of 10 % results with the RCM-ANFIS method. Besides, it outperforms the results obtained with the RCM-ACE technique, an EVM of 12 % for a BR equals to 50 %. Improvements are also achieved when a 16-QAM constellation is employed. Note that EVM results for a 16-QAM constellation are better than for QPSK, due to having a larger IBO value for a 16-QAM constellation which makes avoid largely the clipping effect.

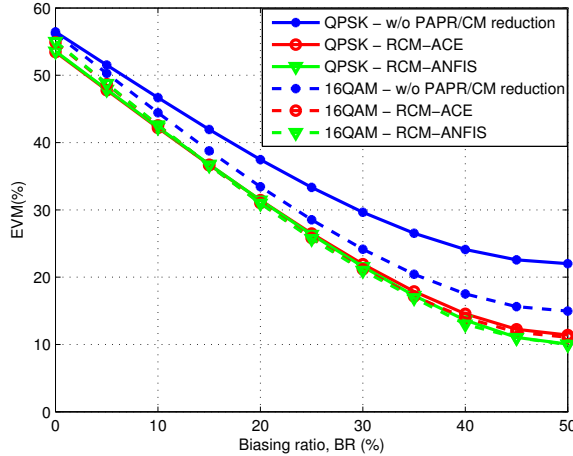


Figure 3.10: EVM versus biasing ratio for QPSK and 16-QAM constellations with an IBO of 8.9 dB and 10.4 dB, respectively.

Constellation	Method	EVM = 10%		EVM = 15%		EVM = 20%	
		IBO (dB)	IBO gain (dB)	IBO (dB)	IBO gain (dB)	IBO (dB)	IBO gain (dB)
QPSK	without PAPR/CM reduction	11.7	-	10.4	-	9.3	-
	RCM-ACE	9.2	2.5	8.1	2.3	7.2	2.1
	RCM-ANFIS (proposal)	8.9	2.8	7.9	2.5	7	2.3
16-QAM	without PAPR/CM reduction	11.7	-	10.4	-	9.3	-
	RCM-ACE	10.6	1.1	9.5	0.9	8.5	0.8
	RCM-ANFIS (proposal)	10.4	1.3	9.3	1.1	8.3	1.0

Table 3.3: IBO values and IBO gains.

Table 3.3 represents the different IBO values and gains resulting from applying the different techniques achieving EVM=10 %, 15 % and 20 %. Note that a gain of up to 2.8 dB is achieved with our proposed method, and it overcomes the RCM-ACE technique by up to 0.3 dB for QPSK and 0.2 dB for a 16-QAM constellation and EVM=10 %. Similar results have been obtained for $K = \{64, 256, 1024\}$.

The VLC system efficiency is evaluated by means of the ICE according to eq. (3.5) [Yu *et al.*, 2013b]. The results are depicted in Figure 3.11, where an improvement regardless the BF is achieved with the proposed RCM-ANFIS over the signal without PAPR/CM reduction technique. It also overcomes the RCM-ACE technique. To obtain these curves, the IBO is configured such that it provides an EVM=10 %.

Figure 3.12 and Figure 3.13 depict the curves of ICE improvement with respect to the signal

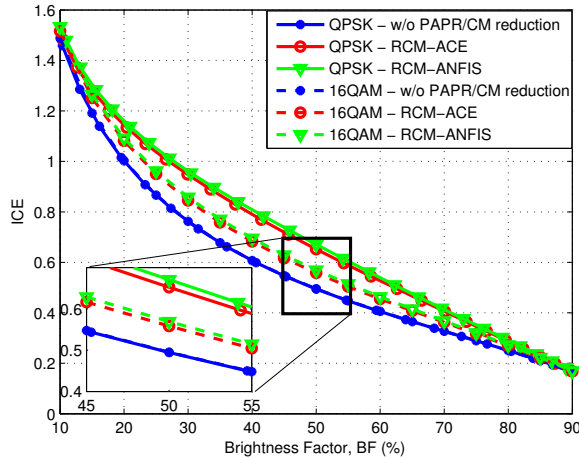


Figure 3.11: ICE versus brightness factor for EVM = 10 % with QPSK and 16-QAM constellations.

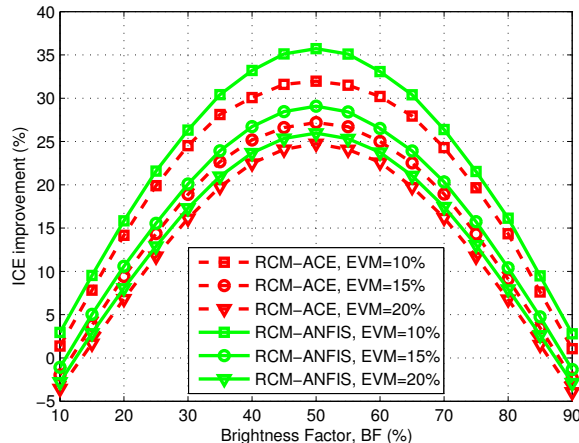


Figure 3.12: ICE improvement versus brightness factor for EVM = {10 %, 15 %, 20 %} and QPSK constellation.

without reduction technique, for QPSK and 16-QAM constellations, respectively, and different values of EVM. Note that an improvement is achieved in the whole BF range comparing to the RCM-ACE technique, but the highest improvement is achieved when the BF is equal to 50 %.

Table 3.4 shows the ICE gains extracted from the Figure 3.12 and Figure 3.13. The improvement of our proposal with respect to the RCM-ACE technique is also included. A maximum ICE gain of 35.8 % is achieved with RCM-ANFIS for a QPSK constellation, and an improvement of up to 3.9 % with respect to the RCM-ACE technique is also obtained. The proposed

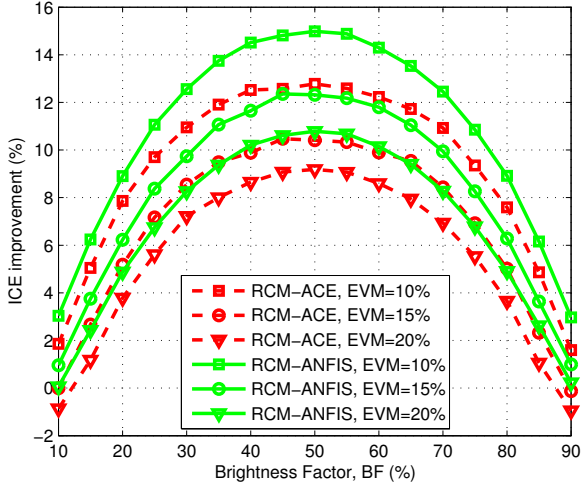


Figure 3.13: ICE improvement versus brightness factor for $EVM = \{10\%, 15\%, 20\%\}$ and 16-QAM constellation.

Constellation	Method	EVM = 10%		EVM = 15%		EVM = 20%	
		ICE Gain (%)	Improvement (%)	ICE Gain (%)	Improvement (%)	ICE Gain (%)	Improvement (%)
QPSK	RCM-ACE	31.9	-	27.1	-	24.7	-
	RCM-ANFIS (proposal)	35.8	3.9	29.1	2.0	26.0	1.3
16-QAM	RCM-ACE	12.7	-	10.4	-	9.1	-
	RCM-ANFIS (proposal)	15.0	2.3	12.4	2.0	10.8	1.7

Table 3.4: ICE gain measured at $BF = 0.5$.

method improves up to a 15 % the original signal for 16-QAM constellation, and a maximum gain of up to 2.3 % is achieved compared to the RCM-ACE technique. Similar results have been obtained for $K = \{64, 256, 1024\}$.

Figure 3.14 depicts the BER analysis of this approach and a comparison with the other techniques. These curves are obtained with a BR of 50 % and an IBO so that the EVM is equal to 10 %. Note that most of the curves have an error floor due to the clipping effect that does not allow decreasing the BER more. This aspect indeed validates the research in new methods for PAPR/CM reduction, and then, this proposal. These curves may be different if another LED model is used.

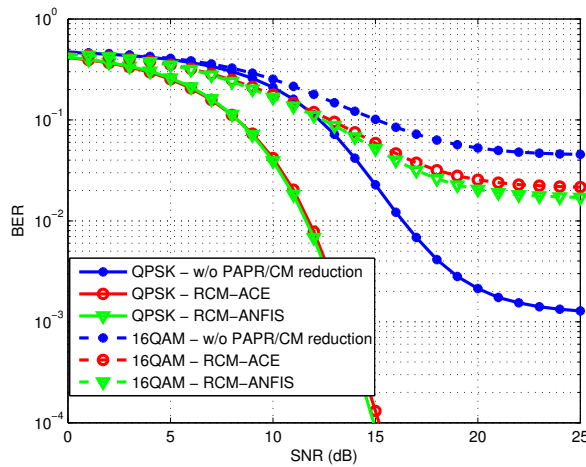


Figure 3.14: BER versus SNR for EVM = 10 % with QPSK and 16-QAM constellations.

The proposed RCM-ANFIS reduces the BER in comparison to the RCM-ACE technique and the signal without reduction technique. Both in QPSK and 16-QAM, signals without reduction technique suffer a saturation and have a noise floor in 10^{-3} and $4 \cdot 10^{-2}$, respectively. It makes clear the need of a CM reduction technique giving a much better BER performance as a result. Results of RCM-ANFIS in QPSK are better than in 16-QAM because the minimum distance between I/Q symbols in QPSK is larger and also has a larger percentage of points to be moved in the constellation: 100 % in QPSK whereas 75 % in 16-QAM. Interior I/Q symbols in a 16-QAM constellation cannot be moved in order not to decrease the minimum distance between symbols and then increase the BER.

Note that these performance differences will be larger if another LED model with a less linear transfer function and smaller dynamic range is used.

3.4 Outdoor

After addressing the non-linearity issue characteristic of the transfer function of the LEDs, the feasibility of VLC in an single-cell outdoor scenario is studied.

VLC has been predominantly studied in indoor environments because of the high density of light fixtures and as a benefit of the reduced background light coming from natural sources. However, VLC has a potential also in outdoor scenarios in the smart cities of the near future. Many of the techniques proposed for indoor VLC are less applicable to outdoor VLC owing to

the following reasons:

- *Scenario*: The heights of the APs and receivers, as well as the coverage area are rather different. The VLC coverage area in outdoor scenarios should ideally be larger than that in indoor ones. The attocell radius R of indoor scenarios is typically around 2-3 m, whereas outdoors it is thought to be approximately 7 m if street lights are used. Furthermore, street lights are typically at the height of 8 m, whereas the indoor light fixture height is around 3 m. The users in indoor scenarios are typically seated at a desk having a height of approximately 0.75 m, whereas the outdoor users are likely to be standing, holding a communicator at the height of 1.20 m.
- *Illumination requirements*: Although they depend on the activity performed, the illumination requirements of indoor scenarios are more strict than the ones for outdoor. Typical values of cell center illuminance in indoor places are hundreds of lux (around 500 lux), while tens of lux are normal values for exterior scenarios. However, the optical transmit power is higher in outdoor scenarios because the street lights have to cover a larger area.
- *Ambient noise*: The contaminating illuminance in indoor scenarios is a few hundred lux, whereas in outdoor scenarios it is tens of thousands of lux. Hence, the outdoor receiver might be ‘blinded’.
- *Shadowing*: The LoS-link blockage in VLC is one of its main drawbacks. In indoor scenarios, the LoS link’s blockage probability increases due to the presence of people and furniture. Hence, cooperative user-centric AP-grouping [Zhang *et al.*, 2015] [Li *et al.*, 2016] techniques may have to be invoked for guaranteeing at least one LoS link with one AP [Genovés Guzmán *et al.*, 2018a] [Genovés Guzmán *et al.*, 2015]. By contrast, the LoS-link blockage probability is reduced in outdoor scenarios due to the higher elevation of the AP and owing to the absence of furniture and extra obstacles.
- *Interference*: Although a wider variety of LEDs can be found in outdoor scenarios (heterogeneous scenario), the interference is expected to be lower than in indoor scenarios, because the cells are likely to be one-dimensional along a street, for example, which can be readily mitigated by using only two orthogonal frequency slots. The density of APs is much lower than in indoor environments.

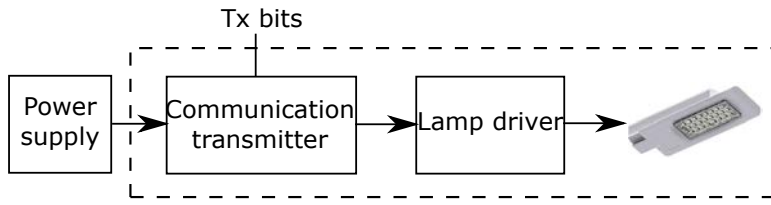


Figure 3.15: Block diagram of the VLC transmitter in an outdoor VLC scenario.

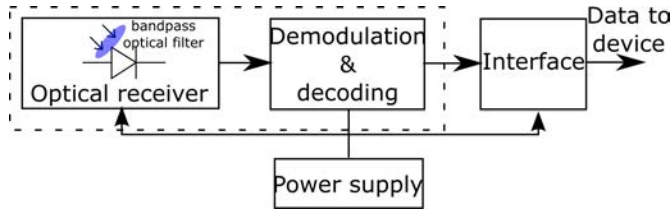


Figure 3.16: Block diagram of the VLC receiver in an outdoor VLC scenario.

3.4.1 System model of a downlink optical-OFDM

Figure 3.15 represents the block diagram of the VLC transmitter that can be used for implementing the system. To convert a traditional street light into a VLC transmitter that provides simultaneous illumination and communication, a “communication transmitter” must be installed. It receives the information to be transmitted and carries out the task of coding and modulation before being superimposed on the electrical signal of the LED lamp. The lamp driver is required for managing the AC/DC conversion in an energy efficient way (dimming mode if desired) and without causing any temperature problem. The dashed-line rectangle, composed by the communication transmitter module and the LED lamp, represents the transmitter of the O-OFDM system diagram used in this PhD Thesis depicted in Figure 2.2.

At the receiver side of Figure 3.16, we find the optical receiver composed of a bandpass optical filter and a PD for converting the optical signal to electrical signal, including the transimpedance amplifier (TIA). Next, we can observe the demodulation and decoding block provided for detecting data. Finally, the receiver has an interface block whose function is to send the data to an external device, such as a PC or a smart-phone. All these modules must be powered adequately. Again, the dashed-line rectangle represents the receiver side of Figure 2.2.

The transmitter may rely on well-known manufacturers’ lamps, which include drivers capable of powering multiple LEDs and they can be modulated simultaneously.

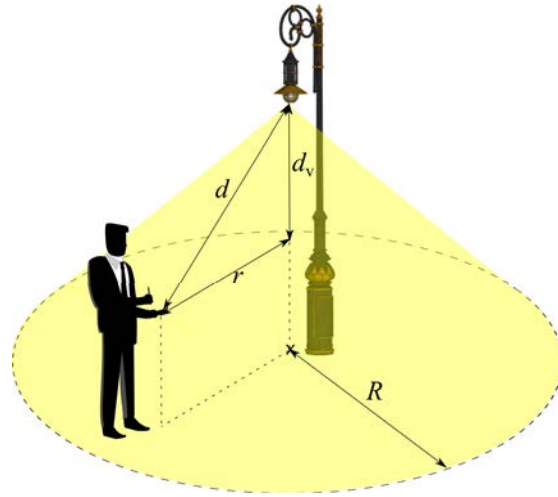


Figure 3.17: AP radiating in an outdoor VLC scenario.

The SNR equations of the DCO-OFDM and ACO-OFDM scenarios are both given by

$$\Gamma(k, r, W) = \frac{\eta_{\text{pd}}^2 \eta_{\text{led}}^2 \sigma_x^2 \rho^2 \xi^2 |H(k, r, W)|^2}{\eta_{\text{pd}}^2 \eta_{\text{led}}^2 \sigma_x^2 \sigma_{\text{clip}}^2 |H(k, r, W)|^2 + \sigma_{\text{rx}}^2(W)}, \quad (3.14)$$

where $H(k, r, W)$ is the FDCHTF of the VLC channel on the k -th FD subcarrier, r is the horizontal distance (see Figure 3.17) and W is the modulation bandwidth. In order to make a fair comparison, since some FD subcarriers do not carry energy, a normalization factor ξ is needed so that both transmit powers are the same. This factor is represented as ξ_{DCO} and ξ_{ACO} according to (2.21) and (2.22), respectively. From the optical and electrical transmit power equations initially formulated in (2.27) and (2.28), respectively, the latter can be further developed as

$$\sigma_x^2 = \frac{P_{\text{opt}}^2}{\eta_{\text{led}}^2 (\zeta + E[V(x(t))])^2} = \frac{\left(\frac{2\pi E_v d_v^2}{(m+1)K_{e/v}}\right)^2}{\eta_{\text{led}}^2 (\zeta + E[V(x(t))])^2}, \quad (3.15)$$

where the parameter E_v represents the illuminance in the area right below the LED, which is also referred to as the illuminance at the cell center, and $K_{e/v}$ is the luminous efficacy. The variable P_{opt} in (3.15) is derived from the calculation of the cell center illuminance as $E_v = \Phi \cdot \frac{H_{\text{fs}}(0)}{A_{\text{pd}}}$, where Φ is the output luminous flux of the LED expressed in lm ($= \text{lx} \cdot \text{m}^2$), that can be written as $\Phi = K_{e/v} \cdot P_{\text{opt}}$ and $H_{\text{fs}}(0)$ is the free-space channel gain between the AP and the cell center where $r = 0$, calculated as the Fourier transform of (2.38).

Considering the optical filter loss G_f and the concentrator gain G_c unitary for simplification, the optical received power is given by

$$P_{\text{opt,Rx}}(r) = P_{\text{opt}} H_{\text{fs}}(r) = \frac{2\pi E_v d_v^2}{(m+1) K_{e/v}} \cdot \frac{A_{\text{pd}}(m+1)d_v^{m+1}}{2\pi (r^2 + d_v^2)^{\frac{m+3}{2}}}, \quad (3.16)$$

where r and d_v denote the horizontal and vertical distance, respectively, between the AP and the PD.

Additionally, the receiver noise variance is formulated as

$$\sigma_{\text{rx}}^2 = \frac{N_0 W}{\xi^2}, \quad (3.17)$$

where N_0 is the power spectral density of the noise computed as (2.16).

By appropriately combining (3.14) with the electrical signal power in (2.28), the noise power in (3.17) and the channel gain in (2.35), the SNR may be expressed as

$$\Gamma(k, d, W) = \frac{C_1}{C_4 + (C_2 \cdot d^{m+3} + C_3 \cdot d^{2(m+3)}) \cdot W \cdot \exp\left(\frac{kW}{KF_{\text{fe}}}\right)}, \quad (3.18)$$

where we have

$$C_1 = (\eta_{\text{pd}} E_v d_v^{m+3} A_{\text{pd}} \xi^2 \rho)^2, \quad (3.19)$$

$$C_2 = 2qE_v K_{e/v} (\zeta + E[V(x(t))])^2 A_{\text{pd}} d_v^{m+3} \eta_{\text{pd}}, \quad (3.20)$$

$$C_3 = \left(2qE_{r,\text{ab}} A_{\text{pd}} \eta_{\text{pd}} + \frac{4\kappa_B T_{\text{abs}}}{R_L} \right) K_{e/v}^2 (\zeta + E[V(x(t))])^2, \quad (3.21)$$

$$C_4 = (\eta_{\text{pd}} E_v h^{m+3} A_{\text{pd}} \xi \sigma_{\text{clip}})^2. \quad (3.22)$$

Note that, as expected, the SNR $\Gamma(k, d, W)$ decreases with the distance d between the LED and the PD (see Figure 3.17), as well as with the modulation bandwidth W . Furthermore, the higher the index k of a FD subcarrier, the lower the SNR becomes due to the FDCHTF shape of the front-end devices formulated in (2.36).

3.4.2 System parameter evaluation

3.4.2.1 SNR statistics

The CDF of the SNR in (3.18) evaluated in terms of γ_{th} can be expressed as

$$\begin{aligned} F_{\Gamma}(\gamma_{\text{th}}) &= \Pr\{\Gamma(k, D, W) < \gamma_{\text{th}}\} \\ &= \Pr\left\{C_4\gamma_{\text{th}} + \left(C_2D^{m+3} + C_3D^{2(m+3)}\right)W \exp\left(\frac{kW}{KF_{\text{fe}}}\right)\gamma_{\text{th}} - C_1 > 0\right\} \\ &= \Pr\{D > d_{\text{th}}(\gamma_{\text{th}}, W, k)\} \\ &= \int_{d_{\text{th}}(\gamma_{\text{th}}, W, k)}^{\sqrt{d_{\text{v}}^2 + R^2}} f_D(d) dd = 1 + \frac{d_{\text{v}}^2 - d_{\text{th}}^2(\gamma_{\text{th}}, W, k)}{R^2}, \end{aligned} \quad (3.23)$$

where $d_{\text{th}}(\gamma_{\text{th}}, W, k) = \left(\frac{-C_2}{2C_3} + \sqrt{\left(\frac{C_2}{2C_3}\right)^2 + \frac{C_1 - C_4\gamma_{\text{th}}}{C_3 W \exp\left(\frac{kW}{KF_{\text{fe}}}\right)\gamma_{\text{th}}}}\right)^{1/(m+3)}$, $d_{\text{th}}(\gamma_{\text{th}}, W, k) \in [d_{\text{v}}, \sqrt{d_{\text{v}}^2 + R^2}]$, and $f_D(d) = \frac{2d}{R^2}$ is the probability density function of the random variable D that represents the Euclidean distance between the LED and the PD, computed assuming that users are uniformly distributed in the circular cell.

When AMC schemes are invoked, the outage probability is obtained from (3.23) as

$$F_{\Gamma|k=1}(\gamma_{\min}) = \Pr\{\Gamma(k=1, D, W) < \gamma_{\min}\} = 1 + \frac{d_{\text{v}}^2 - d_{\text{th}}(\gamma_{\min}, W, k=1)}{R^2}, \quad (3.24)$$

where γ_{\min} corresponds to the minimum SINR required for having a non-zero throughput for the AMC scheme. Again, the higher the FD subcarrier index, the higher the FD attenuation in (2.36) and, because of that, the SNR evaluated in $k = 1$ is considered for computing the outage probability.

3.4.2.2 Average data rate statistics

In a general way, the average data rate $\bar{R}(W)$ can be expressed as a function of the bandwidth W . Assuming the employment of ‘perfect capacity-achieving coding’ (Shannon limit), the

attainable throughput can be formulated as

$$\begin{aligned}\overline{R}_{\text{capacity}}(W) &= \frac{W}{K} \sum_{k \in \mathcal{K}_*} \mathbb{E} [\log_2 (1 + \Gamma(k, d, W))] \\ &= \frac{W}{K} \sum_{k \in \mathcal{K}_*} \int_{d_v}^{\sqrt{d_v^2 + R^2}} \log_2 (1 + \Gamma(k, d, W)) f_D(d) dd,\end{aligned}\quad (3.25)$$

where the factor $\frac{W}{K}$ represents the bandwidth of each FD subcarrier, and \mathcal{K}_* is the set of FD subcarriers indices that carry useful information, depending on the choice of the ACO-OFDM or DCO-OFDM scheme. The SNR equation $\Gamma(k, d, W)$ is represented in (3.18).

By contrast, when using AMC schemes for maximizing the performance attained according to the prevalent channel conditions, the average data rate is expressed as

$$\begin{aligned}\overline{R}_{\text{AMC}}(W) &= \frac{W}{K} \sum_{k \in \mathcal{K}_*} \sum_{n=1}^N \epsilon[n] (\Pr \{ \Gamma(k, d, W) < \gamma_{\text{th}}[n+1] \} - \Pr \{ \Gamma(k, d, W) < \gamma_{\text{th}}[n] \}) \\ &= \frac{W}{K} \sum_{k \in \mathcal{K}_*} \sum_{n=1}^N \epsilon[n] \left(\int_{d_{\text{th}}(\gamma_{\text{th}}[n+1], W, k)}^{\sqrt{d_v^2 + R^2}} \frac{2d}{R^2} dd - \int_{d_{\text{th}}(\gamma_{\text{th}}[n], W, k)}^{\sqrt{d_v^2 + R^2}} \frac{2d}{R^2} dd \right) \\ &= \frac{W}{K} \sum_{k \in \mathcal{K}_*} \sum_{n=1}^N \epsilon[n] \left(\frac{d_{\text{th}}^2(\gamma_{\text{th}}[n], W, k) - d_{\text{th}}^2(\gamma_{\text{th}}[n+1], W, k)}{R^2} \right).\end{aligned}\quad (3.26)$$

Note that $\lim_{W \rightarrow \infty} \Gamma(k, d, W) = 0$ and it decreases exponentially, thus $\lim_{W \rightarrow \infty} \overline{R}_{\text{capacity}}(W) = 0$. Furthermore, $\lim_{W \rightarrow 0} \Gamma(k, d, W) = \frac{C_1}{C_4}$ which is a constant and $\lim_{W \rightarrow 0} \overline{R}_{\text{capacity}}(W) = 0$.

Calculating $\lim_{W \rightarrow \infty} d_{\text{th}}(\gamma_{\text{th}}, W, k) = 0$, then $\lim_{W \rightarrow \infty} \overline{R}_{\text{AMC}}(W) = 0$. Also, $\lim_{W \rightarrow 0} \overline{R}_{\text{AMC}}(W) = 0$ because the order of W is higher than the order of $W^{1/(m+3)}$ ($m > 0$).

Thus, when relying on ‘perfect capacity-achieving coding’ and AMC, the average data rate in both cases satisfies $\lim_{W \rightarrow \infty} \overline{R}(W) = \lim_{W \rightarrow 0} \overline{R}(W) = 0$. Since $\overline{R}(W)$ is a continuous function at every point of its FD W , there is an optimum W that maximizes \overline{R} , leading to the maximal data rate.

3.4.3 Results and discussion

A single-cell scenario having a radius of $R = 7$ m, LED AP height of 8 m and PD height of 1.20 m is considered. This setup results in $d_v = 6.80$ m. The values of the different parameters

Parameter	Description	Value	Unit
R	Cell radius	7	[m]
d_v	Vertical distance between the AP and PD	6.8	[m]
W	Modulation bandwidth	5 to 360	[MHz]
F_{fe}	Front-end device bandwidth factor	31.7	[MHz]
ζ_{DCO}	Ratio DC-standard deviation	5.05	[dB]
ζ_{ACO}	Ratio DC-standard deviation	2.05	[dB]
η_{pd}	PD responsivity	0.4	[A/W]
A_{pd}	PD physical area	1	[cm ²]
K	Number of FD subcarriers	512	
σ_P	Power reduction factor	10	[dB]
E_v	Cell center illuminance from AP	40	[lux]
η_{sun}	Sun luminous efficacy	93	[lm/W]
T_{abs}	Absolute temperature	300	[K]
R_L	Receiver load resistance	50	[Ω]

Table 3.5: System parameters of the outdoor scenario.

are shown in Table 3.5. The modulation bandwidth is the specific parameter under study, and it can assume a value spanning from 5 to 360 MHz. The front-end devices utilized for this study are the same as in [Khalid *et al.*, 2012] and have a bandwidth factor of $F_{fe} = 31.7$ MHz to model their FDCHTF as in (2.36). The normalized bottom (λ_b) and top (λ_t) clipping levels and the DC-bias levels are selected for DCO-OFDM and ACO-OFDM cases as mentioned in Section 2.4.2 in order to minimize the clipping noise.

The power reduction factor (σ_P) is the dual pair of the pathloss in classical RF systems, which quantifies the ratio of the received optical power at the cell center and at the cell edge, and it is configured to be 10 dB in order not to cause much SNR difference among users within a cell. That is, a user located at the cell edge will exhibit 10 dB lower SNR compared to a user located at the cell center, as seen in Figure 3.18. This difference in optical received power is determined by the Lambertian emission order m given by [Chen *et al.*, 2016]

$$m = \frac{\ln \sigma_P}{\ln \left(1 + \frac{R^2}{d_v^2} \right)} - 3. \quad (3.27)$$

Furthermore, $K = 512$ FD subcarriers are used, along with $E_v = 40$ lux, $T_{abs} = 300$ K and $R_L = 50$ Ω. The SPCTRAL2 simulation model [Bird and Riordan, 1986] is utilized in our

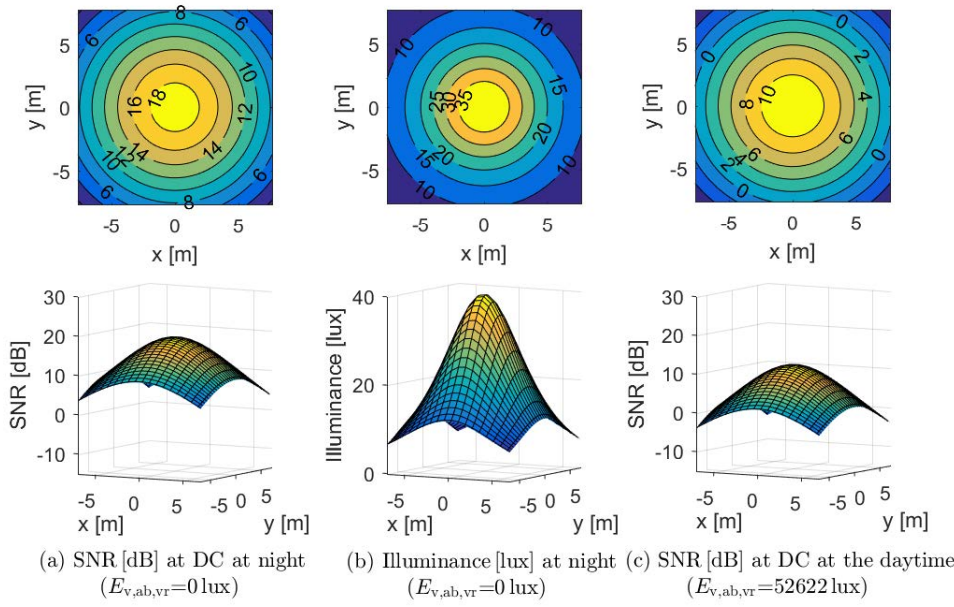


Figure 3.18: Single-cell scenario performance for $W = 360 \text{ MHz}$, DCO-OFDM and different ambient conditions (2D: top, 3D: bottom).

study to compute spectral irradiance measurements in a certain location. The Atacama desert ($24^{\circ}30' \text{S } 69^{\circ}15' \text{W}$) was selected as the worst-case location for this study, noting that in much of the world there is less daylight than in there [Rondanelli *et al.*, 2015]. The highest spectral irradiance in the Atacama desert occurs in December. Thus, data was generated for the 354th day of the year assuming a detector elevation angle of 0° . The phosphor-coated white LEDs suffer from a slow response produced by the phosphor yellow light component [Le Minh *et al.*, 2009]. This bandwidth can be boosted by invoking a bandpass optical blue filter at the receiver. At the same time, it reduces the shot noise and the risk of receiver saturation. Thus, a Semrock (97% transmittance at 452 nm, 45 nm bandwidth) optical blue filter [Khalid *et al.*, 2012] is utilized in our study. Depending on the time of the day, the incident irradiance after the optical blue filter ($E_{r,ab}$) can vary from 0 to 116.71 W/m^2 corresponding to night-time and noon, with illuminances from ambient light in the visible range ($E_{v,ab-vr}$) of 0 and 52622 lux, respectively. The illuminance from ambient light in the visible range and the incident irradiance after the blue filter in the given location are represented in Table 3.6. The illuminance from ambient light after the optical blue filter ($E_{v,ab}$) is expressed as

$$E_{v,ab} = E_{r,ab} \cdot \eta_{\text{sun}}, \quad (3.28)$$

Time of day	6h	7h	8h	9h	10h	11h	12h	13h	14h	15h	16h	17h	18h
Illuminance $E_{v,ab-vr}$ [lux]	1927	11525	23444	34542	43543	49716	52622	52061	48073	40931	31162	19616	7928
Irradiance after filter $E_{r,ab}$ [$\frac{W}{m^2}$]	4.88	23.58	49.57	74.83	95.61	109.95	116.71	115.41	106.13	89.57	67.08	41.03	16.27

Table 3.6: Average illuminance from ambient light in the visible range and incident irradiance after blue filter throughout the day.

where η_{sun} is the sun's luminous efficacy. These values result in an optical transmit power of $P_{\text{opt}} = 61.2 \text{ W}$ computed as explained in (3.15), which is a value within the typical ranges of commercial LED street lights [Jin *et al.*, 2015].

The shot noise is the main noise in a VLC system in outdoor scenarios. Although the ambient light effect may be mitigated by means of filters owing to its slowly-varying DC-like nature, it still causes shot noise at the receiver front-ends. This effect can be seen in Figure 3.18, where a difference of 7.5 dB is observed between the SNR at DC in a DCO-OFDM single-cell scenario at night (Figure 3.18 (a)) and at the daytime using $E_{v,ab-vr} = 52622 \text{ lux}$ and $W = 360 \text{ MHz}$ (Figure 3.18 (c)). The SNR in Figure 3.18 refers to the SNR at DC over all the coverage area points, i.e., the SNR for the subcarrier $k = 0$ and $W = 360 \text{ MHz}$ is expressed as $\Gamma(k=0, r, W=360\text{MHz})$ in (3.14). As (3.17) shows, the lower the sampling frequency, the lower the noise at the receiver becomes, which of course reduces the achieved data rate. Figure 3.18 (b) represents the illuminance at night in the cell, where a cell center illuminance of $E_v = 40 \text{ lux}$ is used according to the ANSI/IESNA RP-8-14 lighting regulation. In the case of Figure 3.18 (a), communications become feasible. However, Figure 3.18 (c) shows the difficulty of having a sufficiently high SNR for reliable communications during the daytime.

The CDF of the SNR at DC at night and during the daytime is depicted in Figure 3.19. Again, there is an SNR loss of 7.5 dB during the daytime in comparison to the performance at night. The reason behind this is the shot noise produced at the receiver due to the ambient light. Furthermore, an SNR difference of 5 dB is observed between DCO-OFDM and ACO-OFDM. The reason for this is the fact that the receiver's noise variance in ACO-OFDM is about half that of the corresponding to DCO-OFDM, because almost half of the FD subcarriers ($K/2 - 1$) carry useful information in DCO-OFDM, whereas only a quarter of them carry useful information in ACO-OFDM. Thus, according to (2.21) and (2.22), we have $\xi_{\text{ACO}}^2 \approx 2\xi_{\text{DCO}}^2$ and as a consequence of (3.17), we have $\sigma_{\text{rx},\text{ACO}}^2 \approx \sigma_{\text{rx},\text{DCO}}^2/2$. Furthermore, part of the electrical power

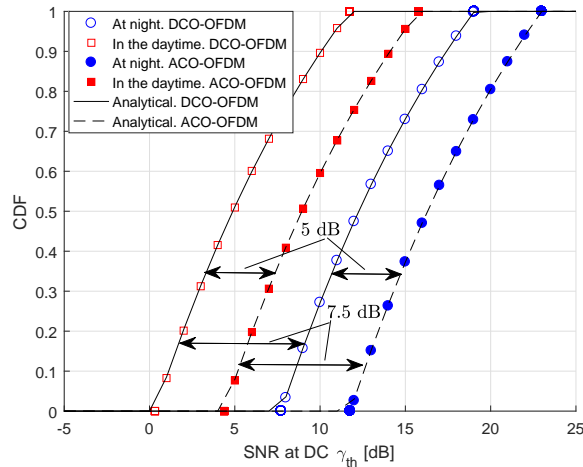


Figure 3.19: CDF of the SNR at FD subcarrier index $k = 0$ (DC) and at a $W = 360$ MHz for different conditions. $F_{\Gamma|k=0,W=360\text{ MHz}}(\gamma_{\text{th}})$.

in DCO-OFDM is wasted for the DC-bias, hence only part of it is used for communication, whereas ACO-OFDM needs much lower power for biasing and therefore more power is used for communications.

Section 3.4.2 demonstrated that the average data rate is a continuous function of W and there is a maximum in its domain of $W > 0$. Two different AMC schemes are investigated, whose operating regions are shown in Table 3.7. The AMC_1 scheme corresponds to uncoded QAM [Xiong, 2006] and the regions are configured for a $\text{BER} = 10^{-3}$, while AMC_2 is more spectrally efficient than AMC_1 and it is reminiscent of the 4G in the LTE scheme [Webster, 2010], where a cyclic redundancy check (CRC) and turbo-coding are utilized. The SINR regions of AMC_2 are not standardized and then they depend on the operator. The ones here utilized are obtained from [Webster, 2010]. The analytical expressions of the average data rate were obtained in (3.25) and (3.26), where the CCMC capacity or realistic AMC schemes were assumed, respectively. These analytical curves are plotted using continuous or dashed lines in Figure 3.20 and Figure 3.21, during the daytime and at night, respectively, together with our simulation results represented by symbols. Note that the simulations closely match the analytical curves, which confirms the accuracy of our analytical expressions for further studies. In Figure 3.20, the illuminance from ambient light in the visible range is set to its maximum value ($E_{v,\text{ab-vr}} = 52622$ lux). The mean cell data rate increases up to a certain point and then degrades, because the larger the bandwidth, the higher the receiver noise becomes according to (3.17). Besides, a larger bandwidth means that power is wasted on subcarriers which are highly

AMC ₁			AMC ₂			
$\gamma_{\text{th}}[n]$ [dB]	Modulation	$\epsilon[n]$ [bits/symbol]	$\gamma_{\text{th}}[n]$ [dB]	Modulation	Code rate	$\epsilon[n]$ [bits/symbol]
7.6 (γ_{min})	BPSK	1	5 (γ_{min})	16QAM	0.369	1.4766
9.8	QPSK	2	8	16QAM	0.476	1.9141
13.4	8QAM	3	9	16QAM	0.602	2.4063
16.5	16QAM	4	11	64QAM	0.455	2.7305
19.6	32QAM	5	12	64QAM	0.554	3.3223
22.5	64QAM	6	14	64QAM	0.650	3.9023
25.5	128QAM	7	16	64QAM	0.754	4.5234
28.4	256QAM	8	18	64QAM	0.853	5.1151
-	-	-	20	64QAM	0.926	5.5547

Table 3.7: Adaptive modulation and coding SINR regions (outdoor study).

attenuated. Thus, each communication setup is configured at the optimal W value that maximizes the average data rate. The maximum capacity of DCO-OFDM is 144.5 Mbps, which is obtained for $W = 140$ MHz; AMC₁ achieves a maximum of 52.37 Mbps for $W = 50$ MHz; and AMC₂ operates at 82.59 Mbps at $W = 75$ MHz. However, although ACO-OFDM exhibits a better SNR performance than DCO-OFDM, since ACO-OFDM uses half of the FD subcarriers of DCO-OFDM, the resultant achievable average data rate is lower. The maximum average data rates obtained by ACO-OFDM are 112.10, 48.53 and 70.89 Mbps for W values of 180, 80 and 110 MHz, at capacity, using AMC₁ and AMC₂, respectively. During the night (Figure 3.21) the background light disappears, which results in a considerable reduction of the shot noise. In this case, the increased modulation bandwidth is not so detrimental and, as a consequence, the achievable mean cell data rates are much higher than during the daytime.

Observe in Figure 3.20 and Figure 3.21 that ACO-OFDM provides a better performance than DCO-OFDM for W values beyond a cross-over point, where the reduction in the noise achieved by ACO-OFDM becomes more important than using more FD subcarriers for carrying information.

Figure 3.22 shows that the uncoded QAM scheme AMC₁ exhibits a high outage probability in comparison to AMC₂. For example, performing ACO-OFDM and obtaining an outage probability of 2 %, the AMC₂ scheme is able to work with a bandwidth larger in 140 MHz in comparison to the bandwidth employed in AMC₁. The analytical outage probability is computed as $F_{\Gamma|k=1}(\gamma_{\text{min}})$ in (3.24). Note that the larger the bandwidth, the higher the noise becomes and, as a consequence, the outage probability increases. Generally DCO-OFDM suffers from a much

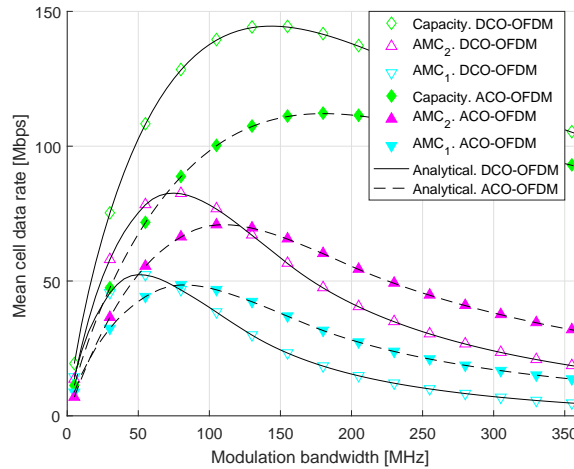


Figure 3.20: Average data rate \bar{R} vs. bandwidth W at capacity, with AMC_1 and AMC_2 , during daytime ($E_{v,ab-vr} = 52622 \text{ lux}$).

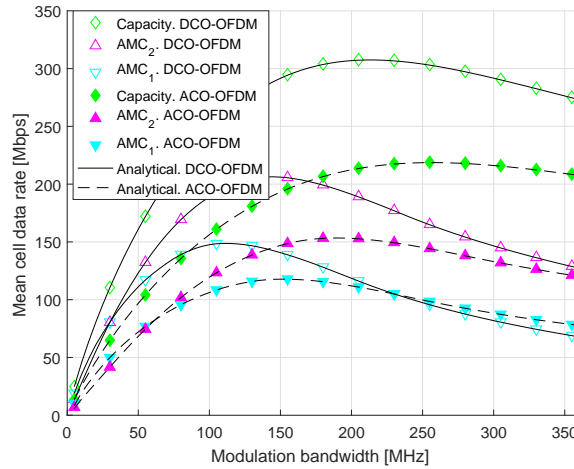


Figure 3.21: Average data rate \bar{R} vs. bandwidth W at capacity, with AMC_1 and AMC_2 , at night ($E_{v,ab-vr} = 0 \text{ lux}$).

higher outage probability than ACO-OFDM, because the SNR performance of ACO-OFDM is better, as seen in Figure 3.19. An outage probability of 10% at most is shown in Figure 3.22 because larger outage probabilities are not interesting for practical systems. Note that the degradation is not as gradual as expected because the working SINR regions are low for all modulation bandwidths due to the high shot noise produced during daytime ($E_{v,ab-vr}=52622 \text{ lux}$). In our future research we will use adaptive layered ACO-OFDM (LACO-OFDM) for avoiding the avalanche-like outage probability degradation imposed by the excessive shot noise inflicted

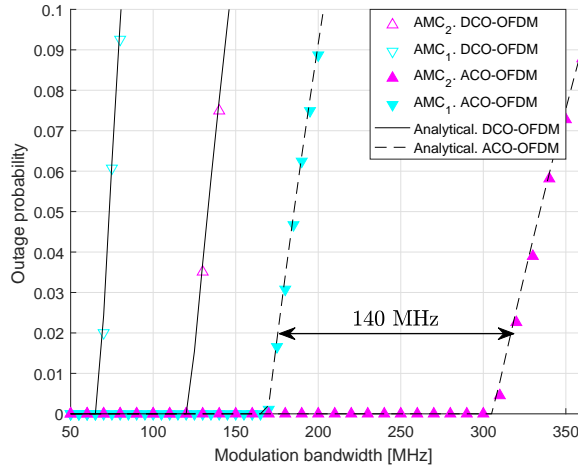


Figure 3.22: Outage probability vs. modulation bandwidth W with AMC_1 and AMC_2 , during daytime ($E_{v,ab-vr} = 52622 \text{ lux}$).

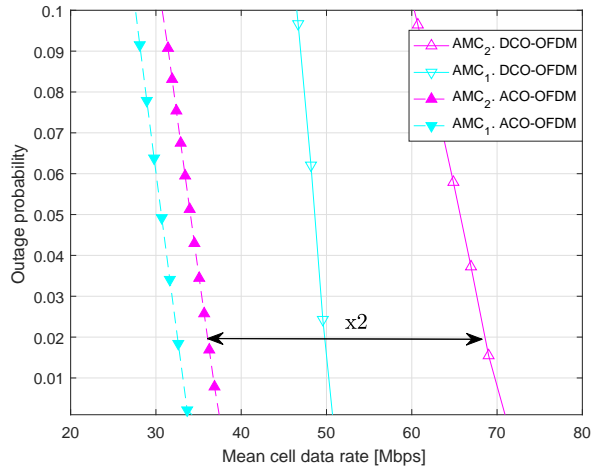


Figure 3.23: Outage probability vs. mean cell data rate with AMC_1 and AMC_2 , during daytime ($E_{v,ab-vr} = 52622 \text{ lux}$).

by intense sunshine [Zhang *et al.*, 2017].

Figure 3.23 shows the relation between the mean cell data rate and the outage probability. A higher outage probability involves a higher modulation bandwidth, as seen in Figure 3.22. Higher mean cell data rates can be achieved for very low values of outage probability, as shown in Figure 3.20 and Figure 3.22. As expected, DCO-OFDM is more efficient than ACO-OFDM because, for the same outage probability, the achieved mean cell data rate is higher even when using a lower modulation bandwidth. For example, for an outage probability of 2 % and us-

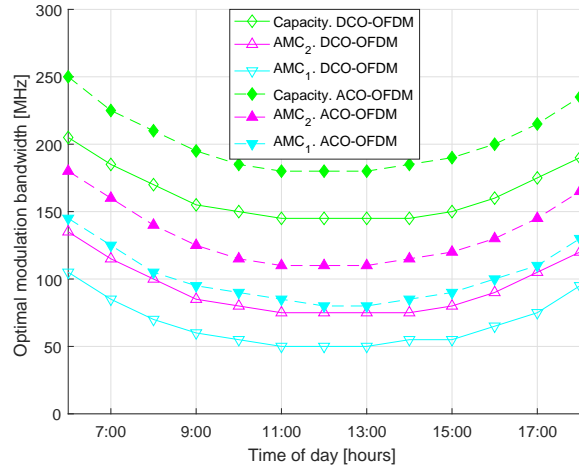


Figure 3.24: Optimal modulation bandwidth for maximizing the average data rate throughout the day.

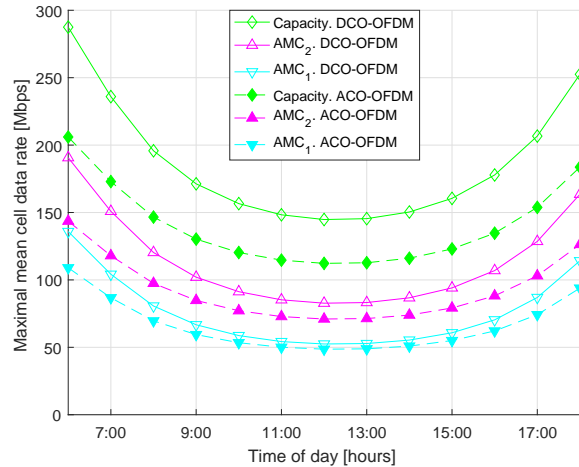


Figure 3.25: Achievable maximal average data rate throughout the day.

ing the AMC_2 scheme, DCO-OFDM almost duplicates the achievable mean cell data rate in comparison with ACO-OFDM.

It has been demonstrated in Figure 3.20, Figure 3.21 and Section 3.4.2 that an optimal W can be found by maximizing the average data rate for certain conditions. It is interesting to study how these optimal W and average data rates vary during the day. Figure 3.24 shows the optimal modulation bandwidth for certain hours of the day that makes the maximal average data rate represented in Figure 3.25 possible. As expected, noon is the most critical time, when the lowest average data rate is obtained in bright sunshine. However, a reasonable value of 83 Mbps can

still be achieved, when DCO-OFDM and AMC₂ are used. Higher average data rate values can be obtained by more spectrally efficient schemes than the uncoded QAM (AMC₁), such as AMC₂. In general, DCO-OFDM outperforms ACO-OFDM. Nevertheless, the higher the background noise power, the lower the differences between DCO-OFDM and ACO-OFDM become.

3.5 Summary

This Chapter studied the effect of high PAPR and CM in multi-carrier systems when realistic LED models are used in VLC. An efficient technique for creating DCO-OFDM signals with low CM based on ANFIS was proposed. Using a proper combination of optimized training models, the proposed RCM-ANFIS obtains efficient power derated DCO-OFDM signals. Once trained, the ANFIS models can work autonomously. Our proposal uses the RCM metric to build a more effective algorithm, achieving a reduction of 8.9 dB with respect to the original DCO-OFDM signal at CCDF = 10⁻⁴, unlike the 7.8 dB reduction obtained by the RCM-ACE method. Since the clipping effect is mitigated due to this power derating technique, the signal degradation is reduced 12 % in EVM at the most for a fixed IBO value. On fixing an EVM value, the RCM-ANFIS technique overcomes the RCM-ACE technique and achieves IBO gains of 2.8 dB (for EVM = 10 %). It produces ICE gains above 35 %, leading to improvements of up to 3.9 % with respect to the RCM-ACE method. Finally, improvements in BER are also obtained. For all the studied parameters and figures of merit, the implementation of this technique in a DCO-OFDM VLC system involves a better efficiency between the communication capacity and the illumination level.

Besides, this Chapter presented a pioneer analytical study of O-OFDM in outdoor VLC scenarios. The modulation bandwidth adaptation results in substantial data rate and outage probability improvements. The background noise increases with the modulation bandwidth, hence the optimum sampling frequencies and bandwidths were found for specific environmental conditions. Although ACO-OFDM can perform at higher modulation bandwidths than DCO-OFDM for the same outage probability, DCO-OFDM provides better performance in terms of mean cell data rate. Generally, DCO-OFDM achieves a better performance than ACO-OFDM in the absence of background noise than during the daytime. For the practical employment of VLC schemes in outdoor scenarios, more robust schemes relying on strong forward error correction-aided (FEC-aided) automatic repeat request (ARQ) schemes and power-efficient modulation arrange-

ments have to be developed, using for example M-ary orthogonal modulation.

Chapter 4

Multi-cell VLC

4.1 Introduction

Multi-cell VLC scenarios are being created to offer a seamless and reliable network. This Chapter studies different multi-cell scenarios with single-carrier and multi-carrier modulation schemes and evaluates their performance.

Since the SSL is replacing other types of lighting technologies, the required infrastructure for VLC is already there to deploy this network and provide Internet access and lighting services simultaneously. However, VLC must still tackle key challenges, such as the presence of strong LoS blockage and inter-cell interference events, which are two phenomena that impact the attainable data rate of the technology, particularly in ultra-dense small cell indoor scenarios.

VLC networks are being proposed and deployed to provide a seamless coverage indoors [Haas, 2013] [Haas *et al.*, 2016]. Performance analysis in multi-cell VLC networks is more critical than in single-cell scenarios due to the impact of inter-cell interference, which is created due to the deployment of multiple light fixtures in the same indoor area required for complying with the stringent lighting regulations (in terms of mean value and variability of illumination). Thus, inter-cell interference mitigation techniques become essential to keep this impairment under control. Besides, when working with wavelengths in the optical spectrum, LoS blockage impacts the communication capabilities notably [Chen and Haas, 2017]. In this case, when there is a NLoS condition between the transmitter and the receiver, most VLC system designs are usually in outage (particularly in presence of strong inter-cell interference).

It is important to highlight that contemporary RF multi-cell systems also suffer from inter-cell interference and LoS-link blockages but to a much lesser extent. Due to the carrier frequency that RF technology uses is much lower than optical wireless technology, the impact of LoS blockages is notably lower. Radio systems are more resilient to LoS blockages because the energy contribution of physical propagation mechanisms in RF bands (i.e., transmission/reflection, diffraction, and refraction, among others) enables the reception of appropriate signal levels even

in case of blockage events; in contrast, optical signals cannot pass opaque objects and the energy contribution of physical propagation mechanisms in NLoS situations is minimal at optical frequencies. In addition, the deployment of RF cells is made by qualified staff that seeks the minimization of the overlapping area among cells for better network coverage. In contrast, an illumination system cannot be easily optimized for data transmission since the placement of the light fixtures is usually pre-defined. Thus, the inter-cell interference and LoS-link blockage phenomena in VLC systems deserve a complete different study.

4.2 State of the art

Different techniques have been traditionally proposed in RF multi-cell systems to mitigate the strong inter-cell interference that exists in cell-edge areas. For example, FFR utilizes different frequency-reuse factors in cell-center and cell-edge areas to keep the inter-cell interference under control [Novlan *et al.*, 2012] [Wang and Yeh, 2011]. The authors of [Chen *et al.*, 2015] and [Kazemi and Haas, 2016] evaluated FFR for VLC scenarios, showing a considerable inter-cell interference reduction for those users located at the borders of the cells. However, in ultra-dense VLC networks, the performance gain of FFR is expected to be much lower as users located at the cell-center areas (i.e., just below the light fixtures) also suffer from a high inter-cell interference level coming from the adjacent lamps.

Similarly, CoMP transmission schemes are also employed in multi-cell RF communication systems with strong inter-cell interference. CoMP transmission and reception techniques were originally proposed in LTE [Sawahashi *et al.*, 2010] and LTE-A [3GPP TR 36.814, V9.0.0, 2010] for improving the cell-edge throughput in multi-cell scenarios. More precisely, the aim of JT CoMP is to convert inter-cell interference coming from different transmission points into useful signal [Jungnickel *et al.*, 2014] [Irmer *et al.*, 2011]. Early studies on frequency allocation for CoMP were made to improve the throughput of cell-edge users when RF base stations deployed directional antennas [Hwang *et al.*, 2012] and when VLC APs were equipped with non-conventional directional LEDs pointing to the cell edges [Chen *et al.*, 2013]. In addition to inter-cell interference mitigation, JT CoMP techniques have gained importance in VLC [Ma *et al.*, 2015] [Ma *et al.*, 2018] because they also combat the LoS-link blockage problem that the technology experiences. However, as VLC-enabled devices may not have the chance to feed back their channel condition frequently (particularly, when the number of devices to be served per small cell is too large), it is desirable that the resource allocation scheme of the multi-cell

VLC system is pre-defined *a priori* to give as good coverage as possible. In addition, since the LoS-link blockage in a fully optical VLC system is bi-directional (i.e., both in downlink and uplink), the transmitter may not receive any feedback information from a blocked user for the whole duration of the event.

The authors of [Demir *et al.*, 2017] proposed to use CoMP to enable smoother handover operations among neighboring VLC APs. Similarly, the use of CoMP was combined with spatial division multiple access (SDMA) techniques [Haas *et al.*, 2016] [Yin *et al.*, 2015] to implement a pre-coded transmission to different groups of users that are properly clustered. Finally, the authors of [Chen and Haas, 2017] considered a dynamic resource allocation and a multiple APs assignment to perform JT CoMP. In general terms, the use of CoMP in VLC has demonstrated a higher level of reliability in communication. However, most of the CoMP techniques proposed in the literature so far for VLC were optimized *ad hoc* for the set active users and, due to that, had a computational complexity that increased with the number of users. Besides, these solutions are not static, making the communication unstable and unreliable when LoS-link blockages with relative short duration happen regularly (e.g., when obstacles pass by quickly). These techniques demand to sense the optical wireless channel permanently and to reallocate resources accordingly if a blockage event is detected; in addition, since the blockage also affects the feedback channel, the user would not have the chance to inform about this situation to the serving AP in fully optical VLC systems.

This Chapter presents and evaluates static JT CoMP techniques in different scenarios, when single-carrier or multi-carrier modulation schemes are invoked.

4.3 Cooperative transmission technique in single-carrier modulation

4.3.1 System model

This Section develops a preliminary examination of LoS-link blockage when a single-carrier modulation scheme in a realistic scenario is considered [Genovés Guzmán *et al.*, 2015]. A typical LED topology in a corridor as the one represented in Figure 4.1 and Figure 4.2 is studied.

The use of OOK modulation in VLC APs is a simple way to transmit data to the receivers. In these scenarios where the coverage needs to be provided by several transmitters, each atto-

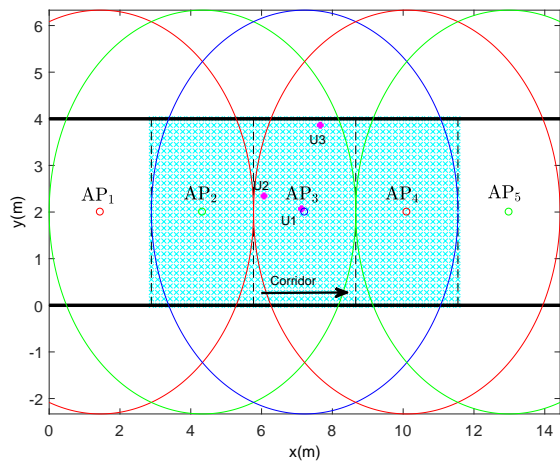


Figure 4.1: Overhead view of a corridor scenario with 5 APs.

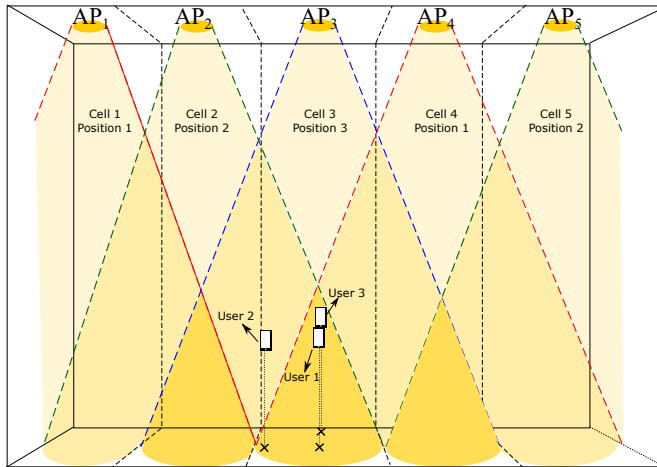


Figure 4.2: Perspective of a corridor scenario with 5 APs.

cell could use a different wavelength for avoiding inter-cell interference [Elgala *et al.*, 2011]. However, this scheme increases complexity at the receiver which needs to be able to detect different wavelengths by using an array of photodetectors with different wavelength sensitivities or filters. Besides, the handover process needs more signal processing.

Otherwise, this preliminary proposal uses a single wavelength band, which can be optimized for specific environmental light conditions. In order to avoid inter-cell interference, a pulse position division multiplexing (PPDM) is carried out at the APs, i.e., each neighboring AP transmits its pulses in a different position within the interval (see Figure 4.3 and Figure 4.4). In this way, several advantages are obtained. Firstly, receivers are simpler because only one centered

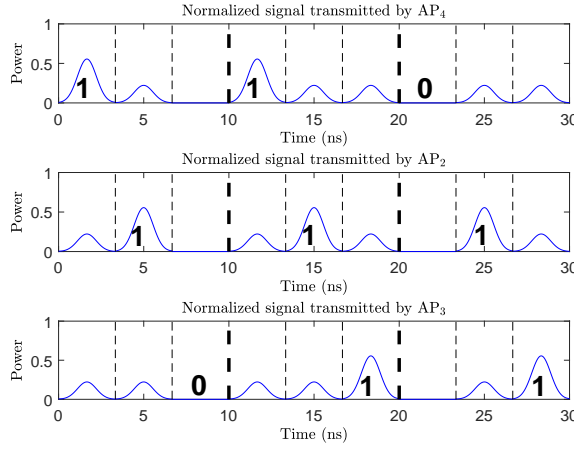


Figure 4.3: OOK PPDM with cooperation.

wavelength has to be detected. Secondly, since the receiver is tuned to the wavelength, it is able to detect signals from the other APs in the neighborhood, and thus, a cooperative transmission and reception can be performed in the following way:

- At each cell, the AP knows the data to transmit, and also the data that has to be transmitted by other neighboring cells, by means of the backhaul feedback link.
- In this way, it could help the other cells in the neighborhood by transmitting their data during the appropriate interval, albeit with less energy (this can be seen in Figure 4.3).
- Consequently, the detected power at the receiver side will come from the serving AP and the cooperating neighboring APs.

Note that cooperating pulses use lower power for a fair comparison and for reducing inter-cell interference.

For the sake of clarity, in the scenario depicted in Figure 4.1 and Figure 4.2, an example of such a transmission scheme is shown in Figure 4.3, where three users are served by: the nearest AP denoted by AP₃, using position 3 within the frame; and two neighboring APs denoted by AP₂ and AP₄, transmitting at positions 2 and 1, respectively. In this example, AP₃ transmits {0, 1, 1} and the neighboring AP₂ and AP₄ transmit {1, 1, 1} and {1, 1, 0}, respectively. As can be seen in Figure 4.4, if there is no cooperation, each AP transmits its data in the proper interval. By contrast, in the proposal, the neighboring APs cooperate in the transmission of the data

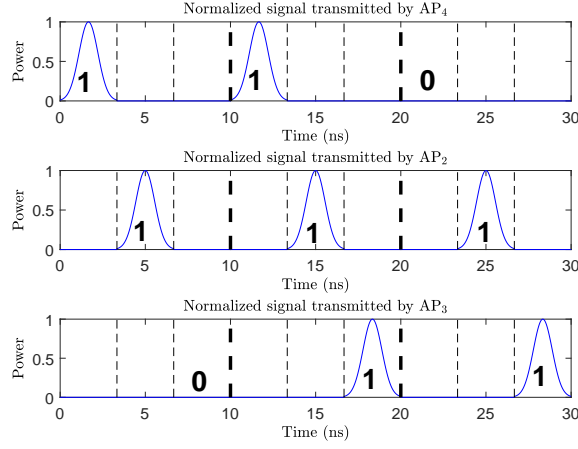


Figure 4.4: OOK PPDM without cooperation.

and therefore help the receiver by following the PPDM scheme (in Figure 4.3 the cooperative sidelobes can be appreciated).

The received optical power by any of the users represented in Figure 4.1 and Figure 4.2, who are in the cell 3 corresponding to AP₃, in the CoMP and no-CoMP schemes are

$$P_{\text{opt,rx}}(r, \theta) \Big|_{\text{CoMP}} = \sum_{i=2,3,4} P_{\text{opt},i} \cdot H_i(r, \theta), \quad (4.1)$$

and

$$P_{\text{opt,rx}}(r, \theta) \Big|_{\text{no-CoMP}} = P_{\text{opt},3} \cdot H_3(r, \theta), \quad (4.2)$$

respectively, where the index i indicates the serving AP, and (r, θ) are the polar coordinates of a user location with respect to the AP₃ location. Note that $H_3 = H_{\text{NLoS},3}$, where $H_{\text{NLoS},3}$ is the Fourier transform of $h_{\text{NLoS},3}(t)$ in (2.37), when user experiences a LoS blockage with respect to its nearest AP (AP₃). However, since the signal is also received from AP₂ and AP₄ in the scheme, the receiver could still decode the data.

Parameter	Description	Value	Unit
P_{opt}	Optical transmit power	72	[W]
d_v	Vertical distance between AP and PD	2.5	[m]
$\phi_{1/2}$	Half-power semi-angle of the LED	70	[deg.]
Ψ_{FoV}	Field-of-view of PD	60	[deg.]
η_{pd}	PD responsivity	0.54	[A/W]
A_{pd}	PD physical area	1	[cm ²]
n_{ref}	Refractive index of the concentrator	1.5	
$\theta_{\text{lightNLoS}}$	Percentage of light arriving in NLoS	30	[%]
ρ_{sidelobe}	Sidelobes' amplitude level	40	[%]

Table 4.1: System parameters for the single-carrier and multi-cell scenario.

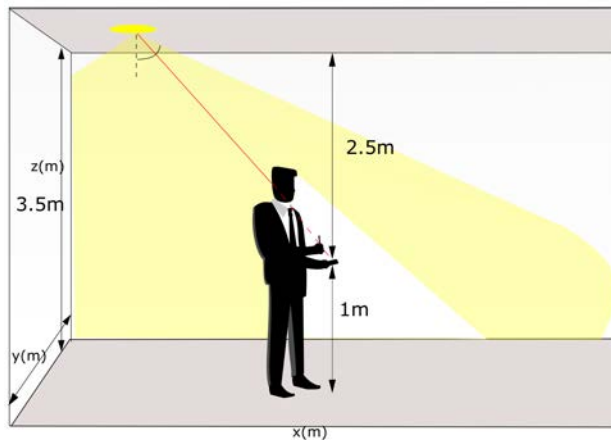


Figure 4.5: Person with a LoS-link blockage.

4.3.2 System parameter evaluation

In this scenario, the SNR at the location (r, θ) can be computed by

$$\Gamma(r, \theta) = \frac{\eta_{\text{pd}}^2 \cdot P_{\text{opt,rx}}^2(r, \theta)}{\sigma_{\text{rx}}^2}, \quad (4.3)$$

where in this case σ_{rx}^2 is computed as [Komine and Nakagawa, 2004] for simplicity, assuming a data rate of 100 Mbps and the system parameters shown in Table 4.1. Figure 4.5 displays the dimensions of the scenario.

Once the scheme was established, some simulations were carried out in order to show the improvements in the SNR at the receiver side when there are obstacles. Note that, to make

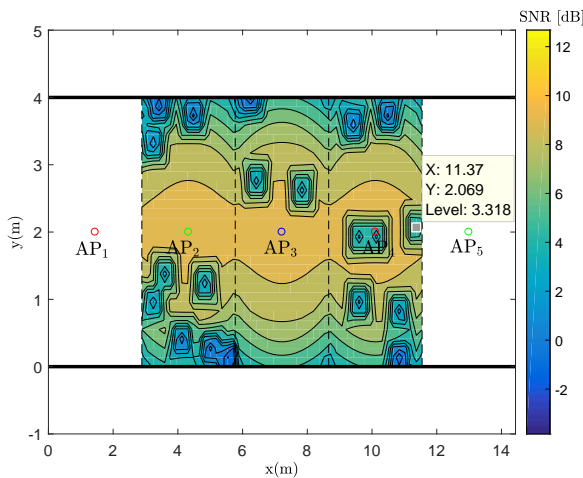


Figure 4.6: SNR with CoMP in a scenario where some users are obstructed.

a fair comparison, the transmitted energy from the two schemes is such that the power of the transmitted signal is the same in both CoMP and the traditional schemes. In this proposal, there is a pair of uncommon parameters that must be defined:

- Percentage of light arriving in NLoS case $\theta_{\text{lightNLoS}}$: it is a simplification in this simple scenario, representing the signal power that arrives at the receiver through the NLoS paths.
- Sidelobes' amplitude level ρ_{sidelobe} : represents the signal power, as a percentage, compared to the main lobe, which is given to the sidelobes in the CoMP scheme.

4.3.3 Results and discussion

Figure 4.6 and Figure 4.7 plot the SNR results in all the possible positions, where some LoS-link blockages with the nearest AP occur. The CoMP solution provides a better performance for the obstructed users, gaining at most 2.55 dB in the SNR. By contrast, the CoMP solution obtains 3 dB at most less than the no-CoMP solution when there is LoS. Thus, when there are no obstacles, the distance from the serving access point is shorter and the optimum solution is to transmit all the power from there. Thus an adaptive solution could be proposed, where CoMP is performed when NLoS occurs and no-CoMP otherwise, at the expense of a small extra feedback load. However, the CoMP scheme is demonstrated to provide a more homogeneous coverage and reliable communication than the no-CoMP scheme.

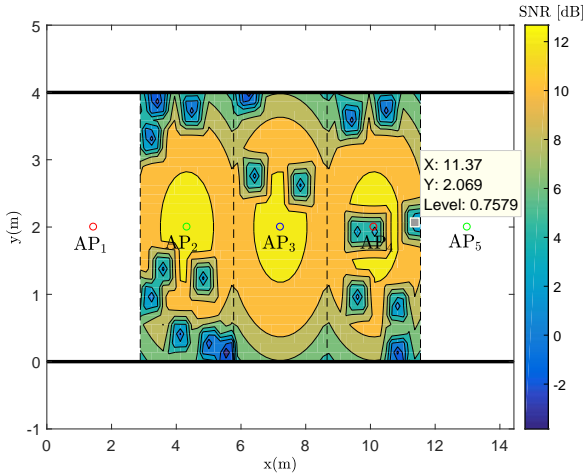


Figure 4.7: SNR without CoMP in a scenario where some users are obstructed.

4.4 Cooperative transmission technique in multi-carrier modulation

Apart from the well-known characteristics that multi-carrier modulation schemes such as OFDM presents, the combination of OFDM with JT CoMP is a good match as it enables the allocation of orthogonal resources among neighboring cells with different granularity levels, simplifying the implementation of different frequency-reuse schemes to combat the inter-cell interference [Pateromichelakis *et al.*, 2013]. Adapted versions of OFDM have been proposed to obtain O-OFDM waveforms that are suitable for VLC. Within O-OFDM, the modulation schemes that have received most attention lately are DCO-OFDM [Carruthers and Kahn, 1996], ACO-OFDM [Armstrong and Lowery, 2006] and layered ACO-OFDM (LACO-OFDM) [Wang *et al.*, 2015a]. Without loss of generality, in this Section we focus on the first one to provide the theoretical performance analysis and the corresponding simulation results of a static JT CoMP scheme that deals with possible LoS-link blockages and high inter-cell interference levels.

4.4.1 Preliminary study

The goal is to mitigate the effect of the LoS-link blockage in scenarios with a high density of obstacles. To cope with this, a cooperative scheme is proposed, where each user is always connected to the nearest AP and receives useful signal from other two neighboring APs. Figure 4.8 shows the frequency reuse among attocells, as well as the power distribution among I/Q signal

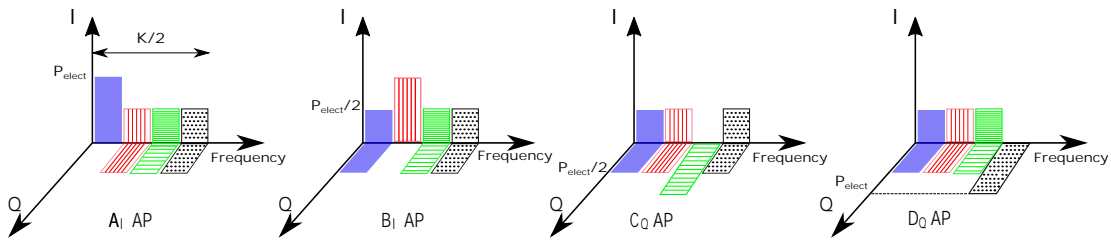


Figure 4.8: Frequency bands assignment to four types of AP (A_I , B_I , C_Q , and D_Q). Equal electrical power allocation is performed on all frequency bands.

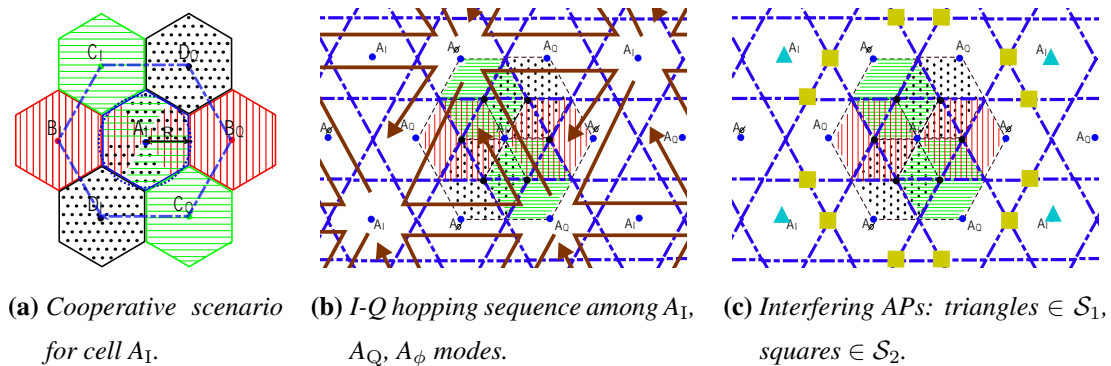


Figure 4.9: Illustration of the proposed cooperative optical wireless cellular scenario in which the central cell A_I is used as reference.

components. The first sub-band carries the information sent to the users located in the central target attocell (A_I). Note that there are 6 different sectors in the central cell of Figure 4.9a where cooperation takes place. Besides, it can be seen that only three different cells cooperate at the same time in any user position. For clarity purposes, the tessellation in Figure 4.9a shows the edges for the reference *anchor* attocell, whereas the (blue dashed) tessellation in Figure 4.9b and Figure 4.9c shows the cooperation edges of the corresponding attocells.

In order to reduce the inter-cell interference, the total electrical bandwidth is divided into four sub-bands as it can be seen in Figure 4.8 (reuse factor $\Delta=4$). Each *anchor* AP uses one sub-band to serve its associated users, whereas cooperation is carried out in the other three sub-bands, cooperating with 2 neighboring attocells per sub-band (one in I and other in Q). In brief, each AP sends information to the users that lie in their own cell coverage area and, in addition, to the users that lie in the cooperative area that overlaps with the six neighboring attocells. In the time domain, each AP alternates the transmission of information to its associated user following an I, Q, and idle mode (\emptyset) sequence, such that a cluster size of 12 is achieved (i.e., 4 frequency bands, 2 orthogonal I/Q signals, and 3/2 IQ-time hopping patterns). This transmission mode

will change in time according to the pattern represented in Figure 4.9b. Figure 4.9c shows the APs interfering to users located in the central target attocell. \mathcal{I}_1 contains the indexes of interfering APs that use the same transmission resources with the same main sub-band (i.e., all attocells named A_I , represented with blue triangles in Figure 4.9c), whereas \mathcal{I}_2 denotes the set of interfering APs that use the same transmission resources but with different main sub-band (i.e., attocells B_I , B_Q , B_ϕ , C_I , C_Q , C_ϕ , D_I , D_Q , and D_ϕ , represented with yellow squares in Figure 4.9c).

The SINR is an important metric to evaluate the performance of a cellular system. An expression for the SINR that is obtained with our proposed scheme on subcarrier k can be presented as

$$\begin{aligned} \Gamma[k] = & \frac{\eta_{pd}^2 \eta_{led}^2 \sigma_x^2 \rho^2 \xi^2 \left| H_0[k] + \frac{1}{\sqrt{2}}(H_1[k] + H_2[k]) \right|^2}{\eta_{pd}^2 \eta_{led}^2 \sigma_x^2 \left(\sigma_{clip}^2 \left| H_0[k] + \frac{1}{\sqrt{2}}(H_1[k] + H_2[k]) \right|^2 + \sum_{i \in \mathcal{I}_1} (\rho^2 + \sigma_{clip}^2) |H_i[k]|^2 + \sum_{i \in \mathcal{I}_2} \frac{1}{2} (\rho^2 + \sigma_{clip}^2) |H_i[k]|^2 \right) + \frac{1}{2} \sigma_{rx}^2} \\ & = \left(\left(\frac{\rho^2 \xi^2 \left| H_0[k] + \frac{1}{\sqrt{2}}(H_1[k] + H_2[k]) \right|^2}{(\rho^2 + \sigma_{clip}^2) \left(\sum_{i \in \mathcal{I}_1} |H_i[k]|^2 + \sum_{i \in \mathcal{I}_2} \frac{1}{2} |H_i[k]|^2 \right) + \frac{N_0 W}{2 \xi^2 \eta_{pd}^2 \eta_{led}^2 \sigma_x^2}} \right)^{-1} + \frac{\sigma_{clip}^2}{\rho^2 \xi^2} \right)^{-1}, \end{aligned} \quad (4.4)$$

where $H_i[k]$ is the frequency response of the VLC channel on the k -th subcarrier received from the i -th AP, and η_{pd} and η_{led} are the responsivity of the PD and the electrical-to-optical conversion efficiency of the LED, respectively. The term σ_x^2 denotes the electrical signal variance, and ρ is an attenuation factor related to the clipping effect that can be approximated as (2.19). Similarly, $\xi = \xi_{DCO} = \sqrt{K/(K-2)}$ is a normalizing factor that compensates the absence of energy on subcarriers 0 and $K/2$ when DCO-OFDM is used. The variance of the clipping noise σ_{clip}^2 and the variance produced at the receiver σ_{rx}^2 are calculated as explained in Section 2.3. Note that the receiver noise variance is divided by 2 because only one dimension, when real-valued symbols are used (either in I or Q component signals), should be considered.

Thus, considering the equations for $|H_i[k]|^2$ in (2.35) and σ_x^2 in (2.28), the SINR can be simplified as

$$\Gamma[k] = \left(\frac{(\rho^2 + \sigma_{clip}^2) \tilde{I} + Z[k]}{\rho^2 \tilde{D}} + \frac{\sigma_{clip}^2}{\rho^2 \xi^2} \right)^{-1}, \quad (4.5)$$

where

$$\tilde{I} = \sum_{i \in \mathcal{I}_1} (r_i^2 + d_v^2)^{-m-3} + \sum_{i \in \mathcal{I}_2} \frac{1}{2} (r_i^2 + d_v^2)^{-m-3}, \quad (4.6)$$

$$\tilde{D} = \xi^2 \left((r_0^2 + d_v^2)^{-\frac{m+3}{2}} + \frac{1}{\sqrt{2}} (r_1^2 + d_v^2)^{-\frac{m+3}{2}} + \frac{1}{\sqrt{2}} (r_2^2 + d_v^2)^{-\frac{m+3}{2}} \right)^2, \quad (4.7)$$

and

$$Z[k] = 2N_0(r)W \exp \left(\frac{kW}{KF_{\text{fe}}} \right) \cdot \left(\frac{\pi(\zeta + E\{V(x(t))\})}{\xi \eta_{\text{pd}} P_{\text{opt}}(m+1) A_{\text{pd}} d_v^{m+1}} \right)^2. \quad (4.8)$$

If P_{opt} is calculated by fixing a cell center illuminance as in (3.15), the equation (4.8) can be extended as

$$Z[k] = \frac{N_0(r)}{2} W \exp \left(\frac{kW}{KF_{\text{fe}}} \right) \cdot \left(\frac{K_{e/v}(\zeta + E\{V(x(t))\})}{\xi \eta_{\text{pd}} E_v A_{\text{pd}} d_v^{m+3}} \right)^2. \quad (4.9)$$

Note that G_f and G_c are unitary for simplification. In the previous equations, r_i is the horizontal distance between the user and the i -th AP. The combined effect of the shot noise (due to received signal and ambient light optical power) and thermal noise is considered in $N_0(r)$ as detailed in Section 2.3. $E\{V(x(t))\}$ denotes the expected value of the data-carrying signal after clipping [Dimitrov *et al.*, 2012], which is approximated to 0 assuming a linear dynamic range from 0 to $2I_{\text{dc}}$. As a consequence, $\lambda_t = -\lambda_b = \zeta$.

The probability that the downlink SINR is less than a threshold γ_{th} is computed as

$$\Pr\{\Gamma[k] < \gamma_{\text{th}}\} = \int_0^R f_r(r) \Pr\{\Gamma[k] < \gamma_{\text{th}} | r\} dr, \quad (4.10)$$

where $f_r(r) = \frac{2r}{R^2}$ when a uniform distribution of users is assumed within each cell and R is the circular cell radius. Since the inter-cell interference follows a periodic distribution (period of $\frac{\pi}{3}$ rad) due to the central symmetric deployment of the interfering APs, \tilde{I} can be estimated using the *flower* model as stated in [Chen *et al.*, 2016] and [Almeroth *et al.*, 2011]. Thus, the conditional probability is derived as

$$\Pr\{\Gamma[k] < \gamma_{\text{th}} | r\} = \Pr \left\{ \cos(6\theta) > \frac{2\rho^2 \tilde{D} \left(\frac{1}{\gamma_{\text{th}}} - \frac{\sigma_{\text{clip}}^2}{\rho^2 \xi^2} \right) - 2Z[k]}{(\rho^2 + \sigma_{\text{clip}}^2) |\tilde{I}_{\frac{\pi}{6}} - \tilde{I}_0|} - \frac{\tilde{I}_{\frac{\pi}{6}} + \tilde{I}_0}{|\tilde{I}_{\frac{\pi}{6}} - \tilde{I}_0|} \Big| r \right\}, \quad (4.11)$$

$\epsilon[n]$ [bits/symbol]	1	2	3	4	5	6	7	8
AMC _{QAM} : $\gamma_{\text{th}}[n]$ [dB]	-	9.8	13.4	16.5	19.6	22.5	25.5	28.4
AMC _{MAM} : $\gamma_{\text{th}}[n]$ [dB]	7.6	14.0	19.8	25.5	31.3	37.1	43.0	48.9

Table 4.2: Adaptive modulation and coding SINR regions in the uncoded QAM and the uncoded MAM for a $\text{BER} = 10^{-3}$.

where $\tilde{I}_{\frac{\pi}{6}}$ and \tilde{I}_0 are the interference of a user located at polar coordinates $re^{j\pi/6}$ and re^{j0} , respectively, which are computed using (4.6). By using AMC schemes, the mean cell data rate of the proposed scheme can be obtained as

$$\overline{R}_{\text{AMC}} = \frac{W}{\frac{3}{2}\Delta K} \sum_{k=1}^{\frac{K}{2}-1} \sum_{n=1}^N \epsilon[n] \left(\Pr\{\Gamma[k] < \gamma_{\text{th}}[n+1]\} - \Pr\{\Gamma[k] < \gamma_{\text{th}}[n]\} \right), \quad (4.12)$$

where the reuse factor $\Delta = 4$, and $\epsilon[n]$ is the spectral efficiency of the n -th AMC level that is obtained with a minimum required SINR for $\gamma_{\text{th}}[n]$. The factor 3/2 in the denominator comes from the IQ-time hopping pattern shown in Figure 4.9b.

4.4.1.1 Results of the preliminary study in multi-carrier modulation

In this Section, SINR and cell data rate performance evaluations are presented using [Chen *et al.*, 2016] as baseline scheme. Two AMC schemes [Xiong, 2006] are used to calculate the cell data rate, as illustrated in Table 4.2: uncoded QAM (AMC_{QAM}) and uncoded M-ary amplitude modulation (AMC_{MAM}). In all figures, the results obtained by the proposed multi-cell transmission scheme with frequency reuse factor 4 (MCFR4) and the baseline single-cell transmission schemes with frequency reuse factor 1 and 3 (SCFR1 and SCFR3, respectively) are represented.

The Lambertian emission order of the LED was selected to verify $m = \frac{\ln \sigma_P}{\ln \left(1 + \frac{R^2}{d_v^2} \right)} - 3$, such that the power decrease factor σ_P , that measures the relation between the received optical power at the cell center and cell edge, equals 12 dB. The vertical separation d_v was set to 2.25 m, the receiver field of view is 90°, and a bandwidth $W = 50$ MHz was chosen to minimize the effect of the low-pass filtering of the LED [Chen *et al.*, 2016]; this way, the equivalent electrical channel is identical for all frequency sub-bands. The number of subcarriers K is equal to

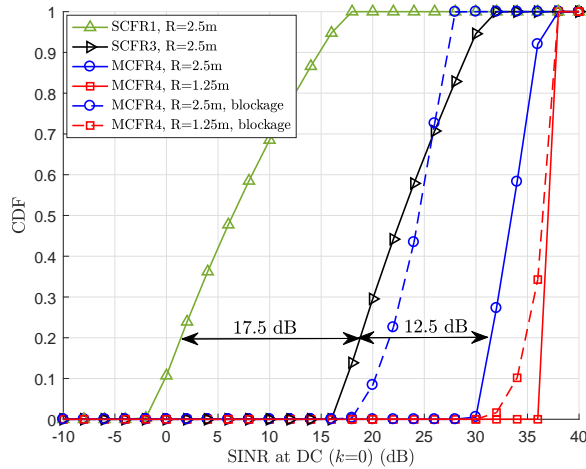


Figure 4.10: CDF of the SINR at DC for different transmission schemes, cell radii, and LoS blockage conditions.

512. Moreover, $\eta_{pd} = 0.4 \text{ A/W}$, $A_{pd} = 1 \text{ cm}^2$, $K_{e/v} = 100 \text{ lm/W}$, $\zeta = 5.05 \text{ dB}$, and $E_v = 500 \text{ lux}$. Relevant parameters to compute $N_0(r)$ [Chen *et al.*, 2016] are the illuminance from ambient light, the absolute temperature and the receiver load resistance, configured as 100 lux, 300 K and 500Ω , respectively.

For the sake of clarity, a blockage happens in presence of an obstacle that interrupts completely the direct link between the nearest AP and user; in this situation, only the optical power from the cooperating APs is received. If not specified, blockage probability equals 1, which means that all users experience blockage in the direct link towards their nearest APs.

Figure 4.10 depicts the CDF of the SINR at DC for the SCFR1, SCFR3 and MCFR4 schemes. The larger the reuse factor, the better the SINR performance, as the inter-cell interference power decreases. For example, for a CDF of SINR of 20 %, the SCFR3 and MCFR4 schemes get gains of 17.5 dB and 30 dB, respectively, with respect to the SCFR1 scheme. Note that, when there is a LoS-link blockage towards the serving (*anchor*) AP, the SINR of SCFR1 and SCFR3 vanishes and, due to that, they are not plotted. Differently, the proposed MCFR4 scheme can provide an acceptable SINR even when the LoS link is blocked. The smaller the size of the attocell, the lower the loss with respect to the LoS case is, because the power received from cooperating APs improves compared to the inter-cell interference.

Results of cell data rate are presented in Figure 4.11. Note that the AMC_{QAM} cannot be used in MCFR4 because useful information to each user is transmitted over only one signal component

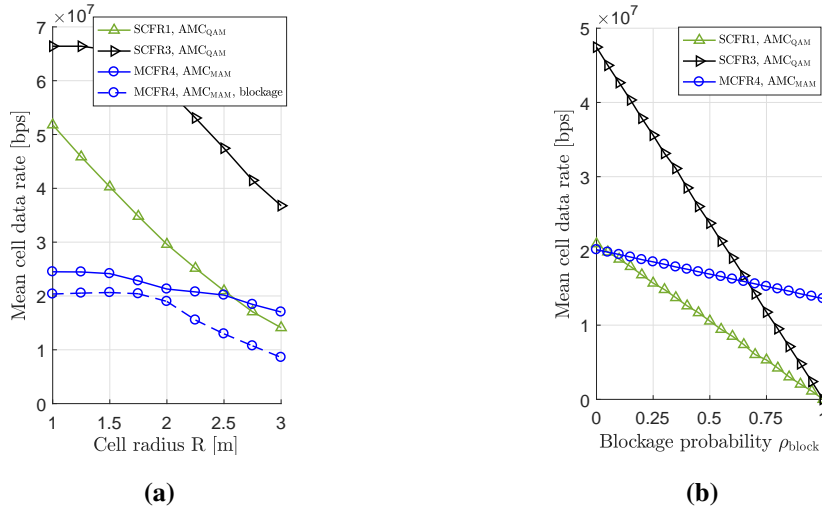


Figure 4.11: Mean cell data rate of different schemes. (a) Effect of the cell radius R . (b) Effect of the blockage probability ρ_{block} in the direct link ($R = 2.5\text{m}$)

(either I or Q). Thus, the AMC_{MAM} scheme is applied. As shown in Figure 4.10, the larger the circular cell radius R , the worse the SINR in reception and the lower the cell data rate in Figure 4.11a is. The SCFR3 scheme manages the interference correctly and achieves a better cell data rate when compared to SCFR1.

The proposed MCFR4 scheme gets lower cell data rate for using an M-ary amplitude modulation (MAM) AMC scheme instead of QAM AMC, besides the additional $3/2$ reuse factor for applying the I-Q rotation scheme shown in Figure 4.9b. However, it is important to highlight that MCFR4 is the only scheme that guarantees connectivity to all users even in presence of LoS link blockage. The performance loss of SCFR3 and MCFR4 with blockage for radii beyond 1.75 m is produced because the likelihood of selecting an AMC mode below the 8-th and 5-th, respectively, is not negligible anymore (see Figure 4.10 and Table 4.2). Figure 4.11b shows the robustness of the proposed MCFR4 scheme against the blockage probability. Let us assume that ρ_{block} is the probability of blockage towards the serving (*anchor*) AP; then, the cell data rate of MCFR4 is higher than the one obtained with SCFR1 (SCFR3) for values beyond $\rho_{block} = 0.05$ ($\rho_{block} = 0.65$). As expected, the variability of the mean cell data rate is lower for the MCFR4 scheme due to the macro-diversity that is exploited when cooperating in the attocell network.

4.4.1.2 Conclusions and possible alternatives

The loss due to the use of time division multiplexing (TDM) and MAM signals is notable. Thus new alternatives that offer a more efficient performance must be investigated. This drawback can be overcome by using RGB(Y) LED technologies, which enable more flexibility by using WDM. Thereinafter, using RGB(Y) LEDs and WDM, a detailed study of all possible resource allocation patterns to maintain an SINR homogeneity in the whole network area is carried out. The performance of different static resource allocation schemes compatible with JT CoMP are presented, without the need of knowing the location of the users in advance to overcome effectively the impact of both inter-cell interference and LoS-link blockage.

This work gives solution to the two key limiting factors in VLC networks, namely the effect of strong inter-cell interference and the impact of frequent LoS-link blockage. To achieve this goal, we state the conditions to be satisfied when allocating resources for cooperative multi-point transmission in a multi-cell network that gives the same spatial SINR distribution in every sector of the network. As a consequence, a homogeneous service is provided in the whole coverage area, and reliable cooperative transmission schemes that do not need to sense continuously the status of the optical wireless channel can be implemented. This way, quick harmful events that block the LoS link with an AP are tackled. On the other hand, a thorough study of all the possible resource-reuse patterns for cooperative transmission is carried out and the most convenient schemes depending on the working conditions of the VLC system are determined.

4.4.2 System model

Optical OFDM-based transmission schemes and RGB(Y) LEDs [Chun *et al.*, 2016] [Wang *et al.*, 2015c] are used in this Section to achieve higher data rates in multi-cell VLC systems. Though the terminology in different references may vary slightly, we start by defining the different concepts that will be used throughout this Section when discussing the system model, namely:

- **Cell:** Area around the VLC AP (LED), such that any user that falls inside it will be served by the AP. For practicality reasons, the cell area is approximated by a hexagon whose HEX radius is $\tilde{R} \approx 1.1R$, where R is the corresponding equal-area circular cell radius as represented in Figure 4.12a.
- **Sector:** Each of the *slices* in which a hexagonal cell can be divided. The index of the

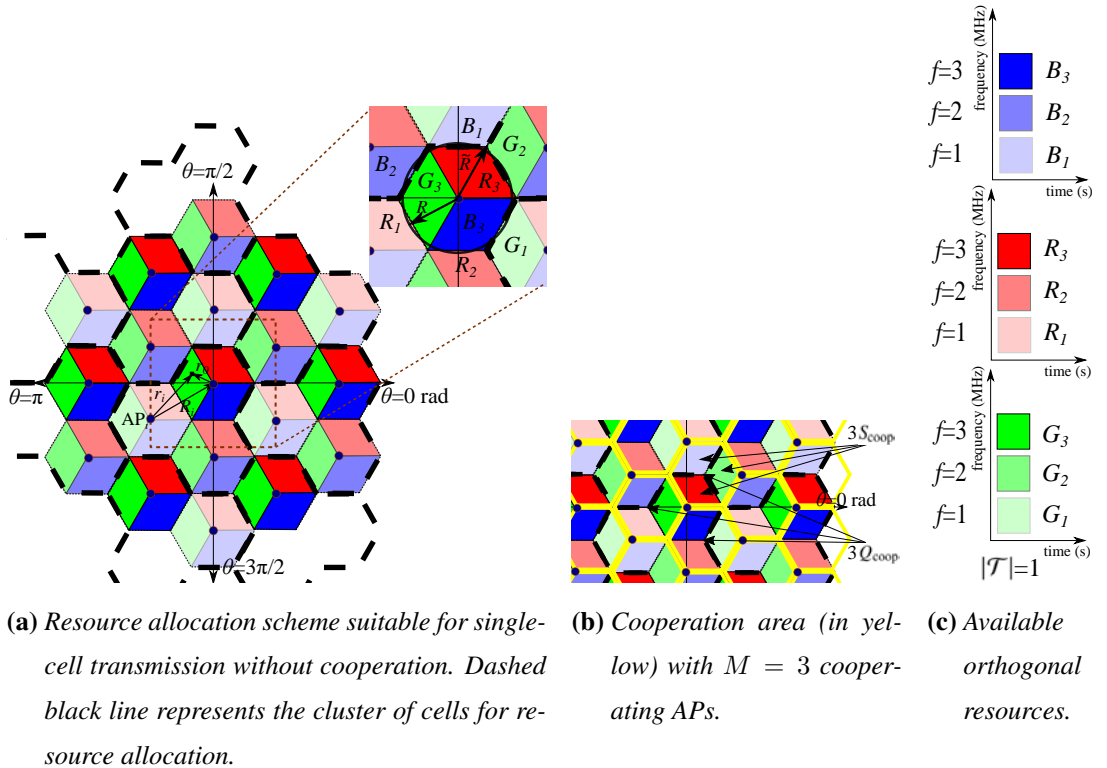


Figure 4.12: Two-tier multi-cell VLC network with $|\mathcal{C}|=3$, $|\mathcal{S}|=3$, and $|\mathcal{F}|=3$.

sectors is identified by $s \in \mathcal{S}$, and the number of sectors per cell is the set cardinality $|\mathcal{S}|$.

- Resource: Any of the orthogonal portions in which the time-frequency-color grid can be divided. Thus, the number of resources is given by

$$N_{\text{res}} = |\mathcal{T}| \cdot |\mathcal{F}| \cdot |\mathcal{C}|, \quad (4.13)$$

where $|\mathcal{T}|$ is the number of orthogonal time slots, $|\mathcal{F}|$ is the number of orthogonal frequency sub-bands of the electrical signal that modulates the intensity of each LED color chip, and $|\mathcal{C}|$ is the number of colors (LED chips) used to generate the white light. In the preliminary study presented in Section 4.4.1 and [Genovés Guzmán *et al.*, 2018a], a robust cooperative transmission scheme was proposed, which was based on a TDMA for serving users located in different sectors, at the expense of reducing the achievable system data rate. Therefore, $|\mathcal{T}| = 1$ is always used in this Section, simplifying (4.13) to $N_{\text{res}} = |\mathcal{F}| \cdot |\mathcal{C}|$. An example of available resources for a multi-cell VLC network is shown in Figure 4.12c, where $|\mathcal{C}| = 3$ (colors) and $|\mathcal{F}| = 3$ (sub-bands), making the number of available resources equal to $N_{\text{res}} = 9$. Users in neighboring cells may utilize the

same resources, and the level of inter-cell interference will depend on the reuse-distance between co-channel APs.

- Adjacent cell: Any of the cells that share a border with the reference cell.
- Cluster: Set of neighboring cells that use orthogonal communication resources and, together, they utilize all the resources available in the VLC system. The cluster size (Q_0) is the number of neighboring cells that compose a cluster defined as

$$Q_0 = \frac{N_{\text{res}}}{|\mathcal{S}|} = \frac{|\mathcal{C}| \cdot |\mathcal{F}|}{|\mathcal{S}|}. \quad (4.14)$$

As an example of all the previous definitions, Figure 4.12 represents a two-tier multi-cell network, where RGB LEDs are used ($|\mathcal{C}| = 3$), each cell is divided into three sectors ($|\mathcal{S}| = 3$), and the electrical bandwidth per color is divided into $|\mathcal{F}| = 3$ sub-bands (each of them illustrated in the figure by a different color brightness). Thus, the number of available resources is $N_{\text{res}} = 9$, and the cluster size without cooperation is $Q_0 = 3$, represented by the black dashed lines in Figure 4.12a.

Cooperation among different APs may be carried out in order to decrease the outage probability (due to blockage) and the inter-cell interference power. Thus, the tessellation is arranged in groups of cooperating cells, which are defined as:

- Cooperation set: Group of cells that cooperate to serve their users jointly within the cooperation area. In Figure 4.12b, cooperation areas are represented with solid yellow lines.

Regarding the cooperative transmission schemes, two new parameters illustrated in Figure 4.12b are now defined, namely:

- S_{coop} : Number of sectors within a cooperation area.
- Q_{coop} : Number of cooperation areas in which an AP cooperates.

Taking into account the cooperation strategy and the sectorization strategy, a final cluster Q will be defined, where all the possible resources combined with all the sectorization modes are contained. Further resource allocation examples suitable for multi-cell VLC systems will

Parameter	Description
$ \mathcal{C} $	Number of colors per LED
$ \mathcal{F} $	Number of sub-bands per color
$ \mathcal{S} $	Number of sectors per cell
N_{res}	Number of available resources
Q_0	Cluster size without cooperation
Q	Cluster size with cooperation
M	Number of APs that cooperate at every location
S_{coop}	Number of sectors within a cooperation area
Q_{coop}	Number of cooperation areas where an AP contributes
W	Bandwidth of the electrical modulation signal per color

Table 4.3: Terminology used to define the different resource allocation schemes for (cooperative) multi-cell transmission.

be presented in the following section. To simplify the interpretation of equations, Table 4.3 summarizes the symbol terminology that is utilized.

4.4.3 Analysis of the SINR homogeneity requirement for the resource allocation schemes

The spatial distribution of the SINR in a cellular network is of paramount importance when designing a wireless communication system. However, the estimation of the SINR that a user would experience at every single location is a hard task, particularly when the network topology is complex. From the whole cellular network point of view, a more practical design approach can be made when the SINR observed in a given area of the network can be representative for the whole network performance. Therefore, the aim of this Section is to study the performance of any of the possible resource configurations, suitable for a multi-cell VLC network, in which the SINR spatial distribution is the same in all sectors. When verifying this requirement, a balanced multi-cell network design is achieved and differences in SINR at every location are minimized. As a consequence, the study of the performance in a single sector can be generalized to all the coverage area of the network, without the necessity of keeping track of the indices that each cell-sector pair has. Not complying with the SINR homogeneity requirement does not mean that the system would not work, but rather that the system may not experience the same performance in all areas, as some sectors may have better SINR statistics than others

and, as a consequence, its optimization would be more complex.

In the following paragraphs, the homogeneity concept is investigated in:

- (a) **Stand-alone mode:** In this situation, transmission is made only from the nearest AP.

Thus, the SINR can be written as

$$\Gamma_{\text{sa}}(r_0, \theta) = \frac{D_0(r_0)}{\sum_{i \in \mathcal{I}} I_i(r_0, \theta) + \sigma_{\text{rx}}^2} = \frac{D(r_0)}{I(r_0, \theta) + \sigma_{\text{rx}}^2}, \quad (4.15)$$

where $D_0(r_0) = D(r_0)$ and $I(r_0, \theta)$ are the received signal power at the output of the PD in polar coordinates (r_0, θ) from the serving AP (desired) and the interfering APs, respectively. The interfering power coming from the individual AP i is denoted as $I_i(r_0, \theta)$, where i is the index that identifies the source of the interference from the set of interfering APs \mathcal{I} . Since the interference $I(r_0, \theta)$ depends on the azimuth angle θ , the homogeneity in the VLC multi-cell network will be attained only if $I(r_0, \theta)$ maintains the same spatial distribution at every sector.

- (b) **Cooperation mode:** Cooperation among neighboring APs is implemented and the SINR in this situation attains the form

$$\Gamma_{\text{coop}}(r_0, \theta) = \frac{\sum_{i \in \mathcal{D}} D_i(r_0, \theta)}{\sum_{i \in \mathcal{I}} I_i(r_0, \theta) + \sigma_{\text{rx}}^2} = \frac{D(r_0, \theta)}{I(r_0, \theta) + \sigma_{\text{rx}}^2}, \quad (4.16)$$

where \mathcal{D} is the set with the indices of cooperating APs from which a user receives its desired signal $D_i(r_0, \theta)$. Thus, besides the stand-alone mode conditions represented in the denominator of (4.15), new conditions must be established to guarantee homogeneity in the numerator $D(r_0, \theta)$ of (4.16).

4.4.3.1 Stand-alone mode (no cooperation among adjacent cells)

To guarantee an SINR homogeneity without cooperation, the following statements must be satisfied at different levels:

Lemma 1 : *Tessellation level.* Any cellular network can increase its aggregate data rate by re-using resources in the different cells. The parameter that in RF cellular systems is known as frequency reuse factor, it is now denoted as resource reuse factor, since a combination of color and frequency sub-band pairs are being arranged. Thus, the resource reuse factor is the rate at

which a certain resource is allocated throughout the cells of the network. For hexagonal cells, the cluster size determines the reuse distance as $R_d = \tilde{R}\sqrt{3Q_0}$. However, to have a tessellation with hexagonal cells that satisfies the reuse distance with six equidistant cells, the cluster size must be a rhombic number, verifying: $Q_0 \in \{i^2 + j^2 + ij\} \forall i, j \in \mathbb{N}$.

Proof: The analogy between an RF cellular network and the proposed VLC multi-cell system can be applied. After all, omnidirectional LEDs are similar to omnidirectional RF antennas, and resources in the multi-cell network are analogous to frequency bands in RF, which are also communication resources. Therefore, it is well-known that a tessellation with hexagonal cells is correctly designed if $Q_0 \in \{i^2 + j^2 + ij\} \forall i, j \in \mathbb{N}$, as demonstrated in [Rappaport, 2002]. ■

Lemma 2 : *Cell level.* This lemma defines the number of sectors in which a cell can be divided in order to verify the SINR homogeneity when studying only one sector. Assuming that Lemma 1 is satisfied, the interfering APs are equidistant in angles of $\pi/3$ and then, the interference follows a flower model with respect to θ that can be approximated as [Chen *et al.*, 2016] [Almeroth *et al.*, 2011]

$$I(r_0, \theta) \approx \frac{I_{\frac{\pi}{6}}(r_0) + I_0(r_0)}{2} + \frac{|I_{\frac{\pi}{6}}(r_0) - I_0(r_0)|}{2} \cos(6\theta), \quad (4.17)$$

where $I_{\frac{\pi}{6}}(r_0)$ and $I_0(r_0)$ are the interference power at polar coordinates r_0 and $\theta = \frac{\pi}{6}$ rad and $\theta = 0$ rad, respectively. The CDF SINR conditioned to r_0 can be obtained by a combination of (4.17) and (4.15) as

$$P[\Gamma_{\text{sa}} < \gamma_{\text{th}} | r_0] = P\left[\cos(6\theta) > \frac{2D(r_0)\frac{1}{\gamma_{\text{th}}} - (I_{\frac{\pi}{6}}(r_0) + I_0(r_0)) - 2\sigma_{\text{rx}}^2}{|I_{\frac{\pi}{6}}(r_0) - I_0(r_0)|} \middle| r_0\right] = P[\cos(6\theta) > \Lambda | r_0]. \quad (4.18)$$

The function $\cos(6\theta)$ has a period $p = \frac{\pi}{3}$ rad, as illustrated in Figure 4.13. Then, $P[\cos(6\theta) > \Lambda | r_0], \theta \in [0, 2\pi] = P[\cos(6\theta) > \Lambda | r_0], \theta \in \left[0, \frac{pk}{2}\right), \forall k \in \mathbb{N}$, being k the possible number of semi-periods in Figure 4.13. Since we want to divide a cell in sectors, $\frac{pk}{2} \cdot |\mathcal{S}| = \frac{\pi k}{6} \cdot |\mathcal{S}| = 2\pi$ must be satisfied, where $|\mathcal{S}| \in \mathbb{N}$ is the number of sectors in which a cell is divided, as defined in Section 4.4.2. Then, the different possibilities are: $k = 1 (|\mathcal{S}| = 12); k = 2 (|\mathcal{S}| = 6); k = 3 (|\mathcal{S}| = 4); k = 4 (|\mathcal{S}| = 3); k = 6 (|\mathcal{S}| = 2); k = 12 (|\mathcal{S}| = 1)$. As a conclusion, only the number of sectors $|\mathcal{S}| \in \{1, 2, 3, 4, 6, 12\}$ are possible to guarantee SINR homogeneity at the *cell level*.

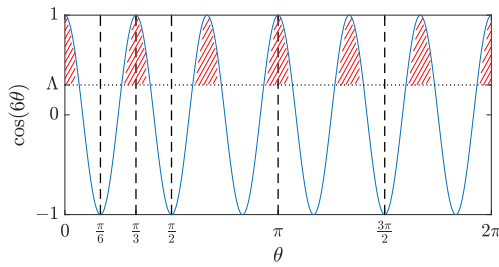


Figure 4.13: Illustration of the probability (red shaded area) that $\cos(6\theta)$ takes a value larger than Λ for different ranges of θ .

Proof: Lemma 2 determines that $P[\Gamma_{\text{sa}} < \gamma_{\text{th}} | r_0] = P[\cos(6\theta) > \Lambda | r_0] = P[\cos(\omega) > \Lambda | r_0]$ is the same for any sector. Let us define ω_{max} as the maximum value of ω , $k_{\text{high}} = \lceil \frac{\omega_{\text{max}}}{2\pi} \rceil$ and $k_{\text{low}} = \lfloor \frac{\omega_{\text{max}}}{2\pi} \rfloor$ represent the number of semi-loops in the intervals $[0, \pi)$ and $[\pi, 2\pi)$ that ω spins, respectively. Considering all the section modes, i.e.,

- $|\mathcal{S}| = 1 \Rightarrow \theta \in [0, 2\pi] \Rightarrow \omega \in [0, 12\pi] \Rightarrow k_{\text{high}} = 6, k_{\text{low}} = 6, f_{\omega}(\omega) = \frac{1}{12\pi},$
- $|\mathcal{S}| = 2 \Rightarrow \theta \in [0, \pi] \Rightarrow \omega \in [0, 6\pi] \Rightarrow k_{\text{high}} = 3, k_{\text{low}} = 3, f_{\omega}(\omega) = \frac{1}{6\pi},$
- $|\mathcal{S}| = 3 \Rightarrow \theta \in [0, \frac{2\pi}{3}] \Rightarrow \omega \in [0, 4\pi] \Rightarrow k_{\text{high}} = 2, k_{\text{low}} = 2, f_{\omega}(\omega) = \frac{1}{4\pi},$
- $|\mathcal{S}| = 4 \Rightarrow \theta \in [0, \frac{\pi}{2}] \Rightarrow \omega \in [0, 3\pi] \Rightarrow k_{\text{high}} = 2, k_{\text{low}} = 1, f_{\omega}(\omega) = \frac{1}{3\pi},$
- $|\mathcal{S}| = 6 \Rightarrow \theta \in [0, \frac{\pi}{3}] \Rightarrow \omega \in [0, 2\pi] \Rightarrow k_{\text{high}} = 1, k_{\text{low}} = 1, f_{\omega}(\omega) = \frac{1}{2\pi},$
- $|\mathcal{S}| = 12 \Rightarrow \theta \in [0, \frac{\pi}{6}] \Rightarrow \omega \in [0, \pi] \Rightarrow k_{\text{high}} = 1, k_{\text{low}} = 0, f_{\omega}(\omega) = \frac{1}{\pi},$

where $f_{\omega}(\omega)$ is the probability density function of ω for each case. Thus, $P[\Gamma_{\text{sa}} < \gamma_{\text{th}} | r_0] = P[\cos(\omega) > \Lambda | r_0] = \sum_{k=1}^{k_{\text{high}}} \int_{2\pi(k-1)}^{2\pi(k-1)+\arccos(\Lambda)} f_{\omega}(\omega) d\omega + \sum_{k=1}^{k_{\text{low}}} \int_{2\pi k - \arccos(\Lambda)}^{2\pi k} f_{\omega}(\omega) d\omega = \frac{\arccos(\Lambda)}{\pi}, \quad \forall (k_{\text{high}}, k_{\text{low}}).$ ■

Lemma 3 : Sector level. This lemma shows the way in which the number of sectors per cell identified in *Lemma 2* must be oriented within a cell.

- If $|\mathcal{S}| \in \{1, 2, 3, 6\}$: The orientation of the sectorization that is applied in each cell does not matter and, thus, the study of a sector can always be generalized to the whole cell and tessellation.
- If $|\mathcal{S}| \in \{4, 12\}$: The sector must be delimited by the following angles:

- For $|\mathcal{S}| = 4$: $b\pi/6 \leq \theta_{\text{sector}} \leq (b+3)\pi/6$, $0 \leq b \leq 9$,
- For $|\mathcal{S}| = 12$: $b\pi/6 \leq \theta_{\text{sector}} \leq (b+1)\pi/6$, $0 \leq b \leq 11$,

where b determines the starting angular point of the sectorization, while the rest of the sectors must be delimited by consecutive angles. Note that the angle directions considered in this Section are the ones illustrated in Figure 4.12a.

Proof: Because of the periodicity of the function $\cos(6\theta)$, the calculation of $P[\cos(\omega) > \Lambda]$ in a sector does not depend on the sector position if the number of semi-loops $[0, \pi)$ and $[\pi, 2\pi)$ are integer verifying $k_{\text{high}} = k_{\text{low}} = \frac{\omega_{\max}}{2\pi} \in \mathbb{N}$. In our case:

- $\frac{\omega_{\max}}{2\pi} \in \mathbb{N} \iff |\mathcal{S}| \in \{1, 2, 3, 6\}$.
- $\frac{\omega_{\max}}{2\pi} \notin \mathbb{N} \iff |\mathcal{S}| \in \{4, 12\}$. Here, the number of semi-loops $[0, \pi)$ and $[\pi, 2\pi)$ that ω takes are not the same and sectors must be limited by the following angles:
 - For $|\mathcal{S}| = 4$: $bp/2 \leq \theta_{\text{sector}} \leq (b+3)p/2$, $0 \leq b \leq 9$, where $p = \frac{\pi}{3}$ is the period of the $\cos(6\theta)$ function.
 - For $|\mathcal{S}| = 12$: $bp/2 \leq \theta_{\text{sector}} \leq (b+1)p/2$, $0 \leq b \leq 11$, where $p = \frac{\pi}{3}$ is the period of the $\cos(6\theta)$ function.

As observed in Figure 4.13, when $|\mathcal{S}| = 4, 12$, $P[\cos(6\theta) > \Lambda]$ is not equal if the two previous items are not satisfied since the area within the section would change.

■

4.4.3.2 Cooperation mode (with cooperation among adjacent cells)

When cooperation among APs happens, SINR homogeneity can be lost although the homogeneity with no cooperation (stand-alone mode) is verified. Thus, additional statements to the ones presented in Section 4.4.3.1 (*Lemma 1-3*) must be identified to maintain the SINR homogeneity in case of multi-point cooperation in transmission.

Lemma 4 : *Resource distribution level.* Concerning the maximum number of available resources, a cooperation transmission scheme can be carried out only if the condition $N_{\text{res}} =$

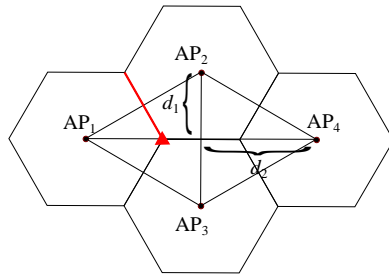
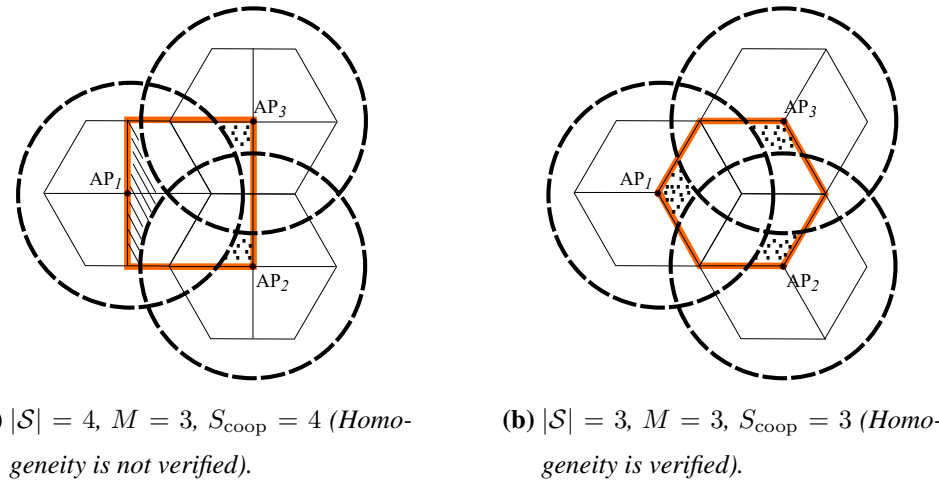


Figure 4.14: A cooperative set with four APs cannot provide a homogeneous distribution of the SINR with cooperation, as no point is equidistant to all the APs. Red line: equidistant points between two APs (AP₁ and AP₂). Red triangle: equidistant point between three APs (AP₁, AP₂ and AP₃).



(a) $|\mathcal{S}| = 4$, $M = 3$, $S_{\text{coop}} = 4$ (Homogeneity is not verified). (b) $|\mathcal{S}| = 3$, $M = 3$, $S_{\text{coop}} = 3$ (Homogeneity is verified).

Figure 4.15: Demonstration of the fact that M must be equal to S_{coop} .

$|\mathcal{C}| \cdot |\mathcal{F}| \geq S_{\text{coop}} \cdot Q_{\text{coop}}$ is satisfied, where S_{coop} is the number of sectors in the cooperation area and Q_{coop} is the number of cooperation areas where an AP cooperates.

Proof: If $N_{\text{res}} \leq S_{\text{coop}} \cdot Q_{\text{coop}}$, then an AP would have to transmit information to more sectors than the number of available orthogonal resources. By definition, this is not possible since the information transmitted by the same AP to users located in different sectors must use orthogonal resources. ■

Lemma 5 : *Cooperation set level.* When cooperation is performed, the sectors where the APs cooperate (S_{coop}) must be a multiple of the number of cooperating APs (M). Besides, as the deployment of APs is done to establish a hexagonal tessellation of cells, the number of cooperating APs cannot be larger than 3 to prevent imbalances in the received signal power

$ \mathcal{S} $	$M = S_{\text{coop}}$	Q_{coop}	$N_{\text{res,min}} = S_{\text{coop}} \cdot Q_{\text{coop}}$
1	1	1($= \mathcal{S} $)	1
1	2	1	2
1	3	1	3
2	1	2($= \mathcal{S} $)	2
2	2	2	4
2	3	2	6
3	1	3($= \mathcal{S} $)	3
3	2	3	6
3	3	3	9
4	1	4($= \mathcal{S} $)	4
4	2	4	8
6	1	6($= \mathcal{S} $)	6
6	2	6	12
6	3	6	18
12	1	12($= \mathcal{S} $)	12
12	2	12	24
12	3	12	36

Table 4.4: Minimum number of resources needed for each cooperation setup.

(i.e., numerator of the SINR). This statement can be formulated as $1 \leq \mu \cdot M = S_{\text{coop}} \leq 3$, where $\mu \in \mathbb{N}$ represents the number of sectors per AP of the cooperation set.

Proof: In order to get the same CDF of SINR in each sector when cooperation is applied, the center of the cooperative set must be equidistant to each of the cooperating APs. Within the region formed by the combination of four APs, there is no point equidistant among them as shown in Figure 4.14. In contrast, the red line and triangle represent the equidistant points between two or among three APs, respectively. Therefore, it is not possible to create a cooperation set of size $M > 3$ that maintains a homogeneous SINR among sectors. Besides, $\mu \cdot M = S_{\text{coop}}$ with $\mu \in \mathbb{N}$ is a necessary condition to guarantee homogeneity because the union of coverage areas of the cooperating APs must be equal at each sector in which they cooperate. In Figure 4.15a, an example where $|\mathcal{S}| = 4$, $M = 3$ and $S_{\text{coop}} = 4$ is shown, thus $\mu \cdot M \neq S_{\text{coop}}$ with $\mu \in \mathbb{N}$. Note that the coverage areas represented by dashed circles of the three APs are not equal at each sector where they cooperate (i.e., the areas represented by parallel lines and by points are not equal). In contrast, Figure 4.15b illustrates the case where $M = S_{\text{coop}} = 3$, and shows that

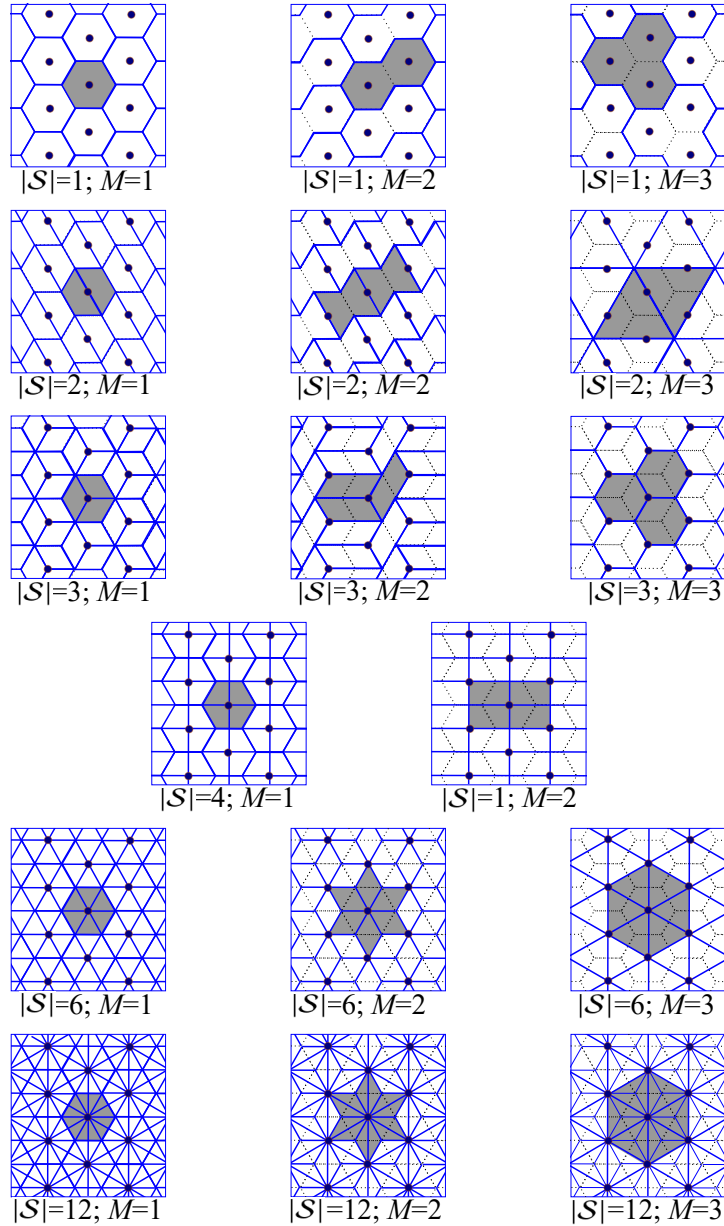


Figure 4.16: Illustration of the cooperation sets that can be established for all possible number of sectors per cell.

the SINR homogeneity at each sector is verified. Without loss of generality, $\mu = 1$ has been considered and then $M = S_{\text{coop}}$. ■

According to Lemma 4 and Lemma 5, Table 4.4 contains the possible cooperation setups and the minimum number of resources needed for each of them. These possible cooperation setups are depicted in Figure 4.16. For clarification purposes, Table 4.4 and Figure 4.16 also include

$ \mathcal{F} $	Freq. bands (per color)	1	2	3	4	5	6	7	8	9
N ($ \mathcal{F} \cdot \mathcal{C} $)	Orthogonal resources	3	6	9	12	15	18	21	24	27
Number of sectors	$ \mathcal{S} = 1$	$3_{(M=1,2,3)}$	6	$9_{(M=1,2,3)}$	$12_{(M=1,2,3)}$	15	18	$21_{(M=1,2,3)}$	24	$27_{(M=1,2,3)}$
	$ \mathcal{S} = 2$	1.5	$3_{(M=1,2,3)}$	4.5	6	7.5	$9_{(M=1,2,3)}$	10.5	$12_{(M=1,2,3)}$	13.5
	$ \mathcal{S} = 3$	$1_{(M=1)}$	2	$3_{(M=1,3)}$	$4_{(M=1,2,3)}$	5	6	$7_{(M=1,3)}$	8	$9_{(M=1,3)}$
	$ \mathcal{S} = 4$	0.75	1.5	2.25	$3_{(M=1,2)}$	3.75	4.5	5.25	6	6.75
	$ \mathcal{S} = 6$	0.5	$1_{(M=1)}$	1.5	2	2.5	$3_{(M=1,2,3)}$	3.5	$4_{(M=1,2,3)}$	4.5
	$ \mathcal{S} = 12$	0.25	0.5	0.75	$1_{(M=1)}$	1.25	1.5	1.75	2	2.25

Table 4.5: Cluster sizes (numbers with no brackets) and possible cooperation setups (numbers between brackets) for a RGB LED ($|\mathcal{C}| = 3$). Gray-shaded cells indicate the configurations that verify the previously listed requirements for homogeneity.

$ \mathcal{F} $	Freq. bands (per color)	1	2	3	4	5	6	7	8	9
N ($ \mathcal{F} \cdot \mathcal{C} $)	Orthogonal resources	4	8	12	16	20	24	28	32	36
Number of sectors	$ \mathcal{S} = 1$	$4_{(M=1,2,3)}$	8	$12_{(M=1,2,3)}$	$16_{(M=1,2,3)}$	20	24	$28_{(M=1,2,3)}$	32	$36_{(M=1,2,3)}$
	$ \mathcal{S} = 2$	2	$4_{(M=1,2)} //$	6	8	10	$12_{(M=1,2,3)}$	14	$16_{(M=1,2)} //$	18
	$ \mathcal{S} = 3$	1.33	2.67	$4_{(M=1,2,3)}$	5.33	6.67	8	9.33	10.67	$12_{(M=1,2,3)}$
	$ \mathcal{S} = 4$	$1_{(M=1)}$	2	3	$4_{(M=1,2)}$	5	6	$7_{(M=1,2)}$	8	$9_{(M=1,2)}$
	$ \mathcal{S} = 6$	0.67	1.33	2	2.67	2.33	$4_{(M=1,2,3)}$	4.67	5.33	6
	$ \mathcal{S} = 12$	0.33	0.67	$1_{(M=1)}$	1.33	1.67	2	2.33	2.67	$3_{(M=1,2,3)}$

Table 4.6: Cluster sizes (numbers with no brackets) and possible cooperation setups (numbers between brackets) for a RGBY LED ($|\mathcal{C}| = 4$). Gray-shaded cells indicate the configurations that verify the previously listed requirements for homogeneity.

the configurations when no cooperation is performed ($M = 1$), in which case Q_{coop} represents the number of sectors ($|\mathcal{S}|$) to which AP transmits. Note that the setup $\{|\mathcal{S}| = 4, M = 3\}$ is not included in Table 4.4 and Figure 4.16 because $S_{\text{coop}} = 4 \neq 3 = M$ as shown in Lemma 5 and Figure 4.15.

Lemma 6 : *Tessellation level.* When cooperation occurs, the final formed cluster (Q) is equal to the initial one without cooperation (Q_0), except for the cooperation setups where there are more than one sectorization mode, which are the configurations $\{|\mathcal{S}| = 2, M = 3\}$ and $\{|\mathcal{S}| = 3, M = 2\}$. In mathematical form, $Q = Q_0 \forall \{|\mathcal{S}|, M\} \setminus \{|\mathcal{S}| = 2, M = 3\} \cup \{|\mathcal{S}| = 3, M = 2\}$. When $\{|\mathcal{S}| = 2, M = 3\}$ or $\{|\mathcal{S}| = 3, M = 2\}$, then $Q = \text{LCM}(Q_0, M)$, where LCM is

the least common multiple of two numbers and M is the number of cooperating APs that also coincides with the number of sectorization modes in these cases.

Proof: The possible cooperation sets represented in Table 4.4 are visualized in Figure 4.16. The shaded regions are the areas where the central AP serves users and cooperates with the neighboring APs when $M > 1$. Note that the sectorization for every cell when no cooperation occurs ($M = 1$) is the same as the sectorization for every cell in case of cooperation ($M > 1$), except for the cases $\{|\mathcal{S}| = 2, M = 3\}$ and $\{|\mathcal{S}| = 3, M = 2\}$. In these latter cases, cells must be sectorized in three and two different sectorization orientations, respectively, increasing the reuse factor as $Q = \text{LCM}(Q_0, 3)$ and $Q = \text{LCM}(Q_0, 2)$ for $\{|\mathcal{S}| = 2, M = 3\}$ and $\{|\mathcal{S}| = 3, M = 2\}$, respectively. ■

For the sake of clarification, the shaded cells in Table 4.5 and Table 4.6 represent the configurations in terms of type of LED (RGB or RGBY), number of frequency sub-bands per color ($|\mathcal{F}|$), and number of sectors per cell ($|\mathcal{S}|$) that comply with *Lemmas 1-6* and, as a consequence, guarantee an SINR homogeneity in the whole tessellation. Numbers without brackets indicate the cluster size Q , whereas numbers between brackets show the number of possible cooperating APs (M). In the remainder of this study, only these shaded configurations will be studied.

4.4.4 Achievable data rate of the VLC system

The block diagram of the VLC system is presented in Figure 4.17. Though the system model is valid for most O-OFDM schemes reported in the literature [Wang *et al.*, 2018], this study focuses on DCO-OFDM for the sake of brevity. At the transmitter side, the stream of input bits is distributed among the three/four independent transmission chains that correspond to each of the colors of the LED technology (i.e., RGB or RGBY). Let c be the color index that is used, such that $c \in \mathcal{C} = \{R, G, B\}$ or $c \in \mathcal{C} = \{R, G, B, Y\}$ for a RGB or RGBY LED, respectively. Once the bits for each color are mapped into QAM symbols, a preprocessing is carried out in transmission to generate blocks of symbols of size K that verify the Hermitian symmetry property needed to obtain a real-valued signal at the output of the IFFT block. Thus, the information symbols transported on the second half of the subcarriers are Hermitian symmetric with respect to the information symbols transported on the first half. Besides, the subcarriers with indices 0 and $K/2$ are zero-valued in DCO-OFDM. Thus, the FD signal for each color attains the form

$$\mathbf{X}_{H,c} = \left[0 \ \{X_c[k]\}_{k=1}^{K/2-1} \ 0 \ \{X_c[K/2-k]^*\}_{k=1}^{K/2-1} \right], \quad c \in \mathcal{C}, \quad (4.19)$$

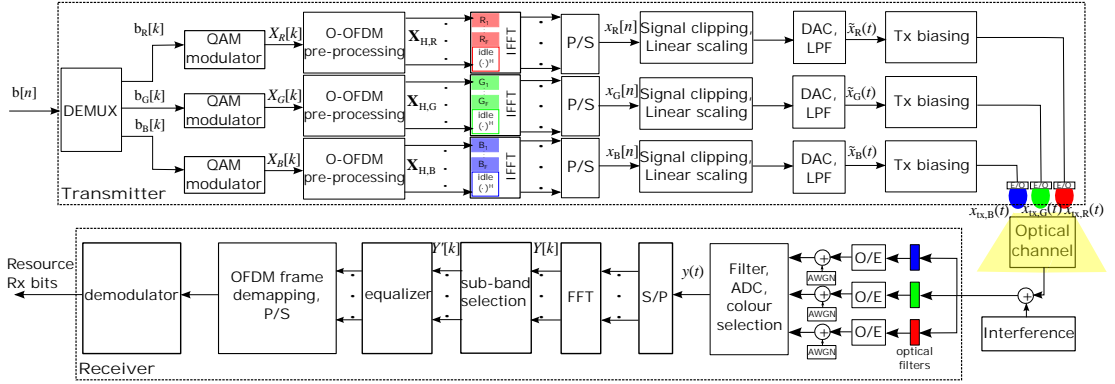


Figure 4.17: Block diagram of a VLC transmission using O-OFDM modulation with a RGB LED. Note that, when a RGBY LED is used, an additional stream for the yellow color LED must be included.

where $X_c[k]$ is the symbol transmitted on the k -th subcarrier by the color chip c . The real signals after the IFFTs are denoted as $x_R[n]$, $x_G[n]$ and $x_B[n]$. Note that $|\mathcal{F}|$ frequency subbands can be defined for each color with the aim of increasing the degrees of freedom when performing the allocation of resources in the optical wireless network. The time-domain signals must be amplified, DC-shifted and upper/lower clipped according to the electrical dynamic range of the LED. It is very important to select the proper amplification factor and DC-bias level for the electrical signal that feeds the different LED chips, in order to make the clipping noise negligible with respect to the optical interference and ambient light noise of the indoor environments. The transmitted signals for each color c can be formulated from (2.24) as

$$x_{tx,c}(t) = \eta_{led,c} (\tilde{x}_c(t) + I_{DC,c}), \quad c \in \mathcal{C}, \quad (4.20)$$

where

$$\tilde{x}_c(t) = \sigma_{x,c} \cdot V [x_c(t)], \quad (4.21)$$

where $\sigma_{x,c}$ is the amplifying factor (i.e. the standard deviation of the Gaussian-like electrical OFDM signal) that corresponds to color c , and

$$V [x_c(t)] = \begin{cases} \lambda_t & : x_c(t) > \lambda_t \\ x_c(t) & : \lambda_t \geq x_c(t) \geq \lambda_b \\ \lambda_b & : x_c(t) < \lambda_b \end{cases}, \quad (4.22)$$

where λ_b and λ_t are the bottom and top clipping levels, respectively. The electrical to optical conversion efficiency for the corresponding LED chip with color c is denoted by $\eta_{\text{led},c}$. Before transmission, the signals are biased by a DC component $I_{\text{DC},c}$ in order to comply with the target white chromaticity and illumination level requirements.

At the receiver side, a white light is received and filtered through three (or four) optical filters to recover the streams of bits that are independently transmitted over the different colors. Then, each user demodulates the sub-band of the electrical signal that is transported on the optical color that corresponds to the sector in which it is located. The wideband signal (i.e., electrical current at the PD output before frequency demultiplexing) that is received on the color of the target sector can be written as

$$y(t) = \eta_{\text{pd}} \eta_{\text{led},c} \left(\sum_{i \in \mathcal{D}} (\tilde{x}_{i,c}(t) + I_{\text{DC},c}) \otimes h_i(t) + \sum_{i \in \mathcal{I}} (\tilde{x}_{i,c}(t) + I_{\text{DC},c}) \otimes h_i(t) \right) + n_{\text{rx},c}(t), \quad c \in \mathcal{C}, \quad (4.23)$$

where \mathcal{D} and \mathcal{I} are the set of cooperating (desired) and interfering APs, respectively. The channel impulse response from the i -th AP to the user under study is denoted by $h_i(t)$. Furthermore, $n_{\text{rx},c}(t)$ is the zero-mean AWGN with variance

$$\sigma_{\text{rx},c}^2 = \frac{N_{0,c}W}{|\mathcal{F}| \xi^2}, \quad c \in \mathcal{C}, \quad (4.24)$$

where $N_{0,c}$ is the noise power spectral density for color c . Note that noise power is divided by a factor of $|\mathcal{F}|$ since the received signal in a sector is conveyed in only one sub-band. The noise power spectral density for color c contains shot and thermal noise terms, and is defined as

$$N_{0,c} = N_{0,s,c} + N_{0,\text{th}} = 2q\eta_{\text{pd}} \left(\sum_i P_{\text{opt},c} H_i + E_{\text{r,ab}} A_{\text{pd}} \right) + \frac{4\kappa_B T_{\text{abs}}}{R_L}, \quad c \in \mathcal{C}, \quad (4.25)$$

where all the parameters are already defined.

The FD received signal on subcarrier k can be represented as

$$Y[k] = \eta_{\text{pd}} \eta_{\text{led},c} \left(\sum_{i \in \mathcal{C}} \tilde{X}_{i,c}[k] H_i + \sum_{i \in \mathcal{S}} \tilde{X}_{i,c}[k] H_i \right) + N_{\text{rx},c}[k], \quad c \in \mathcal{C} \quad (4.26)$$

where $\tilde{X}_{i,c}[k]$ is the QAM symbol transported on the k -th subcarrier of color c from AP with index i (after the TD clipping and amplification), and $N_{\text{rx},c}[k]$ is the equivalent FD noise in reception. If the modulation bandwidth is relatively low, the filtering of the front-end devices can be assumed negligible and then, a flat FD channel transfer function from the i -th AP can be

assumed, with a gain given by (2.35) and (2.38) as

$$H_i = \frac{A_{\text{pd}}(m+1)d_v^{m+1}}{2\pi (r_i^2 + d_v^2)^{\frac{m+3}{2}}} 1(\psi_i), \quad (4.27)$$

where d_v is the vertical separation between the AP and the PD, and

$$m = \frac{-1}{\log_2 (\cos(\phi_{1/2}))} \quad (4.28)$$

is the Lambertian emission order [Komine and Nakagawa, 2004] that depends on the half-power semi-angle of the LED $\phi_{1/2}$. Note that G_f and G_c are unitary for simplification. The horizontal distance with the i -th AP is denoted by r_i (see Figure 4.12a). The polar coordinates of a user location with respect to the central AP are (r_0, θ) , where

$$r_i(r_0, \theta) = \sqrt{r_0^2 + R_i^2 - 2R_i r_0 \cos(\theta - \Theta_i)} \quad (4.29)$$

is the distance between the user located at (r_0, θ) and AP with index i . In (4.29), (R_i, Θ_i) represents the location of AP i in polar coordinates (see Figure 4.12a for further details). Throughout this study, we assume that the light beam of the AP is perfectly vertical, irradiating all its optical power directly to the floor. Similarly, it is considered that the axis of the PD reception cone is also vertical, pointing perfectly upwards towards the ceiling of the room.

Based on (4.20), the optical transmit power for each color is

$$P_{\text{opt},c} = \mathbb{E}\{x_{\text{tx},c}(t)\} = \eta_{\text{led},c} (\mathbb{E}\{\tilde{x}_c(t)\} + I_{\text{DC},c}), \quad c \in \mathcal{C}, \quad (4.30)$$

where $\mathbb{E}\{\cdot\}$ represents the statistical expectation. Assuming $\mathbb{E}\{\tilde{x}_c(t)\} \approx 0$ and defining $\zeta_c = \frac{I_{\text{DC},c}}{\sigma_{x,c}}$ as the ratio of DC-bias level to the standard deviation of the transmitted electrical signal [Genovés Guzmán *et al.*, 2018b], the electrical transmit signal power for each color c can be written as

$$\sigma_{x,c}^2 = \frac{P_{\text{opt},c}^2}{\eta_{\text{led},c}^2 \zeta_c^2}, \quad c \in \mathcal{C}. \quad (4.31)$$

Let us consider that the optical transmission power of an LED is divided equally among the different colors that are used to generate the white light, (i.e., $P_{\text{opt},c} = \frac{P_{\text{opt}}}{|\mathcal{C}|}$). Then, the

electrical transmit signal power for each color becomes

$$\sigma_{x,c}^2 = \sigma_x^2 = \left(\frac{P_{\text{opt}}}{|\mathcal{C}| \eta_{\text{led}} \zeta} \right)^2, \quad c \in \mathcal{C}. \quad (4.32)$$

The SINR, an essential metric to evaluate the link performance in communication systems, can be written as

$$\Gamma_c = \frac{\frac{1}{\nu} \eta_{\text{pd}}^2 \eta_{\text{led}}^2 \sigma_x^2 \xi^2 |\sum_{i \in \mathcal{D}} H_i|^2}{\frac{1}{\nu} \eta_{\text{pd}}^2 \eta_{\text{led}}^2 \sigma_x^2 \xi^2 \sum_{i \in \mathcal{I}} |H_i|^2 + \sigma_{\text{rx}}^2}, \quad c \in \mathcal{C}, \quad (4.33)$$

where ν is the number of frequency sub-bands in color c that are active in each AP. Without loss of generality, the noise power is also assumed identical for all optical colors. Then, combining (4.27) and (4.32) into (4.33), and supposing that the FOV of the PD is 90° (i.e., worst case for optical interference, as all users receive optical signal from all APs), the SINR can be written as

$$\Gamma(r_0, \theta) = \frac{\left| \sum_{i \in \mathcal{D}} (r_i^2(r_0, \theta) + d_{\text{v}}^2)^{-\frac{m-3}{2}} \right|^2}{\sum_{i \in \mathcal{I}} (r_i^2(r_0, \theta) + d_{\text{v}}^2)^{-m-3} + Z}, \quad (4.34)$$

where

$$Z = \frac{N_0 W \nu}{|\mathcal{F}|} \cdot \left(\frac{|\mathcal{C}| \zeta 2\pi}{\xi^2 \eta_{\text{pd}} P_{\text{opt}} A_{\text{pd}} (m+1) d_{\text{v}}^{m+1}} \right)^2. \quad (4.35)$$

The CDF of the SINR in (4.34) evaluated in terms of γ_{th} can be expressed as

$$F_{\Gamma}(\gamma_{\text{th}}) = \Pr \{ \Gamma(r_0, \theta) < \gamma_{\text{th}} \} = \int_{r_0} \int_{\theta} f_{r_0}(r_0) f_{\theta}(\theta) \Pr \{ \Gamma(r_0, \theta) < \gamma_{\text{th}} | r_0, \theta \} dr_0 d\theta. \quad (4.36)$$

In order to estimate the achievable data rate of the VLC system, we use the well-known Shannon spectral efficiency formula to obtain

$$\text{SE}_{\text{Shannon}}(r_0, \theta) = \log_2 (1 + \Gamma(r_0, \theta)). \quad (4.37)$$

Then, assuming the employment of perfect capacity-achieving coding, the mean data rate that

the VLC system can achieve when the number of subcarriers is large enough can be written as

$$\overline{R}_{\text{RGB(Y)}} \approx \frac{|\mathcal{S}| \cdot W}{2 \cdot |\mathcal{F}|} \cdot E \{ \log_2 (1 + \Gamma(r_0, \theta)) \}. \quad (4.38)$$

4.4.5 Verification of the illumination requirements

Special attention is needed to meet the illumination regulation that, in practice, implies the verification of two optical metrics [EN 12464-1:2002 E, 2002]. Firstly, the average illuminance E_{avg} in the whole indoor area must be higher than a threshold value. Secondly, the illuminance uniformity U_{light} , defined as the ratio between the minimum illuminance level to the average illuminance in the area, must be high enough such that people would not observe notably different lighting levels in the same room. The illuminance at polar coordinates (r_0, θ) can be written as

$$E_v(r_0, \theta) = \Phi \cdot \frac{\sum_{\forall i} |H_i(r_0, \theta)|}{A_{\text{pd}}}, \quad (4.39)$$

where Φ is the output luminous flux of every AP computed as

$$\Phi = K_{e/v} \cdot P_{\text{opt}}, \quad (4.40)$$

where $K_{e/v}$ is the luminous efficacy of the white light that the LED generates and is measured in lm/W.

A three-tier multi-cell scenario is considered in this study and the values of the different configuration parameters are shown in Table 4.7. For a fair comparison between schemes with different cell radius R , the optical transmit power per unit area P_{optArea} is fixed to 2 W/m^2 , a value that is consistent with the optical transmit power selected in references like [Chen *et al.*, 2015]. Thus, the optical transmit power per AP, denoted by P_{opt} , changes with R according to $P_{\text{opt}} = P_{\text{optArea}} \cdot \pi R^2$, varying between 2.26 W to 56.55 W when $R_{\min} = 0.6 \text{ m}$ and $R_{\max} = 3.0 \text{ m}$, respectively (see Table 4.8 for more details). According to the setting that is presented in this Section, Table 4.8 represents the average illuminance E_{avg} and illuminance uniformity U_{light} values for specific R and $\phi_{1/2}$ configurations, whereas Figure 4.18 represents the E_{avg} and U_{light} for the whole R and $\phi_{1/2}$ ranges. Note that most homogeneous illumination (i.e., highest U_{light}) are achieved with the LEDs that are least directional (i.e., higher $\phi_{1/2}$) as they distribute more homogeneously the emitted light. On the other hand, LEDs with high directivity (i.e., low $\phi_{1/2}$) concentrate the transmitted light around the center of the cell, where the incidence angle (with respect to the axis of the reception cone of the PD) is small. Thus,

Parameter	Description	Value	Unit
R	Circular cell radius	0.6 to 3	[m]
d_v	Vertical distance between AP and PD	2.25	[m]
$\phi_{1/2}$	Half-power semi-angle of the LED	25 to 75	[deg.]
P_{optArea}	Optical transmit power per unit area	2	[W/m ²]
$K_{e/v}$	Luminous efficacy	300	[lm/W]
W	Modulation bandwidth (electrical signal)	50	[MHz]
ζ	Ratio DC-standard deviation	5.05	[dB]
η_{pd}	APD responsivity	16	[A/W]
A_{pd}	APD physical area	3.14	[mm ²]
K	Number of subcarriers (IFFT size)	512	
$E_{v,\text{ab}}$	Illuminance from ambient light	100	[lux]
T_{abs}	Absolute temperature	300	[K]
R_L	Receiver load resistance	500	[Ω]

Table 4.7: System parameters for the multi-carrier and multi-cell scenario.

larger E_{avg} values are achieved with directional LEDs. The maximum average illuminance is achieved when R grows large, and it is given by

$$\begin{aligned} \lim_{R \rightarrow \infty} E \left\{ \Phi \cdot \frac{\sum_{\forall i} |H_i(r_0, \theta)|}{A_{\text{pd}}} \right\} &= \lim_{R \rightarrow \infty} \int_0^R f_{r_0}(r_0) \cdot \Phi \cdot \frac{|H_0(r_0)|}{A_{\text{pd}}} dr_0 \\ &= \lim_{R \rightarrow \infty} P_{\text{optArea}} K_{e/v} (m+1) h^{m+1} \int_0^R \frac{r_0}{(r_0^2 + h^2)^{\frac{m+3}{2}}} dr_0 = P_{\text{optArea}} \cdot K_{e/v} \text{ [lux].} \end{aligned} \quad (4.41)$$

Note that $\lim_{R \rightarrow \infty} \sum_{\forall i} |H_i(r_0, \theta)| = |H_0(r_0)|$ because neighboring APs are far away and, if the received power comes only from the nearest AP (i.e., the AP with index ‘0’ in the center of the three-tier scenario with 37 cells used in the simulation setting), H uniquely depends on the horizontal distance r_0 . Besides, it is assumed that users are uniformly distributed in the circular cell and, thus, $f_{r_0}(r_0) = \frac{2r_0}{R^2}$. The output luminous flux is formulated as $\Phi = P_{\text{optArea}} \pi R^2 K_{e/v}$ if the optical power per unit area is fixed.

If an office is considered where writing, typing or reading tasks are carried out, the conditions $E_{\text{avg}} > 500 \text{ lux}$ and $U_{\text{light}} > 0.6$ must be verified [EN 12464-1:2002 E, 2002]. Thus, those illumination settings (i.e., optical cell radius R and LED half-power semi-angles $\phi_{1/2}$) that satisfy both requirements are valid to be installed in realistic scenarios. In Figure 4.18, the working points above the horizontal black line verify both mean illumination and uniformity

R [m]	0.6	0.9	1.2	1.5	1.8	2.1	2.4	2.7	3
P_{opt} [W]	2.26	5.09	9.05	14.14	20.36	27.71	36.19	45.80	56.55
$\phi_{1/2}$	30°	585 (0.99)	597 (0.98)	599 (0.92)	600 (0.79)	600 (0.63)	600 (0.47)	600 (0.35)	600 (0.25)
	45°	512 (0.99)	566 (0.99)	584 (0.98)	591 (0.93)	595 (0.86)	596 (0.77)	597 (0.68)	598 (0.59)
	60°	434 (0.99)	512 (0.99)	547 (0.99)	565 (0.97)	575 (0.92)	581 (0.87)	586 (0.81)	588 (0.74)
	75°	373 (0.99)	460 (0.99)	505 (0.99)	530 (0.98)	546 (0.95)	557 (0.91)	565 (0.86)	570 (0.81)

Table 4.8: AP optical power configuration, average illuminance E_{avg} [lux] (upper number in every cell) and illuminance uniformity values U_{light} (lower number between brackets in every cell). Brown-shaded numbers do not comply with the illumination requirements.

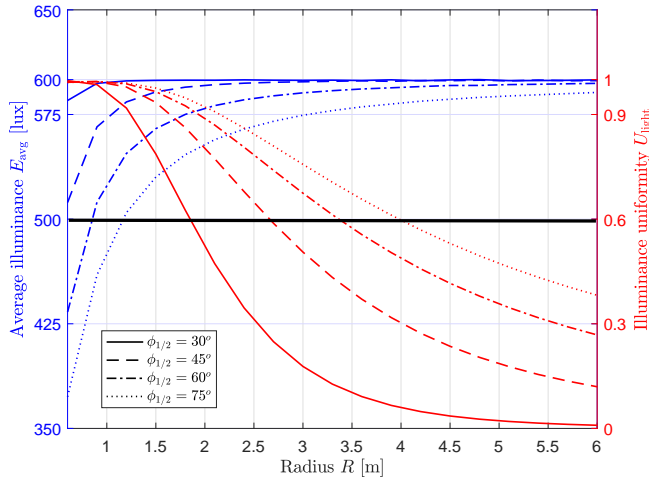


Figure 4.18: Average illuminance E_{avg} (blue lines) and illuminance uniformity U_{light} (red lines) as function of the circular cell radius R for different half-power semi-angle $\phi_{1/2}$.

of illumination requirements, making them appropriate for their use in practice. In Table 4.8, the brown-shaded numbers do not comply with the illumination requirements and, as a consequence, the corresponding configuration is not valid for a real implementation.

4.4.6 Results and discussion

The simulation parameters are summarized in Table 4.7. The electrical modulation bandwidth of the different LED chip colors is 50 MHz to be aligned with the ones observed in commercial LEDs. The DCO-OFDM scheme that is utilized in this study assumes 512 subcarriers allocated in the whole electrical modulation bandwidth of each LED color chip.

4.4.6.1 Performance of resource allocation schemes without cooperation in transmission

The CDF of SINR for different resource allocation schemes when RGB and RGBY LEDs are used is represented in Figure 4.19a and Figure 4.19b, respectively. As expected, the SINR improves when the cluster size Q increases. For low Q values, the (optical) interference power is higher than the noise power; therefore, those resource allocation schemes that provide the same cluster size Q show the same SINR performance, such as

- $\{|\mathcal{C}|=3, |\mathcal{S}|=1, M=1, |\mathcal{F}|=1\}$ and $\{|\mathcal{C}|=3, |\mathcal{S}|=3, M=1, |\mathcal{F}|=3\}$ with $Q=3$
- $\{|\mathcal{C}|=4, |\mathcal{S}|=1, M=1, |\mathcal{F}|=1\}$, $\{|\mathcal{C}|=4, |\mathcal{S}|=3, M=1, |\mathcal{F}|=3\}$ and $\{|\mathcal{C}|=4, |\mathcal{S}|=4, M=1, |\mathcal{F}|=4\}$ with $Q=4$.

In contrast, in those resource allocation schemes in which Q is large, the noise power gains importance and, due to that, the specific values ν , $|\mathcal{C}|$ and $|\mathcal{F}|$ gain relevance when computing the SINR in reception using (4.34). Thus, when comparing two schemes with equally large $Q_1 = \frac{|\mathcal{C}_1| \cdot |\mathcal{F}_1|}{|\mathcal{S}_1|}$ and $Q_2 = \frac{|\mathcal{C}_2| \cdot |\mathcal{F}_2|}{|\mathcal{S}_2|}$, there is a difference SINR ratio of about $\frac{|\mathcal{F}_1| \cdot \nu_2 \cdot |\mathcal{C}_2|^2}{|\mathcal{F}_2| \cdot \nu_1 \cdot |\mathcal{C}_1|^2}$. As an example, comparing the schemes $\{|\mathcal{C}|=3, |\mathcal{S}|=1, M=1, |\mathcal{F}|=4\}$ and $\{|\mathcal{C}|=4, |\mathcal{S}|=3, M=1, |\mathcal{F}|=9\}$ that have a $Q = 12$ and $\nu_1 = \nu_2 = 1$, there is an SINR difference of $10 \cdot \log_{10}(\frac{4 \cdot 16}{9 \cdot 9}) \approx -1$ dB. Also note that, when the effect of the noise power gains importance in the system performance (i.e. in large Q values), schemes with a large number of sub-bands per color ($|\mathcal{F}|$) are better, since the noise is decreased by a factor $|\mathcal{F}|$ as indicated in (4.35). For example, the scheme $\{|\mathcal{C}|=4, |\mathcal{S}|=3, M=1, |\mathcal{F}|=9\}$ offers a better SINR performance than $\{|\mathcal{C}|=4, |\mathcal{S}|=1, M=1, |\mathcal{F}|=4\}$, even when the second scheme has a larger Q . When RGB and RGBY LEDs schemes are compared, no notable differences in SINR have been observed when the resource allocation schemes provide the same cluster size Q .

The mean cell data rate formulated in (4.38) is represented in Figure 4.20a and Figure 4.20b when using RGB and RGBY LEDs, respectively. For the sake of clarity, only $\{|\mathcal{C}|=3, |\mathcal{S}|=1\}$

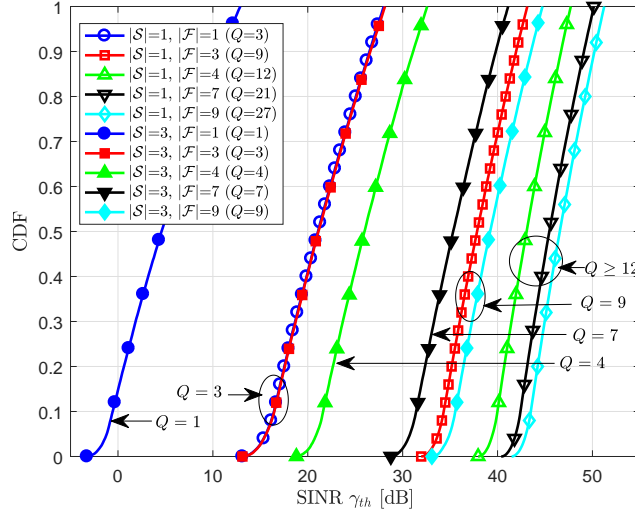
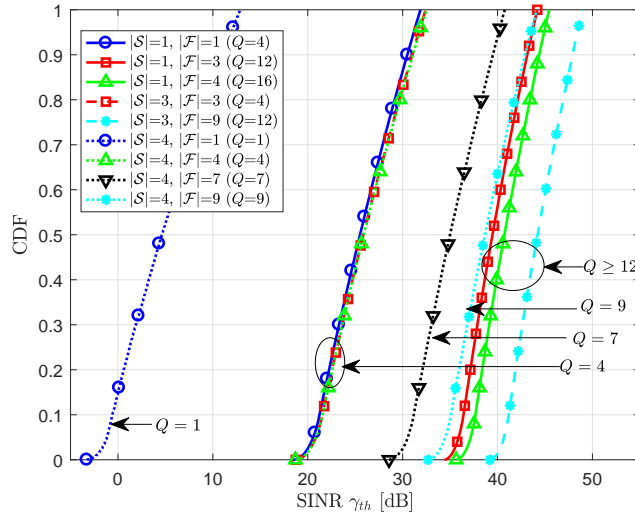
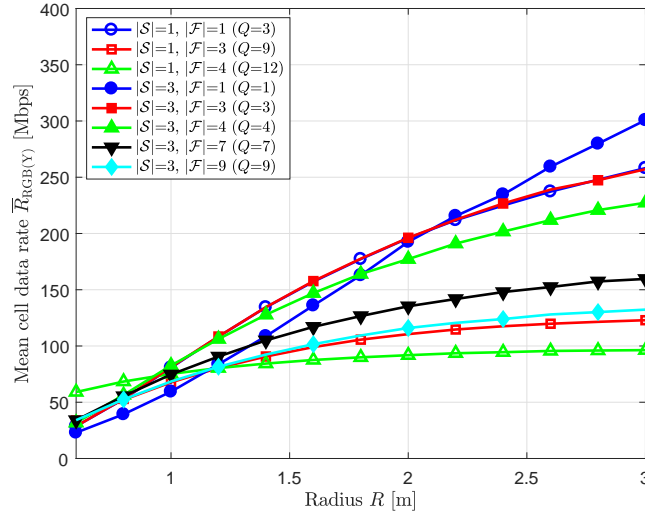
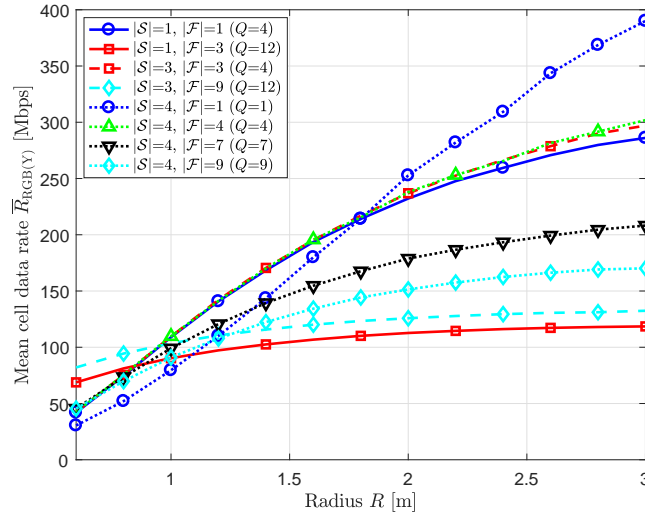
(a) RGB LEDs ($|\mathcal{C}| = 3$).(b) RGYB LEDs ($|\mathcal{C}| = 4$).

Figure 4.19: CDF of the SINR when $R = 1.5\text{ m}$, $\phi_{1/2} = 60^\circ$ and no cooperation ($M = 1$) are assumed for the different resource allocation schemes.

and $\{|\mathcal{C}|=3, |\mathcal{S}|=3\}$ schemes are represented in Figure 4.20a, and $\{|\mathcal{C}|=4, |\mathcal{S}|=1\}$, $\{|\mathcal{C}|=4, |\mathcal{S}|=3\}$ and $\{|\mathcal{C}|=4, |\mathcal{S}|=4\}$ in Figure 4.20b. As expected, the larger is the radius of the cell, the larger is the data rate that can be achieved as the interference of the multi-cell VLC system decreases. When the interference power becomes lower than the noise power (large R values), schemes that result in small cluster sizes Q give the best performance. However, while R decreases, larger Q values are needed to keep under control the inter-cell interfer-



(a) RGB LEDs ($|\mathcal{C}| = 3$).



(b) RGBY LEDs ($|\mathcal{C}| = 4$).

Figure 4.20: Mean cell data rate $\bar{R}_{\text{RGB}(Y)}$ as function of the circular radius R of the cell when $\phi_{1/2} = 60^\circ$ and no cooperation ($M = 1$) are utilized for different resource allocation schemes.

ence power. For example, when using RGB LEDs, in scenarios with $R < 0.9$ [m], resource allocation schemes with $Q = 12$ gives the highest mean cell data rate performance, whereas $Q = 4$ ($Q = 3$) resource allocation schemes behave better when the cell radius lies in the range $0.9 < R < 1.1$ [m] ($1.1 < R < 2$ [m]). Finally, for cell radius $R > 2$ [m], resource allocation schemes with $Q = 1$ are the best choice. The same phenomenon occurs when RGBY LEDs

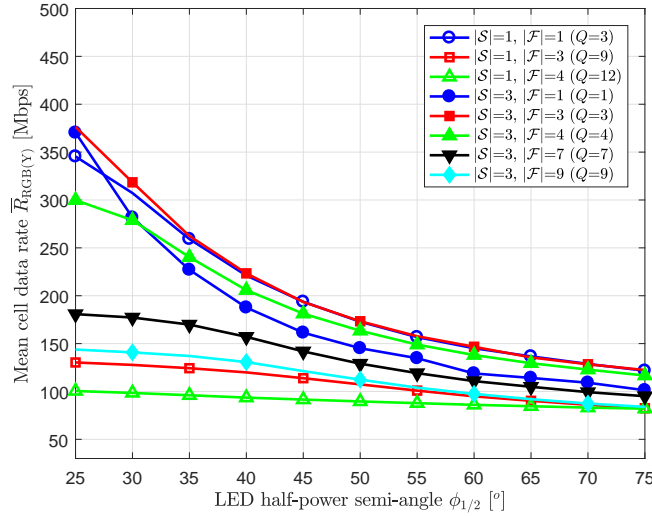
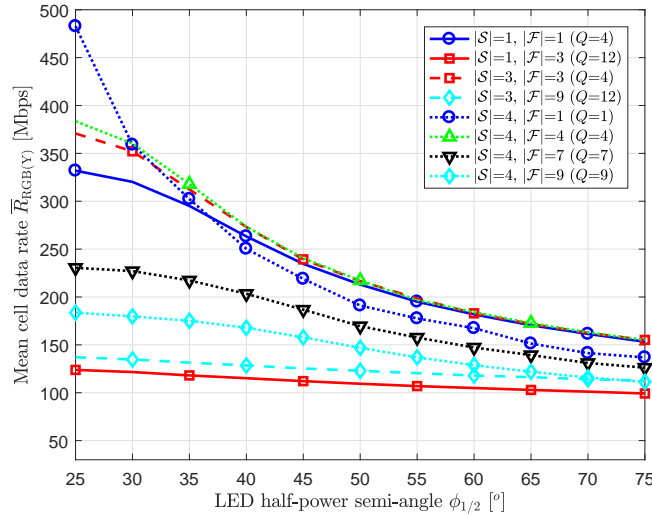
(a) RGB LEDs ($|\mathcal{C}| = 3$).(b) RGBY LEDs ($|\mathcal{C}| = 4$).

Figure 4.21: Mean cell data rate $\bar{R}_{\text{RGB(Y)}}$ as function of the half-power semi-angle of the LED $\phi_{1/2}$ when $R = 1.5 \text{ m}$ and no cooperation ($M = 1$) are utilized for different resource allocation schemes.

are used. In addition, note that for large R values, where the effect of noise gains relevance, there are differences between schemes with the same Q (e.g., resource allocation schemes with $Q = 9$ in RGB LEDs or $Q = 4$ in RGBY LEDs).

When comparing Figure 4.20a and Figure 4.20b, and in line with the analysis that can be ob-

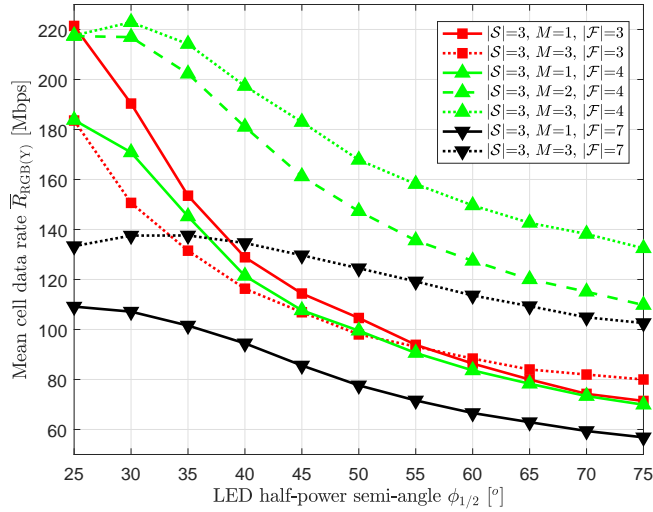


Figure 4.22: Mean cell data rate $\bar{R}_{\text{RGB(Y)}}$ as function of the half-power semi-angle of the LED $\phi_{1/2}$ when RGB LEDs ($|\mathcal{C}| = 3$), $R = 1.5 \text{ m}$ and a blockage probability $\rho_{\text{block}} = 40 \%$ are utilized for different resource allocation schemes.

tained from (4.38), it is possible to see that resource allocation schemes with RGBY LEDs provide a gain in cell data rate in the order of 1/3 (33%) with respect to an equivalent scheme using RGB LEDs (i.e., providing the same cluster size Q). This is because the SINR values are similar in RGB and RGBY LEDs scenarios dominated by optical interference, but RGBY LEDs scenarios have 4/3 times more electrical bandwidth available than its RGB LED counterpart.

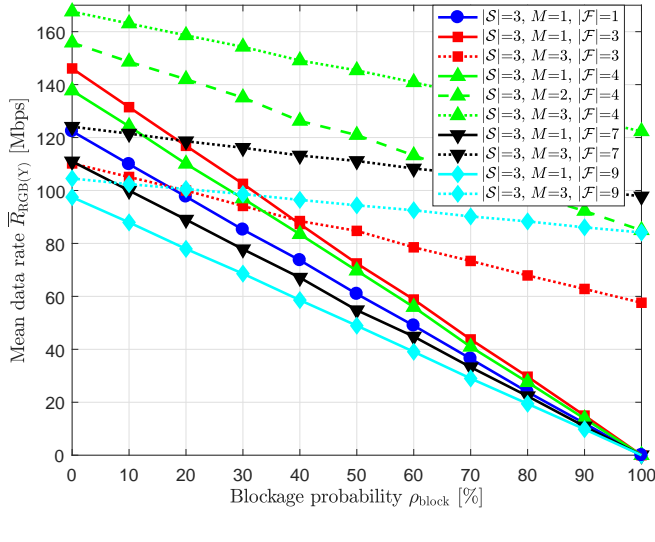
The half-power semi-angle $\phi_{1/2}$ of the LEDs influences the produced interference considerably. The effect of $\phi_{1/2}$ on the mean cell data rate is represented in Figure 4.21a and Figure 4.21b when using RGB or RGBY LEDs, respectively. As expected, the mean cell data rate performance degrades as the $\phi_{1/2}$ increases, because a larger inter-cell interference power is generated. Therefore, those resource allocation schemes that suffer from inter-cell interference more notably (low Q values) experience a considerable improvement when $\phi_{1/2}$ decreases (e.g., schemes with $Q = 1$ are the best with low $\phi_{1/2}$ values). For those LEDs with $\phi_{1/2} \approx 25^\circ$ in RGB and $\phi_{1/2} \approx 30^\circ$ in RGBY, the schemes with $Q = 3$ and $Q = 4$ are the ones that provide the best data rate performance, respectively. After that $\phi_{1/2}$ value, all the schemes degrade equally.

4.4.6.2 Performance of resource allocation schemes with cooperation in transmission

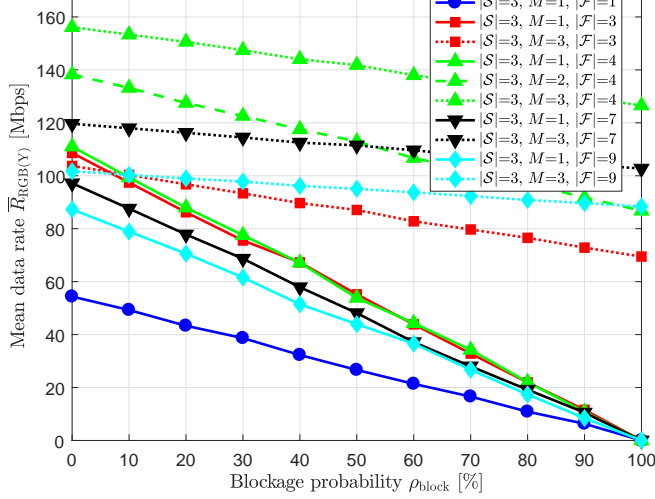
Once the performance of all the possible schemes without cooperation has been evaluated, it is time to evaluate the performance of cooperative schemes focusing only on the RGB LEDs scenarios (similar results are obtained for RGBY LEDs, applying the corresponding scaling factor 4/3). In Figure 4.22, it is represented the mean cell data rate as function of $\phi_{1/2}$ for the tri-sector RGB schemes with a blockage probability $\rho_{\text{block}} = 40\%$. This blockage probability represents the probability of LoS-link blockage with the nearest AP, in such a way that if a user is blocked towards the nearest AP, it only receives data from the cooperating APs. Note that, when no cooperation is implemented in transmission, the mean cell data rate is monotonically decreasing; that is, it is better to select the most directional LED, as long as the illumination requirements in Figure 4.18 are satisfied. In contrast, if cooperation is employed, it is possible to get an optimum $\phi_{1/2}$ to maximize the cell data rate. The reason is that, when cooperation occurs, very directional LEDs spread little optical power towards the area of neighboring cells. Then, an optimum $\phi_{1/2}$ value can be found, from which value on the performance decreases because energy is transmitted farther than what is needed. Note that the loss in the transmit power due to the cooperation, and the high inter-cell interference level generated in $Q = 3$, become notable in the $\{|\mathcal{S}| = 3, |\mathcal{F}| = 3\}$ scheme, where the cooperative scheme does not overcome the non-cooperative scheme up to a high $\phi_{1/2}$ value.

Finally, Figure 4.23 represents the mean data rate of users located in the whole cell area A_{cell} and in the cell-edge area A_{edge} , which is defined as the external ring whose area is 10% of the whole cell area. As expected, the overall tendency is that cooperative schemes offer a better performance than non-cooperative schemes. However, in schemes with low Q values (e.g., $Q = 3$), the cooperative scheme does not provide better performance than the non-cooperative alternatives up to a certain blockage probability. Note that the blockage impacts more notably the schemes with low Q values as the inter-cell interference power that is produced is larger. Thus, in scenarios with a large blockage probability, it could be preferable to select schemes with large Q values. Furthermore, it is interesting to observe that those users located on the cell-edge areas of the VLC network are the most benefited due to the cooperation. The data rate loss that cell-edge users experience due to blockage events is negligible in comparison to the one suffered by the schemes with no cooperation. Besides, comparing the two plots of Figure 4.23, the mean data rate when cooperation is employed is much more homogeneous than in non-cooperative schemes, which means that the coverage is more uniform than if non-cooperative

schemes are utilized.



(a) Users located in the whole cell area



(b) Users located in the cell-edge area — $A_{\text{edge}} = 0.1 \cdot A_{\text{cell}}$

Figure 4.23: Average data rate $\bar{R}_{\text{RGB(Y)}}$ as function of the blockage probability ρ_{block} when RGB LEDs ($|\mathcal{C}| = 3$), $R = 1.5 \text{ m}$, $\phi_{1/2} = 60^\circ$ and some cooperation modes with tri-sector multi-cells are utilized to serve users in different areas of the cell.

4.5 Summary

This Chapter studied the performance of VLC systems in multi-cell scenarios. An initial evaluation of the LoS-link blockage produced in a realistic scenario was carried out in terms of SNR, and a solution when a single-carrier modulation scheme such as OOK was presented. The results showed that a gain of around 3 dB can be obtained with this cooperative system proposal. Although, in case of LoS, the non-cooperative scheme provides a better performance, the cooperative scheme offers a more robust and reliable communication providing a more homogeneous coverage.

Since the new communication systems focus on multi-carrier modulation schemes, a preliminary study was carried out to evaluate its viability, based on a simple TDMA scheme. The potential of the cooperative scheme is observed, although the use of MAM and TDMA damages the cell data rate performance. Thus, the use of RGB(Y) LEDs and WDM were invoked to increase the communication resources and an extensive study of the different resource allocation schemes, with and without cooperation in transmission, was presented. When designing these resource allocation schemes, the homogeneity requirement was sought to maintain the same SINR statistic over the whole coverage area of the VLC network to simplify the network design and its optimization. Therefore, the different combinations of parameters that enable this homogeneity property were clearly stated in the different lemmas that were derived. All the possible schemes in terms of LED type, number of frequency sub-bands per color, and number of sectors per cell were evaluated. Furthermore, working conditions were thoroughly studied in order to determine the transmission schemes that comply with the illumination requirements. As expected, there is no single resource allocation scheme that provides the highest mean data rate for all network settings. Extensive simulation results were presented demonstrating that, with a correct network planning in the allocation of resources per AP, the mean cell data rate can be considerably improved. Besides, it was shown that, in presence of obstacles that usually block the LoS from the serving AP to the user, the implementation of multi-point cooperative transmission schemes is essential. Finally, it was observed that cooperative schemes also offer important gains in mean cell data rate even in case of LoS conditions.

Chapter 5

CoMP transmission based on relay-assisted techniques

5.1 Introduction

As mentioned in previous Sections, the LiFi concept was coined in [Haas, 2013] to refer to a fully networked VLC system, where light fixtures are interconnected providing of Internet access to users located in the room. Each light fixture serves as an AP, and multiple APs create a small-cell network usually known as attocell network [Chen *et al.*, 2013]. A proper arrangement of such a network means an increase in the system spectral efficiency but, as demonstrated, if additional interference mitigation and robustness-increasing techniques are not deployed, this network still suffers from the LoS-link blockages and high inter-cell interference levels. All the techniques that were previously presented here and in the literature need a wired backhaul approach that are often assumed to be ideal [Somekh *et al.*, 2007], i.e. lossless, noiseless and instantaneous, and sometimes they are supposed to involve unlimited capacity [Kamoun and Mazet, 2007], which is an unrealistic scenario. A backhaul link is essential in cellular networks [Tipmongkolsilp *et al.*, 2011]. Thus, a backhaul link must be considered and studied in a realistic way to evaluate the communication system performance. Different wired backhaul techniques for VLC have been demonstrated in the literature, such as PLC [Song *et al.*, 2015] [Bouchet *et al.*, 2010], Ethernet-VLC [Delgado *et al.*, 2010] and optical fiber [Wang *et al.*, 2015b]. However, the use of wired backhaul links imposes an extra cost and cabling infrastructure that sometimes means a high complexity when the network becomes larger. Furthermore, every time the topology changes (e.g. the location of the light fixtures), the wired backhaul needs an update too. Thus, alternative wireless backhaul links must be studied.

5.2 State of the art

Practical wireless backhaul links have been studied using RF systems [Zhao *et al.*, 2015], or using FSO communications [Li *et al.*, 2013] [Li *et al.*, 2015]. The installation of a LiFi system

in a room can be even more unpractical if significant alterations to the room are necessary to equip the light fixtures with LiFi capabilities. To this end, the first work that studies the viability of a wireless backhaul in LiFi systems was published in [Kazemi *et al.*, 2019]. Besides, relay-assisted techniques were considered as suitable alternatives to support the main link and improve the system throughput: [Narmanlioglu *et al.*, 2017] presented a cooperative VLC system using an intermediate light source that acts as a relay terminal; a relay technique using an asymmetrically clipped direct current biased optical OFDM (ADO-OFDM) was proposed in [Na *et al.*, 2018], with the aim of relaying information and transmitting its own data using odd and even subcarriers, respectively; and a relay-assisted VLC system where a main light in the ceiling and one task light are used, was investigated in terms of BER in [Kizilirmak *et al.*, 2015].

Different from the existing studies, this Chapter proposes a cooperative VLC system based on relay-assisted techniques where reflections are used as relaying links. In that way, a single additional PD is needed per AP, different from [Kazemi *et al.*, 2019] where each AP needs 6 extra LEDs in addition to several PDs. This proposal makes LiFi technology stronger in the presence of blocking elements as it is common in indoor scenarios, because the system performance can still be satisfactory even with the blockage of LoS link.

5.3 Reflection-based relaying technique

5.3.1 System model

Figure 5.1 illustrates the reflection-based relaying technique proposed in this work. The system is composed by one source S, one selected relay R and one destination D. The source is the closest AP to the destination and the selected relay is the neighboring AP which is closest to user. Every AP is formed by one LED and one PD, both having a vertical downward orientation. The relay takes advantage of the reflection produced in the floor ($|H^{SR}|$) to receive the signal transmitted by the source, processes it and forwards it to the destination. In that way, the damage caused by a LoS blockage at any link can be avoided by using relaying techniques.

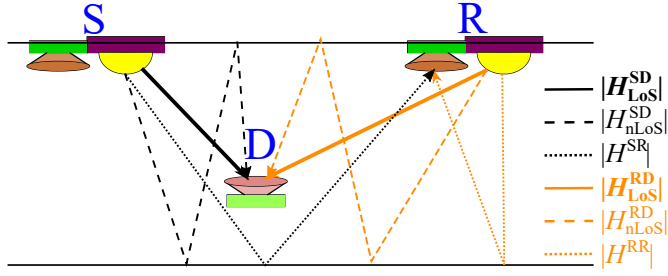


Figure 5.1: Reflection-based relaying scenario.

5.3.1.1 Channel Model

The channel model is mainly influenced by both the front-end devices (LED and PD) and the free-space transmission. The FDCHTF from an LED to a PD is formulated as (2.35)

$$|H[k]| = |H_{\text{fe}}[k]| \cdot |H_{\text{fs}}[k]|, \quad (5.1)$$

where $|H_{\text{fe}}[k]|$ is the FDCHTF of the front-end devices in the k -th subcarrier modeled by (2.36) as

$$|H_{\text{fe}}[k]| = \sqrt{\exp\left(-\frac{kW}{KF_{\text{fe}}}\right)}, \quad (5.2)$$

where K is the number of frequency subcarriers in which the total bandwidth W is divided and F_{fe} is the so-called bandwidth factor that controls the frequency-domain characteristics. The free-space channel gain denoted by $|H_{\text{fs}}[k]|$ is computed from the CIR by the Fourier transform as $|H_{\text{fs}}[k]| = \int_0^\infty h_{\text{fs}}(t)e^{-\frac{2\pi j W t k}{K}} dt$, where $h_{\text{fs}}(t)$ is the CIR composed by the LoS and NLoS components as (2.37). As defined in (2.2), the Lambertian emission order is $m = \frac{-1}{\log_2 \cos(\phi_{1/2})}$.

The NLoS component of the CIR between an LED \hat{p} and a PD \hat{q} denoted by $h_{\text{NLoS}}^{\hat{p}\hat{q}}(t)$ is computed by using the analytical method presented in [Chen *et al.*, 2018], which utilizes the transmitter and user locations with respect to the room, their orientations, A_{pd} , m , ψ_{FoV} and the reflectances of the surfaces ρ_{floor} and ρ_{ceil} .

Figure 5.2 shows the CIRs in TD (Figure 5.2a) and their magnitudes in FD (Figure 5.2b) of the different channel responses represented in Figure 5.1. Note that the CIR between S and R ($h^{\text{SR}}(t)$, $|H^{\text{SR}}[k]|$) is higher than the NLoS CIRs corresponding to S→D ($h_{\text{NLoS}}^{\text{SD}}(t)$, $|H_{\text{NLoS}}^{\text{SD}}[k]|$). It means that, in case of NLoS, the power received by D coming from reflections is much lower than the one received by R coming from S. Thus, if a proper signal processing is made at R, the

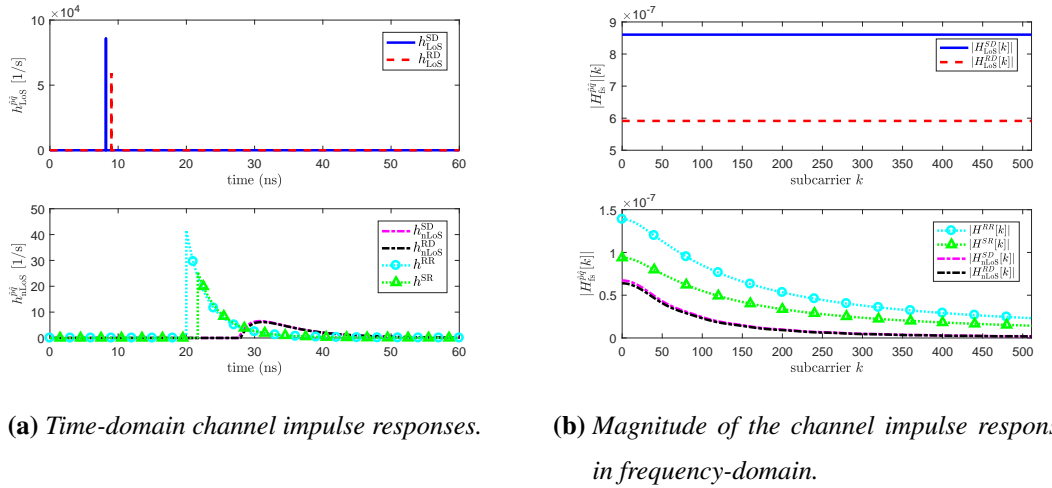


Figure 5.2: Illustration of channel impulse responses in a simple scenario where coordinates of source S, relay R and destination D are in meters [0.5; 2.5; 3], [3; 2.5; 3] and [1.5; 2.5; 0.75], respectively. Parameters: $\rho_{\text{floor}}=0.6$, $\rho_{\text{ceil}}=0.8$, $K = 512$ subcarriers, $W=280 \text{ MHz}$, $n_{\text{ref}}=1.5$, $\psi_{\text{FoV}} = 90^\circ$, $\phi_{1/2} = 60^\circ$, $G_f = 1$, $A_{\text{pd}} = 8.72 \text{ mm}^2$.

signal received by the destination D coming from the relay R will be stronger than if there is no cooperation.

5.3.1.2 Implementation

The proposed reflection-based relaying technique can be implemented easily and its performance in practice is as follows:

1. The user indicates through the uplink (UL) the AP from which the user receives the strongest signal. It is usually the closest AP.
2. The user computes the possible $|H^{\text{SR}}| \otimes |H^{\text{RD}}|$ channels with respect to all adjacent APs and decides the best candidate to act as a relay R.
3. The user notifies through the UL to the corresponding AP its desire of receiving relayed information from it. Besides, the user informs the source identifier whose information must be relayed.
4. The reflection-based relaying scenario illustrated in Figure 5.1 is established.

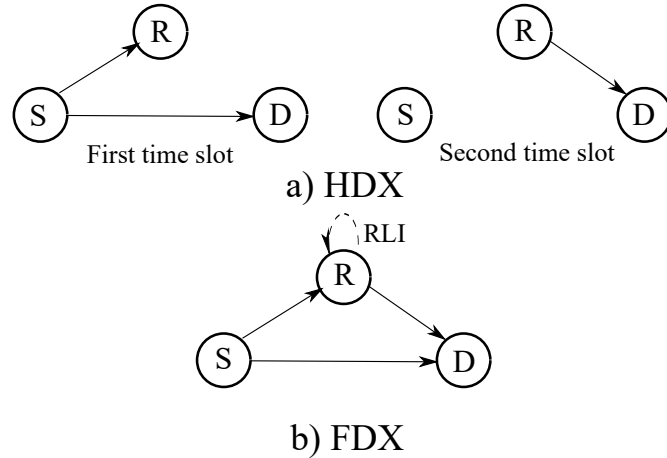


Figure 5.3: Half-duplex and full-duplex cooperative relaying techniques since the source S transmits a symbol until it arrives to the destination D .

5.3.2 Downlink study

As Figure 5.1 illustrates, the generic proposal is composed by the cooperative transmission between two APs, one performing as a source S and the other as a relay R , without using any wired backhaul link. The signal received by a user, also called destination D , is represented by

$$y_D(t) = \eta_{pd,D} \cdot h_{fe}(t) \otimes (x_S(t) \otimes h_{fs}^{SD}(t) + x_R(t) \otimes h_{fs}^{RD}(t)) + n_{rx}(t), \quad (5.3)$$

where $\eta_{pd,D}$ is the responsivity of the PD at the destination D , $h_{fe}(t)$ is the TD channel computed from (5.2), $x_S(t)$ and $x_R(t)$ are the signals transmitted by S and R in the time domain, respectively, and $n_{rx}(t)$ is the receiver noise in the time domain that obeys a zero-mean Gaussian distribution with variance $\sigma_{rx}^2 = \frac{N_0 W}{\xi^2}$ computed as Section 2.3 indicates.

Two main relaying techniques have usually been considered in the literature:

- Amplify and forward (AF): The relay R receives the signal coming from the source S , amplifies it and forwards it to the destination D .
- Decode and forward (DF): The relay R receives the signal coming from the source S , decodes it and forwards it to the destination D . This technique requires an extra signal processing, but, in exchange, errors can be corrected in the relay and may not be forwarded.

Besides, each of them can perform in two different modes, represented in Figure 5.3:

- Half duplex (HDX) mode: The cooperation between S and R is made in two different time slots. In the first one, the source transmits its signal to R and D. The second time slot is utilized by R in order to relay the signal received from S. This mode avoids interference between S and R and it makes possible a low-complexity relay design. However, it reduces by half the spectral efficiency.
- Full duplex (FDX) mode: The cooperation between S and R is made simultaneously. Thus, the spectral efficiency does not decrease as in HDX, but it can produce a residual loop interference (RLI) at R due to the signal reception of its own previous transmission. This RLI can be cancelled by using interference cancellation techniques. This Chapter studies the cooperative relaying techniques both with and without RLI cancellation and shows a comparison of their performances.

The SNR is an important metric to evaluate the performance of a communication system. In this cooperative proposal based on relaying techniques, by using either joint decoding and successive interference cancellation (SIC) techniques in FDX mode [Han *et al.*, 2014] [Chen and Rui, 2012], or maximal ratio combining techniques in HDX mode [Goldsmith, 2005] [Brennan, 1959] [Wang *et al.*, 2007], the total SNR can be computed as

$$\Gamma_{\text{total}}[k] = \Gamma_{\text{SD}}[k] + \Gamma_{\text{SRD}}[k], \quad (5.4)$$

where $\Gamma_{\text{SD}}[k]$ is the SNR in the k -th subcarrier received by D from S and $\Gamma_{\text{SRD}}[k]$ is the SNR in the k -th subcarrier received by D coming from the relay path S→R→D.

To make a fair comparison between HDX and FDX techniques, a total electrical transmit power $P = \left(\frac{P_{\text{opt,max}} - P_{\text{opt,min}}}{\kappa} \right)^2$ is fixed, where $P_{\text{opt,max}}$ and $P_{\text{opt,min}}$ are the maximum and minimum possible optical transmit power and κ is the ratio of peak amplitude to the standard deviation of the signal, also called clipping factor. Thus, in HDX, both S and R transmits $P_{\text{S,tx}} = P_{\text{R,tx}} = P$ Watt because both transmit at different time slots. By contrast, the total electrical transmit power P in FDX is the addition of the power transmitted by S and R: $P = P_{\text{S,tx}} + P_{\text{R,tx}}$, where $P_{\text{S,tx}}$ and $P_{\text{R,tx}}$ in AF/FDX are defined as

$$P_{\text{S,tx}} = \beta \cdot P \quad (5.5)$$

$$P_{R,tx} = (1 - \beta) \cdot P, \quad (5.6)$$

where $\beta \in (0, 1)$ is the power allocation factor. By contrast, in DF/FDX a power allocation per subcarrier k can be done as

$$P_{S,tx}[k] = \beta[k] \cdot P / (K - 2) \quad (5.7)$$

$$P_{R,tx}[k] = (1 - \beta[k]) \cdot P / (K - 2). \quad (5.8)$$

Regarding the capacity, as mentioned before, HDX suffers from a decrease by half in the spectral efficiency due to the transmission in two time slots per channel use.

5.3.2.1 Amplify and forward relaying

In AF, the signal transmitted by R is

$$x_R(t) = G_{AF} \cdot y_R(t), \quad (5.9)$$

where G_{AF} is the amplification factor in AF and $y_R(t)$ is the signal received by R. Both variables depend on the mode that is invoked:

HDX mode:

In AF/HDX, the signal received by R ($y_R(t)$) is composed by the signal transmitted by S ($x_S(t)$) in addition to noise ($n_{rx}(t)$), formulated as

$$y_R(t) = \eta_{pd,R} \cdot x_S(t) \otimes h_{fs}^{SR}(t) \otimes h_{fe}(t) + n_{rx}(t), \quad (5.10)$$

where $\eta_{pd,R}$ is the responsivity of the relay's PD. As mentioned before, the electrical power transmitted by S and R are $P = P_{S,tx} = P_{R,tx}$. Satisfying such an equality, the constant multiplier G_{AF} can be computed by

$$G_{AF/HDX} = \sqrt{\frac{P_{R,tx}}{P_{R,rx}}} = \sqrt{\frac{P}{\eta_{pd,R}^2 \cdot P \cdot E \left\{ |H_{fs}^{SR}[k]|^2 \right\} \cdot E \left\{ |H_{fe}[k]|^2 \right\} + \sigma_{rx}^2}}, \quad (5.11)$$

where $P_{R,rx}$ is the electrical power received by R.

The total SNR formulated in (5.4) is computed by using the SNR in the k -th subcarrier received by D from S given by

$$\Gamma_{\text{SD,AF/HDX}}[k] = \frac{\eta_{\text{pd,D}}^2 \cdot \xi^2 \cdot P \cdot |H_{\text{fe}}[k]|^2 \cdot |H_{\text{fs}}^{\text{SD}}[k]|^2}{\sigma_{\text{rx}}^2} \quad (5.12)$$

and the SNR in the k -th subcarrier received by D coming from the relay path S→R→D formulated as

$$\Gamma_{\text{SRD,AF/HDX}}[k] = \frac{\eta_{\text{pd,D}}^2 \xi^2 G_{\text{AF/HDX}}^2 \eta_{\text{pd,R}}^2 P |H_{\text{fe}}[k]|^4 |H_{\text{fs}}^{\text{SR}}[k]|^2 |H_{\text{fs}}^{\text{RD}}[k]|^2}{\sigma_{\text{rx}}^2 \left(1 + \eta_{\text{pd,D}}^2 |H_{\text{fe}}[k]|^2 |H_{\text{fs}}^{\text{RD}}[k]|^2 G_{\text{AF/HDX}}^2 \right)}. \quad (5.13)$$

FDX mode:

In AF/FDX the signal received by R is calculated as

$$y_R(t) = \eta_{\text{pd,R}} \cdot (x_S(t) \otimes h_{\text{fs}}^{\text{SR}}(t) + x_R(t) \otimes h_{\text{fs}}^{\text{RR}}(t)) \otimes h_{\text{fe}}(t) + n_{\text{rx}}(t), \quad (5.14)$$

where $x_R(t) \otimes h_{\text{fs}}^{\text{RR}}(t)$ is the RLI produced in R by its previous transmission. In this AF/FDX case, the constant multiplier G_{AF} is computed by

$$\begin{aligned} G_{\text{AF/FDX}} &= \sqrt{\frac{P_{\text{R,tx}}}{P_{\text{R,rx}}}} \\ &= \sqrt{\frac{(1-\beta)P}{\eta_{\text{pd,R}}^2 \cdot P \cdot \left(\beta \cdot \mathbb{E} \left\{ |H_{\text{fs}}^{\text{SR}}[k]|^2 \right\} + (1-\beta) \cdot \mathbb{E} \left\{ |H_{\text{fs}}^{\text{RR}}[k]|^2 \right\} \right) \cdot \mathbb{E} \left\{ |H_{\text{fe}}[k]|^2 \right\} + \sigma_{\text{rx}}^2}}}. \end{aligned} \quad (5.15)$$

Thus, the SNR equations needed for computing $\Gamma_{\text{total}}[k]$ indicated in (5.4) are

$$\Gamma_{\text{SD,AF/FDX}}[k] = \beta \Gamma_{\text{SD,AF/HDX}}[k] = \frac{\eta_{\text{pd,D}}^2 \cdot \xi^2 \cdot \beta \cdot P \cdot |H_{\text{fe}}[k]|^2 \cdot |H_{\text{fs}}^{\text{SD}}[k]|^2}{\sigma_{\text{rx}}^2} \quad (5.16)$$

and

$$\Gamma_{\text{SRD,AF/FDX}}[k] = \frac{\xi^2 \eta_{\text{pd,R}}^2 \beta P |H_{\text{fe}}[k]|^2 |H_{\text{fs}}^{\text{SR}}[k]|^2}{\sigma_{\text{rx}}^2 \left(\frac{1}{\eta_{\text{pd,D}}^2 G_{\text{AF/FDX}}^2 |H_{\text{fs}}^{\text{RD}}[k]|^2 |H_{\text{fe}}[k]|^2} + 1 \right) + \eta_{\text{pd,R}}^2 (1-\beta) P |H_{\text{fs}}^{\text{RR}}[k]|^2 |H_{\text{fe}}[k]|^2}. \quad (5.17)$$

5.3.2.2 Decode and forward relaying

In DF, the signal transmitted by R can be defined as

$$x_R(t) = \hat{x}_S(t), \quad (5.18)$$

where $\hat{x}_S(t)$ is a result of decoding and processing the signal transmitted by S ($x_S(t)$). Again, the SNR equations depend on the transmission mode:

HDX mode:

In DF/HDX, the SNR product of the S→D link is the same as in the AF/HDX case

$$\Gamma_{SD,DF/HDX}[k] = \Gamma_{SD,AF/HDX}[k]. \quad (5.19)$$

By contrast, the SNR received by D coming from the relay path S→R→D is determined by the weakest S→R and R→D independent link as [Zhong and Zhang, 2016]

$$\Gamma_{SR,DF/HDX}[k] = \min(\Gamma_{SR,DF/HDX}[k], \Gamma_{RD,DF/HDX}[k]). \quad (5.20)$$

Due to the use of two different time slots in the transmission of S and R, RLI is not present in HDX mode and the SNR between S and R is computed by

$$\Gamma_{SR,DF/HDX}[k] = \frac{\eta_{pd,R}^2 \cdot \xi^2 \cdot P \cdot |H_{fe}[k]|^2 \cdot |H_{fs}^{SR}[k]|^2}{\sigma_{rx}^2}, \quad (5.21)$$

whereas the SNR between R and D is

$$\Gamma_{RD,DF/HDX}[k] = \frac{\eta_{pd,D}^2 \cdot \xi^2 \cdot P \cdot |H_{fe}[k]|^2 \cdot |H_{fs}^{RD}[k]|^2}{\sigma_{rx}^2}. \quad (5.22)$$

FDX mode:

In DF/FDX, the SNR in S→D can be computed as

$$\Gamma_{SD,DF/FDX}[k] = \beta[k] \cdot \Gamma_{SD,DF/HDX}[k] = \Gamma_{SD,AF/FDX}[k]. \quad (5.23)$$

Again, the SNR in the S→R→D relaying link is computed as

$$\Gamma_{\text{SRD,DF/FDX}}[k] = \min(\Gamma_{\text{SR,DF/FDX}}[k], \Gamma_{\text{RD,DF/FDX}}[k]), \quad (5.24)$$

where $\Gamma_{\text{SR,DF/FDX}}[k]$ and $\Gamma_{\text{RD,DF/FDX}}[k]$ are the SNR in the k -th subcarrier in the independent links S→R and R→D, respectively, when DF/FDX technique is employed. In presence of RLI, the SNR of the S→R link is

$$\Gamma_{\text{SR,DF/FDX}_{\text{RLI}}}[k] \approx \frac{\eta_{\text{pd,R}}^2 \xi^2 \beta[k] P |H_{\text{fe}}[k]|^2 |H_{\text{fs}}^{\text{SR}}[k]|^2}{\sigma_{\text{rx}}^2 + \eta_{\text{pd,R}}^2 \xi^2 (1-\beta[k]) P |H_{\text{fe}}[k]|^2 |H_{\text{fs}}^{\text{RR}}[k]|^2}. \quad (5.25)$$

By contrast, this SNR is considerably improved if there is no RLI due to a perfect cancellation, computed as

$$\Gamma_{\text{SR,DF/FDX}_{\text{nRLI}}}[k] \approx \frac{\eta_{\text{pd,R}}^2 \xi^2 \beta[k] P |H_{\text{fe}}[k]|^2 |H_{\text{fs}}^{\text{SR}}[k]|^2}{\sigma_{\text{rx}}^2}. \quad (5.26)$$

In both cases, the SNR of the R→D link is

$$\Gamma_{\text{RD,DF/FDX}}[k] \approx \frac{\eta_{\text{pd,D}}^2 \xi^2 (1-\beta[k]) P |H_{\text{fe}}[k]|^2 |H_{\text{fs}}^{\text{RD}}[k]|^2}{\sigma_{\text{rx}}^2}. \quad (5.27)$$

5.3.3 System analysis

In order to determine which relaying technique offers the best performance, we need to calculate which technique maximizes $\Gamma_{\text{total}}[k]$ formulated in (5.4)

$$\arg \max_{\text{AF, DF}} \Gamma_{\text{total}}[k]. \quad (5.28)$$

It will be determined by comparing

$$\Gamma_{\text{total,AF/*}}[k] = \Gamma_{\text{SD,AF/*}}[k] + \Gamma_{\text{SRD,AF/*}}[k] \quad (5.29)$$

with

$$\Gamma_{\text{total,DF/*}}[k] = \Gamma_{\text{SD,DF/*}}[k] + \Gamma_{\text{SRD,DF/*}}[k], \quad (5.30)$$

where ‘*’ represents HDX and FDX indistinctly. As said in (5.19) and (5.23), $\Gamma_{\text{SD,AF}/*}[k] = \Gamma_{\text{SD,DF}/*}[k]$. Thus, (5.28) is simplified as

$$\arg \max_{\text{AF, DF}} \Gamma_{\text{SRD}}[k]. \quad (5.31)$$

In HDX, according to (5.13), (5.20), (5.21) and (5.22), $\Gamma_{\text{SRD,AF/HDX}}[k] \leq \Gamma_{\text{SRD,DF/HDX}}[k]$ because $\Gamma_{\text{SRD,AF/HDX}}[k] \leq \Gamma_{\text{SR,DF/HDX}}[k]$ and $\Gamma_{\text{SRD,AF/HDX}}[k] \leq \Gamma_{\text{RD,DF/HDX}}[k]$. By contrast, in FDX, by comparing (5.17) with (5.24), (5.25), (5.26) and (5.27), note that $\Gamma_{\text{SRD,AF/FDX}}[k] \leq \Gamma_{\text{SRD,DF/FDX}}[k]$. Thus, we conclude that DF offers a better performance than AF, regardless the mode (HDX, FDX) is invoked. From now on, the study focuses on the DF mode.

Note in Section 5.3.2.2 that the use of FDX mode imposes to share the total available power P between S and R as indicated by (5.7) and (5.8). The power allocation factor between S and R is denoted by $\beta[k]$ and the optimum value in DF/FDX is derived as

$$\begin{aligned} \beta_{\text{opt}_{\text{DF/FDX}}}[k] &= \begin{cases} 1, & \text{if } \left| \frac{\partial \Gamma_{\text{SD,DF/FDX}}[k]}{\partial \beta} \right| > \left| \frac{\partial \Gamma_{\text{RD,DF/FDX}}[k]}{\partial \beta} \right| \\ \beta_{\text{th}_{\text{DF/FDX}}}[k], & \text{if } \left| \frac{\partial \Gamma_{\text{SD,DF/FDX}}[k]}{\partial \beta} \right| \leq \left| \frac{\partial \Gamma_{\text{RD,DF/FDX}}[k]}{\partial \beta} \right| \end{cases} \\ &= \begin{cases} 1, & \text{if LoS in S} \rightarrow \text{D link} \\ \beta_{\text{th}_{\text{DF/FDX}}}[k], & \text{if NLoS in S} \rightarrow \text{D link} \end{cases} \end{aligned} \quad (5.32)$$

where the $\beta_{\text{th}_{\text{DF/FDX}}}[k]$ value depends on implementing RLI cancellation techniques. In presence of RLI due to not invoking any cancellation technique, $\beta_{\text{th}_{\text{DF/FDX}}}[k]$ is

$$\beta_{\text{th}_{\text{DF/FDX,RLI}}}[k] = 1 + \frac{BC + A - \sqrt{4BFA + (BC + A)^2}}{2BF}, \quad (5.33)$$

$$A = \eta_{\text{pd,R}}^2 |H_{\text{fs}}^{\text{SR}}[k]|^2 \sigma_{\text{rx}}^2, \quad (5.34)$$

$$B = \eta_{\text{pd,D}}^2 |H_{\text{fs}}^{\text{RD}}[k]|^2, \quad (5.35)$$

$$C = \sigma_{\text{rx}}^2, \quad (5.36)$$

$$F = \eta_{\text{pd},\text{R}}^2 P |H_{\text{fe}}[k]|^2 |H_{\text{fs}}^{\text{RR}}[k]|^2. \quad (5.37)$$

Note that $\beta_{\text{th}_{\text{DF/FDX,RLI}}}[k] = 1$ (single transmission from S) when $F \rightarrow \infty$ which means that $\text{RLI} \rightarrow \infty$.

By contrast, if perfect RLI cancellation is assumed ($\text{RLI} \rightarrow 0$), $\beta_{\text{th}_{\text{DF/FDX}}}[k]$ is formulated as

$$\beta_{\text{th}_{\text{DF/FDX,nRLI}}}[k] = \left(1 + \frac{\eta_{\text{pd},\text{R}}^2 |H_{\text{fs}}^{\text{SR}}[k]|^2}{\eta_{\text{pd},\text{D}}^2 |H_{\text{fs}}^{\text{RD}}[k]|^2} \right)^{-1}. \quad (5.38)$$

In this case, note that if LoS between S and D exists, single transmission is likely the best choice ($\beta_{\text{opt}_{\text{DF/FDX}}}[k] = 1$). If not, the power allocation serves for boosting either the S→R or R→D path.

The traditional cooperative scheme in communications is managed by a central entity which processes and distributes data using a wired backhaul to allocate and transmit data through different APs. As an upper bound, we want to evaluate also this solution by optimizing its power allocation factor β_{bh} and compare it with our proposal. The total SNR when a wired backhaul-based cooperative scheme is formulated by

$$\Gamma_{\text{total,bh}}[k] \approx \frac{\eta_{\text{pd},\text{D}}^2 \xi^2 P |H_{\text{fe}}[k]|^2 \left| \sqrt{\beta_{\text{bh}}[k]} H_{\text{fs}}^{\text{SD}}[k] + \sqrt{1-\beta_{\text{bh}}[k]} H_{\text{fs}}^{\text{RD}}[k] \right|^2}{\sigma_{\text{rx}}^2}, \quad (5.39)$$

which is maximized with

$$\beta_{\text{opt,bh}}[k] = \left(1 + \frac{|H_{\text{fs}}^{\text{RD}}[k]|^2}{|H_{\text{fs}}^{\text{SD}}[k]|^2} \right)^{-1}. \quad (5.40)$$

Note that an optimal power allocation depends on how strong the channels between APs and user are.

Figure 5.4 represents the optimal value of β for $k=0$ against the ratio between SD and RD horizontal distances for the case of a wired backhaul (Figure 5.4a and 5.4b), DF/FDX-based wireless backhaul in presence of RLI (lower bound) (Figure 5.4c and 5.4d) and DF/FDX-based wireless backhaul with perfect RLI cancellation (Figure 5.4e and 5.4f). Thus, depending on the user location, a β_{opt} is recommended to be used in order to maximize the SNR. The parameters used are the same as the ones indicated in Figure 5.2. For the wired backhaul case when there is LoS between S and D (Figure 5.4a), note that the closer the user D to R, the lower the β_{opt}

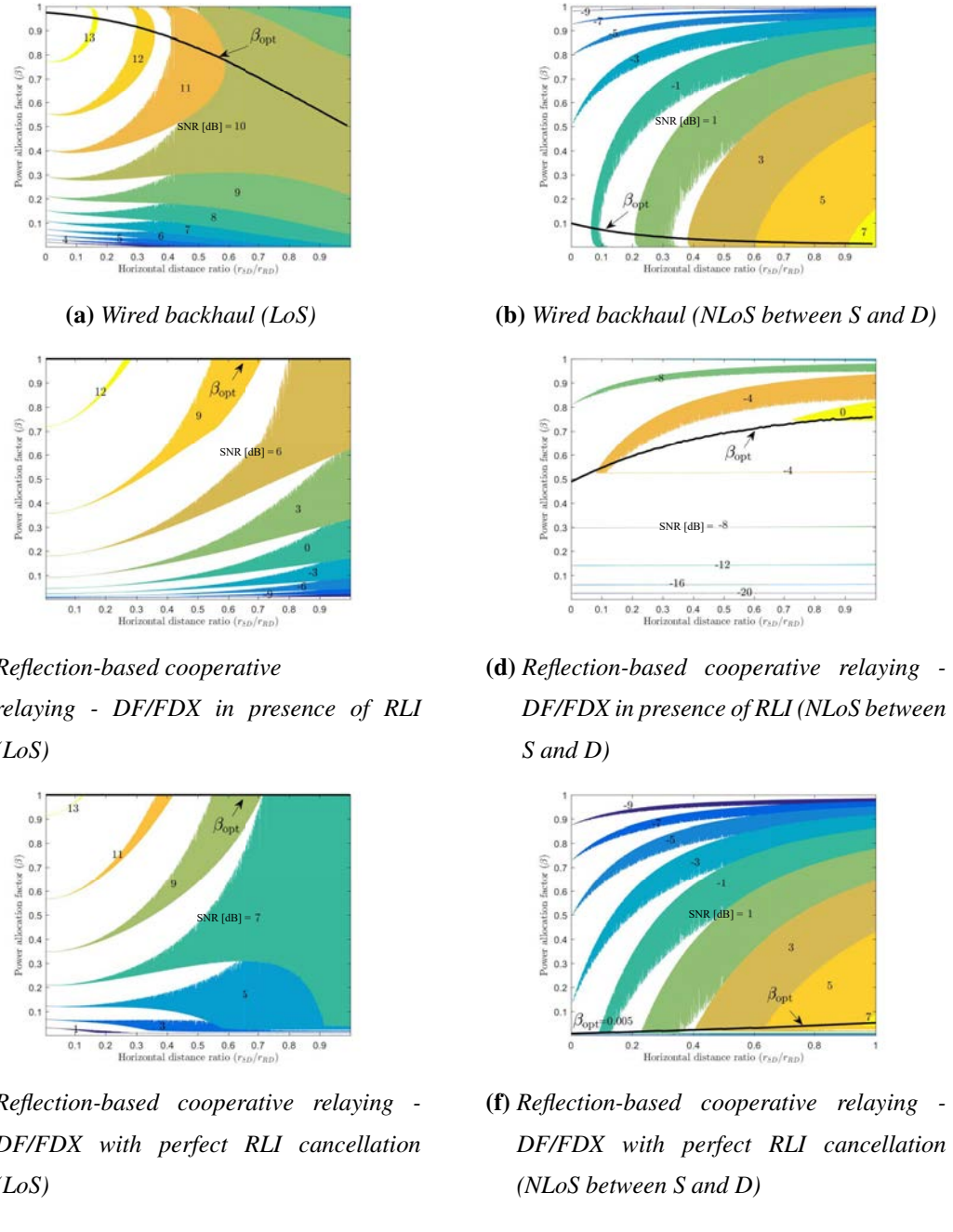


Figure 5.4: Representation of the optimum power allocation factor (β_{opt}) for $k = 0$ against the horizontal distance ratio that determines the user location when a wired backhaul (a)-(b), DF/FDX cooperative-relaying in presence of RLI (c)-(d) or DF/FDX cooperative-relaying with perfect RLI cancellation is utilized (e)-(f). Also, SNR [dB] values for every β and r_{SD}/r_{RD} are represented.

is, which means that a larger power must be allocated to R. When the user is just in the middle point of S and R (i.e. $r_{SD}/r_{RD} = 1$), an equal power allocation (EPA) must be carried out between S and R ($\beta_{opt} = 0.5$) in order to maximize the SNR at D. When NLoS occurs in the wired backhaul solution (Figure 5.4b), most of the power must be transmitted by R. Note that $\beta_{opt} \approx 0.1$ when the user is close to S, where some power must be allocated to S because reflections, which are the unique paths arriving from S to D in NLoS case, influence favorably.

By contrast, when the DF/FDX technique is employed in a scenario with LoS (Figure 5.4c and Figure 5.4e), no cooperation is recommended because the relay path (S→R) degrades considerably. When the S→D path is blocked and there is RLI (Figure 5.4d), most of the power must still be transmitted by S because the RLI signal received by R coming from its previous own transmission is very harmful. However, when the RLI is cancelled in R and the S→D path is blocked (Figure 5.4f), most of the power must be transmitted from R. The larger the horizontal distance ratio, the closer the user D to the relay is, which allows to decrease the power transmitted by R in favor of increasing the power transmitted by S and, as a consequence, improve the quality of the relay path (S→R). By comparing Figure 5.4d and Figure 5.4f, we realize how important is to perform RLI cancellation techniques at R, because a gain of around 7 dB can be obtained with an optimal power allocation factor β_{opt} .

In general, a larger SNR is obtained with the wired backhaul solution. However, it must be highlighted that, when using RLI cancellation techniques, a performance very close to the one obtained with a wired solution can be achieved (see Figure 5.4a-Figure 5.4e and Figure 5.4b-Figure 5.4f), i.e., a maximum SNR of around 13 dB and 7 dB can be obtained when there is LoS and NLoS between S and D, respectively, at both wired backhaul and DF/FDX with perfect RLI cancellation techniques. The wired solution is studied as a bound because of being the traditional and optimal solution, but it involves great difficulties in its deployment when a LiFi network is implemented.

5.3.4 LiFi squared-attocell network

Once the system analysis was detailed, the proposal will be analyzed in a realistic scenario. The most common network model is the square tessellation cellular model where the APs are distributed on a square lattice as shown in Figure 5.5. It involves a simple deployment, a proper illumination distribution and it easily adapts to rectangular-shaped rooms. Thus, this study investigates the performance of the proposal in this kind of scenarios.

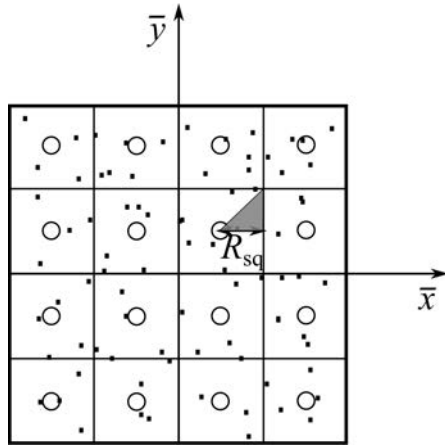


Figure 5.5: Square tessellation cellular model.

5.3.4.1 SNR and Spectral Efficiency analysis

The CDF of the SNR evaluated in terms of γ_{th} is expressed as

$$F_{\Gamma}(\gamma_{\text{th}}) = \Pr \{ \Gamma[k] < \gamma_{\text{th}} \} = \int_0^{R_{\text{sq}}} f_Y(y) \cdot \Pr \{ \Gamma[k] < \gamma_{\text{th}} | y \} dy, \quad (5.41)$$

where x and y are the user Cartesian coordinates with respect to the AP under study. Since the users are uniformly distributed in the cell, the joint probability density function of X and Y is

$$f_{X,Y}(x,y) = f_{X|Y}(x|y) \cdot f_Y(y) = \frac{1}{R_{\text{sq}} - y} \cdot \frac{1}{R_{\text{sq}}}, \quad x \in [y, R_{\text{sq}}), y \in [0, R_{\text{sq}}), \quad (5.42)$$

where R_{sq} is the square cell radius indicated in Figure 5.5. Thanks to the geometry of the cellular system, the study of the shaded region in Figure 5.5 is representative of the whole network.

If LoS in S→D exists, $\beta_{\text{opt}_{\text{DF/FDX}}}[k] = 1 \forall k$ and, with the help of the TD channel gain in case of LoS formulated in (2.38) and the SNR expression in (5.23), the total SNR in DF/FDX can be formulated as

$$\left. \Gamma_{\text{total}_{\text{DF/FDX}}}[k] \right|_{\text{LoS in S}\rightarrow\text{D}} = \Gamma_{\text{single}}[k] = \frac{U}{(x^2 + y^2 + d_v^2)^{m+3}}, \quad (5.43)$$

where $\Gamma_{\text{single}}[k]$ is the SNR obtained with single transmission from S to D equals to (5.12) and

$$U = \frac{\eta_{\text{pd},\text{D}}^2 \xi^2 P |H_{\text{fe}}[k]|^2 (m+1)^2 G_f^2 G_c^2 A_{\text{pd}}^2 d_v^{2m+2}}{4\pi^2 \sigma_{\text{rx}}^2}. \quad (5.44)$$

Thus,

$$\begin{aligned} \Pr \left\{ \Gamma_{\text{total}_{\text{DF/FDX}}}[k] \Big|_{\text{LoS in S} \rightarrow \text{D}} < \gamma_{\text{th}} \middle| Y \right\} &= \Pr \left\{ X^2 > \left(\frac{U}{\gamma_{\text{th}}} \right)^{1/(m+3)} - y^2 - d_v^2 \middle| Y \right\} \\ &= 1 - \frac{\sqrt{\left(\frac{U}{\gamma_{\text{th}}} \right)^{1/(m+3)} - y^2 - d_v^2} - y}{R_{\text{sq}} - y}. \end{aligned} \quad (5.45)$$

The CDF of the SNR, in case of DF/FDX and LoS in the S→D link, can finally be calculated as

$$\Pr \left\{ \Gamma_{\text{total}_{\text{DF/FDX}}}[k] \Big|_{\text{LoS in S} \rightarrow \text{D}} < \gamma_{\text{th}} \right\} = \int_0^{R_{\text{sq}}} \frac{1}{R_{\text{sq}}} \cdot \Pr \left\{ \Gamma_{\text{total}_{\text{DF/FDX}}}[k] \Big|_{\text{LoS in S} \rightarrow \text{D}} < \gamma_{\text{th}} \middle| Y \right\} dy. \quad (5.46)$$

When either DF/FDX is used and there is NLoS in the S→D link, or the wired backhaul solution is employed, $F_{\Gamma}(\gamma_{\text{th}})$ is obtained by numerical methods following the same reasoning as before.

Using AMC schemes, the spectral efficiency is expressed as

$$\text{SE} = \frac{1}{K} \sum_{k=1}^{\frac{K}{2}-1} \sum_{n=1}^N \epsilon[n] (\Pr \{ \Gamma[k] < \gamma_{\text{th}}[n+1] \} - \Pr \{ \Gamma[k] < \gamma_{\text{th}}[n] \}), \quad (5.47)$$

which is decreased by half when HDX mode is employed.

5.3.4.2 Time delay analysis

The proposed scheme involves a higher time delay in the system performance in comparison to the traditional wired backhaul solution. The time delay in the downlink transmission when a traditional wired backhaul scheme is deployed can be computed as

$$t_{\text{wired}} = \max \{ t_{\text{SD}}, t_{\text{RD}} \}, \quad (5.48)$$

where t_{SD} and t_{RD} are the time from the source S to the destination D, and from the relay R to the destination D, respectively, computed as d_{SD}/c_{speed} , and d_{RD}/c_{speed} , where d_{SD} and d_{RD} are the corresponding Euclidean distances from source and relay to the destination. By contrast, the time delay when using the proposed reflection-based technique is computed as

$$t_{\text{reflection-based}} = \max\{t_{SD}, t_{SR} + t_{RD} + \epsilon_{\text{process}}\}, \quad (5.49)$$

where t_{SR} is the time from the source S to the relay R through the reflection path, and $\epsilon_{\text{process}}$ is the processing time in the relay and UE, which is assumed to be negligible.

Parameter	Description	Value	Unit
R_{sq}	Squared cell radius	1.5	[m]
d_v	Vertical distance between AP and user	2.25	[m]
$P_{\text{opt,max}}$	Maximum optical power	22.4	[W]
$P_{\text{opt,min}}$	Minimum optical power	6.3	[W]
$\phi_{1/2}$	Half-power semi-angle	60	[°]
W	Modulation bandwidth	280	[MHz]
K	Number of subcarriers	512	
F_{fe}	Front-end device bandwidth factor	35.6	[MHz]
$\eta_{\text{pd,R}}$	Relay's PD responsivity	16	[A/W]
$\eta_{\text{pd,D}}$	User's PD responsivity	0.4	[A/W]
A_{pd}	PD physical area	8.72	[mm ²]
Ψ_{FoV}	Receiver field of view	90	[°]
G_f	Optical filter loss	1	
n_{ref}	Refractive index of concentrator	1.5	
κ	Clipping factor	3.4	
λ_{ue}	UE density	0.1	[user/m ²]
λ_b	Blocker density	0.1	[user/m ²]
ρ_{ceil}	Reflectance factor of ceil	0.8	
ρ_{floor}	Reflectance factor of floor	0.6	
ρ_{wall}	Reflectance factor of wall	0.65	
N_0	Noise power spectral density	10^{-21}	[A ² /Hz]

Table 5.1: System parameters in the reflection-based relaying study.

$\gamma_{\text{th}}[n]$ [dB]	Modulation	Code rate	$\epsilon[n]$ [bits/symbol]
-6 (γ_{min})	QPSK	0.076	0.1523
-5	QPSK	0.117	0.2344
-3	QPSK	0.188	0.3770
-1	QPSK	0.301	0.6016
1	QPSK	0.438	0.8770
3	QPSK	0.588	1.1758
5	16QAM	0.369	1.4766
8	16QAM	0.476	1.9141
9	16QAM	0.602	2.4063
11	64QAM	0.455	2.7305
12	64QAM	0.554	3.3223
14	64QAM	0.650	3.9023
16	64QAM	0.754	4.5234
18	64QAM	0.853	5.1151
20	64QAM	0.926	5.5547

Table 5.2: Adaptive modulation and coding SINR regions (reflection-based relaying study).

5.3.5 Results and discussion

The simulation parameters are described in Table 5.1. A realistic scenario with dimensions 12 x 12 x 3 m is considered, and a DCO-OFDM transmission scheme is chosen. The number of people with a UE is modeled by the variable λ_{ue} , whereas additional people without a user equipment are called blockers and are modeled by λ_b . Every person is approximated as a cylinder of a radius 0.15 m and a height of 1.75 m [Dong *et al.*, 2012]. The UE is located at a distance of 0.3 m separated from the associated human body, and the azimuth angle follows a uniform distribution $\mathcal{U}[0, 2\pi)$. The reflectance factors depend on the materials, colors and finishes that are employed on the surfaces. The typical values $[\rho_{\text{ceil}}; \rho_{\text{floor}}; \rho_{\text{wall}}] = [0.8; 0.6; 0.65]$ are selected in this work [BS 8300-1:2018/BS 8300-2:2018, 2018] [Taylor, 2009]. A spectrally efficient AMC is considered [Webster, 2010], whose operating regions are displayed in Table 5.2.

Figure 5.6 represents the SNR at DC ($k=0$) when using different transmission schemes: single transmission, DF/HDX, DF/FDX with perfect RLI cancellation and an equal power allocation

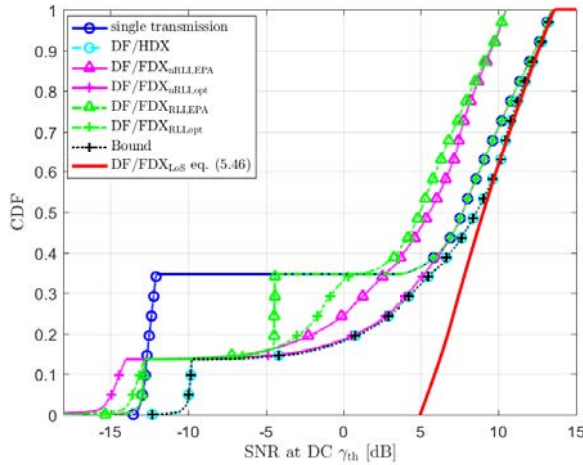


Figure 5.6: CDF of the SNR at subcarrier index $k = 0$ (DC) for different schemes with $\lambda_b = 0.1 \text{ user}/\text{m}^2$.

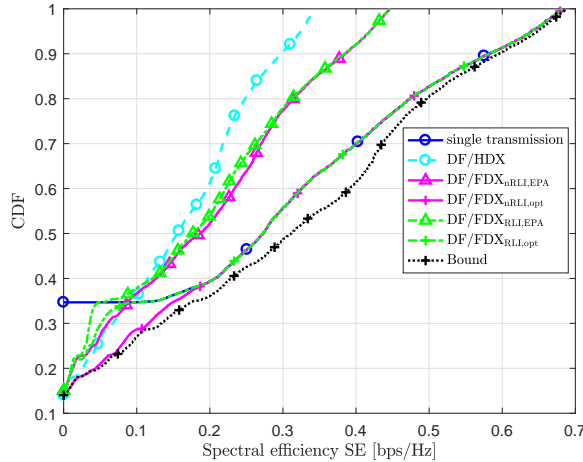


Figure 5.7: CDF of the spectral efficiency for different schemes.

(DF/FDX_{nRLI,EPA}), DF/FDX with perfect RLI cancellation and an optimum power allocation (DF/FDX_{nRLI,opt}), DF/FDX in presence of RLI and an equal power allocation (DF/FDX_{RLI,EPA}), DF/FDX in presence of RLI and an optimum power allocation (DF/FDX_{RLI,opt}) and an upper bound that is the traditional wired backhaul solution with an optimum power allocation. Note that the DF/HDX scheme provides the same performance in terms of SNR as the upper bound, since the maximum available power is used by every AP but using two time slots. DF/FDX_{nRLI,opt} and DF/FDX_{RLI,opt} offer a performance close to the upper bound at high SNR values, in which cases there is LoS between the source and destination and then single transmis-

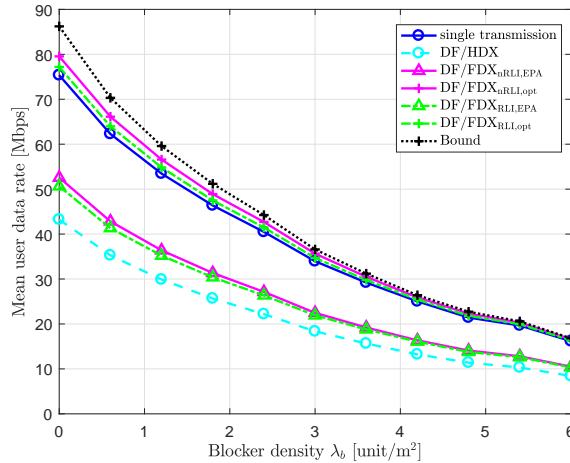


Figure 5.8: Mean user data rate vs. blocker density.

sion is the optimum power allocation. By contrast, the SNR performance of $\text{DF/FDX}_{\text{nRLI},\text{EPA}}$ and $\text{DF/FDX}_{\text{RLI},\text{EPA}}$ degrade around 3 dB at high SNR values. Most of the CDF curves show a steep degradation at some SNR value, which indicates the users that experience a LoS-link blockage with both serving APs (or the only AP in case of single transmission mode). The larger the SNR, the closer the curves to the upper bound. Besides, simulation results fit to the analytical $\text{DF/FDX}_{\text{LoS}}$ curve, which verifies the analytical results obtained in Section 5.3.4.1. The lower the SNR value, the more users in NLoS between S and D are and larger differences with the analytical $\text{DF/FDX}_{\text{LoS}}$ curve are produced.

Figure 5.7 represents the CDF of the spectral efficiency computed as (5.47). Again, single transmission can offer the best performance in users that experience LoS. However, a zero-spectral efficiency, which is equivalent to the outage probability, is obtained with a 35% probability. By contrast, the rest of the schemes decrease this outage probability to 15%. Note that these probabilities are the same as the percentage of users that experience NLoS in Figure 5.6 and suffer from a large degradation in SNR. The $\text{DF/FDX}_{\text{nRLI},\text{opt}}$ gets similar results to the upper bound, whereas DF/HDX suffers from a decrease by half of the spectral efficiency because of using two time slots per transmission.

Figure 5.8 shows the mean user data rate computed by (5.47) multiplied by the subcarrier bandwidth, when it is supposed to have a single user per source-relay association, varying the blocker density. As expected, the larger the blocker density, the lower the mean user data rate is that converges to a scenario where only reflections arrive to the destination. In this extreme situa-

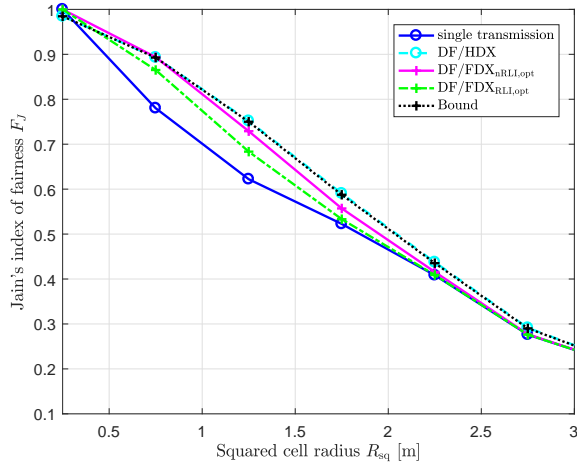


Figure 5.9: Jain's index of fairness vs. cell radius for different schemes.

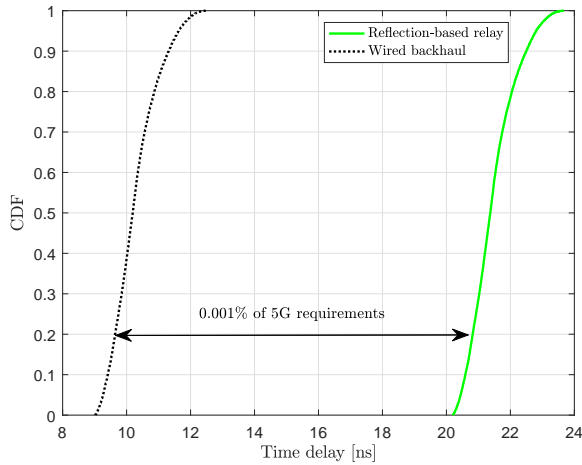


Figure 5.10: Representation of the penalization when using reflection-based relay techniques (end to end time delay).

tion, all curves converge to similar values. In low λ_b values, note that the proposed scenario is close to the upper bound if RLI cancellation and an optimum power allocation is employed. However, EPA schemes provide lower performances. The DF/HDX scheme, despite guaranteeing the best SNR, suffers from a decrease by half in the data rate since two time slots per channel use are employed.

The reflection-based cooperative schemes offer a fairer data rate performance as Figure 5.9 shows. This metric is the well-known Jain's index of fairness [Jain *et al.*, 1984] and evaluates whether users receive a fair share of system resources. The proposed reflection-based scheme

with RLI cancellation provides a performance very close to the upper bound represented by the traditional wired backhaul scheme.

Finally, it is interesting to evaluate how long the proposed scheme delays the system performance. As Figure 5.10 represents, the proposed system requires around 10 ns more in comparison to the traditional wired backhaul scheme, which is a 0.001% of the allowable end-to-end system delay in 5G systems (1 ms) [ETSI TS 122 261 V15.6.0, 2018], i.e., it is negligible and it is not an impediment to satisfy such requirement.

5.4 Summary

This Chapter proposed and evaluated an alternative to the traditional wired-backhaul system. Since this wired system involves a complex installation and it is not scalable in many cases, an ad-hoc wireless backhaul system was proposed that simplifies its installation without affecting the system performance. This system is based on reflections in the floor to transfer information to the neighboring APs that act as relays. The AF and DF relaying techniques were evaluated using both FDX and HDX transmission modes. It was demonstrated that this system, working in the DF/FDX mode, can achieve a very similar SNR and data rate performance to the wired backhaul counterpart, as long as an optimum power allocation and RLI cancellation techniques are employed at the relay. Analytical and simulation SNR results were presented, and data rate, spectral efficiency and Jain's index of fairness were evaluated. Finally, the additional time delay required to perform the proposed system was demonstrated to be negligible to satisfy the 5G requirements.

Chapter 6

Conclusions and future research

6.1 Summary and conclusions

In this Thesis, fundamental studies on physical layer issues of visible light communication have been presented. The studies include investigations about both single-cell/point-to-point and multi-cell related issues. Regarding the VLC point-to-point physical layer issues, it is included a study of the non-linearities of the LED's transfer function and its effect in the TD transmit signal when O-OFDM schemes are employed. Besides, a study of the downlink performance viability of O-OFDM in single-cell outdoor VLC scenarios was presented. Multi-cell VLC scenarios are required to provide a seamless coverage. Thus, cooperative transmission schemes were proposed in indoor scenarios to mitigate the LoS-link blockage problem and to reduce the levels of inter-cell interference. Cooperative scheme proposals were presented using single-carrier and multi-carrier transmission in a simple corridor scenario and a hexagonal cell tessellation, respectively. Finally, a cooperative transmission scheme was proposed based on relaying techniques using the reflections produced in the floor and, in this way, avoiding the use of wires in order to simplify the installation of VLC systems.

After a background of VLC detailed in Chapter 2, Chapter 3 addressed two main issues in a point-to-point VLC system. On the one hand, **the effect of the non-linear LED's transfer function in the TD transmitted signal was studied**, and a proposal to mitigate this impairment was presented. To avoid the use of a great back-off or a detrimental clipping at the input of the LED, PAPR/CM reduction techniques must be invoked to make the input signal work within the linear region of the LED. **A CM reduction technique based on ANFIS, called RCM-ANFIS, was proposed.** Using a proper combination of optimized training models, the RCM-ANFIS obtains efficient power derated DCO-OFDM signals. Once trained, the ANFIS models can work autonomously, providing efficient DCO-OFDM signals with a reduction of 8.9 dB with respect to the original DCO-OFDM signal at $\text{CCDF} = 10^{-4}$. Since the clipping effect is mitigated due to this power derating technique, the output transmit signal improves a 12 % in EVM at the most for a fixed IBO value. On fixing an EVM value, IBO gains

are obtained with respect to state-of-the-art techniques, which makes transmitted signal take advantage of the LED linear region to a greater extent. It produces ICE gains above 35 % with respect to conventional DCO-OFDM signals. Finally, improvements in BER are also obtained. **For all the studied parameters and figures of merit, the implementation of this technique in a DCO-OFDM VLC system involves a better efficiency between the communication capacity and the illumination level.** On the other hand, the enormous skylight and sunlight produced in outdoor environments could blind the receiver and prevent the VLC performance in such environments. **An analytical study of O-OFDM in outdoor VLC scenarios was provided, where its functioning is demonstrated if a proper modulation bandwidth adaptation is configured.** The shot noise produced by the received background illumination increases with the modulation bandwidth, hence the optimum sampling frequencies and bandwidths were found for specific environmental conditions. A comparison between ACO-OFDM and DCO-OFDM in such conditions was carried out, showing that **ACO-OFDM can perform at higher modulation bandwidths than DCO-OFDM for the same outage probability, but that DCO-OFDM provides better performance in terms of mean cell data rate.**

In Chapter 4, several VLC multi-cell scenarios were considered to evaluate the downlink system performance when invoking novel proposed cooperative transmission schemes. Firstly, **the effect of LoS-link blockage was evaluated in a simple corridor scenario, and a cooperative scheme was proposed when a single-carrier modulation is used.** This proposed scheme is based on a PPDM using OOK, where the neighboring APs cooperate transmitting information to users located at adjacent cells. It presents an increased reliability against LoS-link blockages, but **an up-to-date multi-carrier modulation scheme where a generic large scenario arranged in hexagonal cells must be considered.** A preliminary study on this was made, where neighboring APs jointly coordinate their transmission using DCO-OFDM split into two MAMs, one in the real part and the other on the imaginary part of the DCO-OFDM symbol, in addition to a TDMA to decrease the inter-cell interference. In absence of LoS-link blockage, the SINR performance at DC obtained by the cooperating proposal is better than the one obtained by transmission techniques without cooperation. Concerning the mean cell data rate, it was observed that it decreases due to the use of a TDMA among neighboring APs and uncoded MAM AMC. When LoS-link blockage occurs, the SINR performance decreases but, in return, **it is possible to guarantee a minimum data rate to all active users in the system (as opposed to single-cell transmission schemes).** In view of the results, the potential of cooperative transmission schemes in O-OFDM schemes is notable, but the use of TDMA decreases the cell

data rate considerably and new alternatives must be investigated.

As a solution, the RGB(Y) illumination technology in addition to WDM are used to increase the flexibility and communication resources in the optical wireless cellular network to serve multiple users located at different places. Thus, **a thorough study of the different resource allocation patterns for multi-cell cooperative transmission schemes, when tri- and tetrachromatic LEDs and O-OFDM are used, was presented**. Firstly, **guidelines were derived for maintaining the same spatial distribution of the SINR in every sector of the multi-cell environment** in case of single-point (non-cooperative) and multi-point (cooperative) transmission. These guidelines were formulated in the form of six Lemmas that determine: the number of possible cells that can conform a cluster without cooperation, also called cluster size without cooperation; the number of sectors in which a cell can be divided; the orientation of such sectors within a cell; the minimum number of orthogonal resources (number of colors per LED AP, number of frequency sub-bands per color and number of sectors per cell) necessary to perform cooperation among APs; the maximum number of cooperating APs in the same region and the maximum number of sectors within such a region; and finally, the cluster size when cooperation is performed. If these Lemmas are satisfied, the study of one sector is representative for the whole network, which simplifies the whole system performance greatly. Secondly, an evaluation of the achievable data rate was presented for each of the patterns that comply with the SINR homogeneity property satisfying the aforementioned Lemmas. It was evaluated under different working conditions in terms of cell radius length, half-power semi-angle of the LEDs and blockage probability. Furthermore, **working conditions were thoroughly studied in order to determine the transmission schemes that comply with the illumination requirements**, which are based on: the average illuminance in the whole indoor area that must be higher than a threshold value; and the illuminance uniformity defined as the ratio between the minimum illuminance level to the average illuminance in the area, which must be high enough such that people would not observe notably different lighting levels in the same room. As a conclusion, **there is no single resource allocation scheme that provides the highest mean cell data rate for all network settings**. Extensive simulation results were presented demonstrating that, **with a correct network planning in the allocation of resources per AP, the mean cell data rate can be improved considerably and cooperative schemes offer important gains even in case of LoS conditions**. Besides, it was shown that, in presence of obstacles that may block the LoS from the serving AP to the user, the implementation of multi-point cooperative transmission schemes is essential to guarantee a minimum data rate. These resource reuse patterns can be

used directly by the research community if it is desired to provide a homogeneous coverage. Besides, the working conditions will influence the selection of the resource reuse pattern to optimize the system performance.

In Chapter 5, the difficulties of using a wired backhaul in multi-cell VLC scenarios were presented. A wireless backhauling is desired to simplify the deployment of a multi-cell VLC system, in addition to increase the flexibility when the system topology must be changed. To this effect, **it was proposed an ad-hoc wireless backhaul based on the reflections produced in the floor to communicate with neighboring APs**. Thus, this neighboring AP cooperates by using relaying techniques such as amplify-and-forward and decode-and-forward. A comparison of these two relaying techniques was expounded when both half-duplex and full-duplex transmission modes are invoked. In addition, it was presented an optimization of the power allocation factor as a function of the user location and its situation (LoS or non-LoS). It was demonstrated that **this system, working in the decode-and-forward and full-duplex mode, can achieve a very similar SNR and data rate performance to the traditional wired backhaul system**, as long as an optimum power allocation and RLI cancellation techniques are employed at the relay. Analytical and simulation SNR results were presented, and data rate, spectral efficiency and Jain's index of fairness were evaluated. Finally, the additional time delay required to perform the proposed system was demonstrated to be negligible to satisfy the 5G requirements.

6.2 Future research

Following the bases presented in this Thesis, future research directions can be addressed:

- Multi-cell, heterogeneous LED-based systems and advanced communication techniques in outdoor scenarios. For the practical employment of VLC schemes in outdoor scenarios, more robust schemes relying on strong forward error correction-aided (FEC-aided) automatic repeat request (ARQ) schemes and power-efficient modulation arrangements have to be developed, using for example M-ary orthogonal modulation. Besides, an analysis in a multi-cell scenario with a realistic heterogeneity in LED-based systems capable of transmitting information can be considered.
- Least number of assumptions. A great number of factors have been considered in the different studies presented along this Thesis. However, some assumptions have been

supposed either to isolate the problem considering only the relevant factors and make the problem tractable, or because of the unavailability of mathematical or experimental demonstration in the literature and then considering a widespread reasonable assumption. Thus, general studies and findings without limitations can be addressed. Besides, most of the statistic and simulation results presented in this Thesis strongly depend on the scenario parameters such as dimensions, orientation and location of transmitters and receivers. Therefore, a comprehensive study isolating the results from the scenario parameters can be implemented.

- User mobility and uplink consideration. Since a multi-cell VLC scenario is composed by many small cells, the management of user mobility is challenging due to the required multiple handover procedures, which creates extra traffic and complexity in the communication algorithms. This scenario can be considered in the cooperative transmission schemes presented in this Thesis and a new evaluation of them can be studied. In addition, although the role of the uplink is not fundamental in the static resource allocation schemes presented in this Thesis, it gains importance if user mobility is incorporated. Thus, a study of the uplink and the influence of LoS-link blockage on it can be tackled.
- Imperfect synchronization among cooperating APs. A perfect synchronization among APs is assumed in the proposed cooperative transmission schemes. However, this is difficult to fulfill and cooperating signals coming from different APs will reach the receiver with different time delays. This phenomenon creates frequency selectivity at the receiver. Thus, a study of the channel characteristics in case of cooperation among multiple APs can be a future research direction.
- Experimental research. The studies presented in this Thesis are mainly based on analytics and simulations. Thus, experimental results will add value to the research, and validate and consolidate the outcomes here presented.

Bibliography

- [3GPP TR 36.814, V9.0.0, 2010] 3GPP TR 36.814, V9.0.0 (2010). Further advancements for EUTRA physical layer aspects.
- [Abdelhady *et al.*, 2019] Abdelhady, A. M., Amin, O., Chaaban, A., Shihada, B., and Alouini, M. (2019). Downlink resource allocation for dynamic TDMA-based VLC systems. *IEEE Trans. Wireless Commun.*, 18(1):108–120.
- [Adnan-Qidan *et al.*, 2019] Adnan-Qidan, A., Morales Céspedes, M., and García Armada, A. (2019). User-centric blind interference alignment design for visible light communications. *IEEE Access*, 7:21220–21234.
- [Ahmed *et al.*, 2014] Ahmed, A., Boulahia, L. M., and Gaiti, D. (2014). Enabling vertical handover decisions in heterogeneous wireless networks: A state-of-the-art and a classification. *IEEE Commun. Surveys Tuts.*, 16(2):776–811.
- [Aik *et al.*, 2008] Aik, L., Yogan, S., and Jayakumar, O. (2008). A study of neuro-fuzzy system in approximation-based problems. *MATEMATIKA*, 23(2):113–130.
- [Almeroth *et al.*, 2011] Almeroth, B., Fehske, A. J., Fettweis, G., and Zimmermann, E. (2011). Analytical interference models for the downlink of a cellular mobile network. In *Proc. IEEE Globecom Workshops*, pages 739–743.
- [Andrews *et al.*, 2014] Andrews, J. G., Buzzi, S., Choi, W., Hanly, S. V., Lozano, A., Soong, A. C. K., and Zhang, J. C. (2014). What will 5G be? *IEEE J. Sel. Areas Commun.*, 32(6):1065–1082.
- [Andrews *et al.*, 2012] Andrews, J. G., Claussen, H., Dohler, M., Rangan, S., and Reed, M. C. (2012). Femtocells: Past, present, and future. *IEEE J. Sel. Areas Commun.*, 30(3):497–508.
- [Armstrong and Lowery, 2006] Armstrong, J. and Lowery, A. J. (2006). Power efficient optical OFDM. *Electron. Lett.*, 42(6):370–372.
- [Barker and Boucouvalas, 1998] Barker, P. and Boucouvalas, A. C. (1998). Performance modeling of the IrDA protocol for infrared wireless communications. *IEEE Commun. Mag.*, 36(12):113–117.
- [Barros *et al.*, 2012] Barros, D. J. F., Wilson, S. K., and Kahn, J. M. (2012). Comparison of orthogonal frequency-division multiplexing and pulse-amplitude modulation in indoor optical wireless links. *IEEE Trans. Commun.*, 60(1):153–163.
- [Barry *et al.*, 1993] Barry, J. R., Kahn, J. M., Krause, W. J., Lee, E. A., and Messerschmitt, D. G. (1993). Simulation of multipath impulse response for indoor wireless optical channels. *IEEE J. Sel. Areas Commun.*, 11(3):367–379.
- [Bell, 1880] Bell, A. G. (1880). Selenium and the photophone. *Nature*, 22(569):500–503.

Bibliography

- [Bhushan *et al.*, 2014] Bhushan, N., Li, J., Malladi, D., Gilmore, R., Brenner, D., Damnjanovic, A., Sukhavasi, R. T., Patel, C., and Geirhofer, S. (2014). Network densification: the dominant theme for wireless evolution into 5G. *IEEE Commun. Mag.*, 52(2):82–89.
- [Bird and Riordan, 1986] Bird, R. E. and Riordan, C. (1986). Simple solar spectral model for direct and diffuse irradiance on horizontal and tilted planes at the Earth’s surface for cloudless atmospheres. *J. Climate Appl. Meteor.*, 25(1):87–97.
- [Bouchet *et al.*, 2010] Bouchet, O., Porcon, P., Wolf, M., Grobe, L., Walewski, J. W., Nerreter, S., Langer, K., Fernández, L., Vucic, J., Kamalakis, T., Ntogari, G., and Gueutier, E. (2010). Visible-light communication system enabling 73 Mb/s data streaming. In *2010 IEEE Globecom Workshops*, pages 1042–1046.
- [Brennan, 1959] Brennan, D. G. (1959). Linear diversity combining techniques. *Proc. IRE*, 47(6):1075–1102.
- [BS 8300-1:2018/BS 8300-2:2018, 2018] BS 8300-1:2018/BS 8300-2:2018 (2018). Design of an accessible and inclusive built environment. Buildings/External environment. Code of practice.
- [Carruthers and Kahn, 1996] Carruthers, J. B. and Kahn, J. M. (1996). Multiple-subcarrier modulation for nondirected wireless infrared communication. *IEEE J. Sel. Areas Commun.*, 14(3):538–546.
- [Chen *et al.*, 2016] Chen, C., Basnayaka, D. A., and Haas, H. (2016). Downlink performance of optical attocell networks. *J. Lightw. Technol.*, 34(1):137–156.
- [Chen *et al.*, 2018] Chen, C., Basnayaka, D. A., Wu, X., and Haas, H. (2018). Efficient analytical calculation of non-line-of-sight channel impulse response in visible light communications. *J. Lightw. Technol.*, 36(9):1666–1682.
- [Chen and Haas, 2017] Chen, C. and Haas, H. (2017). Performance evaluation of downlink cooperative multipoint joint transmission in LiFi systems. In *Proc. IEEE Globecom Workshops*, pages 1–6.
- [Chen *et al.*, 2013] Chen, C., Tsonev, D., and Haas, H. (2013). Joint transmission in indoor visible light communication downlink cellular networks. In *Proc. IEEE Globecom Workshops*, pages 1127–1132.
- [Chen *et al.*, 2015] Chen, C., Videv, S., Tsonev, D., and Haas, H. (2015). Fractional frequency reuse in DCO-OFDM-based optical attocell networks. *J. Lightw. Technol.*, 33(19):3986–4000.
- [Chen and Rui, 2012] Chen, Q. and Rui, X. (2012). On the performance of full-duplex relaying under fading loop interference channel. In *IET International Conference on Information Science and Control Engineering 2012*, pages 1–4.
- [Chen and Jiang, 2017] Chen, X. and Jiang, M. (2017). Adaptive statistical Bayesian MMSE channel estimation for visible light communication. *IEEE Trans. Signal Process.*, 65(5):1287–1299.

- [Chun *et al.*, 2016] Chun, H., Rajbhandari, S., Faulkner, G., Tsonev, D., Xie, E., McKendry, J. J. D., Gu, E., Dawson, M. D., O'Brien, D. C., and Haas, H. (2016). LED based wavelength division multiplexed 10 Gb/s visible light communications. *J. Lightw. Technol.*, 34(13):3047–3052.
- [Chung and Oh, 2013] Chung, Y. H. and Oh, S. (2013). Efficient optical filtering for outdoor visible light communications in the presence of sunlight or artificial light. In *Proc. Int. Symp. on Intell. Signal Process. and Commun. Syst.*, pages 749–752.
- [Cisco Visual Networking Index, 2018] Cisco Visual Networking Index (2018). Forecast and Trends, 2017–2022. *CISCO, White Paper*.
- [Căilean and Dimian, 2017] Căilean, A. M. and Dimian, M. (2017). Current challenges for visible light communications usage in vehicle applications: A survey. *IEEE Commun. Surveys Tuts.*, 19(4):2681–2703.
- [Cui *et al.*, 2016] Cui, L., Tang, Y., Jia, H., Luo, J., and Gnade, B. (2016). Analysis of the multichannel WDM-VLC communication system. *J. Lightw. Technol.*, 34(24):5627–5634.
- [Da-Shan Shiu and Kahn, 1999] Da-Shan Shiu and Kahn, J. M. (1999). Differential pulse-position modulation for power-efficient optical communication. *IEEE Trans. Commun.*, 47(8):1201–1210.
- [Dahlman *et al.*, 1998] Dahlman, E., Gudmundson, B., Nilsson, M., and Skold, A. (1998). UMTS/IMT-2000 based on wideband CDMA. *IEEE Commun. Mag.*, 36(9):70–80.
- [Dardari *et al.*, 2000] Dardari, D., Tralli, V., and Vaccari, A. (2000). A theoretical characterization of nonlinear distortion effects in OFDM systems. *IEEE Trans. Commun.*, 48(10):1755–1764.
- [Delgado *et al.*, 2010] Delgado, F., Quintana, I., Rufo, J., Rabada, J. A., Quintana, C., and Perez-Jimenez, R. (2010). Design and implementation of an Ethernet-VLC interface for broadcast transmissions. *IEEE Commun. Lett.*, 14(12):1089–1091.
- [Demir *et al.*, 2017] Demir, M. S., Miramirkhani, F., and Uysal, M. (2017). Handover in VLC networks with coordinated multipoint transmission. In *Proc. IEEE International Black Sea Conference on Communications and Networking*, pages 1–5.
- [Dimitrov *et al.*, 2012] Dimitrov, S., Sinanovic, S., and Haas, H. (2012). Clipping noise in OFDM-based optical wireless communication systems. *IEEE Trans. Commun.*, 60(4):1072–1081.
- [Dong *et al.*, 2012] Dong, K., Liao, X., and Zhu, S. (2012). Link blockage analysis for indoor 60GHz radio systems. *Electron. Lett.*, 48(23):1506–1508.
- [Elgala *et al.*, 2009] Elgala, H., Mesleh, R., and Haas, H. (2009). Indoor broadcasting via white LEDs and OFDM. *IEEE Trans. Consum. Electron.*, 55(3):1127–1134.
- [Elgala *et al.*, 2010] Elgala, H., Mesleh, R., and Haas, H. (2010). An LED model for intensity-modulated optical communication systems. *IEEE Photon. Technol. Lett.*, 22(11):835–837.

Bibliography

- [Elgala *et al.*, 2011] Elgala, H., Mesleh, R., and Haas, H. (2011). Indoor optical wireless communication: potential and state-of-the-art. *IEEE Commun. Mag.*, 49(9):56–62.
- [EN 12464-1:2002 E, 2002] EN 12464-1:2002 E (2002). Light and lighting - Lighting of work places - Part 1: Indoor work places.
- [Estrada Jimenez *et al.*, 2019] Estrada Jimenez, J. C., Genoves Guzman, B., Fernandez-Getino Garcia, M. J., and Gil Jimenez, V. P. (2019). Superimposed training-based channel estimation for MISO optical-OFDM VLC. *IEEE Trans. Veh. Technol.*, pages 1–1.
- [ETSI EN 302 755, 2012] ETSI EN 302 755 (2012). Digital video broadcasting (DVB); frame structure channel coding and modulation for a second generation digital terrestrial television broadcasting system (DVB-T2). 1.3.1.
- [ETSI TS 122 261 V15.6.0, 2018] ETSI TS 122 261 V15.6.0 (2018). 5G; Service requirements for next generation new services and markets.
- [ETSI TS 136 300 V13.2.0, 2016] ETSI TS 136 300 V13.2.0 (2016). Evolved universal terrestrial radio access (E-UTRA) and evolved universal terrestrial radio access network (E-UTRAN).
- [Fidler *et al.*, 2010] Fidler, F., Knapek, M., Horwath, J., and Leeb, W. R. (2010). Optical communications for high-altitude platforms. *IEEE J. Sel. Topics Quantum Electron.*, 16(5):1058–1070.
- [Garcia Doblado *et al.*, 2015] Garcia Doblado, J., Cinta Oria Oria, A., Baena-Lecuyer, V., Lopez, P., and Perez-Calderon, D. (2015). Cubic metric reduction for DCO-OFDM visible light communication systems. *J. Lightw. Technol.*, 33(10):1971–1978.
- [Genovés Guzmán *et al.*, 2018a] Genovés Guzmán, B., Dowhuszko, A. A., Gil Jiménez, V. P., and Pérez-Neira, A. I. (2018a). Robust cooperative multicarrier transmission scheme for optical wireless cellular networks. *IEEE Photon. Technol. Lett.*, 30(2):197–200.
- [Genovés Guzmán *et al.*, 2018b] Genovés Guzmán, B., Gil Jiménez, V. P., Aguayo-Torres, M. C., Haas, H., and Hanzo, L. (2018b). Downlink performance of optical OFDM in outdoor visible light communication. *IEEE Access*, 6:76854–76866.
- [Genovés Guzmán *et al.*, 2015] Genovés Guzmán, B., Lancho Serrano, A., and Gil Jiménez, V. P. (2015). Cooperative optical wireless transmission for improving performance in indoor scenarios for visible light communications. *IEEE Trans. Consum. Electron.*, 61(4):393–401.
- [Genovés Guzmán *et al.*, 2019a] Genovés Guzmán, B., Chen, C., Gil Jiménez, V. P., Hanzo, L., and Haas, H. (2019a). Reflection-based relaying techniques in visible light communications. In preparation.
- [Genovés Guzmán *et al.*, 2019b] Genovés Guzmán, B., Dowhuszko, A. A., Gil Jiménez, V. P., and Pérez-Neira, A. I. (2019b). On the allocation of resources for cooperative transmission schemes in optical wireless cellular networks. submitted to *IEEE Trans. Wireless Commun.*
- [Gfeller and Bapst, 1979] Gfeller, F. R. and Bapst, U. (1979). Wireless in-house data communication via diffuse infrared radiation. *Proc. IEEE*, 67(11):1474–1486.

- [Gil Jimenez *et al.*, 2011] Gil Jimenez, V. P., Jabrane, Y., Garcia Armada, A., Said, B. A. E., and Ouahman, A. A. (2011). Reduction of the envelope fluctuations of multi-carrier modulations using adaptive neural fuzzy inference systems. *IEEE Trans. Commun.*, 59(1):19–25.
- [Giustiniano *et al.*, 2012] Giustiniano, D., Tippenhauer, N. O., and Mangold, S. (2012). Low-complexity visible light networking with LED-to-LED communication. In *2012 IFIP Wireless Days*, pages 1–8.
- [Goldsmith, 2005] Goldsmith, A. (2005). *Wireless Communications*. Cambridge University Press, New York, NY, USA.
- [Haas, 2013] Haas, H. (2013). High-speed wireless networking using visible light. *SPIE Newsroom*.
- [Haas *et al.*, 2016] Haas, H., Yin, L., Wang, Y., and Chen, C. (2016). What is LiFi? *J. Lightw. Technol.*, 34(6):1533–1544.
- [Han *et al.*, 2014] Han, J., Baek, J., Jeon, S., and Seo, J. (2014). Cooperative networks with amplify-and-forward multiple-full-duplex relays. *IEEE Trans. Wireless Commun.*, 13(4):2137–2149.
- [Han and Lee, 2005] Han, S. H. and Lee, J. H. (2005). An overview of peak-to-average power ratio reduction techniques for multicarrier transmission. *IEEE Wireless Commun.*, 12(2):56–65.
- [Hanzo *et al.*, 2012] Hanzo, L., Haas, H., Imre, S., O’Brien, D., Rupp, M., and Gyongyosi, L. (2012). Wireless myths, realities, and futures: From 3G/4G to optical and quantum wireless. *Proc. IEEE*, 100(Special Centennial Issue):1853–1888.
- [Hwang *et al.*, 2012] Hwang, J., Yu, S. M., Kim, S., and Jantti, R. (2012). On the frequency allocation for coordinated multi-point joint transmission. In *Proc. IEEE Vehicular Technology Conference*, pages 1–5.
- [IEEE 802.11bb, 2017] IEEE 802.11bb (2017). IEEE 802.11 Light Communication TG.
- [IEEE Std. 802.15.7-2011, 2011] IEEE Std. 802.15.7-2011 (2011). IEEE Standard for Local and Metropolitan Area Networks—Part 15.7: Short-Range Wireless Optical Communication Using Visible Light.
- [Irmer *et al.*, 2011] Irmer, R., Droste, H., Marsch, P., Grieger, M., Fettweis, G., Brueck, S., Mayer, H., Thiele, L., and Jungnickel, V. (2011). Coordinated multipoint: Concepts, performance, and field trial results. *IEEE Commun. Mag.*, 49(2):102–111.
- [Islim *et al.*, 2018] Islim, M. S., Videv, S., Safari, M., Xie, E., McKendry, J. J. D., Gu, E., Dawson, M. D., and Haas, H. (2018). The impact of solar irradiance on visible light communications. *J. Lightw. Technol.*, 36(12):2376–2386.
- [Jabrane *et al.*, 2010] Jabrane, Y., Jimenez, V. P. G., Armada, A. G., Said, B. A. E., and Ouahman, A. A. (2010). Evaluation of the effects of pilots on the envelope fluctuations reduction based on neural fuzzy systems. In *2010 IEEE 11th International Workshop on Signal Processing Advances in Wireless Communications*, pages 1–5.

Bibliography

- [Jain *et al.*, 1984] Jain, R., Chiu, D., and Hawe, W. (1984). A quantitative measure of fairness and discrimination for resource allocation in shared computer system. *DEC Technical Report 301*.
- [Jang, 1993] Jang, J.-S. (1993). ANFIS: Adaptive-Network-based Fuzzy Inference System. *IEEE Trans. Syst., Man, Cybern.*, 23(3):665–685.
- [Jin *et al.*, 2015] Jin, H., Jin, S., Chen, L., Cen, S., and Yuan, K. (2015). Research on the lighting performance of LED street lights with different color temperatures. *IEEE Photon. J.*, 7(6):1–9.
- [Johnson *et al.*, 1994] Johnson, N. L., Kotz, S., and Balakrishnan, N. (1994). *Continuous univariate distributions*, volume 1. John Wiley & Sons Ltd., 2nd edition.
- [Jungnickel *et al.*, 2014] Jungnickel, V., Manolakis, K., Zirwas, W., Panzner, B., Braun, V., Lossow, M., Sternad, M., Apelfrojd, R., and Svensson, T. (2014). The role of small cells, coordinated multipoint, and massive MIMO in 5G. *IEEE Commun. Mag.*, 52(5):44–51.
- [Kahn and Barry, 1997] Kahn, J. M. and Barry, J. R. (1997). Wireless infrared communications. *Proc. IEEE*, 85(2):265–298.
- [Kamoun and Mazet, 2007] Kamoun, M. and Mazet, L. (2007). Base-station selection in cooperative single frequency cellular network. In *2007 IEEE 8th Workshop on Signal Processing Advances in Wireless Communications*, pages 1–5.
- [Kazemi and Haas, 2016] Kazemi, H. and Haas, H. (2016). Downlink cooperation with fractional frequency reuse in DCO-OFDMA optical attocell networks. In *Proc. IEEE International Conference on Communications*, pages 1–6.
- [Kazemi *et al.*, 2019] Kazemi, H., Safari, M., and Haas, H. (2019). A wireless optical backhaul solution for optical attocell networks. *IEEE Trans. Wireless Commun.*, 18(2):807–823.
- [Khalid *et al.*, 2012] Khalid, A. M., Cossu, G., Corsini, R., Choudhury, P., and Ciaramella, E. (2012). 1-Gb/s transmission over a phosphorescent white LED by using rate-adaptive discrete multitone modulation. *IEEE Photon. J.*, 4(5):1465–1473.
- [Khalighi and Uysal, 2014] Khalighi, M. A. and Uysal, M. (2014). Survey on free space optical communication: A communication theory perspective. *IEEE Commun. Surveys Tuts.*, 16(4):2231–2258.
- [Kinoshita *et al.*, 2014] Kinoshita, M., Yamazato, T., Okada, H., Fujii, T., Arai, S., Yendo, T., and Kamakura, K. (2014). Motion modeling of mobile transmitter for image sensor based I2V-VLC, V2I-VLC, and V2V-VLC. In *Proc. IEEE Globecom Workshops*, pages 450–455.
- [Kizilirmak *et al.*, 2015] Kizilirmak, R. C., Narmanlioglu, O., and Uysal, M. (2015). Relay-assisted OFDM-based visible light communications. *IEEE Trans. Commun.*, 63(10):3765–3778.
- [Knobloch, 2015] Knobloch, F. (2015). Channel gain and frame error rate for optical street lighting communication. In *Proc. Int. Conf. Telecommun.*, pages 1–5.

- [Komine and Nakagawa, 2004] Komine, T. and Nakagawa, M. (2004). Fundamental analysis for visible-light communication system using LED lights. *IEEE Trans. Consum. Electron.*, 50(1):100–107.
- [Larsson *et al.*, 2014] Larsson, E. G., Edfors, O., Tufvesson, F., and Marzetta, T. L. (2014). Massive MIMO for next generation wireless systems. *IEEE Commun. Mag.*, 52(2):186–195.
- [Le Minh *et al.*, 2009] Le Minh, H., O’Brien, D., Faulkner, G., Zeng, L., Lee, K., Jung, D., Oh, Y., and Won, E. T. (2009). 100-Mb/s NRZ visible light communications using a post-equalized white LED. *IEEE Photon. Technol. Lett.*, 21(15):1063–1065.
- [Lee *et al.*, 2009] Lee, I. E., Sim, M. L., and Kung, F. W. L. (2009). Performance enhancement of outdoor visible-light communication system using selective combining receiver. *IET Optoelectronics*, 3(1):30–39.
- [Lee *et al.*, 2012] Lee, S. J., Kwon, J. K., Jung, S. Y., and Kwon, Y. H. (2012). Simulation modeling of visible light communication channel for automotive applications. In *Proc. Int. IEEE Conf. on Intell. Transp. Syst.*, pages 463–468.
- [Li *et al.*, 2016] Li, X., Jin, F., Zhang, R., Wang, J., Xu, Z., and Hanzo, L. (2016). Users first: User-centric cluster formation for interference-mitigation in visible-light networks. *IEEE Trans. Wireless Commun.*, 15(1):39–53.
- [Li *et al.*, 2015] Li, Y., Pappas, N., Angelakis, V., Pióro, M., and Yuan, D. (2015). Optimization of free space optical wireless network for cellular backhauling. *IEEE J. Sel. Areas Commun.*, 33(9):1841–1854.
- [Li *et al.*, 2013] Li, Y., Pióro, M., and Angelakisi, V. (2013). Design of cellular backhaul topology using the FSO technology. In *2013 2nd International Workshop on Optical Wireless Communications*, pages 6–10.
- [Ling *et al.*, 2018] Ling, X., Wang, J., Ding, Z., Zhao, C., and Gao, X. (2018). Efficient OFDMA for LiFi downlink. *J. Lightw. Technol.*, 36(10):1928–1943.
- [Lopez-Hernandez *et al.*, 2000] Lopez-Hernandez, F. J., Perez-Jimenez, R., and Santamaria, A. (2000). Ray-tracing algorithms for fast calculation of the channel impulse response on diffuse IR wireless indoor channels. *Opt. Eng.*, 39(10):2775–2780.
- [Louiej *et al.*, 2018] Louiej, A., Jabrane, Y., Gil Jiménez, V. P., and García Armada, A. (2018). Practical guidelines for approaching the implementation of neural networks on FPGA for PAPR reduction in vehicular networks. *Sensors*, 19(1).
- [Ma *et al.*, 2015] Ma, H., Lampe, L., and Hranilovic, S. (2015). Coordinated broadcasting for multiuser indoor visible light communication systems. *IEEE Trans. Commun.*, 63(9):3313–3324.
- [Ma *et al.*, 2018] Ma, H., Mostafa, A., Lampe, L., and Hranilovic, S. (2018). Coordinated beamforming for downlink visible light communication networks. *IEEE Trans. Commun.*, 66(8):3571–3582.

Bibliography

- [Mesleh *et al.*, 2010] Mesleh, R., Mehmood, R., Elgala, H., and Haas, H. (2010). Indoor MIMO optical wireless communication using spatial modulation. In *Proc. IEEE Int. Conf. Commun.*, pages 1–5.
- [Meyer-Arendt, 1968] Meyer-Arendt, J. R. (1968). Radiometry and photometry: Units and conversion factors. *Appl. Opt.*, 7(10):2081–2084.
- [Modepalli and Parsa, 2013] Modepalli, K. and Parsa, L. (2013). Dual purpose HB-LED driver for illumination and visible light communication. In *2013 Twenty-Eighth Annual IEEE Applied Power Electronics Conference and Exposition (APEC)*, pages 875–880.
- [Morales-Céspedes *et al.*, 2018] Morales-Céspedes, M., Paredes-Paredes, M. C., García Armada, A., and Vandendorpe, L. (2018). Aligning the light without channel state information for visible light communications. *IEEE J. Sel. Areas Commun.*, 36(1):91–105.
- [Na *et al.*, 2018] Na, Z., Wang, Y., Xiong, M., Liu, X., and Xia, J. (2018). Modeling and throughput analysis of an ADO-OFDM based relay-assisted VLC system for 5G networks. *IEEE Access*, 6:17586–17594.
- [Narmanlioglu *et al.*, 2017] Narmanlioglu, O., Kizilirmak, R. C., Miramirkhani, F., and Uysal, M. (2017). Cooperative visible light communications with full-duplex relaying. *IEEE Photon. J.*, 9(3):1–11.
- [Novlan *et al.*, 2012] Novlan, T. D., Ganti, R. K., Ghosh, A., and Andrews, J. G. (2012). Analytical evaluation of fractional frequency reuse for heterogeneous cellular networks. *IEEE Trans. Commun.*, 60(7):2029–2039.
- [Ntogari *et al.*, 2011] Ntogari, G., Kamalakis, T., Walewski, J., and Sphicopoulos, T. (2011). Combining illumination dimming based on pulse-width modulation with visible-light communications based on discrete multitone. *IEEE/OSA J. Opt. Commun. Netw.*, 3(1):56–65.
- [OSRAM, 2003] OSRAM (2003). Golden Dragon LA W57B Datasheet. *OSRAM Opto Semiconductors GmbH*.
- [Pateromichelakis *et al.*, 2013] Pateromichelakis, E., Shariat, M., u. Quddus, A., and Tafazolli, R. (2013). On the evolution of multi-cell scheduling in 3GPP LTE / LTE-A. *IEEE Commun. Surveys Tuts.*, 15(2):701–717.
- [Pathak *et al.*, 2015] Pathak, P. H., Feng, X., Hu, P., and Mohapatra, P. (2015). Visible light communication, networking, and sensing: A survey, potential and challenges. *IEEE Commun. Surveys Tuts.*, 17(4):2047–2077.
- [Qiu *et al.*, 2018] Qiu, Y., Chen, S., Chen, H., and Meng, W. (2018). Visible light communications based on CDMA technology. *IEEE Wireless Commun.*, 25(2):178–185.
- [Rahmatallah and Mohan, 2013] Rahmatallah, Y. and Mohan, S. (2013). Peak-to-average power ratio reduction in OFDM systems: a survey and taxonomy. *IEEE Commun. Surveys Tuts.*, 15(4):1567–1592.
- [Rahnema, 1993] Rahnema, M. (1993). Overview of the GSM system and protocol architecture. *IEEE Commun. Mag.*, 31(4):92–100.

- [Rajagopal *et al.*, 2012] Rajagopal, S., Roberts, R. D., and Lim, S. (2012). IEEE 802.15.7 visible light communication: modulation schemes and dimming support. *IEEE Commun. Mag.*, 50(3):72–82.
- [Rappaport, 2002] Rappaport, T. (2002). *Wireless communications: Principles and practice*. Prentice Hall communications engineering and emerging technologies series. Prentice Hall, 2nd edition.
- [Rappaport *et al.*, 2013] Rappaport, T. S., Sun, S., Mayzus, R., Zhao, H., Azar, Y., Wang, K., Wong, G. N., Schulz, J. K., Samimi, M., and Gutierrez, F. (2013). Millimeter wave mobile communications for 5G cellular: It will work! *IEEE Access*, 1:335–349.
- [Rondanelli *et al.*, 2015] Rondanelli, R., Molina, A., and Falvey, M. (2015). The Atacama surface solar maximum. *Bull. Amer. Meteorol. Soc.*, 96(3):405–418.
- [Sawahashi *et al.*, 2010] Sawahashi, M., Kishiyama, Y., Morimoto, A., Nishikawa, D., and Tanno, M. (2010). Coordinated multipoint transmission/reception techniques for LTE-advanced [Coordinated and Distributed MIMO]. *IEEE Wireless Commun.*, 17(3):26–34.
- [Schulze, 2016] Schulze, H. (2016). Frequency-domain simulation of the indoor wireless optical communication channel. *IEEE Trans. Commun.*, 64(6):2551–2562.
- [Shaw *et al.*, 2007] Shaw, W. T., Wong, S. W., Cheng, N., Balasubramanian, K., Zhu, X., Maier, M., and Kazovsky, L. G. (2007). Hybrid architecture and integrated routing in a scalable optical-wireless access network. *J. Lightw. Technol.*, 25(11):3443–3451.
- [Somekh *et al.*, 2007] Somekh, O., Simeone, O., Bar-ness, Y., Haimovich, A. M., Spagnolini, U., and Shamai, S. (2007). *An Information Theoretic View of Distributed Antenna Processing in Cellular Systems*. Auerbach Publication, CRC Press.
- [Song *et al.*, 2015] Song, J., Ding, W., Yang, F., Yang, H., Yu, B., and Zhang, H. (2015). An indoor broadband broadcasting system based on PLC and VLC. *IEEE Trans. Broadcast.*, 61(2):299–308.
- [Sun *et al.*, 2017] Sun, Z. G., Yu, H., and Zhu, Y. J. (2017). A superimposed relaying strategy and power allocation for outdoor visible light communications. *IEEE Access*, 5:9555–9561.
- [Takagi and Sugeno, 1985] Takagi, T. and Sugeno, M. (1985). Fuzzy identification of systems and its applications to modeling and control. *IEEE Trans. Syst., Man, Cybern.*, SMC-15(1):116–132.
- [Takai *et al.*, 2013] Takai, I., Ito, S., Yasutomi, K., Kagawa, K., Andoh, M., and Kawahito, S. (2013). LED and CMOS image sensor based optical wireless communication system for automotive applications. *IEEE Photon. J.*, 5(5):6801418–6801418.
- [Taylor, 2009] Taylor, J. L. (2009). Reflectance measurements of materials used in the solar industry. *Technical Note, UV/Vis/NIR*.
- [TDoc R1-060023, 2006] TDoc R1-060023 (2006). Cubic Metric in 3GPP-LTE. *3GPP TSG RAN WG1, Tech. Rep.*

Bibliography

- [Tellado, 2000] Tellado, J. (2000). Multicarrier modulation with low PAR: Applications to DSL and wireless. *New York, NY, USA: Springer*.
- [Tipmongkolsilp *et al.*, 2011] Tipmongkolsilp, O., Zaghloul, S., and Jukan, A. (2011). The evolution of cellular backhaul technologies: Current issues and future trends. *IEEE Commun. Surveys Tuts.*, 13(1):97–113.
- [Tsonev *et al.*, 2014] Tsonev, D., Chun, H., Rajbhandari, S., McKendry, J. J. D., Videv, S., Gu, E., Haji, M., Watson, S., Kelly, A. E., Faulkner, G., Dawson, M. D., Haas, H., and O’Brien, D. (2014). A 3-Gb/s single-LED OFDM-based wireless VLC link using a gallium nitride μ LED. *IEEE Photon. Technol. Lett.*, 26(7):637–640.
- [Tugnait and He, 2010] Tugnait, J. K. and He, S. (2010). Multiuser/MIMO doubly selective fading channel estimation using superimposed training and Slepian sequences. *IEEE Trans. Veh. Technol.*, 59(3):1341–1354.
- [Uysal *et al.*, 2015] Uysal, M., Ghassemlooy, Z., Bekkali, A., Kadri, A., and Menouar, H. (2015). Visible light communication for vehicular networking: performance study of a V2V system using a measured headlamp beam pattern model. *IEEE Veh. Technol. Mag.*, 10(4):45–53.
- [Vucic *et al.*, 2010] Vucic, J., Kottke, C., Nerreter, S., Langer, K., and Walewski, J. W. (2010). 513 Mbit/s visible light communications link based on DMT-modulation of a white LED. *J. Lightw. Technol.*, 28(24):3512–3518.
- [Wang *et al.*, 2015] Wang, F., Wang, Z., Qian, C., Dai, L., and Yang, Z. (2015). Efficient vertical handover scheme for heterogeneous VLC-RF systems. *IEEE/OSA J. Opt. Commun. Netw.*, 7(12):1172–1180.
- [Wang and Yeh, 2011] Wang, L. and Yeh, C. (2011). 3-cell network MIMO architectures with sectorization and fractional frequency reuse. *IEEE J. Sel. Areas Commun.*, 29(6):1185–1199.
- [Wang *et al.*, 2015a] Wang, Q., Qian, C., Guo, X., Wang, Z., Cunningham, D. G., and White, I. H. (2015a). Layered ACO-OFDM for intensity-modulated direct-detection optical wireless transmission. *Opt. Express*, 23(9):12382–12393.
- [Wang *et al.*, 2007] Wang, T., Cano, A., Giannakis, G. B., and Laneman, J. N. (2007). High-performance cooperative demodulation with decode-and-forward relays. *IEEE Trans. Commun.*, 55(7):1427–1438.
- [Wang *et al.*, 2015b] Wang, Y., Chi, N., Wang, Y., Tao, L., and Shi, J. (2015b). Network architecture of a high-speed visible light communication local area network. *IEEE Photon. Technol. Lett.*, 27(2):197–200.
- [Wang and Haas, 2015] Wang, Y. and Haas, H. (2015). Dynamic load balancing with handover in hybrid Li-Fi and Wi-Fi networks. *J. Lightw. Technol.*, 33(22):4671–4682.
- [Wang *et al.*, 2015c] Wang, Y., Tao, L., Huang, X., Shi, J., and Chi, N. (2015c). 8-Gb/s RGBY LED-based WDM VLC system employing high-order CAP modulation and hybrid post equalizer. *IEEE Photon. J.*, 7(6):1–7.

- [Wang *et al.*, 2015] Wang, Z., Tsonev, D., Videv, S., and Haas, H. (2015). On the design of a solar-panel receiver for optical wireless communications with simultaneous energy harvesting. *IEEE J. Sel. Areas Commun.*, 33(8):1612–1623.
- [Wang *et al.*, 2018] Wang, Z., Wang, Q., Huang, W., , and Xu, Z. (2018). *Visible Light Communications: Modulation and Signal Processing*. Wiley-IEEE Press.
- [Webster, 2010] Webster, S. (2010). Designing an LTE network using EDX SignalPro. *EDX Wireless, Technology White Paper*.
- [Wu *et al.*, 2017] Wu, L., Cheng, J., Zhang, Z., Dang, J., and Liu, H. (2017). Channel estimation for optical-OFDM-based multiuser MISO visible light communication. *IEEE Photon. Technol. Lett.*, 29(20):1727–1730.
- [Xiong, 2006] Xiong, F. (2006). *Digital modulation techniques*. Artech House, Inc., Norwood, MA, USA, 2nd edition.
- [Yang *et al.*, 2015] Yang, L., Hasna, M. O., and Gao, X. (2015). Performance of mixed RF/FSO with variable gain over generalized atmospheric turbulence channels. *IEEE J. Sel. Areas Commun.*, 33(9):1913–1924.
- [Yin *et al.*, 2015] Yin, L., Wu, X., Haas, H., and Hanzo, L. (2015). Low-complexity SDMA user-grouping for the CoMP-VLC downlink. In *Proc. IEEE Global Communications Conference*, pages 1–6.
- [Yu, 2014] Yu, Z. (2014). Optical wireless communications with optical power and dynamic range constraints. *Ph.D. dissertation, Dept. Elect. and Comp. Eng., Georgia Inst. Tech., Atlanta, GA, USA*.
- [Yu *et al.*, 2013a] Yu, Z., Baxley, R. J., and Zhou, G. T. (2013a). Multi-user MISO broadcasting for indoor visible light communication. In *Proc. IEEE Int. Conf. Acoust., Speech, Signal Process.*, pages 4849–4853.
- [Yu *et al.*, 2013b] Yu, Z., Baxley, R. J., and Zhou, G. T. (2013b). Peak-to-average power ratio and illumination-to-communication efficiency considerations in visible light OFDM systems. In *2013 IEEE International Conference on Acoustics, Speech and Signal Processing*, pages 5397–5401.
- [Zhang *et al.*, 2015] Zhang, R., Wang, J., Wang, Z., Xu, Z., Zhao, C., and Hanzo, L. (2015). Visible light communications in heterogeneous networks: Paving the way for user-centric design. *IEEE Wireless Commun.*, 22(2):8–16.
- [Zhang *et al.*, 2018] Zhang, T., Zou, Y., Sun, J., and Qiao, S. (2018). Improved companding transform for PAPR reduction in ACO-OFDM-based VLC systems. *IEEE Commun. Lett.*, 22(6):1180–1183.
- [Zhang *et al.*, 2017] Zhang, X., Wang, Q., Zhang, R., Chen, S., and Hanzo, L. (2017). Performance analysis of layered ACO-OFDM. *IEEE Access*, 5:18366–18381.
- [Zhao *et al.*, 2015] Zhao, J., Quek, T. Q. S., and Lei, Z. (2015). Heterogeneous cellular networks using wireless backhaul: Fast admission control and large system analysis. *IEEE J. Sel. Areas Commun.*, 33(10):2128–2143.

Bibliography

- [Zhong and Zhang, 2016] Zhong, C. and Zhang, Z. (2016). Non-orthogonal multiple access with cooperative full-duplex relaying. *IEEE Commun. Lett.*, 20(12):2478–2481.